



Investigating air quality in the marine environment of the North and Baltic Sea with MAX-DOAS measurements

Dissertation
zur Erlangung des akademischen Grades
Doktor der Naturwissenschaften
am Fachbereich Physik
der Universität Bremen

vorgelegt von
M.Sc. André Seyler

Bremen, November 2020

1. Gutachter:	Prof. Dr. John P. Burrows
2. Gutachter:	Prof. Dr. Markus Quante
Dissertation eingereicht am:	10.11.2020
Datum des Kolloquiums:	27.01.2021

Abstract

This thesis presents MAX-DOAS measurements of the air pollutants NO_2 and SO_2 focusing on air quality in the marine environment of the North and Baltic Sea and the surrounding coastal areas.

As the first part, the results from more than three years of MAX-DOAS measurements on the island Neuwerk in the German Bight are presented. After the introduction of stricter fuel sulfur content limits (from 1 % to 0.1 %) on 1 January 2015 in the North Sea, a significant reduction in SO_2 levels was observed both in the SO_2 to NO_2 ratios from more than 2000 investigated ship plumes and also in the overall pollution levels. The relative contributions of ships and land-based sources to air pollution levels in the German Bight have been estimated to be around 40 % : 60 % for NO_2 as well as SO_2 in 2013/2014, dropping to 14 % : 86 % for SO_2 in 2015/2016. In addition to that, a clear diurnal and weekly pollution cycle was observed, again pointing at a substantial influence of land-based pollution from road traffic, even on this remote site close to a main shipping lane.

As the second part, a novel application of an "onion peeling" like approach to MAX-DOAS measurements of shipping emissions on Neuwerk was developed, aiming at investigating the strong horizontal inhomogeneities in NO_2 over a shipping lane. The ability to derive the approximate plume positions in the observed area is demonstrated as well as the ability to detect enhanced NO_2 concentrations several kilometers away from the instrument under wind conditions unfavorable for the on-site in-situ instrumentation. Using a Gaussian plume model, in-plume NO_2 volume mixing ratios could be derived from the MAX-DOAS measurements, and were validated with airborne imaging DOAS measurements from the NOSE campaign in August 2013.

In the third part, expanding the research area from the German North Sea coast to the entire greater North Sea area and the German part of the Baltic Sea, shipborne MAX-DOAS measurements for air quality assessment have been performed for the first time on a regular basis in this area on routinely conducted survey cruises in cooperation with the German Federal Hydrographic Agency (Bundesamt für Seeschifffahrt und Hydrographie, BSH). Exemplarily, results from four out of six ship campaigns in the North and Baltic Sea area are presented, including measurements of pollutant plumes emitted from individual passing ships, emissions from shore-based emitters like power plants and oil refineries, an overview on the NO_2 pollution in the whole area which generally agrees with satellite measurements, and a drop of SO_2 pollution levels since 2015 on the open sea. A short lifetime estimation for NO_2 in the marine boundary layer is also included, giving a value of about 4 hours.

List of publications

As first author:

Seyler, A., Meier, A. C., Wittrock, F., Kattner, L., Mathieu-Üffing, B., Peters, E., Richter, A., Ruhtz, T., Schönhardt, A., Schmolke, S., and Burrows, J. P. (2019). “Studies of the Horizontal Inhomogeneities in NO₂ Concentrations above a Shipping Lane Using Ground-Based Multi-Axis Differential Optical Absorption Spectroscopy (MAX-DOAS) Measurements and Validation with Airborne Imaging DOAS Measurements”. In: *Atmos. Meas. Tech.* 12(11), 5959–5977. DOI: 10.5194/amt-12-5959-2019.

Seyler, A., Wittrock, F., Kattner, L., Mathieu-Üffing, B., Peters, E., Richter, A., Schmolke, S., and Burrows, J. P. (2017). “Monitoring Shipping Emissions in the German Bight Using MAX-DOAS Measurements”. In: *Atmos. Chem. Phys.* 17(18), 10997–11023. DOI: 10.5194/acp-17-10997-2017.

As co-author:

Donner, S., Kuhn, J., Van Roozendaal, M., Bais, A., Beirle, S., Bösch, T., Bognar, K., Bruchkouski, I., Chan, K. L., Dörner, S., Drosoglou, T., Fayt, C., Frieß, U., Hendrick, F., Hermans, C., Jin, J., Li, A., Ma, J., Peters, E., Pinardi, G., Richter, A., Schreier, S. F., Seyler, A., Strong, K., Tirpitz, J.-L., Wang, Y., Xie, P., Xu, J., Zhao, X., and Wagner, T. (2020). “Evaluating Different Methods for Elevation Calibration of MAX-DOAS (Multi AXis Differential Optical Absorption Spectroscopy) Instruments during the CINDI-2 Campaign”. In: *Atmos. Meas. Tech.* 13(2), 685–712. DOI: 10.5194/amt-13-685-2020.

Kattner, L., Mathieu-Üffing, B., Burrows, J. P., Richter, A., Schmolke, S., Seyler, A., and Wittrock, F. (2015). “Monitoring Compliance with Sulfur Content Regulations of Shipping Fuel by in Situ Measurements of Ship Emissions”. In: *Atmos. Chem. Phys.* 15(17), 10087–10092. DOI: 10.5194/acp-15-10087-2015.

- Kreher, K., Van Roozendael, M., Hendrick, F., Apituley, A., Dimitropoulou, E., Frieß, U., Richter, A., Wagner, T., Lampel, J., Abuhassan, N., Ang, L., Anguas, M., Bais, A., Benavent, N., Bösch, T., Bogner, K., Borovski, A., Bruchkouski, I., Cede, A., Chan, K. L., Donner, S., Drosoglou, T., Fayt, C., Finkenzeller, H., Garcia-Nieto, D., Gielen, C., Gómez-Martín, L., Hao, N., Henzing, B., Herman, J. R., Hermans, C., Hoque, S., Irie, H., Jin, J., Johnston, P., Khayyam Butt, J., Khokhar, F., Koenig, T. K., Kuhn, J., Kumar, V., Liu, C., Ma, J., Merlaud, A., Mishra, A. K., Müller, M., Navarro-Comas, M., Ostendorf, M., Pazmino, A., Peters, E., Pinardi, G., Pinharanda, M., Piders, A., Platt, U., Postylyakov, O., Prados-Roman, C., Puertedura, O., Querel, R., Saiz-Lopez, A., Schönhardt, A., Schreier, S. F., Seyler, A., Sinha, V., Spinei, E., Strong, K., Tack, F., Tian, X., Tiefengraber, M., Tirpitz, J.-L., van Gent, J., Volkamer, R., Vrekoussis, M., Wang, S., Wang, Z., Wenig, M., Wittrock, F., Xie, P. H., Xu, J., Yela, M., Zhang, C., and Zhao, X. (2020). “Intercomparison of NO₂, O₄, O₃ and HCHO Slant Column Measurements by MAX-DOAS and Zenith-Sky UV-Visible Spectrometers during CINDI-2”. In: *Atmos. Meas. Tech.* 13(5), 2169–2208. DOI: 10.5194/amt-13-2169-2020.
- Meier, A. C., Schönhardt, A., Bösch, T., Richter, A., Seyler, A., Ruutz, T., Constantin, D. E., Shaiganfar, R., Wagner, T., Merlaud, A., Van Roozendael, M., Belegante, L., Nicolae, D., Georgescu, L., and Burrows, J. P. (2017). “High-Resolution Airborne Imaging DOAS Measurements of NO₂ above Bucharest during AROMAT”. In: *Atmos. Meas. Tech.* 10(5), 1831–1857. DOI: 10.5194/amt-10-1831-2017.
- Peters, E., Ostendorf, M., Bösch, T., Seyler, A., Schönhardt, A., Schreier, S. F., Henzing, J. S., Wittrock, F., Richter, A., Vrekoussis, M., and Burrows, J. P. (2019). “Full-Azimuthal Imaging-DOAS Observations of NO₂ and O₄ during CINDI-2”. In: *Atmos. Meas. Tech.* 12(8), 4171–4190. DOI: 10.5194/amt-12-4171-2019.
- Peters, E., Pinardi, G., Seyler, A., Richter, A., Wittrock, F., Bösch, T., Van Roozendael, M., Hendrick, F., Drosoglou, T., Bais, A. F., Kanaya, Y., Zhao, X., Strong, K., Lampel, J., Volkamer, R., Koenig, T., Ortega, I., Puertedura, O., Navarro-Comas, M., Gómez, L., Yela González, M., Piders, A., Remmers, J., Wang, Y., Wagner, T., Wang, S., Saiz-Lopez, A., García-Nieto, D., Cuevas, C. A., Benavent, N., Querel, R., Johnston, P., Postylyakov, O., Borovski, A., Elokhov, A., Bruchkouski, I., Liu, H., Liu, C., Hong, Q., Rivera, C., Grutter, M., Stremme, W., Khokhar, M. F., Khayyam, J., and Burrows, J. P. (2017). “Investigating Differences in DOAS Retrieval Codes Using MAD-CAT Campaign Data”. In: *Atmos. Meas. Tech.* 10(3), 955–978. DOI: 10.5194/amt-10-955-2017.
- Wang, Y., Beirle, S., Hendrick, F., Hilboll, A., Jin, J., Kyuberis, A. A., Lampel, J., Li, A., Luo, Y., Lodi, L., Ma, J., Navarro, M., Ortega, I., Peters, E., Polyansky, O. L., Remmers, J., Richter, A., Puertedura, O., Van Roozendael, M., Seyler, A., Tennyson, J., Volkamer, R., Xie, P., Zbovy, N. F., and Wagner, T. (2017). “MAX-DOAS Measurements of HONO Slant Column Densities during the MAD-CAT Campaign: Inter-Comparison, Sensitivity Studies on Spectral Analysis Settings, and Error Budget”. In: *Atmos. Meas. Tech.* 10(10), 3719–3742. DOI: 10.5194/amt-10-3719-2017.

Contents

1. Motivation and objectives	1
2. Atmosphere and air pollution	3
2.1. History of Earth and its atmosphere(s)	4
2.2. Composition of the contemporary atmosphere	6
2.3. The vertical structure of the atmosphere	11
2.4. Air pollution	16
2.5. NO _x chemistry in the troposphere	20
2.6. SO ₂ chemistry in the troposphere	23
3. Shipping: trends, emissions, regulations	25
3.1. Shipping – a fast growing sector	25
3.2. Shipping emissions	31
3.3. Influence of shipping emissions on air quality and climate	33
3.4. Emission regulations	34
3.5. Studies on the effectiveness of the SO ₂ emission regulation measures	38
3.6. DOAS measurements of shipping emissions – previous studies	39
4. Interaction of light and matter	41
4.1. Electromagnetic radiation	41
4.2. Absorption and emission of light	44
4.3. Molecular spectra and transitions	49
4.4. Scattering in the atmosphere	53
4.5. Electromagnetic radiation in solid matter and at interfaces	55
5. Differential Optical Absorption Spectroscopy (DOAS)	63
5.1. The DOAS method	64
5.2. The DOAS fitting routine	73
5.3. DOAS measurement setups and applications	73
5.4. MAX-DOAS measurement geometry and the selection of a reference spectrum	74
6. MAX-DOAS measurements of shipping emissions of NO₂ and SO₂ on Neuwerk	79
6.1. Measurement site Neuwerk: Instrumentation, measurement geometry and collected data base	79

6.2. O ₄ scaling method – retrieval of path-averaged near-surface VMRs from MAX-DOAS DSCDs	88
6.3. O ₄ scaling method – statistics and validity check	92
6.4. O ₄ scaling method – application to NO ₂ measurements	94
6.5. Comparison of MAX-DOAS path-averaged VMRs to in-situ measurements	96
6.6. Diurnal and weekly variability of NO ₂ – Influence of coastal air masses on air quality on Neuwerk	101
6.7. Influence of recent fuel sulfur content regulations on SO ₂ emissions	103
6.8. Long term analysis maps	118
6.9. Summary and conclusions	121
7. Studies of the horizontal inhomogeneities in NO₂ concentrations above a shipping lane	123
7.1. “Onion peeling” MAX-DOAS approach	123
7.2. Application to ship emission measurements on Neuwerk	127
7.3. Plume modeling	129
7.4. Northerly wind scenario	142
7.5. Southerly wind scenario	148
7.6. In-plume NO ₂ VMRs from MAX-DOAS and validation with airborne imaging DOAS	152
7.7. Summary and conclusions	165
8. Shipborne MAX-DOAS measurements in North and Baltic sea	167
8.1. Shipborne MAX-DOAS: Setup, measurement geometry and data analysis	169
8.2. Celtic Explorer 2013: SO ₂ and NO ₂ from ships	185
8.3. Celtic Explorer 2015: Impact of emission regulations	196
8.4. Celtic Explorer 2016: NO ₂ overview and comparison to satellite measurements	199
8.5. Celtic Explorer 2017: SO ₂ and NO ₂ pollution from shore-based emitters and NO ₂ lifetime estimation	210
8.6. Summary and conclusion	222
9. Summary and conclusions	225
A. Appendix	231
A.1. DOAS fit examples	231
A.2. AIS ship traffic density maps	232
List of abbreviations	235
References	237

Motivation and objectives

Air pollution is a major environmental risk to health (WHO, 2020), causing heart diseases, strokes, lung cancer and both acute and chronic respiratory diseases, including asthma. The World Health Organization (WHO) estimates that worldwide, 7 million deaths annually can be attributed to air pollution, from this about 4.2 million from ambient (outdoor) air pollution (in 2016), and that 9 out of 10 people worldwide breathe polluted air.

Shipping, a sector which featured enormous growth rates in the last decades, is one of the major contributors to air pollution, especially in coastal regions and harbor towns. The North Sea, the main region-of-interest of this thesis, has some of the busiest shipping routes in the world, and a very important one runs from the North Sea into the river Elbe towards both the port of Hamburg and the Kiel canal, the main shortcut into the Baltic Sea. This shipping lane is located close to the German Coast, making the vast ship traffic a very probable air pollution source in this region.

In the last years, the International Maritime Organization (IMO) has tackled this problem by introducing stricter limits on nitrogen oxide (NO_x) emissions as well as the sulfur content of the marine fuels, which is directly proportional to the sulfur dioxide (SO_2) emissions and the production of sulfate aerosols therefrom. In special designated sea areas, the so-called emission control areas (ECAs), even stricter limits and regulations have been set into force. The region-of-interest of this thesis, which comprises the North and Baltic Sea area and its coastal boundaries, is one of these established emission control areas. Inside ECAs, an important reduction step in the allowed marine fuel sulfur content has been taken during the time span of this thesis, from 1 January 2015 on it sank from 1 % to 0.1 %, a drastic reduction, requiring the ships to burn 90 % less “dirty” fuel.

Objectives of this thesis

The first main goal of this thesis was to determine how strong the influence of the ships' emissions on the coastal air quality really is, especially compared to the contributions of land-based pollution sources, and to investigate whether the new IMO fuel sulfur content regulations have a significant impact on air quality and can reduce coastal air pollution levels with respect to SO_2 .

The second objective was to develop a method to retrieve in-plume NO_2 pollutant concentrations from MAX-DOAS measurements of ship emissions. In order to do this, several

problems needed to be solved, including estimation of the total light path length and the fraction of the light path actually passing through the ship's emission plume. Another challenge is the strong in-homogeneity of the pollution field above the shipping lane, where typical assumptions on the pollutant profiles used for urban polluted areas do not hold. Thus, developing new methods and applying and expanding existing approaches to ship emission measurements was one of the main goals of this thesis, to increase the knowledge gained from MAX-DOAS measurements in marine environments.

The third objective of this thesis was to investigate NO₂ and SO₂ pollution levels in the greater North and Baltic Sea area to assess the air quality on the open sea as well as along the coastal boundaries, and to determine the contributions of both marine and shore-based pollution sources like power plants and oil refineries. For this, for the first time in the greater North Sea area, shipborne MAX-DOAS measurements were performed on a regular campaign-basis on routinely conducted survey cruises in cooperation with the German Federal Hydrographic Agency (Bundesamt für Seeschifffahrt und Hydrographie, BSH).

The availability of additional measurement techniques like in-situ trace gas analyzers and airborne imaging DOAS measurements enables to evaluate their applicability for ship emission measurements and to answer the question whether these additional measurements can be used to validate the MAX-DOAS results and to prove the developed concepts and approaches.

Outline of this thesis

The outline of this thesis is as follows: First, the motivation for measurements of air pollution by ships is explained in more detail in both Chapter 2, introducing the Earth's atmosphere and the problem of air pollution, and Chapter 3, that gives an introduction on the shipping sector, shipping emissions and their regulations. Chapter 4 gives an overview on the physics of light and its interaction with the atmosphere for a better understanding of the measurement process and principle, which is explained in Chapter 5.

Chapter 6 describes the measurement station on the island Neuwerk and presents long term trends of ship emission measurements and estimations of the contributions of ship and land-based pollution sources on air quality in a coastal region close to a main shipping lane. Chapter 7 describes a new approach for investigating the horizontal inhomogeneities in the NO₂ field above a shipping lane with MAX-DOAS measurement and deriving in-plume pollutant concentrations from MAX-DOAS atmospheric trace gas columns. Chapter 8 gives an overview on the various shipborne MAX-DOAS measurement campaigns in the North and Baltic Sea onboard the research vessel Celtic Explorer and presents, exemplarily, the most important results trying to answer the above-mentioned questions.

Finally, Chapter 9 summarizes the results and gives an outlook on future tasks.

Atmosphere and air pollution

“*For the first time in my life I saw the horizon as a curved line. It was accentuated by a thin seam of dark blue light – our atmosphere. Obviously this was not the ocean of air I had been told it was so many times in my life. I was terrified by its fragile appearance.*

— **Ulf Merbold**
(ESA Astronaut)

Space often seems to be very far away from us. Although there is no well-defined top of the atmosphere, as density continues to decrease exponentially with height, the Kármán line at 100 km height, where approximately 99.9999 % or all but one millionth of the mass of the atmosphere can be found below, is an often used attempt to define an atmospheric boundary. Admittedly, 100 km is not nearby, but for many people space is closer than the sea. Compared to the Earth's radius of about 6400 km, the atmosphere is a very thin layer around our planet. Life on Earth critically depends on that thin, fragile, mostly transparent shell.

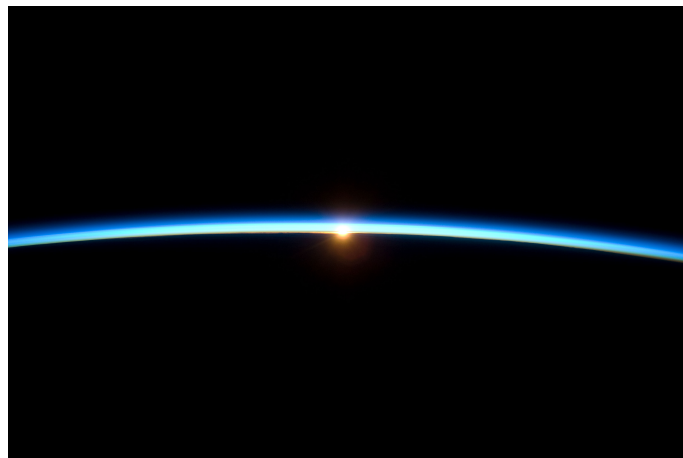


Figure 2.1.: Earth's atmosphere from space, photographed by the crew of the ISS.¹

This chapter provides a short history of the Earth and its atmosphere, gives an overview on its composition and structure, gives a short introduction into air pollution and describes the atmospheric chemistry of the air pollutants of interest for this thesis, NO₂ (or NO_x, respectively) and SO₂.

2.1 History of Earth and its atmosphere(s)

Earth, Venus and Mars all have secondary atmospheres that were formed by outgassing of volatiles like carbon monoxide (CO), carbon dioxide (CO₂), methane (CH₄), hydrogen (H₂), water vapor (H₂O), nitrogen (N₂) and ammonia (NH₃) from condensed materials like minerals during and/or after their formation in the planetary accretion (Schaefer and Fegley, 2010; Wayne, 1992, 2000). After the formation of the Earth about 4.54 ± 0.05 billion years ago (Dalrymple, 2001), “shortly” after the formation of the solar system 4.568 billion years ago (Bouvier and Wadhwa, 2010), Earth’s first and earliest atmosphere was composed of gases captured by gravitational attraction from the solar nebula from which the solar system and all its bodies originated. This primary atmosphere consisted most probably² mainly of hydrogen (H₂), by far the most abundant element in the Universe, and simple hydrides like H₂O, CH₄ and NH₃ (Zahnle et al., 2010)³.

On the inner planets, the terrestrial worlds, the primary atmosphere’s gas molecules were blown away by solar winds after the fusion in the Sun was ignited, but also simply escaped the gravitational pull to space, the latter being determined by a combination of surface temperature, mass of the molecules/atoms and the escape velocities of the planets. The much more massive, but also colder outer Jovian worlds (Jupiter, Saturn, Uranus and Neptune) held their primary atmospheres due to a combination of gravity-related higher escape velocities and temperature-related lower average molecule velocities, making it much less likely for gas molecules to escape to space. (Fegley Jr and Schaefer, 2012; Zahnle et al., 2010)

For Earth, the widely accepted theory of the collision with a (proto-)planet roughly the size of Mars⁴ around 30 to 100 million years after the formation of the Solar system (Zahnle et al., 2010), which probably created the Moon, might have helped to enhance the temperature in the primary atmosphere to a level where many molecules easily reach escape velocity. If H₂O was present, hydroxy radicals (OH) would have been formed photochemically attacking both CH₄ and NH₃ on times very short compared to geological time scales. Hydrogen and Helium are able to escape the Earth’s atmosphere even today. (Wayne, 1992, 2000)

¹NASA image of the day 23 Nov. 2009, public domain, https://www.nasa.gov/multimedia/imagegallery/image_feature_1529.html

²As there is little if any geological record, or “rock record”, from this time (Fegley Jr and Schaefer, 2012; Zahnle et al., 2010)

³Similar to the gas mixtures used in the famous Miller–Urey experiment’s synthesis of organic compounds (Miller and Urey, 1959; Zahnle et al., 2010)

⁴The hypothetical (proto-)planet “Theia”, which is believed to have formed from the solar nebular in the same distance from the Sun as Earth and thus in a similar orbit as Earth, probably in the Lagrange point L₄ of the Sun-Earth-system (Belbruno and Gott III, 2005)

Heating of the inner planets by impacts of infalling bodies, radioactive decay and the accretion process itself led to outgassing of the secondary atmospheres; meteorites and comets may also have contributed (Wayne, 1992, 2000). The volatiles released from minerals to form this secondary atmospheres on Earth, Venus and Mars were mainly H₂O and CO₂, with some N₂ and small amounts or traces of sulfur dioxide (SO₂), CO, H₂ and noble gases (Schaefer and Fegley, 2010; Wayne, 2000; Zahnle et al., 2010).

What happened to the H₂O in the atmosphere, after the planets cooled down, depended on the temperature (and pressure). On Earth, the surface temperature ended up in the suitable range for the existence of liquid water, so the water vapor in the “steam” atmosphere condensed and rained out and formed the oceans, around 4.2 to 4.4 billion years ago (Cavosie et al., 2005; Fegley Jr and Schaefer, 2012; Mojzsis et al., 2001). On Venus, being closer to the sun, the higher temperatures as the brightness of the sun increased might have led to a so-called runaway greenhouse effect. Liquid water on the surface evaporated and the resulting water vapor in the atmosphere, having a strong greenhouse potential blocking outgoing radiation, led to a further warming and again increased evaporation. This positive feedback process caused in a cascade-like effect the vaporization of all surface water, which was then, in geological time scales, photodissociated and the hydrogen escaped to space, leaving back a very dry, hot atmosphere with high surface pressure being dominated by CO₂ (Wayne, 1992, 2000). On Mars, being further from the sun, channels on the surface suggest that once liquid water existed, but today almost all of the water is frozen and exists as ice at the polar caps, while only traces of water vapor exist in its atmosphere (Jakosky and Haberle, 1992; Wayne, 1992). As a consequence, Mars’ atmosphere is also dominated by CO₂. On Earth, the tendency of CO₂ to being dissolved in liquid water and to form insoluble carbonates led to the bulk of CO₂ being bound in sedimentary carbonate rocks leaving a mildly reducing secondary atmosphere at first (Wayne, 2000).

At some point during the “heavy bombardment” period with several large (≥ 100 km diameter) impactors hitting the Earth-moon system⁵ between approximately 4.5 and 3.8 billion years ago⁶ (Kasting, 1993), life originated on Earth (Bada, 2004; Fegley Jr and Schaefer, 2012).

After oxygenic photosynthesis has evolved in cyanobacteria, phototrophic microorganisms converted CO₂ to oxygen (O₂), leading to the first rising of O₂ levels in the atmosphere between 2.45 and 2.3 billion years ago, the so-called “Great Oxidation Event” (GOE) (e.g. Kasting, 2002; Kasting, 2013). The increasing accumulation of O₂ in the atmosphere in the following changed its character from mildly reducing to an oxidizing atmosphere,

⁵The craters can still be seen on the moon today.

⁶Some of the earliest rock records from Isua Greenstone Belt in Greenland suggest that this happened not later than 3.8 billion years ago (Arndt and Nisbet, 2012; Sleep et al., 2012), while the investigation of ancient zircon crystals from Jack Hills, Western Australia, the oldest records on Earth, going back to up to 4.4 billion years ago, dates the origin of life back to 4.1 billion years ago at the latest (Bell et al., 2015).

completely changing the nature of chemical interactions between geological substrates like rocks or sand, the air and oceans (Kasting, 1993; Zahnle et al., 2010). Ozone (O_3) was photochemically produced from the accumulated O_2 in the atmosphere and an ozone layer developed, allowing for life outside of the oceans by absorbing harmful UV radiation and thereby shielding Earth's surface (e.g. Kasting, 1993; Wayne, 1992). The presence of oxygen gave rise to a breakthrough in metabolic evolution, peaking in the Cambrian animal radiation (or "Cambrian explosion") about 541 million years ago (Budd and Jackson, 2016; Maloof et al., 2010; Sperling et al., 2013).

In the last centuries since the onset of industrialization, impacts of human activities on the environment have drastically increased, in many ways outcompeting natural processes. Be it the strong increase in emission of air pollutants and greenhouse gases or geological impacts like land-use change or deforestation, mankind has substantially shaped the natural environment, for which "it is justified to assign the term *anthropocene* to the current geological epoch" (Crutzen, 2006).

2.2 Composition of the contemporary atmosphere

Today's atmosphere is mainly composed of N_2 (78 %) and O_2 (21 %) and small amounts of Argon (1 %), the most abundant noble gas, and water vapor (highly variable, 0–5 % depending on humidity conditions, evaporation and precipitation), see Table 2.1 for an overview. The noble gases are chemically inert and their volume fraction in the atmosphere is stable. The remaining constituents, the trace gases, make up less than 1 % of the atmosphere, but play a crucial role in Earth's radiative balance and in its atmospheric chemistry. Most of the trace gases' concentrations have been underlying a rapid change over the last two centuries, the time since the industrial revolution, while the concentrations of N_2 , O_2 and the noble gases, being controlled by the biosphere, uptake and release as well as degassing from the crust and interior of the Earth, only change over geological time scales. (Seinfeld and Pandis, 2006)

Due to its strong triple covalent bond, the nitrogen molecule is practically inert and only reacts under addition of high energy under high temperatures (Zel'dovich mechanism, see Section 2.5) caused by combustion processes or due to ionization by lightning or cosmic radiation. Nitrogen, being an essential nutrient for all living organisms, in the form of N_2 is not useful to most organisms and has to be converted to nitrogen compounds first (the so-called nitrogen fixation). Naturally, this is accomplished by a few microorganisms in soils using nitrogenase enzymes for N_2 fixation (Seinfeld and Pandis, 2006). In the early

1900s, Fritz Haber and Carl Bosch invented the industrial nitrogen fixation to ammonia in the so-called Haber–Bosch process,



and revolutionized the agricultural industry (Dincer and Zamfirescu, 2011; Sommer et al., 2013, e.g.).

99.99% of the nitrogen in the atmosphere exists as nitrogen gas (N_2) and is practically not involved in the chemistry of the troposphere and stratosphere, and more than 99% of the remaining nitrogen is nitrous oxide (N_2O), an important greenhouse gas. Although the other nitrogen compounds in the atmosphere are only present in traces (see Table 2.1), they are nevertheless of crucial importance in atmospheric chemistry. Ammonia (NH_3) is the only basic gas in the atmosphere, and nitrogen oxides ($\text{NO}_x = \text{NO} + \text{NO}_2$) play important roles in the chemistry of both troposphere (see Section 2.5) and stratosphere. (Seinfeld and Pandis, 2006; Wallace and Hobbs, 2006)

The other dominant constituent of Earth’s atmosphere is diatomic oxygen (O_2), which is of crucial relevance for respiration of almost all living organisms on Earth. As discussed above, the present O_2 level is a balance between production of O_2 in oxygenic photosynthesis and removal of O_2 from the atmosphere by respiration and decay of organic matter. Photodissociation of O_2 molecules produces oxygen radicals, which play an important role in the atmospheric oxidation chemistry (see Section 2.4) and in the production of ozone (O_3). Ozone in the stratosphere (about 90% of the total atmospheric ozone), the “good ozone”, is very important for life on Earth, as it forms the ozone layer which absorbs and shields the surface from harmful UV radiation, while at the same time being responsible for the stratospheric temperature profile. Ozone⁷ in the troposphere (about 10% of the total ozone), the “bad ozone”, however, is a main constituent of photochemical smog and considered as hazardous to human health and plants. (Seinfeld and Pandis, 2006; Wallace and Hobbs, 2006)

Being in a balanced cycle with oxygen, the CO_2 level in the atmosphere depends on the uptake of CO_2 by photosynthesis and the release of CO_2 by respiration and decay of organic carbon and therefore shows a seasonal variability. Since the onset of the industrial revolution, the seasonal cycle of CO_2 is superimposed with an increasing trend due to anthropogenic combustion of fossil fuels. CO_2 belongs to the so-called greenhouse gases, a group of molecules that are highly effective at absorbing and trapping Earth’s

⁷The name “ozone” is based on the Greek word *ozein*, “to smell”, giving a hint on the peculiar odor of the gas. It has been used for therapy purposes to cure various diseases in the past, but nowadays it is considered as ineffective and toxic (Palmer, 2017).

outgoing infrared radiation⁸ working as atmospheric thermal insulators⁹, and its increasing concentration is contributing to global warming. Other important greenhouse gases are water vapor, methane (CH₄), nitrous oxide (N₂O), carbon monoxide (CO), ozone and some halocarbons, especially the chlorofluorocarbons (CFCs) (Seinfeld and Pandis, 2006; Wallace and Hobbs, 2006). Water vapor is the most powerful greenhouse gas in Earth's atmosphere and accounts for roughly half of the present-day greenhouse effect (Schmidt et al., 2010; Sherwood et al., 2018). Methane is about 30 times more effective as a greenhouse gas than CO₂, but its residence time¹⁰ in the atmosphere is shorter (IPCC, 2013, and references therein). Its atmospheric abundance has more than doubled since pre-industrial times, from ~700 ppb to 1800 ppb and it contributes with about 20 % to the anthropogenic greenhouse effect, the so-called “global warming” (IPCC, 2013, and references therein). The amount of N₂O in the atmosphere has also increased due to the agricultural sector (Seinfeld and Pandis, 2006).

The infrared radiation emitted by the Earth corresponds to a blackbody with an “effective” temperature of $-18\text{ }^{\circ}\text{C}$ (255 K), which is 33 K below the global mean surface temperature of $15\text{ }^{\circ}\text{C}$ (288 K), the difference being due to the natural greenhouse effect of Earth's atmosphere. $-18\text{ }^{\circ}\text{C}$ (255 K) would therefore be the temperature of an hypothetical planet Earth without its atmosphere, a temperature below the freezing point of water, which shows how crucial the greenhouse effect is for life on Earth. (Brasseur, 1999; Wayne, 2000).

CFCs are an impressive example on how an atmospheric trace species is able to perturb large-scale atmospheric chemistry (Seinfeld and Pandis, 2006). First synthesized in 1928 on the search of a nonflammable, nontoxic refrigerant, CFCs have been industrially manufactured for more than half a century under the trade name *Freon* and have been widely used as refrigerants, propellants in aerosol cans, inflating agents for foams, solvents and cleansing agents. The most common chlorofluorocarbons are CFC-11 (CFCl₃) and CFC-12 (CF₂Cl₂). Due to their chemical inertness and thus, very long tropospheric residence times, CFCs spread globally and eventually found their way to the stratosphere¹¹, where they absorb UV radiation and photodissociate, releasing chlorine, which can destroy ozone in catalytic cycles (Wallace and Hobbs, 2006).

Being so effective in depleting stratospheric ozone, at some point CFCs caused the essentially complete disappearance of ozone in the Antarctic stratosphere during austral spring, the so-called “ozone hole” (Seinfeld and Pandis, 2006). CFCs have been banned in the Montreal protocol, adopted in 1987, enforced in 1989, being maybe the most effective climate

⁸While the Earth's atmosphere is relatively transparent to incoming solar radiation, it is practically opaque to the outgoing infrared radiation which is re-emitted from Earth's surface.

⁹Although part of the absorbed infrared radiation is re-emitted into space, a part is emitted back to the surface, trapping energy in the atmosphere and causing an additional heating.

¹⁰The time until a new steady state is reached after emission

¹¹Such a troposphere–stratosphere crossing is possible in the tropical tropopause.

contract ever. Since then, with a long delay due to the CFCs' long lifetimes, the loss of stratospheric ozone has stopped and the ozone layer slowly started to recover (Strahan and Douglass, 2018).

The hydroxy radical (OH), despite its very low abundance in the atmosphere (see Table 2.1), is highly reactive and plays an important role in the oxidation and thus removal of other chemical compounds from the atmosphere (Wallace and Hobbs, 2006). Although due to its short lifetime of less than 1 second it has a very short spatial transport scale in the order of centimeters, it is continuously produced while sunlight is present and is the major chemical scavenger in the atmosphere, controlling the atmospheric lifetimes of many trace gases (see Section 2.4 for details) (Seinfeld and Pandis, 2006; Turekian and Holland, 2013).

The trace gas amounts and spatial distributions in the atmosphere do not only depend on the sources and sinks, but also on (photo-)chemical transformations in the atmosphere and transport. The average lifetime of a trace gas molecule in the atmosphere can range from seconds to millions of years (see Table 2.1), depending on the effectiveness of its removal mechanisms.

In addition to gases, the atmosphere also contains liquid (droplets, cloud droplets) and solid particles (ice crystals, smoke, dust) from both natural sources like volcanoes, wildfires, windborne dust, seaspray and meteoric debris, or anthropogenic activities like combustion processes in industry and traffic, and biomass-burning. Liquid or solid particles suspended in the atmosphere are called aerosols¹² or particulate matter (PM). Atmospheric aerosols are either directly emitted as particles (primary aerosol) or formed in the atmosphere (secondary aerosol, e.g. sulfate aerosols as a sink of sulfur dioxide gas (SO₂), see Section 2.6). Aerosols range from a few nanometers to tens of micrometers in size. The designation as particulate matter (PM) is usually used together with a size classification, like PM₁₀ for particles with a diameter <10 μm and PM_{2.5} for particles with a diameter <2.5 μm (Seinfeld and Pandis, 2006).

Even though aerosols only account for a small fraction of the mass of the atmosphere (Wallace and Hobbs, 2006), they are important¹³ for the condensation of water vapor to form clouds by acting as cloud condensation nuclei (CCN), they serve as sites for heterogeneous reactions (reactions involving multiple phases on the aerosol surfaces), they give rise to a variety of atmospheric optical effects by influencing the radiative transfer and thus they can directly impact the radiation budget (by absorption and scattering) and determine atmospheric visibility. Furthermore, small aerosol particles can have adverse health effects and cause premature mortality (Lelieveld et al., 2015).

¹²Although technically an aerosol is defined as an suspension of fine liquid or solid particles in a gas and thus denotes the suspension in total, common usage in atmospheric sciences refers to the aerosol as solely the particulate component (Seinfeld and Pandis, 2006).

¹³Or even mandatory, as without aerosols there would be no clouds in Earth's atmosphere

Table 2.1.: Major constituents of the atmosphere (Brasseur, 1999; Wallace and Hobbs, 2006; Wayne, 2000)

Constituent	VMR ^a	Lifetime ^b	Major sources
Nitrogen (N ₂)	78.08 %	1.6 × 10 ⁷ years	Biological
Oxygen (O ₂)	20.95 %	3000–4000 years	Biological
Argon (Ar)	0.93 %	–	Radiogenic, anthropogenic
Carbon dioxide (CO ₂)	410 ppm ^c	3–4 d (50–200 a) ^d	Biol., oceanic, combustion
Neon (Ne)	18 ppm	–	–
Helium (He)	5 ppm	–	Radiogenic
Methane (CH ₄)	1.8 ppm	~10 years	Biological, anthropogenic
Krypton (Kr)	1 ppm	–	Radiogenic
Hydrogen (H ₂)	0.5 ppm	~2 years	Biological, anthropogenic
Nitrous oxide (N ₂ O)	0.3 ppm	120–150 years	Biological, anthropogenic
Carbon monoxide (CO)	50–200 ppb	~60 days	Radiog., combust., anthrop.
Ozone (O ₃) (strat.)	0.5–10 ppm	Hours–weeks	Photochemical
Ozone (O ₃) (trop.)	10–500 ppb	Days–weeks	Photochemical
NMHC ^e	5–20 ppb	Variable	Biological, anthropogenic
Halocarbons ^f	3.8 ppb	Variable ^f	Mainly anthropogenic
Hydrogen peroxide (H ₂ O ₂)	0.1–10 ppb	~1 day	Photochemical
Formaldehyde (HCHO)	0.1–1 ppb	~1.5 hours	Photochemical
Nitrogen oxides (NO _x)	10 ppt–1 ppm	Hours–days	Anthrop., soil, lightning
Ammonia (NH ₃)	10 ppt–1 ppb	2–10 days	Biological
Sulfur dioxide (SO ₂)	10 ppt–1 ppb	Days	Anthropogenic, volcanic
Hydroxyl radical (OH)	0–0.4 ppt	<1 second	Photochemical
Not included in above dry atmosphere:			
Water vapor (H ₂ O)	0 to 5 %	~9 days	Evaporation

^a Volume mixing ratio, fraction of volume of air occupied by the species. Units: Percentage or parts per million (ppm), parts per billion (ppb) or parts per trillion (ppt)

^b Atmospheric residence time

^c As of 2019 (annual mean). Data source: Dr. Pieter Tans and Dr. Ed Dlugokencky, NOAA/ESRL (www.esrl.noaa.gov/gmd/ccgg/trends/)

^d 3–4 days until a CO₂ molecule is taken up by plants or dissolved in the ocean, 50–200 years after a change in sources or sinks until a new equilibrium is reached

^e Non-methane hydrocarbons (NMHC): all hydrocarbons other than methane (CH₄), including volatile organic compounds (VOCs)

^f Including chlorofluorocarbons (CFCs), which have very long lifetimes up to 100 years and more and are responsible for stratospheric ozone depletion and the “ozone hole”

2.3 The vertical structure of the atmosphere

By intuition, with increasing height in the atmosphere the pressure should decrease, as the weight of the atmosphere above, the mass of gas molecules exerting a downward force due to the Earth's gravitational attraction, should decrease. By assuming a hydrostatic equilibrium, where all forces (pressure and gravity) on an atmospheric air parcel should balance, and neglecting the height dependence of the temperature¹⁴, one can easily derive the so-called barometric equation, which describes the exponential decrease of air pressure with height:

$$p(z) = p_0 \exp\left\{-\frac{z}{H}\right\} \quad \text{with the scale height} \quad H = \frac{RT}{Mg}, \quad (2.1)$$

with the surface pressure (or sea-level pressure) p_0 , molar mass of air M , temperature T and universal gas constant $R = 8.3145 \text{ J K}^{-1} \text{ mol}^{-1}$. The scale height H , the height at which the pressure is reduced by a factor of $1/e \approx 1/3$, depends on the temperature T and the molar mass of the gas mixture in air M . The lower the temperature, the stronger the decrease in pressure per meter (Roedel and Wagner, 2011).

For the Earth's atmosphere, H is in the range of 6 to 8.5 km, a typical value is 8 km. This means that 50% of the mass of the atmosphere are located in the first 5.5 km up from the surface and that every 5.5 km the air pressure is reduced by a factor of 2. In an altitude of 30 km already 99% of the atmosphere are below (Wayne, 2000). The scale height H can also be interpreted as the height of an hypothetical homogeneous atmosphere with constant density, which would be 8 km thick (Roedel and Wagner, 2011).

As H depends on the molar mass and air is a mixture of molecules of different molar masses, one could think that as each atmospheric constituent has its own scale height inversely depending on its molecular weight, demixing of the species must occur with the heaviest molecules residing close to the ground. In fact, such a demixing is not observed until about 85 to 105 km altitude, where the mean free path length between molecule collisions is large enough (about 1 m at 105 km compared to $0.06 \mu\text{m}$ close to the surface) for gas kinetics to work. Below this height, mixing by turbulent fluid motions is much more dominant and molecular-kinetic motions are negligible. This lower part of the atmosphere up to about 100 km is therefore called *homosphere* and the layer above that height is called *heterosphere*. In the heterosphere, due to the demixing the relative abundances of the lighter species increase with height until in the outermost atmosphere only the lightest molecular species can be found, H, H₂ and He. Here, hydrogen atoms can receive enough energy from the sun to reach velocities higher than the escape velocity of the Earth and to

¹⁴Which in a first assumption is reasonable, as the temperature in the atmosphere varies by less than a factor of 2, while the pressure varies by six orders of magnitude (Seinfeld and Pandis, 2006)

escape into space, as discussed in Section 2.1. (Roedel and Wagner, 2011; Wallace and Hobbs, 2006)

While the pressure profile gives an idea of the vertical extent of the Earth's atmosphere, the temperature profile gives an idea on the structure of the atmosphere and divides it into four layers with alternating negative and positive temperature gradients, the *troposphere*, the *stratosphere*, the *mesosphere*, and the *thermosphere*. The lowest layer is the *troposphere*, ranging up to 18 km in the tropics, up to 12 km in the mid-latitudes and up to 6–8 km at the poles. It contains approximately 80–90 % of the mass of the entire atmosphere and almost all water vapor and aerosol particles.

Sunlight heats the Earth's surface and the surface warms the air close to the ground. As pressure and density of air decrease with height (barometric equation (2.1)), with increasing altitude the air expands and is thereby adiabatically cooled with an average lapse rate¹⁵ of about 6.5 K km^{-1} (Seinfeld and Pandis, 2006). Through the whole troposphere, temperature decreases nearly linearly with height. This negative temperature gradient enables hot air masses from the heated surface to rise, which leads to convection and turbulent mixing of the troposphere, making it a highly dynamic, unstable layer with permanent mixing, although at a slower rate in the upper troposphere.

If the rising air masses cool down below the dew point, water vapor can condense¹⁶ and form clouds. Thus, the troposphere is permanently cleansed by cloud droplets and precipitation scavenging the aerosol particles. Almost all known weather phenomena happen in the troposphere.

In a height of about 18 km at the tropics and 9 to 13 km in the higher latitudes the linear temperature decrease stops and a temperature minimum is reached, marking the top of the troposphere, the so-called *tropopause* (Roedel and Wagner, 2011). In the following layer above the tropopause, the *stratosphere*, the temperature increases again due to the absorption of solar UV radiation by ozone molecules which warms the air (Brasseur, 1999). This layer, which extends up to about 50 km, is extremely dry and rich in ozone. Between heights of 15–35 km, the so-called ozone layer is located, with maximum concentrations between 20–30 km, which is highly variable with altitude and intensity changing with latitude, season and meteorological conditions (Wallace and Hobbs, 2006). The stratosphere contains approximately 90 % of the total atmospheric ozone (Wayne, 2000).

The positive temperature gradient in the stratosphere prevents convection to occur and causes a stable stratification¹⁷, effectively inhibiting vertical mixing. It also creates a

¹⁵Atmospheric adiabatic lapse rates range from 5 to 10 K km^{-1} (from moist to dry air), depending on the water content of the air.

¹⁶In the presence of cloud condensation nuclei (CCN), see Section 2.2 above

¹⁷Thus the name, *stratosphere*

temperature inversion that prevents air (due to increasing temperatures) from rising further up than the tropopause and entering the stratosphere, the tropopause acting like a barrier. The spreading of cloud tops when reaching the tropopause level creating an anvil-shaped cloud can sometimes be seen on intense thunderstorms in a distance, like in Fig. 2.2a. At certain regions, though, like in the tropics, exchange between troposphere and stratosphere is possible. (Wallace and Hobbs, 2006)



- (a) Anvil cloud (Cumulonimbus incus) of a thunderstorm reaching and spreading at the barrier-like temperature inversion at the tropopause, making it indirectly visible. Photographed from an airplane by Hussein Kefel, CC BY-SA 3.0, <https://commons.wikimedia.org/w/index.php?curid=30774773>
- (b) Limb view of the Earth's atmosphere from the International Space Station (ISS) showing the troposphere (red-orange layer), the tropopause (sharp brown transition) and noctilucent clouds in the stratosphere (silvery-white layer). The upper regions of the atmosphere – the mesosphere, thermosphere and exosphere – fade from shades of blue to the blackness of space. Photograph taken by the Expedition 28 crew of the ISS on 31 July 2011, https://eoimages.gsfc.nasa.gov/images/imagerecords/76000/76534/iss028e020072_lrg.jpg

Figure 2.2.: Examples of photographs in which the layers of the atmospheric are directly or indirectly visible by eye

The dry character of the stratosphere causes a much longer residence time of aerosol particles, that were brought there by volcanic eruptions or human activities, in the stratosphere than in the troposphere (Wallace and Hobbs, 2006).

The stratosphere extends up to the *stratopause* in about 50 km altitude where the temperature has a local maximum and the temperature gradient is reversing. The next layer extending from 50 to 85 km is the *mesosphere*. As the ozone concentration decreases with increasing altitude, the effect of heating due to absorption of solar UV radiation by ozone molecules decreases and the temperature decreases with height. The negative temperature gradient of the mesosphere causes this layer to be dynamically unstable and to show a lot of vertical mixing, similar as in the troposphere (Brasseur, 1999).

The *mesopause* being reached in a height of about 85 km is the coldest point of the entire atmosphere. Above the mesopause follows the *thermosphere*, where temperature increases

again rapidly with height. It ranges up to about 600 km. While troposphere, stratosphere and mesosphere belong to the well-mixed homosphere, the thermosphere above 100 km belongs to the heterosphere, which is characterized by the demixing of light and heavy components. The relative abundance (or volume fraction) of atomic oxygen increases with height, at some point exceeding those of N₂ and O₂, which decrease due to rapid photodissociation. The whole layer is strongly influenced by solar winds¹⁸ and very short-wave radiation (X-ray and extreme ultraviolet radiation at wavelengths <170 nm) from the Sun, which is almost completely absorbed within the thermosphere by molecular and atomic nitrogen and oxygen, which are ionized and form a plasma of very fast particles having high kinetic energies corresponding to very high temperatures reaching up to 2000 K¹⁹ above 500 km, with strong diurnal variation and depending on solar activity (Brasseur and Solomon, 2005; Roedel and Wagner, 2011). The region where the ions are produced by photoionization in the upper mesosphere and the lower thermosphere is called *ionosphere*. (Brasseur, 1999; Seinfeld and Pandis, 2006).

The final layer above the thermosphere is the *exosphere*, the transition layer to space (Brasseur, 1999). Figure 2.2b shows a photograph from on-board the International Space Station, on which most of the atmospheric layers are visible even by eye.

Of special interest for this thesis is the lowermost part of the troposphere, the *planetary boundary layer* (PBL), also known as the *atmospheric boundary layer* (ABL), where surface interactions play an important role and most emissions of air pollutants (see Section 2.4 on a description of air pollution) take place. The remaining, upper part of the troposphere above the planetary boundary layer is called the *free troposphere*.

The PBL as the layer closest to the ground is dominated by influences from the surface. Heating from the surface creates convection and turbulence. Contrary to the geostrophic wind in the free troposphere, the wind flow field in the PBL is strongly influenced by friction at the ground, vegetation and structures on the surface and the resulting wind shear is creating turbulent eddies. The combination of shear-induced eddies and surface-heating-induced convective eddies makes it a very turbulent layer with strong vertical mixing (Foken and Nappo, 2008; Holton, 2004).

The PBL reaches up to 1 km on average, but its vertical extent is highly variable ranging between a maximum value of 3 km during day (under highly convective conditions) and a minimum value of 100 m or even less at night, depending on the time of the day and meteorological conditions (Brasseur, 1999; Cox and Wathes, 1995; Holton, 2004). Under conditions of large static stability that cause a strong stable stratification its thickness can go down to 10 m or less (Foken and Nappo, 2008).

¹⁸A stream of charged particles emitted from the Sun

¹⁹However, the number density of the particles is so very low, that one would not feel the high temperature, and the main free path length is in the order of several kilometers.

At night, without sunlight-induced heating from the surface, no convection is established and the cold dense air descends. Especially in calm, cloud-free nights, the surface is even colder due to radiative cooling. This creates a positive temperature gradient close to the ground, with cold (heavy) surface air lying below the warmer (lighter) air. This nightly temperature inversion (or radiation inversion) leads to a very stable stratification close to the ground (Ahrens and Henson, 2015; Seinfeld and Pandis, 2006). Despite the stable stratification at night, some turbulent mixing is still happening in the lower part of the PBL due to wind.

In urban areas, where temperatures are generally higher (known as the urban heat island effect), night-time inversions occur less frequently and are less strong due to the warmer surface, mainly caused by the large heat capacity of buildings and streets causing a nightly release of heat stored in concrete and asphalt during the day (Ahrens and Henson, 2015; McCormac, 2012; Stull, 1988).

After sunrise, the sunlit surface warms the air near the ground and convection sets in, eroding the stratification. Usually well before noon, the stable inversion has been replaced by a well-mixed surface layer increasing to a maximum height around afternoon and prevailing until around sunset when the night-time inversion starts to develop again. On a cloudless day, the convective mixed layer can capture the whole PBL up to 1–2 km. In winter times, the developing mixed layer is much thinner. Clouds and/or strong winds can also weaken the daily cycle (McCormac, 2012).

Often, the top of the mixed layer is bounded by a temperature inversion with statically stable air called the *entrainment zone*, which acts as a cap. Air pollutants which are mostly emitted close to the ground, are trapped within or beneath an inversion, i.e., at day in the mixed layer, at night in the ground inversion. The closer the inversion is located to the surface, the higher the pollutant concentrations become close to the ground (Jacobson, 2012; Stull, 1988). This is the reason why during night-time, pollution levels at the ground are often enhanced. Moreover, during night-time, no OH radicals are produced, which are an important sink for most pollutants.

Over the oceans, the situation is different: The heat capacity of a few meters of water is similar to that of the entire (dry) atmosphere above (National Research Council, 1997), the total heat capacity of the oceans is roughly 1000 times the heat capacity of the atmosphere (Mason et al., 2016). Thus, due to the large thermal inertia of the water, the temperature of the ocean water is very stable and changes happen on monthly time scales. Water temperatures are dominated by an annual cycle while a diurnal cycle like on land is nearly non-existent. With this, the diurnal boundary layer cycle described above does not exist in marine environments. The large heat capacity of the ocean water leads to the water temperature cycle being delayed by one or two months compared to the annual cycle of air temperature. Because of this, the *marine boundary layer* (MBL) shows a stable stratification



(a) Aerosols trapped in the surface layer below a nightly temperature inversion in the boundary layer reflect light pollution over Berlin, photograph by Ralf Steikert, CC BY-SA 3.0, <https://commons.wikimedia.org/w/index.php?curid=16629383>

(b) Smog trapped in the mixed layer below a temperature inversion over the city of Almaty (Kazakhstan), photograph by Igors Jefimovs, CC BY 3.0, <https://commons.wikimedia.org/w/index.php?curid=30796742>

Figure 2.3.: Examples of air pollution (aerosols) trapped below temperature inversions in the planetary boundary layer

when water is colder than air which happens in late winter, spring and early summer and is an unstable, mixed layer when water is warmer than air which happens in late summer, autumn and early winter (Böttcher, 2013; Emeis, 2010; Garratt, 1994).

2.4 Air pollution

Concerns about air quality and reports on air pollution problems are not new, but date back long ago. The first reports on health concerns regarding air pollution originate from ancient Rome, where writers were aware of adverse effects on human health. Originally, air pollution was considered to be a local phenomenon in cities and industrial regions (Bell and Treshow, 2002; Jorgensen, 2012). Moses Maimonides, a rabbi, jurist, astronomer, and physician from the 12th century visited Cairo, Egypt, and reported the “air of cities” to be like “befouled water”, “stagnant, turbid, thick, misty, and foggy” in the “narrowness of its streets”, having effects on the “actions of the psyche” like “dullness of understanding, failure of intelligence, and defect of memory ...” (Finlayson-Pitts and Pitts, 1986; Gaffney and Marley, 2003).

Maybe the best documented concerns about air pollution related health effects originate from the city of London, dating back to medieval times, when coal of high sulfur content imported by sea was first used for combustion in many European cities at that time, but particularly in London. Reports of the city being typically lost in a cloud of smoke from wood and dirty coal burning with strong effects on mortality, vegetation and rain

contaminating water can be found in John Evelyn's famous pamphlet *Fumifugium*²⁰ from 1661 (Gaffney and Marley, 2003). The air pollution continued to plague London until the 20th century and peaked in the so-called *killer smog*²¹ events in the 1950s. In the famous London smog episode that occurred from 5 to 9 December 1952, often called the *Great Smog of London*, several thousand people were killed. Increased burning of cheap, sulfur-rich coal in a period of unusually cold winter weather together with a low thermal inversion trapping the pollution close to the ground in a layer less than 100 m thick created a thick fog of a toxic mixture of smoke particles, carbon dioxide, hydrochloric acid (HCl), nitric acid (HNO₃), hydrofluoric acid (HF), arsenic containing acids and especially large amounts of sulfur dioxide which were rapidly oxidized to sulfate aerosols (H₂SO₄). The created haze of concentrated sulfuric acid was very probably the most critical component (Brimblecombe, 2002; Brunekreef and Holgate, 2002; Kim et al., 2009; Sabljic, 2009). It led to the passing of the Clean Air Act of 1956, an important example of environmental legislation very much influencing future legislation (Brimblecombe, 2002; Brimblecombe, 2006; Vallero, 2008).

This London-type smog (or "pea souper smog"), has nothing in common with the Los Angeles phenomena first observed in the early 1940s, which showed strong oxidizing instead of acidic properties (Bell and Treshow, 2002; Gaffney and Marley, 2003; Sabljic, 2009). The cause of the Los-Angeles-type smog²², or photochemical smog, is different to that of London smog: instead of primary pollutants, secondary oxidation products of hydrocarbons and other organic gases (so-called volatile organic compounds, VOCs) in presence of nitrogen oxides in ambient air under strong solar irradiation created especially high concentrations of tropospheric ozone and aerosols which led to the observed reduction in visibility (Gaffney and Marley, 2003; Kim et al., 2009; Sokhi, 2008). The most likely source of the organic precursor molecules were emissions from combustion of hydrocarbon fuels by automobiles and oil refineries (Gaffney and Marley, 2003; Leighton, 1961).

While London smog occurs on cold winter days with high relative humidities accompanied with fog under surface inversions, peaking in the early morning and is therefore also called *winter smog*, Los Angeles smog occurs on warm summer days with low relative humidities under a clear sky accompanied with overhead inversions and is also called *summer smog*. The acid-rich, reducing London smog causes bronchial irritation, the oxidizing Los Angeles smog causes eye irritation and harms plants, while both reduce visibility (Leighton, 1961).

²⁰Subtitle: "The inconveniencie of the aer and smoak of London dissipated. Together with some remedies humbly proposed by J.E. esq. to His Sacred Majestie, and to the Parliament now assembled" [sic]

²¹The term "smog" is a combination, a contraction (portmanteau), of the words "smoke" and "fog" (Seinfeld and Pandis, 2006).

²²Although neither smoke nor fog was involved, it is still called "smog", which nowadays refers to extensive contamination of the air by aerosols, sometimes used loosely for any contamination of the air (Kim et al., 2009; Seinfeld and Pandis, 2006).

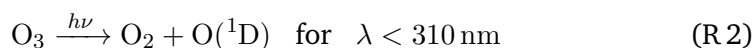
The Los-Angeles-type photochemical smog has since been observed all over the world and marked a major transition of the twentieth century with primary pollutants from stationary sources becoming less important than photochemical precursors from mobile sources (Sokhi, 2008). In the early years of the 21st Century, together with global warming and climate change, global air pollution and the resulting effects have taken on a greater urgency, both within the scientific community and the general public (Vallero, 2008).

Although a number of natural sources for air pollutants exist like volcanoes or forest fires, the major cause of environmental air pollution are anthropogenic activities. Hazardous chemicals escape to the environment either by accident or are released from industrial facilities, emitted from fossil fuel combustion in traffic, heating and power generation and many other activities and may cause adverse effects on human health (both acute and chronic) and the natural environment. The main air pollutants of major health concern are gaseous pollutants such as carbon monoxide (CO), ozone (O₃), nitrogen oxides (NO_x), sulfur dioxide (SO₂) or volatile organic compounds (VOCs), heavy metals like lead or mercury, and respirable particulate matter (especially PM_{2.5} and PM₁₀, and probably ultra fine particles (UFP)). They all differ in their chemical properties, reactivity, lifetime, sources and sinks, and ability to diffuse in long or short distances. Particles, for example, can even absorb and transfer other pollutants on their surface (Kampa and Castanas, 2008).

In our oxidizing atmosphere the main removal of trace gases like the gaseous air pollutants is oxidation. Especially in the troposphere, where most of the atmospheric mass is located and almost all pollutants are emitted, oxidation is of key importance. The oxidation brings the respective substance into a higher oxidation state, increasing the polarity and thus water solubility of the molecules, making wet deposition by precipitation as a sink process more probable (Jacob, 1999).

The most important oxidant²³ in both troposphere and stratosphere is the hydroxy radical (OH) (Jacob, 1999; Lelieveld et al., 2002), the “cleaning agent” or “detergent” of the atmosphere. It is highly reactive and thus short-lived (see Table 2.1 in Section 2.2).

Reaction with OH radicals is the first step in the removal processes of most trace gases during the day, when OH is formed by reaction of water vapor (H₂O) with excited oxygen atoms (O(¹D)) produced from photolysis of ozone by UV radiation:



²³While O₂ and O₃ are the most abundant oxidants, they have large bond energies and are hence relatively unreactive except towards radicals, whereas oxidation of non-radical species by O₂ and O₃ is negligibly slow (Jacob, 1999).

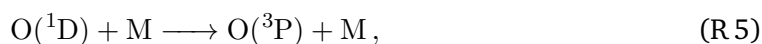
However, most of the O(¹D) atoms dissipate their excess energy as heat (see Reaction (R 5)) and eventually recombine with O₂ to form O₃ and only a small fraction of about 1 % of the O(¹D) react with water vapor (Wallace and Hobbs, 2006). The net reaction is



Critical to the generation of OH is the production of O(¹D) atoms by the photolysis of ozone in (R 2) (Jacob, 1999). While in the stratosphere photons of short-wave UV radiation below 310 nm are plentiful available, in the troposphere the photolysis reaction can only occur over a very narrow spectral interval, between 290 nm and 310 nm, due to the strong ozone absorption in the stratosphere's ozone layer (Levine, 2003). The less intense UV radiation and thus slower production of O(¹D) in the troposphere is compensated in terms of OH production by the larger H₂O mixing ratios (100–1000 times higher than in the stratosphere, where water vapor is sparse) (Jacob, 1999).

Some OH is also produced by photodissociation of nitrous acid (HONO) or photooxidation of formaldehyde (HCHO) and acetone (Clemitshaw, 2015).

Unlike in the stratosphere, in the troposphere with much lower ambient ozone concentrations the availability of O₃ molecules for Reaction (R 2) is crucial for the creation of OH radicals and hence for the self cleaning ability of the troposphere²⁴. The required ozone in the troposphere is in parts transported from the stratosphere or generated by the rapid reaction of ground state oxygen atoms (O(³P)) with oxygen molecules (see Reaction (R 12)). Ground state oxygen atoms are produced by collisions of excited oxygen atoms with air molecules (mostly N₂ or O₂), removing its excess energy and quenching O(¹D) to its ground state²⁵ O(³P),



or more importantly by photolysis of NO₂ (see Reaction (R 11) in Section (2.5), which covers the basic photochemical cycle of NO₂, NO and O₃) (Seinfeld and Pandis, 2006). Dominant sinks for OH are the reactions with CO, methane (CH₄), VOCs, and NO₂ forming nitric acid (HONO₂) and in forests also the reaction with isoprene (C₅H₈) (Clemitshaw, 2015; Wallace and Hobbs, 2006).

In the following, the tropospheric chemistry of the pollutants NO₂ (NO_x) and SO₂ are described in more detail, as those are the trace gases this thesis is focusing on.

²⁴Which is a bit paradox, since tropospheric O₃ is a major air pollutant

²⁵Since the spontaneous O(¹D) → O(³P) transition is forbidden (Seinfeld and Pandis, 2006)

2.5 NO_x chemistry in the troposphere

The global budget of nitrogen oxides (NO_x) is dominated by combustion of fossil fuels, which accounts for about half of the global source. Biomass burning for agriculture and deforestation is another important source, especially in tropic regions. While part of the emitted nitrogen is due to oxidation of the organic nitrogen present in the fuel (depending on the kind of fuel), the main part of NO_x emissions is often due to thermal decomposition of air at the high combustion temperatures. At temperatures above about 2200 K, thermal nitrogen monoxide (“thermal NO”) is produced in the following reactions after thermolysis of oxygen:



At high temperatures, the equilibria in (R 6) to (R 8) are shifted to the right promoting NO formation (Jacob, 1999). In the first reaction, for the heat transfer a stable additional air molecule (M) of high energy is needed to break the bounds of O₂. Reactions (R 7) and (R 8) are known as “Zel’dovich mechanism”²⁶.

In a balanced net reaction, one yields:



Apart from the “thermal NO” there is also the above-mentioned “fuel NO”, especially for petroleum, coal and biomass, while natural gas does not contain nitrogen (Gardiner, 1999).

The same thermal mechanism applies to NO emission from lightning, which is another source of nitrogen oxides in the troposphere (Jacob, 1999). Other important sources include soils (microbes), ammonia (NH₃) oxidation, aircraft emissions and transport from the stratosphere (Wallace and Hobbs, 2006).

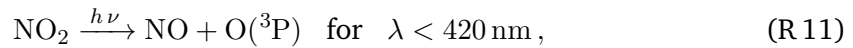
While the NO_x emitted into the troposphere is mainly NO, it quickly reacts with tropospheric ozone (O₃) to form nitrogen dioxide (NO₂):



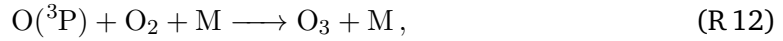
the so-called NO titration or NO_x titration.

²⁶Named after the Russian physicist Yakov Borisovich Zel’dovich, who first proposed the mechanism (Zeldovich, 1946)

During the day, NO₂ molecules can be photolyzed by UV radiation



recovering NO molecules and creating ground state oxygen atoms (O(³P)), which mostly react in a three-body-collision reaction²⁷ with molecular oxygen forming ozone:



which is the only significant source of ozone in the atmosphere (Jacob, 1999; Seinfeld and Pandis, 2006; Singh, 1987).

Reactions (R 10), (R 11) and (R 12) form a cycle, known as the Leighton relationship (Leighton, 1961), which describes the tropospheric ozone concentrations in the presence of NO_x. During the day, this is a so-called *null cycle*, where these gases are continuously transformed into each other, but not lost, resulting in a dynamic equilibrium between NO and NO₂, a so-called *photostationary state*.

The rate limiting step for the production of ozone is the creation of ground state oxygen atoms by the NO₂ photolysis in (R 11), while the O(³P) radical is so reactive, that it disappears by Reaction (R 12) as fast as it is formed by (R 11). Thus, the steady-state approximation can be assumed, giving the following relation between the steady-state NO, NO₂ and O₃ concentrations:

$$[\text{O}_3] = \frac{j_{\text{R}11}[\text{NO}_2]}{k_{\text{R}10}[\text{NO}]}, \quad (2.2)$$

where $j_{\text{R}11}$ is the NO₂ photolysis rate in Reaction (R 11) and $k_{\text{R}10}$ is the rate coefficient of the reaction of NO and O₃ to NO₂ in (R 10).

Thus, the ratio between the NO and NO₂ concentrations stays nearly constant, $[\text{NO}]/[\text{NO}_2] = \text{const.}$, and is proportional to the ozone concentration. Because of the rapid transformations and cycling between NO and NO₂ on time scales of a minute during daytime, the sum of both constituents is often summarized as NO_x = NO + NO₂ (Jacob, 1999; Seinfeld and Pandis, 2006).

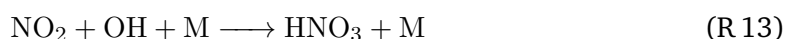
The more intense sunlight is present and/or the more NO₂ is present, the higher the tropospheric ozone concentration. In the presence of sunlight and reduced carbon compounds like CO, or hydrocarbons like VOCs, the production of tropospheric ozone can be even further increased, up to the photochemical smog levels described in Section 2.4.

Typical values of the ratio $[\text{NO}]/[\text{NO}_2]$ are <1 at the surface, 2–3 at 5 km and 12–13 at 10 km height (Seinfeld and Pandis, 2006). In the air close to the surface, $[\text{NO}]/[\text{NO}_2]$ ratios

²⁷An additional compound, M, which usually is an oxygen (O₂) or nitrogen molecule (N₂) is needed for absorbing the excess energy.

range between 0.2–0.5 during the day and even 0.1 during noon, tending to zero at night (Burrows et al., 2011; Hewitt and Jackson, 2009; Seinfeld and Pandis, 2006), when no photolysis of NO_2 occurs and practically all NO_x is available as NO_2 due to Reaction (R 10) (Wayne, 2000).

During daytime, the principal removal path for NO_x from the troposphere is the reaction of NO_2 with the hydroxy radical (OH) forming nitric acid (HNO_3):



The lifetime of NO_x varies from a few hours in the boundary layer to several days in the upper troposphere (Borrell et al., 1997).

In the presence of liquid water, the created nitric acid (HNO_3), which is easily soluble in water, is scavenged by precipitation and released from the atmosphere (wet deposition). Hence, cloud formation and precipitation are a very important sink for NO_x in the lower troposphere and especially in the PBL (Brasseur, 1999; Jacob, 1999).

During night, the fact that NO_2 does not photolyze changes the entire chemistry of the NO_x family. As indicated above, any NO present at night reacts rapidly with ozone and is converted to NO_2 . As NO_2 does not photolyze, it can react with O_3 to produce the nitrate radical (NO_3) (Wayne et al., 1991):



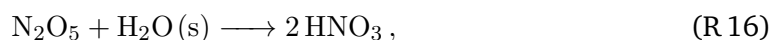
This reaction is the only direct source of NO_3 radicals in the atmosphere (Seinfeld and Pandis, 2006). During daytime the NO_3 is not stable and rapidly photolyzed to NO or NO_2 for wavelengths shorter than 700 nm and 580 nm, respectively, giving it a lifetime of ~ 5 s around noon. During night, as the photochemically produced hydroxy radical (OH) is due to its very short lifetime only present during the day, NO_3 takes over as the major reactive oxidant in the troposphere. Although being less reactive, NO_3 is present in much higher concentrations than OH is during daytime and can serve as an effective oxidizing agent during night (Wallace and Hobbs, 2006).

For example, it is the major sink of NO_x during the night, when it reacts with NO_2 producing N_2O_5 ,



which can thermally decompose back to NO_2 and NO_3 , reverting the reaction and forming an equilibrium on a time scale of a few minutes. At cold temperatures, the forward reaction is much more efficient and the equilibrium is shifted to the right, e.g., in the free troposphere, while in warmer air masses the backward reaction can release NO_2 . In a

heterogeneous (particle-phase) hydrolysis on wet aerosol surfaces, from N_2O_5 again nitric acid (HNO_3) is formed by



which is removed from the atmosphere by wet deposition, making this together with the $\text{OH} + \text{NO}_2$ reaction one of the major removal paths for atmospheric NO_x (Seinfeld and Pandis, 2006). As the principal removal paths for NO_x in the troposphere are based on oxidation to nitric acid (HNO_3) and subsequent solution in liquid water and precipitation, NO_x is an important precursor for acid rain formation just as sulfur dioxide (SO_2), whose chemistry is described in the next section.

2.6 SO_2 chemistry in the troposphere

Like nitrogen, which is essential for living organisms on Earth and contained in various important bio-molecules like amino acids (the building blocks of proteins) and nucleotides (the building blocks of DNA and RNA), sulfur is contained in essential amino acids. Plants and some bacteria can directly assimilate sulfur and some protobacteria's metabolism is completely based on sulfur²⁸ while animals need to ingest sulfur with their food. Release of sulfur compounds as an end product of metabolism plays an important role in the atmospheric sulfur cycle.

Sulfur compounds in the atmosphere, the most important gases being sulfur dioxide (SO_2), hydrogen sulfide (H_2S), dimethyl sulfide (DMS), carbonyl sulfide (COS) and carbon disulfide (CS_2), have both natural and anthropogenic sources. However, the atmospheric sulfur cycle is dominated by anthropogenic activities (about 75 %). Anthropogenic sources include combustion processes of sulfur-containing fossil fuels like coal and oil, smelting of sulfur-containing ores, and biomass burning, releasing mostly sulfur dioxide (SO_2) (Brasseur, 1999; Wallace and Hobbs, 2006; Wayne, 2000). In contrast to NO_x , the amount of SO_2 produced in the combustion depends only on the sulfur content of the fuel. Especially marine fuels like the heavy fuel oils²⁹ used to power ship engines (see Section 3.2) have a high sulfur content, while SO_2 emissions of power plants strongly decreased in the last decades due to the introduction of flue-gas desulfurization by environmental legislation in industrialized countries.

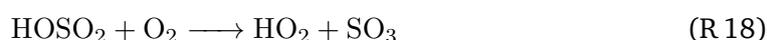
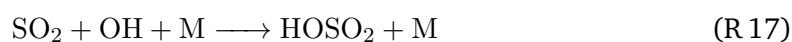
Natural sources of sulfur compounds are dominated by emission of SO_2 from volcanoes (by outgassing and eruptions) and wildfires, and the release of DMS from marine phytoplankton,

²⁸The anaerobic sulfur metabolism was very important on Earth before oxygen levels in the atmosphere increased.

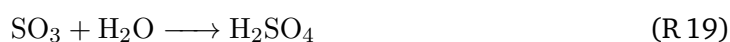
²⁹Which are practically the dirty, residual “waste” of refineries

which is the dominant sulfur compound emitted from the Earth's oceans, but biogenic reactions in terrestrial vegetation, soils and wetlands contribute, too. CS₂ and COS also have mainly biogenic sources. The latter is very stable and has the longest lifetime, making it the sulfur gas with the largest concentration in unpolluted atmospheric regions that can even be transported into the stratosphere, where it is the dominant source of sulfate particles. Very strong volcanic eruptions that directly inject SO₂ into the stratosphere contribute as well to the formation of a stratospheric layer of sulfate aerosols which has a negative radiative forcing effect. In contrast to anthropogenic sources which concentrate on the northern hemisphere (about 90%), the natural sources are nearly equally distributed in northern and southern hemisphere. (Brasseur, 1999; Seinfeld and Pandis, 2006; Wallace and Hobbs, 2006)

Sulfur compounds exist in both reduced and oxidized states, with oxidation numbers ranging from -2 to +6, while Earth's atmosphere has an oxidizing character. Hence, the reduced sulfur compounds of mostly biogenic origin which are released into the atmosphere are generally oxidized – mainly by reaction with OH – to the +4 oxidation state of SO₂, which is apart from the anthropogenic and volcanic emissions the most important source of atmospheric SO₂. Eventually, they are further oxidized to the +6 oxidation state of sulfuric acid (H₂SO₄), the stable form of sulfur in an oxygen-rich atmosphere. This is the main sink for SO₂ which starts with the oxidation by the OH radical forming sulfur trioxide (SO₃):



The produced SO₃, which is the anhydride of sulfuric acid (H₂SO₄), is extremely hygroscopic and reacts rapidly with liquid water:



The created H₂SO₄ aerosol is then removed from the troposphere by wet deposition. Another path is the direct solution of SO₂, which itself is moderately soluble, in water droplets forming sulfurous acid (H₂SO₃). Producing such strong acids, SO₂, similar to NO_x, is an important precursor of acid rain. (Brasseur, 1999; Seinfeld and Pandis, 2006)

As it is for most air pollutants, the SO₂ lifetime is based on the reaction with the OH radical and amounts to about one week in the free troposphere. In addition to that, SO₂ is also one of the gases that is quite efficiently removed from the atmosphere by dry deposition. With a dry deposition velocity of about 1 cm s⁻¹, its lifetime in a boundary layer of 1 km height computes to about one day. When in addition clouds (water droplets) are present, the removal is enhanced even more, making the lifetime even shorter (Seinfeld and Pandis, 2006).

Shipping: trends, emissions, regulations

“*Tankers, bulk carriers and container ships are the most important means of transportation of our time. Each year they carry billions of tonnes of goods along a few principal trade routes. Containerization has revolutionized global cargo shipping, bringing vast improvements in efficiency.*

— **World Ocean Review 2010**
(Bollmann et al., 2010, p.164)

3.1 Shipping – a fast growing sector

Throughout the course of history, shipping has always been an important mode of transportation. Unlike a few decades ago, nowadays ships are almost exclusively carrying freight rather than people, with the exception of a small percentage of ferries and – recently booming – cruise ships. In the last decades, globalization of markets has led to an immense increase in world trade and shipping volumes. Since the 1950s, growth rates were almost consistently about twice that of the world gross domestic product (GDP) (Bollmann et al., 2010).

Ship traffic has increased massively in the last decades. The capacity of the global merchant fleet has nearly doubled since the year 2000, tripled since 1990 and quadrupled since 1985, as can be seen from Fig. 3.1.

Although growth rates have been lower in the last years than before the 2008 economic crisis, seaborne trade is typically growing faster than the rest of the transportation sector, with annual growth rates of 3.5–4.5 % in the years 2012 to 2014, nearly twice as high as the 2.2–2.6 % growth of the total global merchandise volume and GDP (UNCTAD, 2014, 2015). The world fleet capacity has been steadily growing even during the crisis and the year 2012 saw the turn of the largest shipbuilding cycle in recorded history (UNCTAD, 2013).

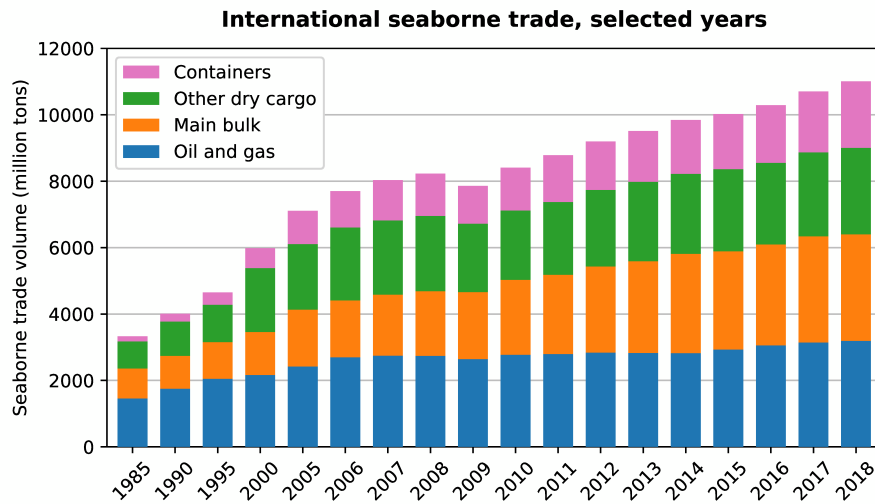


Figure 3.1.: International seaborne trade volume in million tons for selected years. Main bulk includes iron ore, grain and coal. Numbers taken from UNCTAD (2018b) and UNCTAD (2019).

In the last decades, the main reason behind the massive increase in shipping was the growth in world trade (Bollmann et al., 2010). But not only the global seaborne trade volume has seen a massive increase, also the global trade structure and patterns have changed drastically over the last 50 years. Over the whole time, developing countries have been the main exporting countries with nearly two-thirds of the global exported trade volume originating in their territories, as can be seen in Fig. 3.2. The dip in the 1980s occurred due to oil trade developments.

On the importing side, developing countries did not play an important role until about the year 2000. In the time before, we clearly had a colonial trade pattern, with developing countries exporting large volumes of raw materials and importing low volumes of manufactured goods, mainly consumer goods. Since about the year 2000, the situation has changed dramatically with many developing countries participating in globalized production and primary product trades, now importing raw materials as well as finished and semi-finished goods and exporting manufactured goods. Today, developing countries dominate both global export and import with about two-third percentages (see Fig. 3.2) (UNCTAD, 2018a).

The massive increase in international trade over the last decades has to a large extent been driven by the increase in trade between developing countries, rising from less than 10% in 1980 to about a third in 2011, while the relative importance of trade between industrialized countries has fallen from around 50% to about one-third (UNCTAD, 2013, 2018a).

Participation in world trade has, however, not developed equally in all developing regions. Especially the African participation declined in the last 50 years, but also Latin America

Participation of developing economies in world seaborne trade

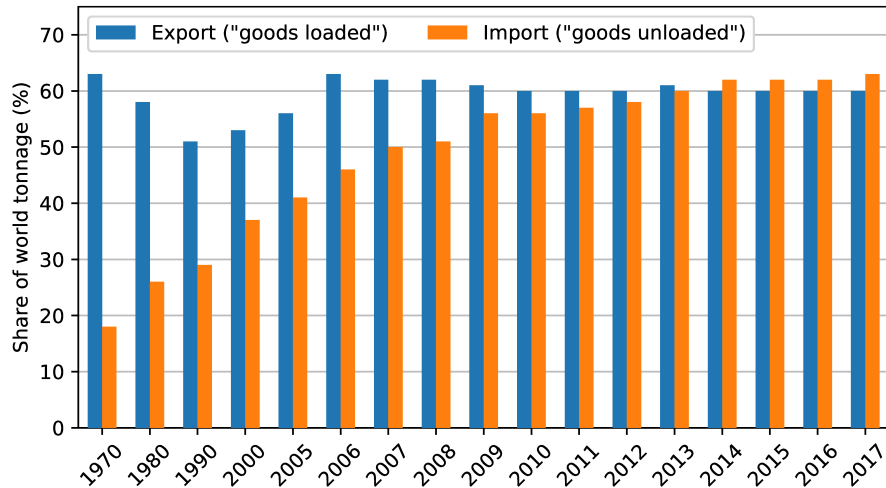
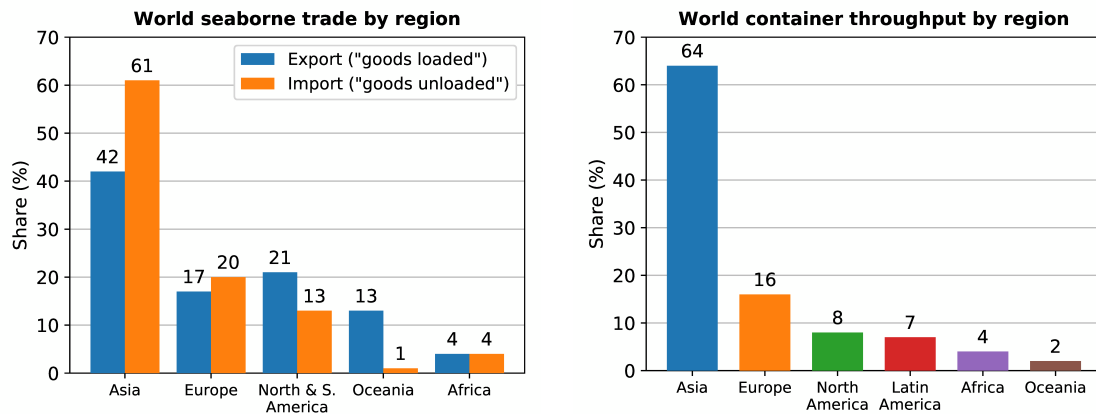


Figure 3.2.: Participation of developing countries in global seaborne trade as percentage of world tonnage for selected years. Numbers taken from UNCTAD (2018b).

has seen a decline, while Asia saw a strong increase and is now dominating the total global seaborne trade for both exports and imports, and is even stronger dominating the containerized trade (UNCTAD, 2018a), as can be seen in Fig. 3.3.



(a) Percentage share of world seaborne trade (tons) by regions in 2017. Numbers taken from (UNCTAD, 2018b). **(b)** Percentage share of world container throughput (TEUs) by regions in 2018. Numbers taken from (UNCTAD, 2019).

Figure 3.3.: World seaborne trade and container throughput by regions

Of the global top 20 ports by cargo throughput in tons in 2017, 17 are located in Asia and 14 of these in China (including Hong Kong). The other ports outside of Asia are Port Hedland, Australia’s most important iron ore terminal, on rank 8, Rotterdam, Netherlands, (an important oil and gas terminal) on rank 10 of the list and South Louisiana, the most important grain export terminal in the US, on rank 15 (UNCTAD, 2018b).

Of the global top 20 ports by container throughput in 2017, again 16 are located in Asia. The most important container ports in Europe are Rotterdam, Antwerp and Hamburg on ranks 11, 13 and 18 of the list, respectively (UNCTAD, 2018b). These three large ports are located in the region-of-interest of this thesis, comprising the North and Baltic Sea area.

China, Japan and the Republic of Korea dominate the global ship production, with together 90 % of all shipbuilding activities. Bangladesh is the main country of ship demolition (UNCTAD, 2019). Ship scrapping is another source of environmental pollution, it pollutes seas and soils, and damages workers' health, especially in the developing world (Ghosh et al., 2016).

The example of container shipping is particularly suited to highlight the major trends in modern global seaborne trade (see Fig. 3.4): both the average and maximum ship size (in TEUs¹) as well as the amount of transported containers (TEUs) are strongly increasing and have doubled in the ten years between 2004 and 2014, while the total number of ships and the number of liner shipping companies are declining.

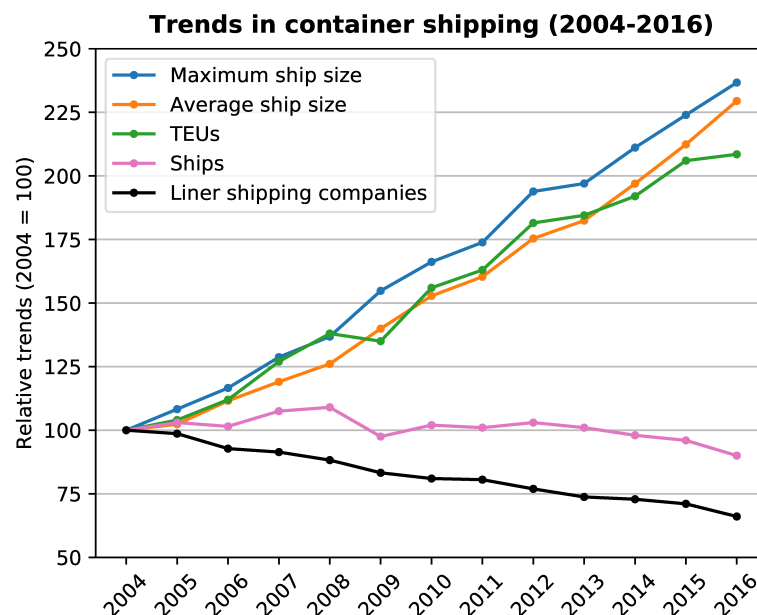


Figure 3.4.: Relative trends in container shipping since the year 2004 regarding maximum and average ship size (in TEUs), total number of TEUs, number of ships, and number of liner shipping companies. Numbers taken from UNCTAD (2016) and UNCTAD (2018b).

Compared to other means of transportation, shipping is generally the most energy efficient way to transport freight with the lowest greenhouse gas emissions per tonne per kilometer (see Fig. 3.5). Rail transportation is the next most efficient, followed by road and, the least efficient, air transport (Bollmann et al., 2010; IEA, 2009). Even though shipping is

¹TEU = twenty-foot equivalent unit, referring to the 20-foot-long (6.1 m) standard intermodal container size

unbeatable in terms of energy efficiency (Bollmann et al., 2010), shipping at the same time accounts for four fifths of the worldwide total merchandise trade volume (UNCTAD, 2018b). In consequence, shipping accounts for a significant part of the emissions of pollutants from the transportation sector (Eyring et al., 2005b).

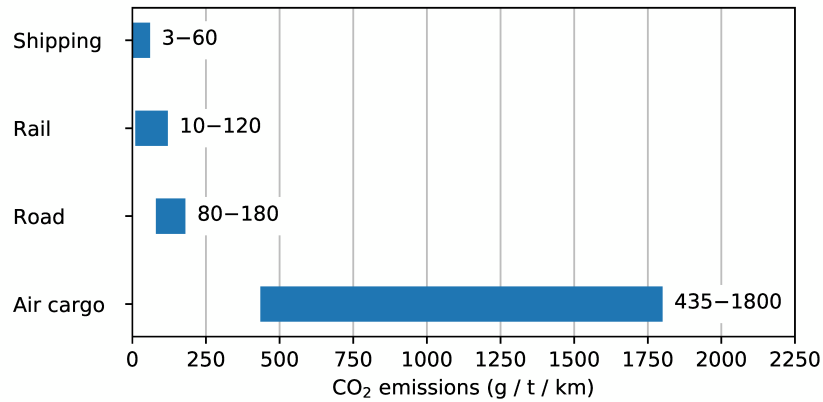


Figure 3.5.: CO₂ emissions in gram per ton per kilometer for the different modes of transportation. Numbers taken from Bollmann et al. (2010) and IEA (2009).

The total shipping volume of 9.84 billion tons in 2014 (UNCTAD, 2015) is enormous compared to the total air cargo transport volume of 51.3 million tons in 2014 (International Air Transport Association (IATA), 2015), for example. In 2018, the global seaborne trade volume reached an all-time high of 11 billion tons (see Fig. 3.1) (UNCTAD, 2019).

Table 3.1 shows how the number of ocean-going ships larger than 100 GT, the total fuel oil consumption and the emissions increased in the last decades. For the future, Eyring et al. (2005b) predicted that the trend of shipping emissions might depend more on imposed regulations and on development and usage of new technologies than on economic growth rates.

There is a relatively small number of principal global shipping routes, and these pass through only a few areas of the world’s oceans, as can be seen in Fig. 3.6. The busiest waterways are the approaches to the ports of Europe, East Asia and the United States. Narrow straits further concentrate maritime traffic. Bottlenecks include the Straits of Dover, Gibraltar, Malacca (between Malaysia and Sumatra) and Hormuz (between the Persian Gulf and the Gulf of Oman), and the Cape of Good Hope at the southern tip of Africa.

The North Sea, on which this thesis is mainly focusing on, “has some of the busiest shipping lanes in the world and maritime transport continues to increase. Construction activities have also been increasing this decade, with more coastal structures and wind farms being built and operated, and more tourist traffic.” (OSPAR Commission, 2010, p.154)

Table 3.1.: Estimates of the annual shipping emissions and fuel consumption for 1950, 1970, 2001 and predictions for 2050

	1950 ^a	1970 ^a	2001	2050 ^d
No. of ships (> 100 GT)	30 800	52 400	89 000 ^a	126 800–172 400
CO₂ [Tg C]	51	98	249 ^b / 222 ^c	302–546
NO_x [Tg N]	1.6	3.3	6.87 ^b / 6.5 ^c	1.7–20.9
SO₂ [Tg S]	1.4	2.7	6.49 ^b / 6.0 ^c	1.8–13.0
PM₁₀ [Tg]	0.39	0.74	1.64 ^b / 1.67 ^c	1.45–3.92
Hydrocarbons [Tg]	0.9	1.74	0.769 ^b / 3.92 ^c	3.65–6.53
Fuel consumption [Mt]	64.5	124	289 ^b / 280 ^c	402–725

^a Eyring et al. (2005b)

^b Corbett and Koehler (2003)

^c Eyring et al. (2010b)

^d Eyring et al. (2005a), number ranges represent different future scenarios

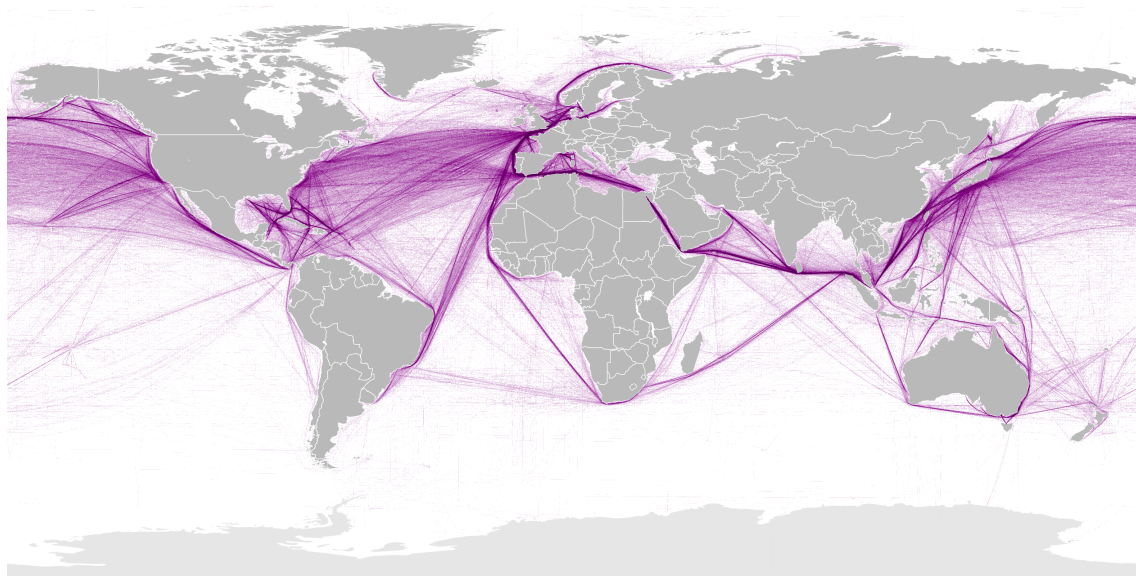


Figure 3.6.: Map showing the relative global commercial shipping density (as gridded data of 1 km resolution), derived from a work of B.S. Halpern (T. Hengl; D. Groll), CC BY-SA 3.0, <https://commons.wikimedia.org/w/index.php?curid=18755723>, based on Halpern et al. (2008).

3.2 Shipping emissions

The most important air pollutants emitted by ships are carbon dioxide (CO₂), carbon monoxide (CO), nitrogen oxides (NO_x = NO + NO₂), sulfur dioxide (SO₂), black carbon (BC), volatile organic compounds (VOCs), and particulate matter (PM) (Eyring et al., 2010a).

NO_x is predominantly formed thermally during high temperature combustion processes in ship engines from atmospheric molecular nitrogen (N₂) and oxygen (O₂) in the so-called Zeldovich mechanism (see Section 2.5), which creates NO. For some fuel types that contain nitrogen, in addition to the “thermal NO”, also “fuel NO” is produced, which is the case for petroleum-based fuels but not for natural gas. Although the emitted NO_x at first comprises mainly NO, in presence of tropospheric ozone in the emitted exhaust plume the produced NO can be rapidly converted to NO₂.

Alföldy et al. (2013) measured emission factors of 497 ships in two weeks in the port of Rotterdam and found that less than 25 % of NO_x was being emitted as NO₂. A similar result was published by Zhang et al. (2016), who measured emission factors for gaseous and particulate pollutants on-board three Chinese vessels and found that more than 80 % of the NO_x in the fresh exhaust was emitted as NO and that emission factors can vary significantly during different operation modes.

Inside ship plumes, Chen et al. (2005) found a substantially reduced lifetime of NO_x of only about 1.8 h compared to approximately 6.5 h in the ambient marine boundary layer, which is attributed to enhanced levels of OH radicals in the plume.

Unlike for NO_x, where emissions are not directly linked to the fuel, ship emissions of CO₂ and SO₂ are linearly related to the fuel consumption and, in the case of SO₂, to the sulfur content of the fuel (Aulinger et al., 2016). Around 86 % of the fuel sulfur content is emitted as SO₂, as a study from Balzani Lööv et al. (2014) showed. The fuel's sulfur content is dependent on the type of fuel used (Aulinger et al., 2016). The main fuel types are heavy fuel oil (HFO), also called marine fuel oil (MFO) or Bunker C or No. 6, which is pure or nearly pure residual oil from the distillation process of crude oil in the refinery and thus cheap and dirty, and marine gas oil (MGO), which is made from distillate only and similar to heating oil or diesel fuel. Intermediate blends of both exist, too, which can be distinguished by different shares of HFO and MGO. Intermediate fuel oil (IFO), for example, contains more HFO, while marine diesel oil (MDO) contains a higher fraction of MGO (Narula, 2018). Low-grade marine fuel oil, i.e., heavy fuel oil, may contain 3500 times more sulfur than road diesel (Wan et al., 2016).

In the years 2010 to 2014, heavy fuel oil accounted for 86 to 87 % of shipping fuel consumption globally, and 82 to 86 % of shipping fuel consumption in the EU, with gas oils

accounting for the remainder (FuelsEurope, 2015). In 2015, due to the introduction of stricter sulfur limits in emission control areas by the International Maritime Organisation (IMO), discussed in Section 3.4 below, the share of HFO dropped to 80 % globally and 64 % in the EU (FuelsEurope, 2016; Goldthau et al., 2018).

Particle emissions from ships consist of black carbon (BC), sulfate, organic carbon (OC), elemental carbon (EC), ash and metals (Andersson et al., 2016). Emission measurements on-board a HFO-burning large cargo vessel found the main components to be organic carbon, sulfate aerosols and ash (Moldanova et al., 2009). The amount of particles emitted depends on the fuel type (Winnes and Fridell, 2009) and the operation mode of the ship, with enhanced emissions during maneuvering (Winnes and Fridell, 2010). Alföldy et al. (2013) found a linear relationship between SO₂ and sulfate particle emission and that only around 4.8 % of the total sulfur content is either directly emitted as or immediately transformed into particles after the emission.

From their measurements on the shore of the English Channel, Yang et al. (2016) estimated the lifetime of SO₂ in the marine boundary layer to be about half a day.

In 2001, shipping emissions accounted for 15 % of all anthropogenic NO_x emissions and provided 8 % of all anthropogenic SO₂ emissions worldwide (Eyring et al., 2010a).

According to the Third IMO Greenhouse Gas Study 2014 (Smith et al., 2015), in the period from 2007 to 2012, shipping was estimated to account for 15 % of the global annual NO_x emissions from anthropogenic sources, 13 % of SO_x and 3 % of CO₂ emissions. For Europe in 2013, the shares were estimated to be even higher, with ships contributing 18 % of NO_x emissions, 18 % of SO_x emissions and 11 % of particles less than 2.5 μm in size (PM_{2.5}). For road transport, the corresponding figures were 33 %, 0 % and 12 %, respectively, while aviation, by contrast, accounted for only 6 %, 1 % and 1 % and rail transport accounted for even less, with 1 %, 0 % and 0 %, respectively (Smith et al., 2015; Wan et al., 2016).

An AIS²-based model study was conducted by Johansson et al. (2017) using the STEAM3 model. The authors found the highest SO_x and PM_{2.5} emissions per unit area in the Eastern and Southern China Seas, in the sea areas in Southeast and South Asia, in the Red Sea, in the Mediterranean, in the North Atlantic near the European coast, in the Gulf of Mexico and the Caribbean Sea, and along the western coast of North America. The strongest emission hotspots on a small local scale were found, in decreasing order, in Singapore, Hong Kong, Antwerp, Shanghai, Los Angeles and Rotterdam.

For the North Sea, the main region-of-interest of this thesis, the impact of shipping emissions for different regulation scenarios was investigated in a model study by the Helmholtz-Zentrum Geesthacht (HZG) within the scope of the Clean North Sea Shipping project

²Automatic Identification System, see Section 6.1.5

(Aulinger et al., 2016; Matthias et al., 2016). For current emissions, Aulinger et al. (2016) estimated a relative contribution of shipping emissions to air pollution in North Sea coastal regions of up to 25 % in summer and 15 % in winter for NO₂, and 30 % in summer and 12 % in winter for SO₂.

This thesis focuses on measurements of the UV-vis-absorbing pollutants NO₂ and SO₂, two main components of air pollution by ships. Both are emitted in considerable amounts and both absorb light in the UV-visible spectral range and therefore can readily be measured by Differential Optical Absorption Spectroscopy (DOAS), which is explained in Section 5.

3.3 Influence of shipping emissions on air quality and climate

(Sulfate) aerosols can influence climate both directly by scattering and absorption of solar radiation and indirectly by increasing cloud condensation, changing clouds' reflectivity and lifetime (Eyring et al., 2010b; Lauer et al., 2007; Lawrence and Crutzen, 1999).

In the presence of volatile organic compounds (VOCs), nitrogen oxides (NO_x) are important precursors in the formation of tropospheric ozone and hence photochemical smog (see Sections 2.4 and 2.5).

As the atmospheric removal processes of both NO₂ and SO₂ include the formation of acids (see Sections 2.5 and 2.6), the release of NO_x and SO₂ by ships can lead to an increase in acidification of 3–10 % in coastal regions, contributing significantly to acid rain formation, which can significantly damage ecosystems (Endresen et al., 2003; Jonson et al., 2000). The deposition of reactive nitrogen compounds on the surface causes eutrophication of ecosystems and decreases biodiversity (Galloway et al., 2003).

Around 70 % of ship traffic and thus shipping emissions occur within 400 km of land (Corbett et al., 1999), contributing substantially to air pollution situations in coastal areas (Eyring et al., 2010b). Exhaust emissions from ships were also found to provide a dominant source of air pollution in harbor cities (Eyring et al., 2010a). In addition to that, tropospheric ozone and aerosol precursors can be transported over several hundreds of kilometers, affecting air quality, human health and vegetation further inland, far away from their coastal emission points (Corbett et al., 2007; Eyring et al., 2010a,b).

Air pollution by high levels of NO_x and SO₂ can cause a variety of respiratory problems. Tropospheric ozone is harmful to both plants and animals and can cause various health problems. As discussed above, both NO₂ and SO₂ play a role in the formation of particles. Fine particles are associated with various health impacts like lung cancer, heart attacks,

asthma and allergies (Corbett et al., 2007; Pandya et al., 2002; WHO, 2006; Winebrake et al., 2009).

3.4 Emission regulations

The regulation of international shipping is subject to the International Maritime Organization (IMO). Environmental pollution through shipping is regulated by the *International Convention for the Prevention of Pollution from Ships (MARPOL 73/78)*. Shipping emissions in particular are subject-matter of MARPOL 73/78 Annex VI, which was added to the convention in 1997 and entered into force in 2005 (DNV, 2008; IMO, 2009). A revision, implementing more stringent emission limits, was adopted in 2008 (IMO, 2008a) and entered into force in 2010 (IMO, 2013). Since then, the MARPOL convention protocol and the Annex VI has been consistently updated, the last major amendments concerned the designation of the North and Baltic Sea Emission Control Areas (ECAs) for NO_x control and updated the Tier III enforcement date to 1 January 2021 (IMO, 2017), and the prohibition on the carriage of non-compliant fuel oil for combustion purposes for propulsion or operation on board a ship (IMO, 2018), which entered into force on 1 March 2020.

MARPOL Annex VI sets limits on sulfur oxide (SO₂) and nitrogen oxide (NO_x) emissions from ship exhausts and prohibits deliberate emissions of ozone depleting substances. The revised Annex VI introduced a progressive reduction globally in emissions of SO_x, NO_x and particulate matter and it introduced designated emission control areas (ECAs) as regions with more stringent standards for SO₂, NO_x and particulate matter emissions, designated sea areas where emissions of those air pollutants shall be further reduced. (Brodie, 2015; Ćampara et al., 2018; IMO, 2008a)

Under the revised MARPOL Annex VI and its amendments, the global fuel sulfur content limit has been reduced from initially 4.5 % to 3.5 %, effective from 1 January 2012, to 0.5 %, effective from 1 January 2020 (compare Fig. 3.7). In ECAs, the initial limit of 1.5 % has been reduced to 1.0 %, effective from 1 July 2010, to 0.1 %, effective from 1 January 2015 (compare Fig. 3.7) (IMO, 2008a). The latter, drastic reduction directly concerned the North and Baltic Sea ECA, the region-of-interest of this thesis, and fell into the time span of the presented MAX-DOAS measurements, being the major motivation for the presented study investigating the impact of ship exhaust regulations on coastal air quality.

To comply with the more stringent sulfur regulations, either fuels with lower sulfur content have to be used like distillate fuels like marine gas oil (MGO), or alternative fuels like liquefied natural gas (LNG) or biofuels. LNG, which consists predominantly of methane (CH₄) with some mixture of other hydrocarbons (HC) like ethane (C₂H₆), has the advantages of nearly no SO₂ emissions due to the very low, negligible sulfur content, with typical

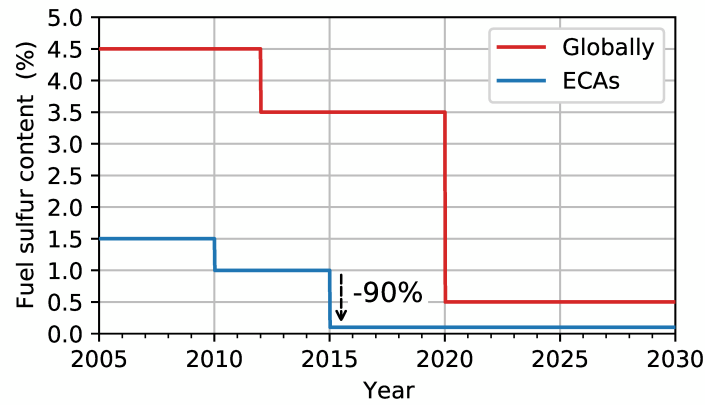


Figure 3.7.: Fuel sulfur content limits globally and inside an emission control area (ECA) according to MARPOL Annex VI.

sulfur levels of less than 0.004 % due to removal of sulfur compounds like hydrogen sulfide (H_2S) to trace levels (Adamchak and Adede, 2014; North P&I, 2019), 20–30 % lower CO_2 emissions, due to the higher hydrogen content in the molecule respect to HFO/MDO, about 85 % less NO_x emissions (for LBSI³ and LPDF⁴ engines) and more than 90 % reduction in particulate matter (PM) emissions due to the low sulfur content and the simple fuel molecules, burning with low soot and PM formation (Marinò and Bucci, 2018; Stenersen and Thonstad, 2017). The disadvantage is the escape of unburned methane from combustion, the so-called “methane-slip”, which has a very high greenhouse potential (see Section 2.2), and emissions of formaldehyde (HCHO) (Stenersen and Thonstad, 2017). LNG and biofuel are predicted to account for 50 % of shipping energy demand by 2050 (Chu Van et al., 2019). A future alternative might also be renewable-energy-based methods like wind-aided propulsion or hybrid technologies (Narula, 2018).

Heavy oil fuel (HFO) as a residual oil has a very high sulfur content of up to 3.5 %, which is 3500 times more sulfur than truck diesel may contain, which has a sulfur limit of 0.001 % or 10 ppm. The 1 % fuel sulfur content limit valid in the ECAs before 2015 could still be fulfilled with desulfurized HFO, so-called low sulfur fuel oil (LSFO) with less than 1 % sulfur content, whereas to comply with the 0.1 % sulfur content limit set into force in the ECAs on 1 January 2015, a switch to the cleaner but also more expensive distillate fuels like MGO has to be done (Kabashkin et al., 2018). This marine gas oil with a sulfur content below 1 % still contains 100 times more sulfur than truck diesel. For compliance with the global 0.5 % sulfur cap effective from 2020, either MGO has to be used or the newly available even-further desulfurized HFO, the so-called very low sulfur fuel oil (VLSFO)

³Lean Burn Spark Ignition gas engine, an Otto cycle concept (Stenersen and Thonstad, 2017)

⁴Low Pressure Dual Fuel gas engine, a compromise between the Diesel cycle with compression ignition of fuel oil and Otto cycle with a mixture of air and gas prior to the compression stroke. Because of the Diesel ignition, diesel oil is available as a backup fuel for operation (Stenersen and Thonstad, 2017).

with a sulfur content below 0.5 %. As the aim of the fuel sulfur content regulations is the reduction of SO₂ emissions, the use of approved secondary control methods like exhaust gas cleaning systems, so-called “scrubbers”, which remove the SO₂ molecules from the exhaust gas after their formation is also possible (Čampara et al., 2018). In such scrubbers, which are available as wet (open-loop or closed-loop or hybrid) or dry systems, the exhaust is passed through a cleaning medium like sea water, fresh water or dry absorber, practically removing (“washing out”) all SO₂ from the exhaust (Lange et al., 2014). This allows the ship owners to keep using HFO and still be ECA compliant (Kabashkin et al., 2018).

The revised MARPOL Annex VI and its amendments also established progressive reductions in NO_x emissions from marine diesel engines, with three tiers for engines installed on ships constructed on or after specific dates (see Table 3.2 and Fig. 3.8) and is even applied retroactively: Tier I for ships constructed in the years 2000 to 2010, Tier II for ships constructed in the years 2011 to 2015 and Tier III for ships constructed on or after 1 January 2016 (North American ECA), or 1 January 2021 (North and Baltic Sea ECA), respectively. Tier I and II are valid globally, Tier III for ships operating in ECAs. The NO_x emission limits depend on the engine’s rated speed, i.e., the crankshaft revolutions per minute (in rpm), as can be seen from Fig. 3.8. The NO_x Technical Code 2008 (NTC 2008) (IMO, 2008b) provides the mandatory procedures for testing, measurement and certification of the ships’ engines (Čampara et al., 2018; IMO, 2013). To comply with the Tier III NO_x regulations, either alternative fuels like the above-mentioned LNG, or selective catalytic reduction (SCR) systems (using ammonia or urea with the aid of a catalyst) known from cars have to be used (Azzara et al., 2014; Harndorf and Reißig, 2017).

Table 3.2.: Nitrogen oxides (NO_x) emission limits depending on ship construction date and engine speed according to MARPOL Annex VI (IMO, 2008a).

Tier	Ship construction date: on or after	Total weighted cycle emission limit (g/kWh) for engine’s rated speed n (rpm)		
		$n < 130$	$130 \leq n \leq 1999$	$n \geq 2000$
I	1 January 2000	17.0	$45 \cdot n^{-0.2}$	9.8
II	1 January 2011	14.4	$44 \cdot n^{-0.23}$	7.7
III	1 January 2016*	3.4	$9 \cdot n^{-0.2}$	2.0
	1 January 2021**			

* ships operating in the North American or the US Caribbean ECA

** ships operating in the North and Baltic Sea ECA

As the enforcement of the major NO_x emission reduction (Tier III) in the North and Baltic Sea ECA was delayed by several years, it could not be investigated in the scope of this thesis but might be subject to future work and measurement studies or campaigns.

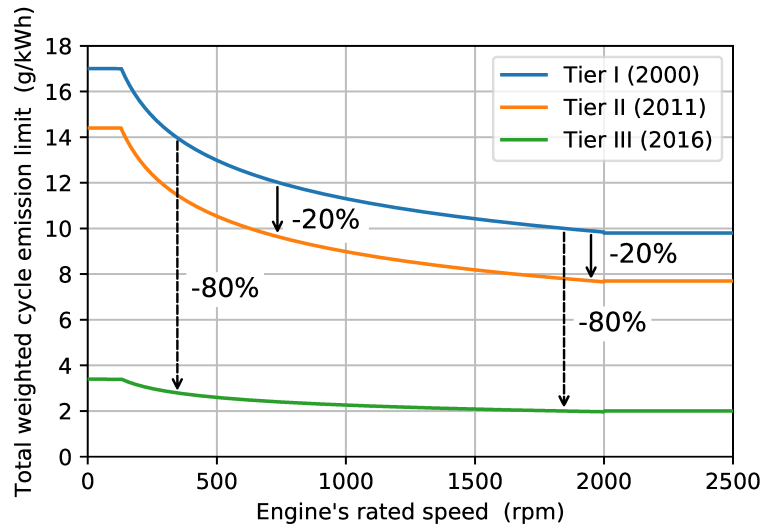


Figure 3.8.: Nitrogen oxides (NO_x) emission limits depending on ship construction date: Tier I between 2000 and end of 2010, Tier II between 2011 and end of 2015, Tier III since 2016. Based on numbers and calculation formulas from Table 3.2.

The existing emission control areas as of today are the North American ECA (including Hawaii), the United States Caribbean sea ECA (waters under the jurisdiction of the US surrounding Puerto Rico and the US Virgin Islands) as well as the Baltic Sea ECA and the North Sea ECA (see Fig. 3.9). Various other possible future ECAs are under discussion, Fig. 3.9 shows a selection.

Apart from the MARPOL regulations by the International Maritime Organization (IMO), other legislation have been introduced aiming to decrease air pollution from shipping. The European Union, for example, established a sulfur content limit of 0.1 % for inland waterway vessels and ships at berth in community ports, which is in force since 1 January 2010 (EU, 2005, 2016). China established three emission control areas (ECAs) around the nation's most highly populated areas with heavy ship traffic, the Bohai-rim Waters (Beijing, Tianjin and Hebei Province), the Yangtze River Delta and the Pearl River Delta, to control the sulfur emissions from ships and improve the air-quality in China's coastal areas. In these ECAs, a fuel sulfur content limit of 0.5 % must not be exceeded, set into force on 1 January 2019 (Wan et al., 2019).

For the greater North Sea region, the main area-of-interest of this thesis, for the year 2030, Matthias et al. (2016) predict the contribution of the continuously growing shipping sector to the NO₂ concentrations to decrease, while the extent of reduction depends on the date on which the stricter Tier III NO_x regulations in the North Sea ECA enter into force⁵ and on the fraction of the fleet which has to comply to the regulations, i.e., the age of

⁵Which was unclear at that time and only recently was set to 1 January 2021

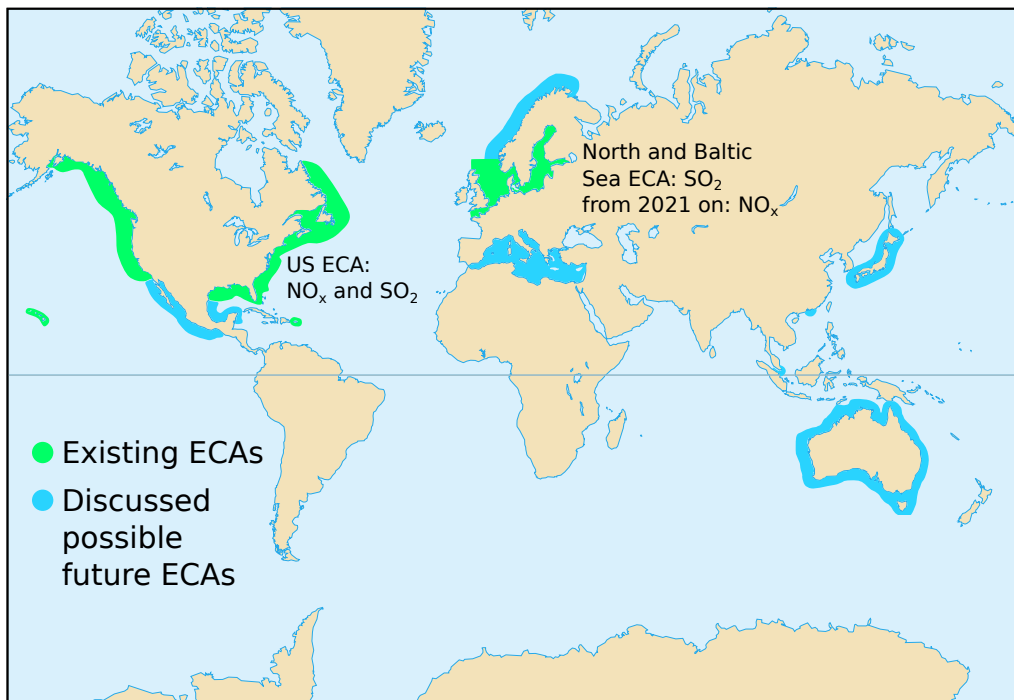


Figure 3.9.: Existing and potential future emission control areas (ECAs). Background map by Eric Gaba, Public Domain, <https://commons.wikimedia.org/w/index.php?curid=1318610>. Point coordinates for the geodesic lines enclosing the ECAs taken from (IMO, 2020).

the fleet. Up to 80 % reduction was predicted if all ships are going to comply⁶. For SO₂, the established fuel sulfur content limits of 0.1 % (ECA) and 0.5 % (globally) will lead to significant reductions, a further decrease is expected if the fraction of LNG powered ships grows.

3.5 Studies on the effectiveness of the SO₂ emission regulation measures

Several studies have been conducted to assess the effectiveness of existing fuel sulfur content regulations on the measured SO₂ emissions. This section gives a short overview on some of the main results.

Carrying out airborne in-situ measurements in several flight campaigns in the English Channel as well as the North and Baltic Sea in 2011 and 2012, Beecken et al. (2014) measured a 85 % compliance rate with the 1 % fuel sulfur content limit.

⁶In the improbable case of a new-ships-only fleet

In the Gulf of Finland and Neva Bay area, Beecken et al. (2015) found a 90 % compliance rate with the 1 % fuel sulfur content limit in 2011 and a 97 % compliance rate in 2012 by performing ground-based, ship-based and helicopter-based in-situ measurements.

Utilizing in-situ measurements in Wedel (Germany) at the bank of the river Elbe, a few kilometers downstream from the city of Hamburg, Germany, Kattner et al. (2015) showed that in late 2014 more than 99 % of the measured ships complied with existing 1 % sulfur content limit and in early 2015 already 95.4 % of the measured ships complied with the newly introduced 0.1 % sulfur content limit.

By analyzing one and a half years of in-situ SO₂ measurements on the shore of the English Channel at the Penlee Point Atmospheric Observatory near Plymouth, United Kingdom, Yang et al. (2016) found a three-fold reduction in SO₂ from 2014 to 2015.

Lack et al. (2011), by performing airborne in-situ measurements, measured a substantial drop of SO₂ emissions by 91 % when the investigated container ship entered the Californian ECA and switched from heavy fuel oil (HFO) with 3.15 % fuel sulfur content to marine gas oil (MGO) with 0.07 % fuel sulfur content.

3.6 DOAS measurements of shipping emissions – previous studies

Optical remote sensing of shipping emissions using the DOAS technique (differential optical absorption spectroscopy, see Section 5) has been conducted before. This section provides an exemplarily overview of the previous studies in this field.

Masieri et al. (2009) and Premuda et al. (2011) performed ground based MAX-DOAS measurements of NO₂ and SO₂ of individual ships across the Giudecca Channel in the Venice lagoon, Italy, and estimated flow rate emissions, i.e., the emitted pollutant mass per second.

Berg et al. (2012) performed airborne (airplane and helicopter-based) DOAS measurements of NO₂ and SO₂ in ship plumes by measuring sea-surface-scattered light. McLaren et al. (2012) measured nocturnal NO₂ to SO₂ ratios in ship plumes in the Strait of Georgia with the active long-path-DOAS technique.

Balzani Lööv et al. (2014) tested and compared optical remote sensing methods (DOAS, LIDAR, UV camera) and in-situ (sniffer) methods for the measurement of shipping emissions in the framework of the SIRENAS-R campaign in the harbor of Rotterdam in 2009. Prata (2014) showed that a UV (SO₂) imaging camera can be used to measure SO₂ in ship plumes at the Kongsfjord at Ny-Ålesund, Svalbard, and the harbor of Rotterdam.

In a very recent study, Cheng et al. (2019) presented shore-based MAX-DOAS emissions of NO₂ and SO₂ emitted from ships under different traffic conditions at three sites in China's ship emission control areas (ECAs) in Shanghai and Shenzhen, China.

The global shipping pathways can be observed in time averaged NO₂ measurements from various satellite instruments: from GOME over the Indian Ocean (Beirle et al., 2004), from SCIAMACHY on board ENVISAT over the Indian Ocean and the Red Sea (Richter et al., 2004), in even more detail with a lot more visible ship tracks from GOME-2 on board MetOp-A (Richter et al., 2011). The higher resolution of OMI yielded ship tracks in the Baltic Sea (Ialongo et al., 2014) and in all European seas (Vinken et al., 2014). The much higher spatial resolution of S5P/Tropomi (Veeffkind et al., 2012) should make it possible to distinguish the ship tracks with a much better resolution and the better signal-to-noise ratio should facilitate the use of shorter total data averaging times. The resolution might even be sufficient to detect plumes of individual ships, as a new study from Georgoulas et al. (2020) suggests.

Airborne imaging DOAS measurements, like the ones from Meier (2018) that are used for validating the MAX-DOAS measurements in Chapter 7, provide a much higher resolution than satellites and can be used to study individual plumes in detail.

Interaction of light and matter

” *Thus, the photons which constitute a ray of light behave like intelligent beings: Out of all the possible curves they always select the one which will take them most quickly to their goal.*

— **Max Planck**

Scientific Autobiography, and Other Papers (1949)

After having introduced the atmosphere in Chapter 2, focusing especially on the boundary layer, where both the main sources of the investigated air pollutants NO_2 and SO_2 are located and our measurements have their highest sensitivity, Chapter 3 focused on the fast growing shipping sector as a major air pollution source in the investigated marine environment. This chapter introduces the physical processes involved during the journey of the photons from the Sun through the Earth's atmosphere to our measurement instrument.

In this chapter, the sections on electromagnetic radiation in general, the electromagnetic spectrum, the interactions with solid matter (refractive index) and at interfaces (reflection and refraction), and the physics of optical fibers and diffraction gratings are mainly based on Demtröder (2009), Hecht (2005), and Vojnovic and Volpi (2012). The sections on light emission and the solar spectrum, light absorption, molecular spectra and transitions as well as scattering in the atmosphere are mainly based on Demtröder (2007, 2010, 2013) and Haken and Wolf (2004, 2006).

4.1 Electromagnetic radiation

As light is an electromagnetic phenomenon, it is subject to the laws of electrodynamics. The explanation of any electrodynamic phenomenon starts with the Maxwell equations, the fundamental laws of the electrodynamics, describing the basic characteristics of electric and magnetic fields.

4.1.1 Maxwell equations

The classical theory of electrodynamics is based on five equations: the four Maxwell equations and the Lorentz law of force. Maxwell's equations in their differential form are given by:

$$\vec{\nabla} \cdot \vec{E} = \frac{\rho}{\varepsilon_0} \quad \text{Electric charge is the source of electric field.}^1 \quad (4.1)$$

$$\vec{\nabla} \cdot \vec{B} = 0 \quad \text{The magnetic field has no sources.}^2 \quad (4.2)$$

$$\vec{\nabla} \times \vec{E} = -\frac{\partial \vec{B}}{\partial t} \quad \text{A changing magnetic field creates an electric field.} \quad (4.3)$$

$$\vec{\nabla} \times \vec{B} = \mu_0 \vec{j} + \mu_0 \varepsilon_0 \frac{\partial \vec{E}}{\partial t} \quad \text{Currents and changing E-fields create magnetic fields.} \quad (4.4)$$

with the electric field $\vec{E} = \vec{E}(\vec{r}, t)$, the magnetic field $\vec{B} = \vec{B}(\vec{r}, t)$, the electric charge density ρ , the electric current density \vec{j} , the vacuum permeability μ_0 and the vacuum permittivity ε_0 . $\vec{\nabla}$ is the del or nabla operator³, $\vec{\nabla} \cdot \vec{A} = \text{div } \vec{A}$ is the divergence⁴ (source density) of the vector field \vec{A} , and $\vec{\nabla} \times \vec{A} = \text{curl } \vec{A} = \text{rot } \vec{A}$ is the curl⁵ (or rotation) of \vec{A} .

4.1.2 Electromagnetic waves

In a free space without charges ($\rho = 0$) and currents ($\vec{j} = 0$), like a vacuum, the Maxwell equations reduce to:

$$\vec{\nabla} \cdot \vec{E} = 0 \quad (4.5)$$

$$\vec{\nabla} \cdot \vec{B} = 0 \quad (4.6)$$

$$\vec{\nabla} \times \vec{E} = -\frac{\partial \vec{B}}{\partial t} \quad (4.7)$$

$$\vec{\nabla} \times \vec{B} = \mu_0 \varepsilon_0 \frac{\partial \vec{E}}{\partial t} \quad (4.8)$$

¹This means that the electrical field lines have a start and end, connecting positive and negative charges.

²This means that the magnetic field lines are closed lines, and thus: no magnetic monopoles!

³Defined as $\vec{\nabla} = \sum_{i=1}^3 \vec{e}_i \frac{\partial}{\partial x_i} = \vec{e}_x \frac{\partial}{\partial x} + \vec{e}_y \frac{\partial}{\partial y} + \vec{e}_z \frac{\partial}{\partial z} = \left(\frac{\partial}{\partial x}, \frac{\partial}{\partial y}, \frac{\partial}{\partial z} \right)$ in \mathbb{R}^3

⁴With $\vec{\nabla} \cdot \vec{A} = \frac{\partial A_x}{\partial x} + \frac{\partial A_y}{\partial y} + \frac{\partial A_z}{\partial z}$

⁵With $(\vec{\nabla} \times \vec{A})_i = \varepsilon_{ijk} \nabla_j A_k$, with $\varepsilon_{ijk} = \begin{cases} +1 & \text{if } (i, j, k) \text{ is an even permutation of } (1, 2, 3) \\ -1 & \text{if } (i, j, k) \text{ is an odd permutation of } (1, 2, 3) \\ 0 & \text{if } i = j, \text{ or } j = k, \text{ or } k = i \end{cases}$,

the so-called Levi-Civita tensor in \mathbb{R}^3 , and implying Einstein's summation convention

Taking the curl of both sides of the third Maxwell equation (4.7) (Faraday's Law) and applying the triple product expansion vector identity, also-called Lagrange's formula or simply "BAC-CAB" rule, $\vec{\nabla} \times \vec{\nabla} \times \vec{A} = \vec{\nabla}(\vec{\nabla} \cdot \vec{A}) - \vec{\nabla}^2 \vec{A}$, on the left side yields

$$\vec{\nabla}(\vec{\nabla} \cdot \vec{E}) - \vec{\nabla}^2 \vec{E} = -\vec{\nabla} \times \frac{\partial \vec{B}}{\partial t} = -\frac{\partial}{\partial t}(\vec{\nabla} \times \vec{B}),$$

where on the right side Schwarz' theorem has been applied (the partial time derivative commutes with the spatial derivatives in the curl operator). Using (4.6) on the left side and (4.8) (Ampère's Law) on the right side yields

$$-\vec{\nabla}^2 \vec{E} = -\frac{\partial}{\partial t}(\mu_0 \epsilon_0 \frac{\partial \vec{E}}{\partial t}) = -\mu_0 \epsilon_0 \frac{\partial^2 \vec{E}}{\partial t^2} \iff \vec{\nabla}^2 \vec{E} - \mu_0 \epsilon_0 \frac{\partial^2 \vec{E}}{\partial t^2} = 0,$$

or more elegant with the Laplace operator $\Delta = \text{div grad} = \vec{\nabla}^2$:

$$\Delta \vec{E} - \mu_0 \epsilon_0 \frac{\partial^2 \vec{E}}{\partial t^2} = 0. \quad (4.9)$$

This is a wave equation describing electromagnetic waves. A comparison to the mechanical wave equation

$$\Delta y(\vec{r}, t) - \frac{1}{c^2} \frac{\partial^2 y(\vec{r}, t)}{\partial t^2} = 0$$

shows that for the phase speed c of the electromagnetic waves the following condition does apply:

$$\frac{1}{c^2} = \mu_0 \epsilon_0 \implies c = \frac{1}{\sqrt{\mu_0 \epsilon_0}} = 299\,792\,458 \text{ m/s} \approx 3 \times 10^8 \text{ m/s}, \quad (4.10)$$

the speed of light. Solutions to the electromagnetic wave equation (4.9) can be described as a linear superposition of plane waves of the form

$$\vec{E}(\vec{r}, t) = \vec{E}_0 \cos(\vec{k} \cdot \vec{r} - \omega t + \varphi) \quad \text{and} \quad \vec{B}(\vec{r}, t) = \vec{B}_0 \cos(\vec{k} \cdot \vec{r} - \omega t + \varphi), \quad (4.11)$$

respectively, with the wave vector \vec{k} pointing in the direction of wave propagation, the phase angle φ , and the angular frequency $\omega = 2\pi\nu = \frac{2\pi}{T}$ (with frequency ν and period T). The magnitude of the wave vector is the wave number $k = |\vec{k}| = \frac{\omega}{c} = \frac{2\pi\nu}{c} = \frac{2\pi}{\lambda}$.

Apart from the wave nature of light, which has been first described by Huygens' wave model in the 17th century and has been experimentally proven by Young (double slit interference) and Fresnel (diffraction) in the 18th century (Aspect, 2017), other experimental phenomena like the black-body radiation, the photoelectric effect and the Compton effect proved that light also has a particle character ("wave-particle duality"). The light particle, or photon, has an energy $E = h\nu$ and a momentum $\vec{p} = \hbar \vec{k}$ (with $\hbar = h/2\pi$) pointing in the direction

of wave propagation, with a magnitude $p = |\vec{p}| = h\nu/c = h/\lambda$, where h is Planck's constant $h = 6.626 \times 10^{-34}$ J s.

Electric and magnetic field oscillate perpendicular to the waves's propagation direction (transverse waves). The geometrical orientation of the oscillating electric field vector over time determines the wave's *polarization*. For an electromagnetic wave propagating in z -direction, the electric and magnetic field oscillate in the x - y -plane. For linearly polarized light, the orientation of the electric field vector is constant over time, while for circular or elliptic polarization, due to a phase shift of its components, it loops around the propagation axis.

4.1.3 The electromagnetic spectrum

The known electromagnetic spectrum covers electromagnetic waves with frequencies (or wavelengths) varying over more than 24 orders of magnitude, as can be seen from Fig. 4.1. As frequencies range from below 1 Hz (ultra long radio waves) to above 1×10^{25} Hz (gamma rays), the corresponding wavelengths range from thousands of kilometers down to a fraction of the size of an atomic nucleus.

Although the Sun emits radiation across most of the electromagnetic spectrum, for life on Earth the most important spectral regions are the spectral ranges of the UV, visible and infrared (highlighted in a magnified view in Fig. 4.1), where the Sun emits the bulk of its radiation: about 7% UV, 43% visible and 49% near-infrared at the top of the Earth's atmosphere, and less than 11% in total being emitted as X-rays, gamma rays and radio waves (Ahrens and Henson, 2015; Mohanakumar, 2008).

Although "light" in the proper sense refers only to electromagnetic radiation in the visible spectral range, the word is often used to refer to UV radiation and infrared radiation as well.

4.2 Absorption and emission of light

4.2.1 Blackbody radiation

The Sun, the light source of our measurements, to a good approximation emits as a blackbody. A blackbody is an idealized concept of a physical body that "absorbs all the incident [electromagnetic] radiation" of all frequencies and under all incidence angles⁶,

⁶Thus the name *blackbody*

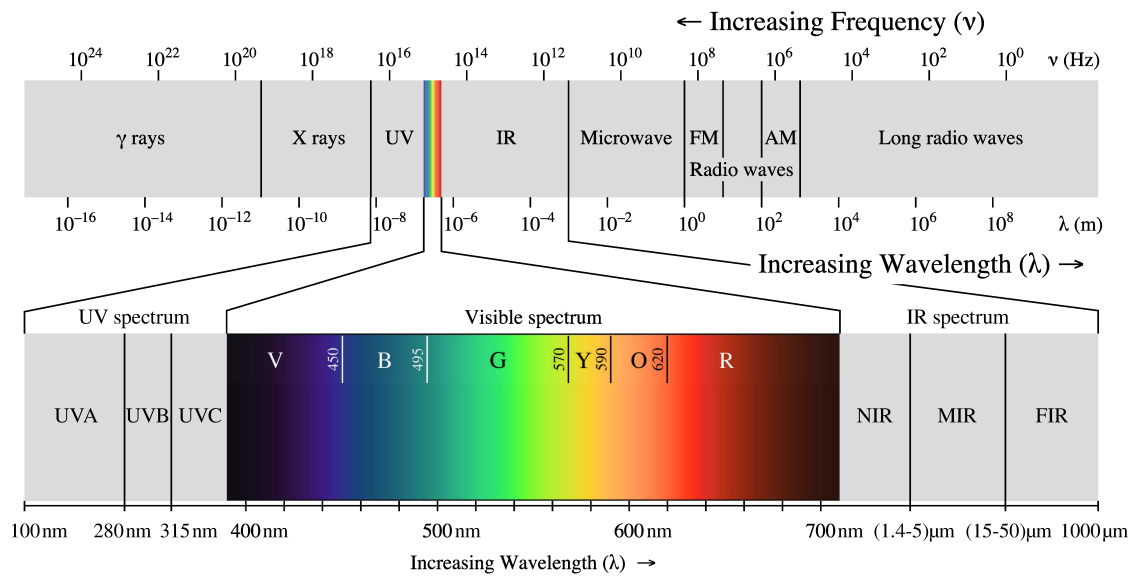


Figure 4.1.: Electromagnetic spectrum with UV, visible light and infrared highlighted, adapted from a work by Philip Ronan, Gringer, CC BY-SA 3.0, <https://commons.wikimedia.org/w/index.php?curid=24746679>.

and at the same time, it is an ideal emitter, which means that at every frequency “its emissive power is larger than that of any other body at the same temperature” (Planck and Masius, 1914).

A commonly used experimental setup to model the behavior of a blackbody is a cavity built from opaque walls, absorbing on the interior, with a small hole. Radiation that enters the cavity through the hole is reflected several times and absorbed, so that it is very unlikely to be re-emitted out of the cavity if the cavity is large and the opening is small. If the cavity is heated to a specific temperature T and its walls are kept at constant temperature, a thermal equilibrium (a steady state) is formed between the walls and the thermal radiation which is emitted and again absorbed inside the cavity, and the hole acts as a source of electromagnetic radiation.

Combining the spectral mode density of the standing waves in a cavity resonator with the equipartition theorem for the classical harmonic oscillator, an equation for the spectral energy density can be derived,

$$u(\nu) d\nu = \frac{8\pi \nu^2}{c^3} k_B T d\nu, \quad (4.12)$$

the so-called Rayleigh-Jeans law. Although it describes the infrared range quite good, for larger frequencies the fact that $u(\nu) \propto \nu^2$ leads inevitably to the so-called *ultraviolet catastrophe*.

Planck proposed a radical hypothesis to avoid the UV catastrophe: the atoms in the walls act as oscillators that absorb and emit electromagnetic waves, not with continuous energies like classical oscillators, but with quantized energy levels⁷.

With this assumption, using Boltzmann's distribution for the energy level occupation numbers and by incorporating (4.12) as a classical limiting case for small frequencies one yields Planck's law,

$$u(\nu) d\nu = \frac{8\pi h}{c^3} \frac{\nu^3}{e^{\frac{h\nu}{k_B T}} - 1} d\nu, \quad (4.13)$$

which describes the radiation spectrum of a blackbody at a specific temperature. For the wavelength maximum of such a Planck curve, which can be found by differentiating with respect to the wavelength⁸, Wien's law applies,

$$\lambda_{\max} T = \text{const.} \approx 2898 \mu\text{m K}, \quad (4.14)$$

which tells us that the peak frequency is linearly related to the temperature. For the surface temperature of the Sun of about 5800 K, one yields a maximum solar intensity at about 500 nm (corresponding to bluish-green light).

Integrating Planck's law (4.13) over all frequencies ν and the half-sphere delivers the so-called Stefan-Boltzmann law for the emitted power P ,

$$P = \sigma \cdot T^4, \quad (4.15)$$

which contains the so-called Stefan-Boltzmann constant σ as a proportionality factor.

4.2.2 Solar radiation spectrum

Optical spectra can be distinguished into continuous spectra, line spectra, and band spectra. Continuous spectra are emitted by glowing solids or gases like our sun, which to a good approximation emits as a blackbody, as can be seen from Fig. 4.2. Comparing the solar spectrum at the top of the atmosphere (TOA) to the theoretical Planck curve for a blackbody at a temperature of 5778 K (the mean surface temperature of the Sun), one sees a very good agreement, confirming the blackbody assumption. The deviations in the UV (actual intensity lower than prediction) and visible (actual intensity higher than prediction) are due to the facts that the Sun has no well-defined surface. The radiation the Sun emits into space comes primarily from the Sun's photosphere, a roughly 400 km thick layer at

⁷Einstein expanded the proposed quantization of energies from the surface atoms onto the electromagnetic radiation itself.

⁸Note that $d\lambda = -(c/\nu^2) d\nu$

the outer shell of the Sun. Its temperature ranges from about 6500 K at the bottom to about 4000 K at the top (NASA, 2017), which means that we see a mixture of light from multiple temperature sources, and the “surface temperature” stated above is an effective temperature representative for the emitted radiation. Also, the Sun does not exactly satisfy the simplifying blackbody assumptions, it just comes astoundingly close to it.

Line spectra, often grouped in characteristic series, can be assigned to atoms. A prominent example are the Fraunhofer lines in the solar spectrum, which are produced by atomic absorption in the Sun’s “atmosphere”, its outer shell composed of the photosphere, chromosphere, transition region, and corona. One example is the well-known sodium⁹ (Na) doublet at 589.0 nm and 589.6 nm. Fraunhofer lines can be seen in the spectra shown in Fig. 4.2 (especially in the UV and visible range) and even better in the example measurements shown in Fig. 5.2 in Section 5.1. Another example for a line spectrum is the Mercury-Cadmium (HgCd) spectrum of a typical wavelength calibration lamp.

Band spectra can be assigned to molecules and contain groups of multiple lines very close to each other. In addition to electronic excitations observed in atoms, molecules show also vibrational and rotational excitations (see Section 4.3). Strong absorption bands of gases like water vapor, CO₂, O₂ and O₃ make the atmosphere practically opaque at various spectral ranges, especially in the infrared and UV, as can be seen from the surface spectrum shown in Fig. 4.2.

4.2.3 Atomic spectra and line broadening

When a photon of the appropriate frequency ν is emitted or absorbed by an atom, the energy state of the atom changes according to

$$\Delta E = E_2 - E_1 = h\nu. \quad (4.16)$$

Experimentally, it can be seen that not all transitions occur and that the spectral lines have different intensities, from which directly follows that the transitions must have different probabilities. The electronic energy states are characterized by sets of quantum numbers: (n, l, m_l, m_s) for one-electron¹⁰ systems, (L, S, J, M_s, M_L) for many-electron¹⁰ systems. Transitions have to obey quantum mechanical selection rules, which describe whether a transition is allowed and which intensity the according spectral line has. In presence of an

⁹The fact that such heavy elements exist in the Sun, which is mainly composed of hydrogen (92%) and helium (8%), and fuses hydrogen to helium and only in the end phase of its life can produce heavier elements up to oxygen by fusing helium, proves that the solar system must have formed from debris of a supernova.

¹⁰With reference to the outermost shell

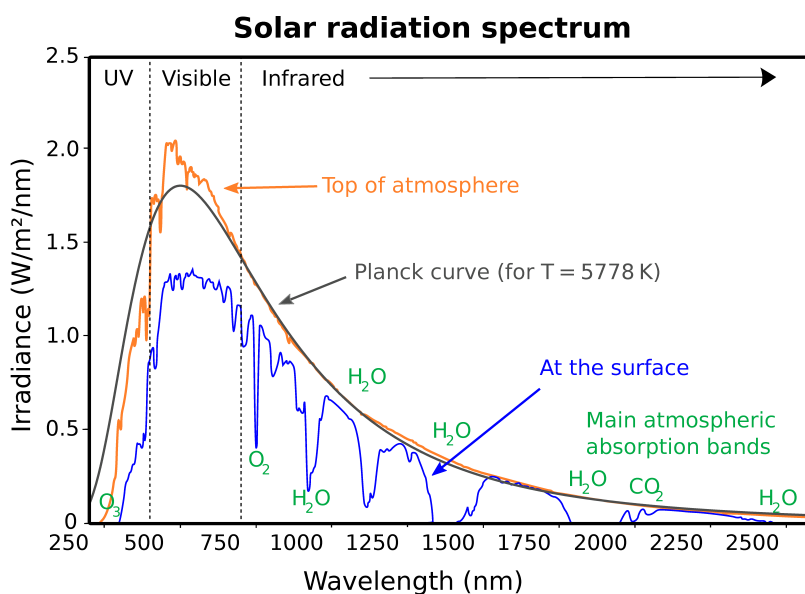


Figure 4.2.: Solar spectrum at the top of the atmosphere (without absorptions in the Earth's atmosphere) and at the surface, compared to a Planck curve for a blackbody at a temperature of 5778 K. In the surface spectrum, the main absorption bands are labeled with the corresponding atmospheric compounds. Adapted from a work by Nick84, CC BY-SA 3.0, <https://commons.wikimedia.org/w/index.php?curid=24648395>.

external electric field (Stark effect) or magnetic field (Zeeman effect), shifting and splitting of otherwise degenerate energy levels of spectral lines can occur.

For special importance for tropospheric chemistry are the two oxygen radicals $O(^3P)$ (ground state oxygen or triplet oxygen), created by the photolysis of NO_2 , and $O(^1D)$ (excited oxygen or singlet oxygen), created by the photolysis of ozone (see Sections 2.4 and 2.5). A direct radiative transition (fluorescence) from the singlet to the triplet state, that means from $O(^1D)$ to $O(^3P)$, is forbidden (selection rule: $\Delta S = 0$, which means that the multiplicity $2S + 1$ must not change), instead, the transition happens radiationless through quenching by an air molecule (M).

Even when observed with a perfect spectrometer with the highest imaginable resolution, the spectral lines from the transitions in an absorption or emission spectrum are not strictly monochromatic, but show a finite width and a specific line shape, and thus differ from the theoretically via (4.16) expected Dirac delta function shape. This *line broadening* is caused by various effects:

- The *natural line broadening* is a result of the limited lifetime of an excited state. According to Heisenberg's energy-time uncertainty principle, $\Delta E \cdot \Delta t \geq \hbar/2$, the faster an excited state decays, the larger the energy uncertainty and the broader the emission line. The resulting spectral line shows a Lorentzian profile.

- *Doppler broadening* is due to the thermal velocity distribution in a gas. The Doppler effect creates a velocity-dependent positive or negative wavelength shift, depending on the movement of the atom relative to the observer. The higher the temperature, the larger the velocity spread and the broader the effective (combined) line, which shows a Gaussian shape.
- *Pressure broadening*, also known as collisional broadening, is caused by elastic or inelastic collisions between gas atoms. The collisions, whose probability increase with increasing pressure, can change the energy levels in the approaching atoms and can interrupt emission processes and shorten the lifetimes, both of which lead to line broadening. The resulting line shape is, like for the natural line shape, a Lorentzian profile.

In the visible spectral range, Doppler broadening has an about two orders of magnitude stronger effect than the natural line broadening at room temperature (Demtröder, 2010). In the troposphere, pressure broadening is even stronger and the dominant effect, while higher up in the atmosphere Doppler broadening becomes more important due to the lower pressure (Hartmann, 2016). Thus, Doppler broadening and pressure broadening are typically the relevant processes to be considered, making the line shape a mixture of a Gaussian and a Lorentzian profile.

4.3 Molecular spectra and transitions

Compared to atoms, molecules have additional internal degrees of freedom, and their energy state is not only determined by the electron cloud but also by vibrations of the nuclei around their equilibrium positions and rotations of the molecule as a whole. Hence, in a molecule, for each electronic state there exist a large number of vibrational and rotational energy levels (see Fig. 4.3a).

A molecule consisting of N atoms has $3N$ degrees of freedom. Like for atoms, 3 degrees of freedom are reserved for translational movement. Non-linear molecules have three rotational degrees of freedom (3 axes), linear molecules have only two¹¹, which leaves $3N - 6$ (or $3N - 5$, respectively) degrees of freedom for vibration modes.

The respective transition lines can only be observed if the molecule has a permanent electric dipole moment and if the rotation or vibration movement changes its orientation or magnitude. Molecular spectra are categorized according to the transition energies, that differ significantly ($h\nu_{\text{rot}} \ll h\nu_{\text{vib}} \ll h\nu_{\text{el}}$) for the different excitation types:

¹¹Rotation around the connecting bond can be neglected because the corresponding moment of inertia is very small and the electric dipole moment does not change, which is a prerequisite for the interaction with light.

- Pure rotational spectra are caused by transitions between rotational levels of the same vibrational and electronic state and have wavelengths in the microwave.
- Rotational-vibrational spectra are caused by transitions between rotational levels of different vibrational states of the same electronic state and have wavelengths in the mid-infrared.
- Electronic spectra, caused by transitions between two different electronic states and their rotational and vibrational levels, have wavelengths in the UV, visible and near-infrared. Such an electronic spectrum comprises many vibrational bands, that again each contain many rotational lines.

4.3.1 Rotational spectra

For rotational transitions, where only the quantum number of rotation J changes, the quantum mechanical selection rule $\Delta J = \pm 1$ has to be applied. Pure rotational spectra consist of many closely spaced, nearly equidistant lines of different intensities, with an intensity maximum somewhere in the middle as a compromise between the increasing $2J+1$ degeneracy and the exponentially decreasing thermal population of states (Boltzmann distribution). The distance between the lines decreases slightly with increasing J and thus increasing distance between the atoms¹².

4.3.2 Vibrational spectra

Measurements of vibrational spectra with low resolution show a strong line at frequency ν and several weaker overtones at 2ν , 3ν , etc. High resolution measurements reveal that every line is a band consisting of many nearly equidistant rotational transition lines, as both J and the vibrational quantum number ν change. As opposed to the harmonic oscillator with its equidistant energy levels, the distance between the vibrational energy levels decreases towards the dissociation continuum, as can be seen in Fig. 4.3a, which, together with the occurrence of the overtones, can be explained by the model of an anharmonic oscillator combined with the empirically determined Morse potential¹³ for the electronic states of the molecule.

Although vibration and rotation are coupled, vibrations are much faster than rotations as during one rotation the molecule vibrates several hundred or thousand times (Haken and Wolf, 2006; Kakkar, 2015; McLauchlan, 2004).

¹²Which can be explained when expanding the simple rigid rotor model (giving equidistant lines) to a non-rigid rotor

¹³Which in contrast to the parabolic potential of the harmonic oscillator allows for dissociation

The rotational selection rule $\Delta J = \pm 1$ leads to the formation of two branches¹⁴, the P-branch ($\Delta J = -1$) with longer wavelengths and diverging lines for increasing J , and the R-branch ($\Delta J = +1$) with shorter wavelengths and converging lines for increasing J . The Q-branch in the center, the pure vibrational transition for $\Delta J = 0$, is often forbidden.

With $3N - 6$ (non-linear molecules) or $3N - 5$ (linear molecules) degrees of freedom left for vibration modes, for a diatomic molecule, which is always linear, one gets $6 - 5 = 1$ vibration mode, called stretching. For heteronuclear molecules like CO, the stretching mode is infrared-active because the dipole moment changes, while homonuclear molecules like N_2 have to be ionized first (N_2^+). For linear triatomic molecules like CO_2 , $9 - 5 = 4$ degrees of freedom are left for vibration modes: symmetrical stretching, asymmetrical stretching and bending (scissoring), the latter being two-fold degenerate. For CO_2 , the symmetric stretching is infrared-inactive, whereas the other vibration modes are infrared-active (greenhouse gas). For non-linear triatomic molecules like H_2O , $9 - 6 = 3$ vibration modes (symmetrical stretching, asymmetrical stretching and one bending mode) occur and all are infrared-active, because the molecule's dipole moment changes in all of them.

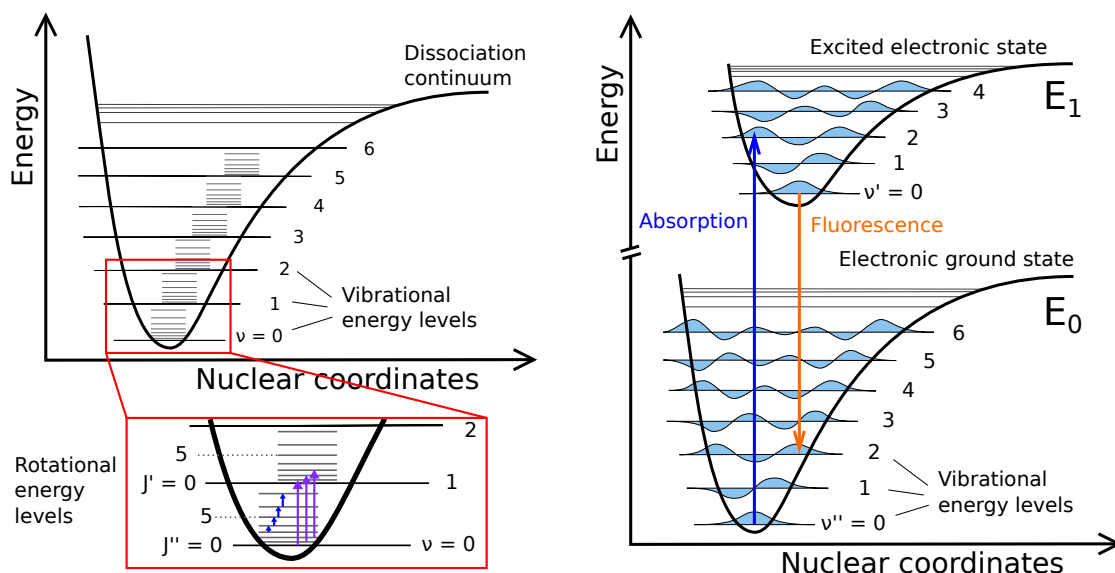
4.3.3 Electronic spectra

As opposed to atoms, electronic transitions in molecules also incorporate changes of the vibrational and rotational states, and the resulting electronic spectrum is a band system. It contains all vibrational bands of the respective electronic transition, each with its rotational structure. As opposed to pure rotational and vibrational transitions, electronic transitions occur also if the molecule does not have a permanent electric dipole moment.

Molecular orbitals can either be bonding or anti-bonding. In a potential energy diagram (energy plotted vs. distance of the nuclei), the first can be described with the well-known Morse potential, which incorporates both the repulsion for very small distances and a dissociation energy as a limit for nuclear distances tending towards infinity, with a minimum energy (bonding) in-between. The anti-bonding orbital can be described with an exponentially decreasing, purely repulsive curve.

For vibronic (electronic + vibrational) transitions, for example from the electronic ground state with $\nu'' = 0, 1, 2, \dots$ to the first excited state with $\nu' = 0, 1, 2, \dots$, the so-called Franck-Condon principle applies: As the Born-Oppenheimer approximation states that the movement of the electron is very fast in comparison to the core's, the electronic transitions in the energy level diagram occur vertically, without changes in the core coordinates, as it is shown in Fig. 4.3b.

¹⁴Which, viewed individually, appear quite similar to a pure rotational spectrum



- (a) Rotational and vibrational energy levels in a molecule's electronic potential curve. Rotational transitions are shown with blue arrows, vibrational transitions with purple arrows.
- (b) Franck-Condon principle for electronic transitions between the vibrational levels of two electronic states. The wave functions of the vibrational modes are indicated in cyan.

Figure 4.3.: Rotational, vibrational and electronic energy levels and transitions in a molecule, based on a work by Onno Gabriel, Public Domain, <https://commons.wikimedia.org/w/index.php?curid=2552083>

The probability for a transition is determined by the overlap of the vibrational wave functions, which can be evaluated with the overlap integral

$$\int \psi_{\nu'}^* \psi_{\nu''} dR, \quad \text{or in Dirac's bra-ket notation: } \langle \psi_{\nu'} | \psi_{\nu''} \rangle, \quad (4.17)$$

which can be deduced from the transition dipole moment (or transition matrix element) by incorporating the Born-Oppenheimer approximation. The intensity of the transition is proportional to the square of the overlap integral. Transitions between states with smaller overlap of the vibrational wave functions can occur, but are less probable and the corresponding vibronic bands are less intense in the spectrum.

Inside of an electronic state, the thermal occupation (Boltzmann) favors the lowest vibrational level, where the probability of presence, which is determined by the square of the wave function's amplitude, is highest in the center. The shift of the distance between the nuclei in the excited state compared to the ground state determines the relative intensities of the vibronic bands: If the two potential curves are not shifted, the highest intensity is found for the band with $\nu'' = 0 \rightarrow \nu' = 0$. If a shift exists, the intensity is highest for the transition to a larger ν' , i.e. for larger $\Delta\nu$, like in Fig. 4.3b. If the shift is large enough, the transition can lead into the dissociation continuum, and the resulting spectrum is continuous.

After an absorption process, the excited molecule relaxes to its vibrational ground state, from which then the transition back to the electronic ground state occurs, which is called *fluorescence*. The emitted photons typically have a lower energy (longer wavelength) than the absorbed ones. Because of this behavior, the absorption spectrum of a molecule is representative for the vibrational structure of its excited state, while the fluorescence spectrum gives the vibrational structure of its ground state.

Predissociation is a phenomenon that can occur when the potential curve of two electronic states cross each other and the higher energy state (bonding or anti-bonding) has a lower dissociation energy. At the intersection, a radiation-less transition (internal conversion) is possible, which shortens the lifetime of the lower state and broadens the rotational lines, smearing out the vibronic bands.

4.4 Scattering in the atmosphere

Scattering occurs when electromagnetic radiation hits a particle in the atmosphere, polarizes it by displacing its centers of charge (causing a periodical oscillation), and after a certain amount of time, the radiation is re-emitted, either with the same energy (elastic scattering, like Rayleigh or Mie scattering) or with a changed energy (inelastic scattering, like Raman scattering).

The different types of elastic scattering in the atmosphere can be distinguished by the so-called particle size parameter α , for a given wavelength λ defined as

$$\alpha = \frac{2\pi r}{\lambda} \quad (4.18)$$

with the particle radius r . Depending on the size of α one distinguishes:

- Rayleigh scattering occurs on particles which are small compared to the light wavelength ($\alpha \ll 1$) like air molecules and small aerosols. It has a strong wavelength dependence $\propto \lambda^{-4}$, which explains the blue color of the cloudless sky, the yellow color of the sun (although its intensity maximum is more in the green) and the red color of the setting sun, all because shorter wavelength radiation (blue) is scattered more strongly away from the beam direction than longer wavelength radiation (red). The Rayleigh phase function $P_{\text{Ray}}(\lambda) = 3/4(1 + \cos^2 \vartheta)$ causes non-polarized, incoming light to be approximately equally distributed (within a factor of two) in all directions. The scattered light is non-polarized in forward and backward direction and maximum linearly polarized perpendicular to the incident light beam¹⁵.

¹⁵The effect can be seen by looking at the sky through a polarizing filter and even stronger when photographing with an ultra wide-angle objective combined with a polarizing filter, which causes large dark zones in the sky.

- Mie scattering occurs on particles which are nearly equal in size to the light's wavelength ($\alpha \approx 1$) like aerosol particles or water droplets in clouds. Its scattering cross-section is proportional to λ^{-a} with $a = 0.5 \dots 2.5$ being the so-called Ångström exponent. As opposed to Rayleigh scattering, the phase function of Mie scattering shows a strong angular dependence with a very strongly pronounced maximum in forward direction and several additional, much smaller maxima and minima in other directions.
- On large particles ($\alpha \gg 1$), the scattering process can be described by simple geometric optics.

The Mie theory contains Rayleigh scattering and geometric scattering as special cases for very small and very large particles, respectively.

On air molecules, additionally to Rayleigh scattering about 2–4 % of the scattered photons undergo inelastic scattering, mainly due to Raman scattering, also known as the Raman effect. Typically this involves vibrational (and rotational) energy being gained by a molecule and the re-emitted photons being shifted to lower energies (Stokes scattering) or vice versa (anti-Stokes scattering), the latter being less probable and thus less intense.

A Raman spectrum contains a very strong peak at the frequency of the incident light, the so-called Rayleigh line, and the directly adjacent rotational lines of the (purely) rotational Raman scattering, called the O branch ($\Delta J = -2$) and the S branch ($\Delta J = 2$). In a distance corresponding to the vibrational energy appear the Stokes and anti-Stokes lines of the vibrational Raman scattering, again with adjacent rotational branches O and S, while the pure vibrational lines in the center are called the Q branch. Thus, a Raman spectrum looks quite similar to a vibrational spectrum, but the distance between the rotational lines is twice as large.

All molecules with an anisotropic polarizability, i.e. all diatomic molecules, even the non-polar ones like N_2 or H_2 , show a rotational Raman effect, while symmetrical tetrahedron-shaped molecules like CH_4 have an isotropic polarizability and thus are not Raman-active. Vibrational Raman scattering occurs for infrared-inactive vibration modes like the symmetrical stretching in the CO_2 molecule, whereas infrared-active vibrations are Raman-inactive.

The filling-in of Fraunhofer lines known as the Ring effect (Grainger and Ring, 1962) is caused by rotational Raman scattering, and its effect can be one order of magnitude larger than trace gas absorptions. It thus has to be included in the trace gas retrieval (see Chapter 5) as a pseudo-absorber cross-section (Solomon et al., 1987).

4.5 Electromagnetic radiation in solid matter and at interfaces

This section focuses on the interaction of light with solid matter with respect to how light propagates through materials like glass and what happens on air-solid interfaces, as our MAX-DOAS measurement instrument contains a lens to collect photons in the telescope, a spectrometer consisting of collimating mirrors and a refractive grating, and an optical light fiber to transmit the photons from the outside-located telescope about 20 m to the inside-located spectrometer.

4.5.1 Electromagnetic waves in matter – the refractive index

If electromagnetic waves hit matter and travel through a transparent medium the oscillating electric field of the wave disturbs the electrons in the atoms, which then oscillate back and forth in the direction of the electric field vector, forming oscillating dipoles. These dipoles emit again electromagnetic waves of the same frequency ω , but with a phase delay added¹⁶, slowing down the wave while traveling through the medium by a factor n ,

$$v_{\text{ph}} = \frac{c}{n} \quad \text{with} \quad n = \sqrt{\mu_r \varepsilon_r} \quad (4.19)$$

the so-called refractive index, that depends on the electrical and magnetic characteristics of the material, i.e., the relative permittivity ε_r and relative permeability μ_r . The value of n and thus the phase speed of the electromagnetic waves in the medium depends not only on the properties of the medium itself, but also on the wavelength of the radiation: $n = n(\lambda)$ and $v_{\text{ph}} = v_{\text{ph}}(\lambda)$. This is called *dispersion* and explains the splitting up of white light into a spectrum by a prism. Typical values for the refractive index are 1.0003 for air, about 1.33 for water and around 1.5 for glass.

To take into account that some part of the light is attenuated, a complex refractive index can be defined,

$$n = n_r - i \kappa, \quad (4.20)$$

where the real part n_r is the known refractive index and the imaginary part κ is an extinction or absorption coefficient of the medium, in which the radiation intensity is exponentially decreasing (Beer-Lambert's law).

In metals, the absorption coefficient is large and thus the penetration depth is very short, in the order of nanometers or fractions of nanometers. Radiation cannot penetrate into the

¹⁶Similar to the sinusoidally driven harmonic oscillator

medium (only a few atomic layers) and is mostly reflected back from the surface, causing the typical metallic gloss.

In optically transparent media, like air, water and glass, the absorption coefficient is very small and thus the penetration depth large, so that the imaginary part of the refractive index can be neglected: $n \approx n_r$.

4.5.2 Reflection and refraction on interfaces

If light (or electromagnetic radiation in general) is reflected on a surface, the incident angle of the incoming wave equals the angle of reflection of the outgoing, reflected wave (which is located on the other side of the normal to the reflection surface):

$$\theta_i = \theta_r, \quad (4.21)$$

the so-called *law of reflection*. Incident ray, the reflected ray and the normal to the surface lie in the same plane.

In general, for optically transparent media, some part of the incident light is reflected and some part penetrates into the medium. As a light wave passes from one medium into another one with a different refractive index, its phase speed changes and with this, its propagation direction. This effect is called *refraction* and is described by the well-known *Snell's law*:

$$\frac{\sin \theta_2}{\sin \theta_1} = \frac{v_{ph,2}}{v_{ph,1}} = \frac{n_1}{n_2} \quad (4.22)$$

If the light wave passes from an optically thinner medium into a thicker one, like from air to glass, the transmitted ray is bent toward the surface normal, and vice versa if the speed of light in the second medium is greater than in the first (see Fig. 4.4). The refracted ray lies in the same plane as the incident and reflected rays.

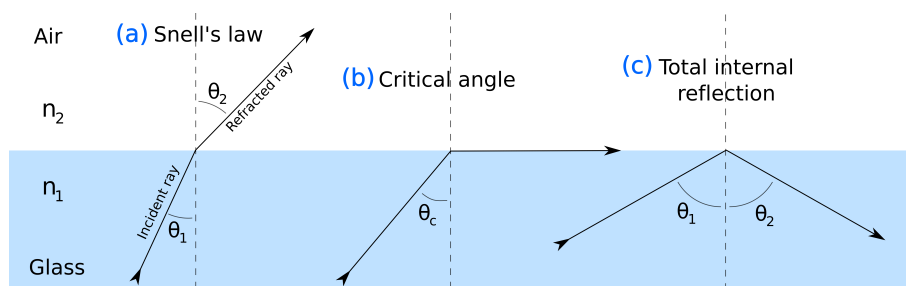


Figure 4.4.: Refraction of light at the interface between two media according to Snell's law (a), critical angle of total internal reflection (b), and (total internal) reflection of light on the interface (c). Adapted from a work by Josell7, CC BY-SA 3.0, <https://commons.wikimedia.org/w/index.php?curid=21670922>.

For the passage from an optically thicker medium into a thinner one (e.g. from glass to air) a critical angle θ_c exists, for which no light is refracted into the second, thinner medium anymore and the refracted waves travel along the interface,

$$\sin \theta_c = \frac{n_2}{n_1}, \quad (4.23)$$

the *critical angle of total internal reflection*. For incident angles larger than θ_c , all light is reflected on the interface. This phenomenon is utilized for example for optical fibers (see Section 4.5.4), which can transmit electromagnetic waves over long distances and through curvatures with low signal loss in-between.

The reflectance, the fraction of the reflected light on an interface, is minimal for normal incidence and around 4% for air-glass interfaces. For the two boundaries of a lens or a single glass pane, it sums up to 8%. To have the lowest possible reflectance and thus lowest light loss (highest transmittance), photographic lens manufacturers apply special coatings¹⁷ to their objectives, which are usually constructions of many lens elements (sometimes up to 20 or more) in several groups. However, this can introduce spectral structures and is not used in differential optical absorption spectroscopy (DOAS).

Reflected light is partially polarized. Under a special incident angle θ_B , the Brewster angle, for which $\theta_i + \theta_t = 90^\circ$ holds, the reflected light is perfectly linearly polarized. Not only the polarization plane changes when light hits an interface and is reflected, also a phase shift of 180° or π is introduced when light is reflected off an optically thicker medium ($n_2 > n_1$), but no phase shift in the opposite case.

4.5.3 Refraction in the Earth's atmosphere

As the air density in the Earth's atmosphere decreases exponentially with height (see Section 2.3), also the refractive index n decreases, which leads to the deviation of light rays (or other electromagnetic waves) from a straight line to a curved line as they pass through the atmosphere. The atmospheric refraction causes astronomical objects to appear higher above the horizon than they actually are. One prominent example is the sunset, where, when the lower edge of the Sun apparently touches the horizon, in reality the Sun has already completely set below the horizon. Also the distortion of the Sun's apparent shape shortly before sunset can be attributed to this effect.

¹⁷Stacked layers with different refractive indices that cause destructive interference of the reflected light beams

4.5.4 Optical fibers

The fiber-optic cable used to connect our MAX-DOAS telescope with the spectrometer unit is a bundle of cylindrical, thin and flexible optical fibers (quartz fibers).

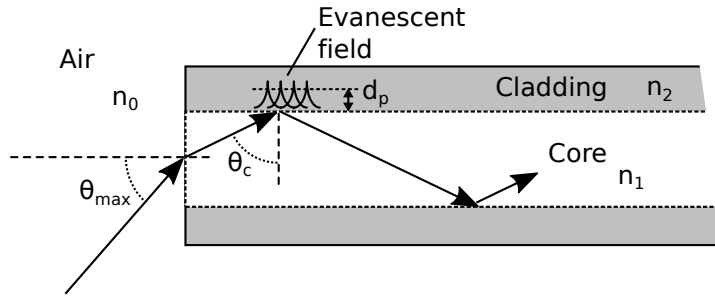


Figure 4.5.: Working principle of an optical fiber. The sketch shows how the maximum acceptance angle θ_{\max} depends on the critical angle of total internal reflection θ_c and illustrates the evanescent field penetrating into the cladding, with d_p being the so-called penetration depth.

The individual optical fiber consists of an inner core, the surrounding cladding and an outer protective coating (buffer or jacket) made of plastics, like it is sketched in Fig. 4.5. In a so-called step index fiber, like the one sketched here, the core has a higher refractive index (typical value $n_2 = 1.48$) than the cladding ($n_1 = 1.46$) (Mathur, 2018), while in a graded index fiber the refractive index decreases with radial distance from the center, with a near parabolic profile. In a multimode step index fiber like the one used in our MAX-DOAS instrument, a light wave, injected into the core, propagates along the light fiber due to total reflection at the interface of core and cladding (see Section 4.5.2 on total internal reflection). The critical angle of total internal reflection θ_c determines the maximum acceptance angle of the fiber θ_{\max} due to the refraction on the air-glass interface on the fiber entrance, which leads to the following equations:

$$\sin \theta_{\max} = \frac{1}{n_0} \sqrt{n_1^2 - n_2^2} \quad \Longleftrightarrow \quad n_0 \sin \theta_{\max} = \sqrt{n_1^2 - n_2^2} =: \text{NA}, \quad (4.24)$$

where the latter is defined as the numerical aperture (NA) of the fiber. The maximum acceptance solid angle cone and the cross-sectional area of the core define the throughput or étendue $(\pi^2/4) d_{\text{core}}^2 \text{NA}^2$, with the core diameter d_{core} . When internal reflection takes place, a certain portion of the electric field of the wave penetrates outside the core into the cladding, where its amplitude exponentially decreases, the so-called *evanescent field*. The penetration depth d_p (see Fig. 4.5) is given by

$$d_p = \frac{\lambda n_1}{2\pi \sqrt{\text{NA}^2 - n_1^2 \cos^2(\beta)}}, \quad (4.25)$$

where β is the reflectance angle. A typical value is ~ 5 times the wavelength of the light.

Light fibers make it possible to transmit light over long distances with low conduction losses. Conduction losses are due to absorption as well as Mie and Rayleigh scattering on impurities, the latter being the dominant effect for modern fibers. Although optical fibers enable to transmit light through curvatures, fiber bending is another loss process. One distinguishes two processes: First, bending of a multimode fiber reduces the number of modes that can propagate through the fiber and introduces a light leak proportional to the fiber diameter and inversely proportional to the bending radius and the square of the numerical aperture; thin fibers with high numerical apertures¹⁸ minimize this problem. The second process is due to the fact that part of the wave front is propagating inside the cladding and when bending, on the outer side needs a higher speed than in the fiber core to keep up but cannot exceed the natural speed of light in the medium, leading to radiation of energy out into the surrounding.

If illuminated at an angle less than the maximum acceptance angle θ_{\max} , the emitted light cone should theoretically preserve the illumination angle. However, bending and scattering can broaden this angle towards the maximum allowable θ_{\max} . Apart from special fiber types, bending and small manufacturing imperfections causing random birefringence lead to a complete destruction of a possible polarization state, especially when several fibers are combined to a fiber-optic cable. This is a desirable side effect for our instrument as radiation with different polarization states would be diffracted with different efficiency by the diffraction grating and then the division of spectra measured at different relative solar azimuth angles would create spectral structures.

The flexibility of optical fibers makes it possible to use fiber-optic cables like normal electrical cables. Although, such a fiber is capable of channeling light through relatively tight bends, to maintain the proper functioning, the bending of the fibers must not exceed a certain minimum specified bend radius to avoid damage and excessive light loss.

In the case of our MAX-DOAS instrument, the length and flexibility of an optic fiber cable enables us to spatially separate the telescope and spectrometer. A weatherproof positioning of the spectrometer unit inside a building, for example, facilitates the temperature stabilization of spectrometer and CCD detector.

4.5.5 Diffraction gratings

In our MAX-DOAS instrument, a grating spectrometer containing a so-called diffractive reflection grating is used for the spectral decomposition of light.

Diffraction describes the phenomenon which occurs if light waves pass near a barrier, that they tend to bend around that barrier and become spread out, as opposed to the

¹⁸I.e., larger acceptance angle and thus steeper critical angles of total internal reflection

phenomenon of refraction, where light bends as it crosses a boundary between two different media with different refractive indices. Diffraction of electromagnetic waves occurs when a wave passes by a corner, or through an opening or slit that is physically the approximate size of, or smaller than its wavelength.

Historically, one of the first diffraction experiments were Young's single and double slit interference experiments, which can be explained by the Huygens–Fresnel principle that states that every point on a wavefront is itself a source of spherical wavelets itself, with the secondary wavelets emanating from different source points mutually interfering so that the resulting amplitude in each point is the superposition of all wavelets' amplitudes with the envelope of the secondary wavelets forming the new wavefront. Behind the slit or double slit, interference patterns can be observed with a strong intensity peak in the center, and various other equally-distant side-maxima of decreasing intensity to the sides of the center peak, where constructive interference occurred.

In comparison to Young's well-known single and double slit interference patterns, a diffraction grating, which practically is a large number of small, evenly spaced parallel slits¹⁹, provides much sharper and narrower, and much better separated intensity maxima of higher peak intensity. For monochromatic light, its interference pattern can be computed via the grating equation, which describes the relation between the path difference Δs , the line spacing d and the incidence and diffraction angles α and β :

$$\Delta s = d \cdot (\sin \alpha + \sin \beta) = m \cdot \lambda, \quad (4.26)$$

with the order of diffraction m , which for integer values results in constructive interference (maxima) and for half-integer values results in destructive interference (minima), respectively. By convention, the incidence angle α is always positive whereas the diffraction angle β is positive when incident and diffracted ray are located on the same side of the grating normal and negative otherwise²⁰. For polychromatic light, a grating can resolve wavelengths at a high spectral resolution.

Diffractive gratings can be transmissive (like a multi-slit) or reflective, the latter being easier to manufacture. Reflection gratings are typically produced by scratching rules or grooves into a plane glass surface and overcoating the grooved surface with a reflecting material such as aluminum. Its zero-order maximum (light that is not diffracted), according to Eq. (4.26) is found at a reflection angle equal to the incident angle.

Modern reflection gratings are so-called *blazed* gratings, a special design which was invented to counteract the problem of having to throw away the photons of the white, undispersed light of the intense center maximum (zero-order maximum). It consists of a multitude of

¹⁹And thus a high number of secondary wavelet source points according to the Huygens–Fresnel principle

²⁰As the grooves can be tilted, grating normal and groove (or step) normal do not have to be the same.

tilted, step-shaped grooves, like it is sketched in Fig. 4.6. The step (or groove) normal is tilted with respect to the grating normal by the so-called *blaze angle*:

$$\theta_B = \frac{\alpha + \beta}{2}, \quad (4.27)$$

with α and β being the incident and diffracted ray angles with respect to the grating normal. With respect to the step (or groove) normal, the incident angle is $\theta_i = \alpha - \theta_B$ and the reflected angle is $\theta_r = \theta_B - \beta$. According to the above-mentioned convention, the angle β in Fig. 4.6 is negative.

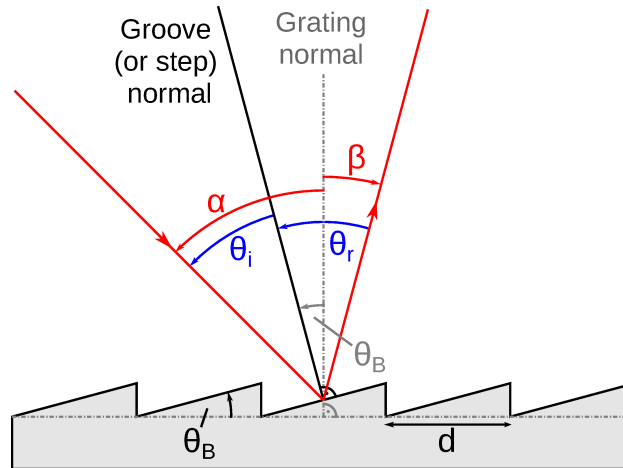


Figure 4.6.: Diffraction at a blazed grating, adapted from a work of Patrick87, public domain, <https://commons.wikimedia.org/w/index.php?curid=21807350>

Adjusting the blaze angle and thus the shape of the steps optimizes the grating for a specific wavelength range, for which the efficiency is maximal. The blaze angle θ_B for a given wavelength range $\Delta\lambda$ is selected in such a way, that the beam diffracted at the grating (under the angle β_m for the interference maximum of the m -th order) and the beam reflected at the steps (under the angle θ_r) are both deflected into the same direction. In this case, nearly all the reflected intensity is shifted into the m -th order.

The diffraction-limited maximum spectral resolution of a grating with N lines is given by

$$\frac{\lambda}{\Delta\lambda} = m N, \quad (4.28)$$

which can only be obtained if the grating is optimally (fully) illuminated.

Differential Optical Absorption Spectroscopy (DOAS)

The first spectroscopic studies of the atmosphere date back more than 100 years, to the discovery of ozone absorptions in the Earth's atmosphere by Cornu and Spottiswoode (1879) and the discovery of ozone bands in the UV and visible light by Hartley (1880, 1881) and Chappuis (1880). After first concentrating on the identification of atmospheric gases, it was Dobson who constructed the first spectrometer for regular measurements of atmospheric ozone (Dobson and Harrison, 1926).

The Differential Optical Absorption Spectroscopy (DOAS) is one of the most frequently used spectroscopic techniques for measurements of trace gases that absorb in the UV-vis spectral range in the atmosphere. The first DOAS applications reach back to Noxon (1975), Perner et al. (1976) and Platt and Perner (1980). It has been improved on the measurement and analysis side and adopted to the detection of more trace gases during the last decades (e.g. Richter, 1997; Solomon et al., 1987). While first being used for ground-based measurements, later on measurements from other platforms like satellites (e.g. Bovensmann et al., 1999; Burrows et al., 1999) or airplanes (e.g. Meier et al., 2017; Schönhardt et al., 2015; Wang et al., 2005) became important, too. In Bremen, at the Institute of Remote Sensing and Institute of Environmental Physics of the University of Bremen, DOAS measurements are performed on a continuous basis since early 1993 (Richter, 1997).

Detailed introductions into the DOAS method can be found in Platt and Stutz (2008) and Burrows et al. (2011), upon which also this chapter is based along with Peters (2013) and Richter (1997), that also describe the IUP Bremen MAX-DOAS instruments. In this chapter, first the theoretical basis of the DOAS method and the DOAS data analysis routines are explained. After that, a short overview of DOAS applications is given. The general multi-axis DOAS (MAX-DOAS) measurement geometry for ground-based measurements is sketched, whereas more detailed descriptions on special viewing geometries can be found in the respective chapters for ground-based measurements on Neuwerk and shipborne measurements on-board the research vessel Celtic Explorer.

5.1 The DOAS method

The basic principle of absorption spectroscopy is the investigation of the wavelength-dependent attenuation of radiation which passed through an absorbing medium. The fundamental theoretical basis for this is given by the well-known Lambert-Beer law (also known as Beer-Lambert-Bouguer law), which describes the exponential decrease of light intensity of a given wavelength with distance traveled by the photons in an absorbing medium (see Fig. 5.1). The degree of the exponential decrease depends on the concentration or number density of the absorber n and the wavelength dependent absorption cross section σ of the individual absorber molecules. Consequently, the product of n and σ is referred to as the absorption coefficient.

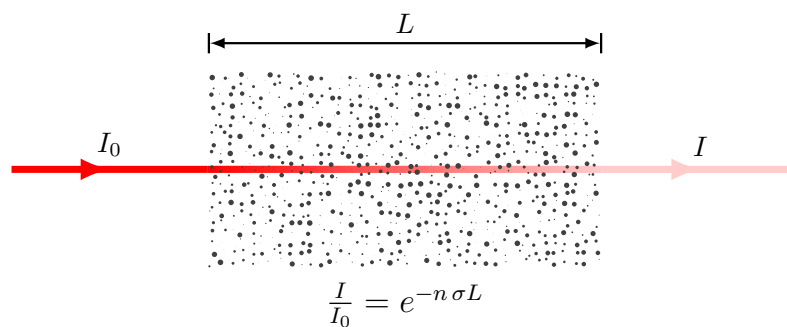


Figure 5.1.: Attenuation of light while passing through an absorber with concentration (number density) n and absorption cross section σ

While under laboratory conditions n and σ can be held constant along the light path s , for atmospheric measurements under field conditions the number density as well as the absorption cross section of the absorbing trace gas do in general depend on height and thus depend on the light path through the atmosphere, $n = n(s)$ and $\sigma = \sigma(\lambda, s)$. For the absorption cross section, this is a result of the temperature and pressure dependence, $\sigma(\lambda, s) = \sigma(\lambda, T(s), p(s))$. In this more general case, for electromagnetic radiation of initial intensity I_0 passing through an anisotropic medium along the light path s , the attenuated intensity I at a given wavelength λ is given by

$$I(s, \lambda) = I_0(\lambda) \exp \left\{ - \int_0^s n(s') \sigma(\lambda, s') ds' \right\} \quad (5.1)$$

Outside of the controllable conditions in a lab, for field measurements in the atmosphere for example, not only one but several trace gases of different abundances n_i and with different wavelength-dependent absorption cross sections $\sigma_i(\lambda)$ can contribute to the total light extinction with simultaneous absorption in the same spectral regions.

As we know from the radiative transfer equation, in addition to absorption also light extinction by scattering processes (see Section 4.4) has to be taken into account. This is mainly light scattering on air molecules (Rayleigh scattering), scattering on larger particles like water droplets or aerosol particles (Mie scattering) as well as inelastic scattering by air and trace gas molecules (Raman scattering), the latter being responsible for the Ring effect filling up absorption lines. To take the Rayleigh and Mie scattering into account in the Lambert-Beer law, the respective scattering cross sections are used as pseudo absorption cross sections $\sigma_j(\lambda)$. The Ring effect (see Section 4.4) can also be described by a pseudo cross section (Solomon et al., 1987).

Extending Beer-Lambert's law to multiple absorbing trace gases and including all above-mentioned scattering processes, one obtains for the measured spectrum $I(\lambda)$ at the location of the instrument:

$$I(\lambda) = I_0(\lambda) \exp \left\{ - \int \left[\sum_{i=1}^N n_i(s) \sigma_i(\lambda, s) + n_j(s) \sigma_j(\lambda, s) \Big|_{j=\text{Ray, Mie, Ring}} \right] ds \right\} \quad (5.2)$$

If assuming that the cross-sections are independent of height and thus light path¹, the equation can be simplified by factoring out the $\sigma_i(\lambda)$ and $\sigma_j(\lambda)$ of the integral. The remaining path integrals of the number densities,

$$\text{SCD}_i = \int n_i(s) ds, \quad (5.3)$$

are referred to as slant column densities (SCDs), or often simply called slant columns (SCs), with the dimension of molecules per unit area². Equation 5.2 then simplifies to

$$I(\lambda) = I_0(\lambda) \exp \left\{ - \left[\sum_{i=1}^{N+1} \sigma_i(\lambda) \text{SCD}_i + \sigma_{\text{Ray}}(\lambda) \text{SCD}_{\text{Ray}} + \sigma_{\text{Mie}}(\lambda) \text{SCD}_{\text{Mie}} \right] \right\}, \quad (5.4)$$

where the Ring effect is treated as an additional absorber (N+1).

The SCDs, the integrated trace gas concentrations along the light path, are the unknown quantities to be retrieved from the measured spectra with the DOAS method. From this equation, however, the individual contributions cannot be separated. Especially clouds can cause strong and broadband fluctuations of the light intensity by orders of magnitude, which can completely mask the comparatively weak trace gas absorptions.

¹Which is not an unreasonable approximation, as most trace gases are not homogeneously spread across the atmosphere but reside in layers at certain altitudes so that the effect of the temperature dependence of the absorption cross sections is not very pronounced, while the pressure dependency of UV-vis spectra for typical atmospheric pressures is quite small, anyway. To compensate for the impact of the simplification in this assumption, multiple cross sections of the same trace gas measured at different temperatures can be included to account for the temperature dependency, as it is usually done for ozone, for example.

²Although being a non-coherent SI unit, molecules/cm² has been widely adopted in the DOAS community as the commonly used unit for the SCD, nowadays sometimes being replaced by mol/m².

To overcome these problems, the key and original idea of the differential optical absorption spectroscopy (DOAS) is to separate the wavelength dependent extinction into two components, a low frequency part (broad-band structures) and a high frequency part (narrow-band structures), which is used for the retrieval of atmospheric absorptions. Therefore, the absorption cross-sections $\sigma(\lambda)$ are separated into a slowly varying function $\sigma_0(\lambda)$ accounting for elastic scattering and broadband absorption structures and a rapidly varying part $\sigma'(\lambda)$, the *differential* cross-section, accounting for the narrow-band absorption structures (Platt and Perner, 1980; Platt and Stutz, 2008): $\sigma(\lambda) = \sigma_0(\lambda) + \sigma'(\lambda)$. This “separation” is practically achieved by fitting and subtracting a low order polynomial which accounts for the smooth broad-band structures: $\sigma'(\lambda) = \sigma(\lambda) - \sum_i c_i \lambda^i$. As the wavelength dependencies of the Rayleigh and Mie scattering cross sections follow simple power laws (see Section 4.4), the effect of both Rayleigh scattering ($\propto \lambda^{-4}$) and Mie scattering ($\propto \lambda^{-\kappa}$, $\kappa = 0 \dots 2$) can also be approximated by a polynomial.

Introducing one combined polynomial in Eq. 5.4, accounting for broad-band structures in the absorption cross sections, Rayleigh and Mie scattering as well as instrumental effects like wavelength dependent changes in the light throughput of the instrument, yields:

$$I(\lambda) = I_0(\lambda) \exp \left\{ - \left[\sum_{i=1}^{N+1} \text{SCD}_i \sigma'_i(\lambda) + \sum_p c_p \lambda^p \right] \right\} \quad (5.5)$$

Taking the logarithm,

$$\ln I(\lambda) = \ln I_0(\lambda) - \sum_{i=1}^{N+1} \text{SCD}_i \sigma'_i(\lambda) - \sum_p c_p \lambda^p, \quad (5.6)$$

and re-arranging for the optical depth (or optical density) $\ln I_0/I =: \tau$ yields:

$$\tau(\lambda) = \ln \left(\frac{I_0(\lambda)}{I(\lambda)} \right) = \sum_{i=1}^{N+1} \sigma'_i(\lambda) \text{SCD}_i + \sum_p c_p \lambda^p, \quad (5.7)$$

the so-called **DOAS equation**. It links the measurements τ in a linear equation to the quantities of interest, the slant column densities of the absorbing trace gases.

The DOAS approach has the benefit that all multiplicative effects that appear in both I and I_0 in Eq. (5.7) are canceled out if I and I_0 are measurements from the same instrument performed relatively close-in-time. Thus, an absolute radiometric calibration of an instrument’s measured intensity is not needed, an important advantage of the DOAS method. If an effectivity factor is introduced in Eq. 5.2 to account for the fact that scattered light is measured and not direct sunlight, it is also accounted for here by the polynomial.

From the DOAS equation, the SCDs and polynomial coefficients can be retrieved with simple linear least squares fits from the measured spectra. For this fit to not be underdetermined,

the wavelength window must be chosen large enough so that the number of sampling points in wavelength-space is at least as high as the combined number of included absorption cross sections and polynomial coefficients, usually the number is much larger, making this an overdetermined problem.

Taking absorption cross sections from laboratory measurements as an input, a least squares fit is performed on the measured optical depth τ_{meas} according to Eq. (5.7). In this process, the difference between the measured optical depth and the fit result τ_{fit} for each sampled wavelength step λ_k is minimized in a least squares sense:

$$\sum_k r_k^2 \rightarrow \min \quad \text{with} \quad r_k = \tau_{\text{meas}}(\lambda_k) - \tau_{\text{fit}}(\lambda_k). \quad (5.8)$$

This differences r_k for all λ_k form a so called residual spectrum, or residual, $r(\lambda)$, which contains all spectral structures which have not been accounted for in the DOAS fit, and the measurement noise³.

A simple quality criterion for the DOAS fit on overall is the root mean square (RMS) of the residual spectrum,

$$\text{RMS} = \sqrt{\frac{1}{N} \sum_k r_k^2}, \quad (5.9)$$

or the χ^2 statistics.

As the resolution of the laboratory-measured absorption cross sections taken from literature is usually much higher than the resolution of the instrument and thus of the measured spectra $I(\lambda)$ and $I_0(\lambda)$, the measured quantity is the intensity convoluted with the spectrometers slit function. Because convolution and logarithm in Eq. (5.6) do not commute, in theory the logarithm cannot simply be taken on both sides. The result is an incomplete cancellation of Fraunhofer structures in the optical depth which can lead to problems when structures of weak absorbers overlap with strong and structured absorptions. For a more detailed description of this so-called I_0 effect see Peters (2013) and Richter (1997). A correction, the so-called I_0 correction, is possible (Aliwell et al., 2002; Richter, 1997) but involves the guess of a typical slant column. However, for most practical applications, it is sufficient to just convolute the absorption cross sections with the instrument's slit function to bring them to the instrument's coarser resolution.

As the influence of the I_0 correction on the measured slant columns of NO_2 in this study is practically too small to be visible in the data, the I_0 effect is neglected in the following.

Figures 5.2, 5.3 and 5.4 illustrate again the DOAS data analysis procedure on the example of two subsequent spectra measured on Neuwerk on 26 May 2014 around noon.

³In the best case the residual only contains the measurement noise and thus looks like random noise, whereas systematic structures in the residual point at omitted absorbers or other effects.

Figure 5.2 shows the first steps of the DOAS data retrieval from the measured spectra to the differential optical depth. In the first row, the two subsequent off-axis measurements in 1° elevation are shown, spectrum A in panel a and spectrum B in panel b, representing the measured intensity $I(\lambda)$. The Fraunhofer structures in the spectra can easily be seen. In panel c below, the reference spectrum I_0 is shown, a zenith sky measurement taken in-between the two presented off-axis measurements. This spectrum is used as a common reference for both off-axis measurements.

The next row comprising of panel d and e, shows for both spectra A and B the ratio of I_0 divided by I . While the spectra A and B in panel a and b look very similar due to the strong Fraunhofer lines superimposing and thus masking the weak absorption signals of the trace gases, already by taking the ratio I_0/I the Fraunhofer structures in both I and I_0 cancel out and the spectral structures of the trace gas absorptions become visible in panel d and e. Comparing panel d and e, it can now be seen that spectrum B contains more narrow-band absorption structures.

In the next row (panel f and g), the natural logarithm is taken to gain the optical depth $\tau = \ln I_0/I$. Visually, this changes very little but the scale of the y-axis. Additionally, in these panels a polynomial of degree 5 is plotted which has been fitted to the optical depth to account for the smooth broad-band structure of the curves. By subtracting the polynomial from the optical depth, the differential optical depth is yielded, shown in panels h and i in the last row.

Comparing the differential optical depth of measurement A and B, similar spectral structures can be seen at 475 nm and especially pronounced around 505 nm, while in the other parts of the spectrum measurement B shows much more and stronger absorption features than measurement A.

In Fig. 5.3, the preparation procedure of the absorption cross sections for the DOAS fit is shown on the example of the trace gases nitrogen dioxide (NO_2) and water vapor (H_2O). High resolution absorption cross section are available from literature and were obtained from high resolution laboratory measurements. The first line of Fig. 5.3 shows such high resolution UV-vis absorption cross sections of NO_2 at 298 K (Vandaele et al., 1996) in panel a and H_2O at 293 K ((Lampel et al., 2015)) in panel b.

In the next row (panel c and d), again the high resolution absorption cross sections are shown, but restricted to the wavelength range of the Neuwerk instrument's visible channel spectrometer of 399 to 538 nm, highlighted as a gray area in the panels in the first row. The magnified inlet in panel d illustrates the extremely highly resolved spectral structures in the H_2O absorption cross section not even visible in the plot.

Convolving the high resolution laboratory cross sections with the slit function of the instrument plotted in panel e takes the cross sections to the instrument's coarser optical

resolution of about 0.6 to 0.7 nm (FWHM of the slit function), as it is shown in panel f and g. The resolution difference is especially visible for water vapor in panel g.

In the next step, a fitted polynomial is subtracted to gain the differential absorption cross sections at instrument's resolution.

Figure 5.4 puts the differential optical depth of the measurements A (panel a) and B (panel b) from Fig. 5.2 side by side with the three differential absorption cross sections of O_4 (panel c), H_2O (panel d) and NO_2 (panel e) for comparison.

For measurement A, the strong similarity of the differential optical depth (panel a) and the absorption cross sections of the two most important absorbers O_4 and water vapor and that the differential optical depth is a result of absorption processes on O_4 and H_2O molecules in the air is obvious by eye. The strong spectral features of O_4 around 475 nm and of H_2O around 505 nm can be seen one-to-one in the differential optical depth of measurement A. The same is true for the weaker O_4 band around 530 nm, while the structures of O_4 and H_2O between 440 and 450 nm overlap.

In the optical depth of measurement B in panel b, taken 4 minutes later in the same direction, again the strong water vapor absorption around 505 nm is very pronounced and the O_4 absorption band around 475 nm can also be seen. However, this measurement's optical depth is clearly dominated by the absorption structure of NO_2 , as a comparison to NO_2 's differential absorption cross section (panel e) shows. As both measurements contain an equal amount of O_4 and H_2O absorption, this means that in the short time span between measurement A and measurement B, a large number of light-absorbing NO_2 molecules has moved into the light path of the MAX-DOAS instrument leading to NO_2 's absorption structures being imprinted onto the measured spectrum B (and especially its optical depth). While measurement A can be considered as clean air, in measurement B, taken 4 minutes later, the air is polluted with NO_2 .

According to Eq. (5.7), the scaling factor between the differential absorption cross section and the differential optical depth is the slant column of the absorber. For NO_2 in measurement B, the optical depth is up to 0.04, while the differential absorption cross section goes up to $2 \times 10^{-19} \text{ cm}^2/\text{molecule}$, yielding in rough approximation a slant column density of about $2 \times 10^{17} \text{ molecules/cm}^2$. Figure A.1a in the appendix shows the DOAS NO_2 fit result for the settings listed in Table 6.1 (p. 85) for this measurement. The DOAS fit retrieved a NO_2 DSCD of $2.3 \times 10^{17} \text{ molecules/cm}^2$ from the measured spectrum, with a very low fit error of 0.2%.

The last panel in Fig. 5.4 shows this day's time series of NO_2 slant columns measured in this off-axis direction. Measurement A and B are marked with colored circles in the plot. As discussed, at the time of measurement A the air was relatively clean, while 4 minutes later

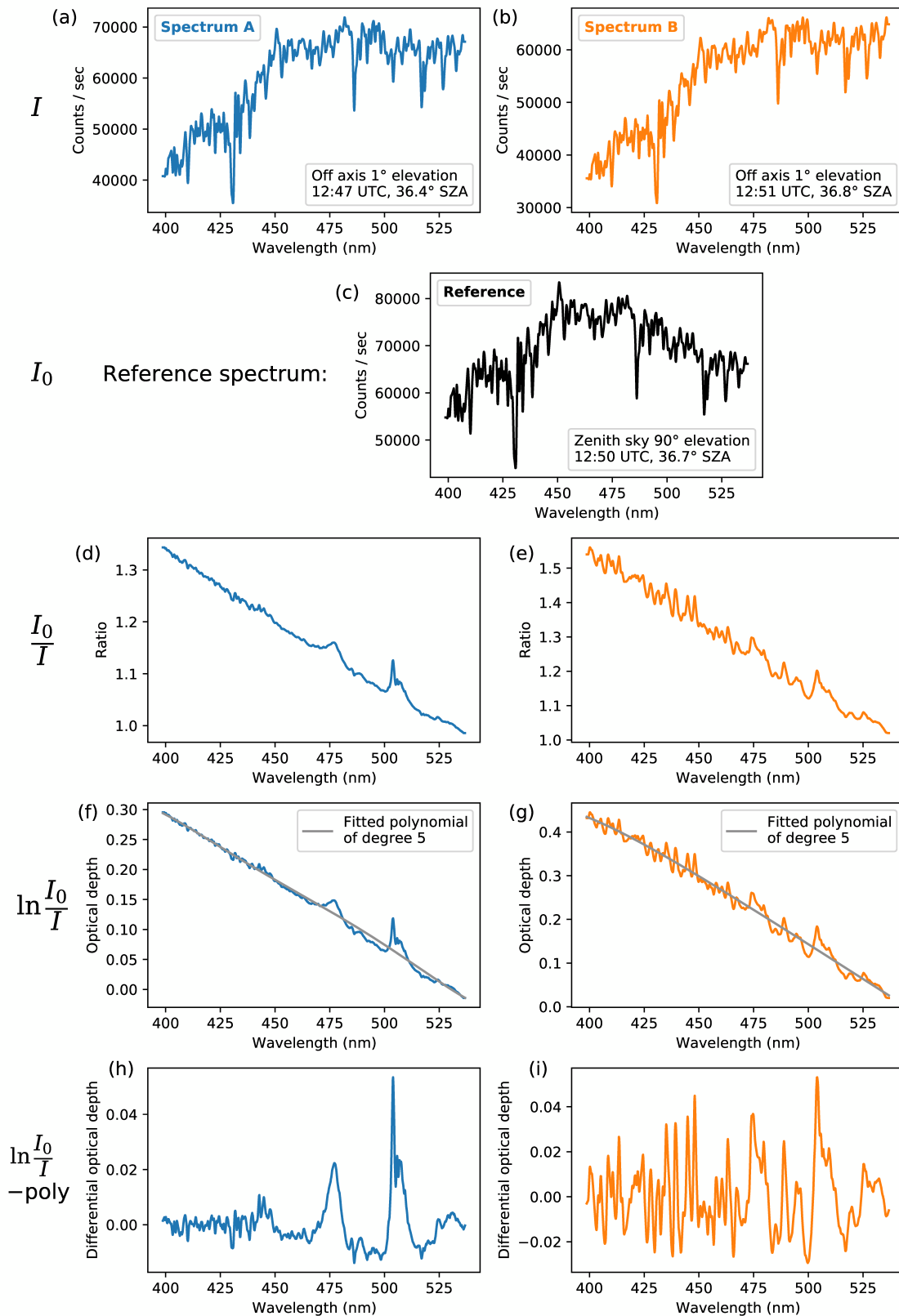


Figure 5.2.: First steps of the DOAS retrieval procedure from measured spectra to differential optical depth for two example measurements A and B taken on Neuwerk on 26 May 2014 around noon.

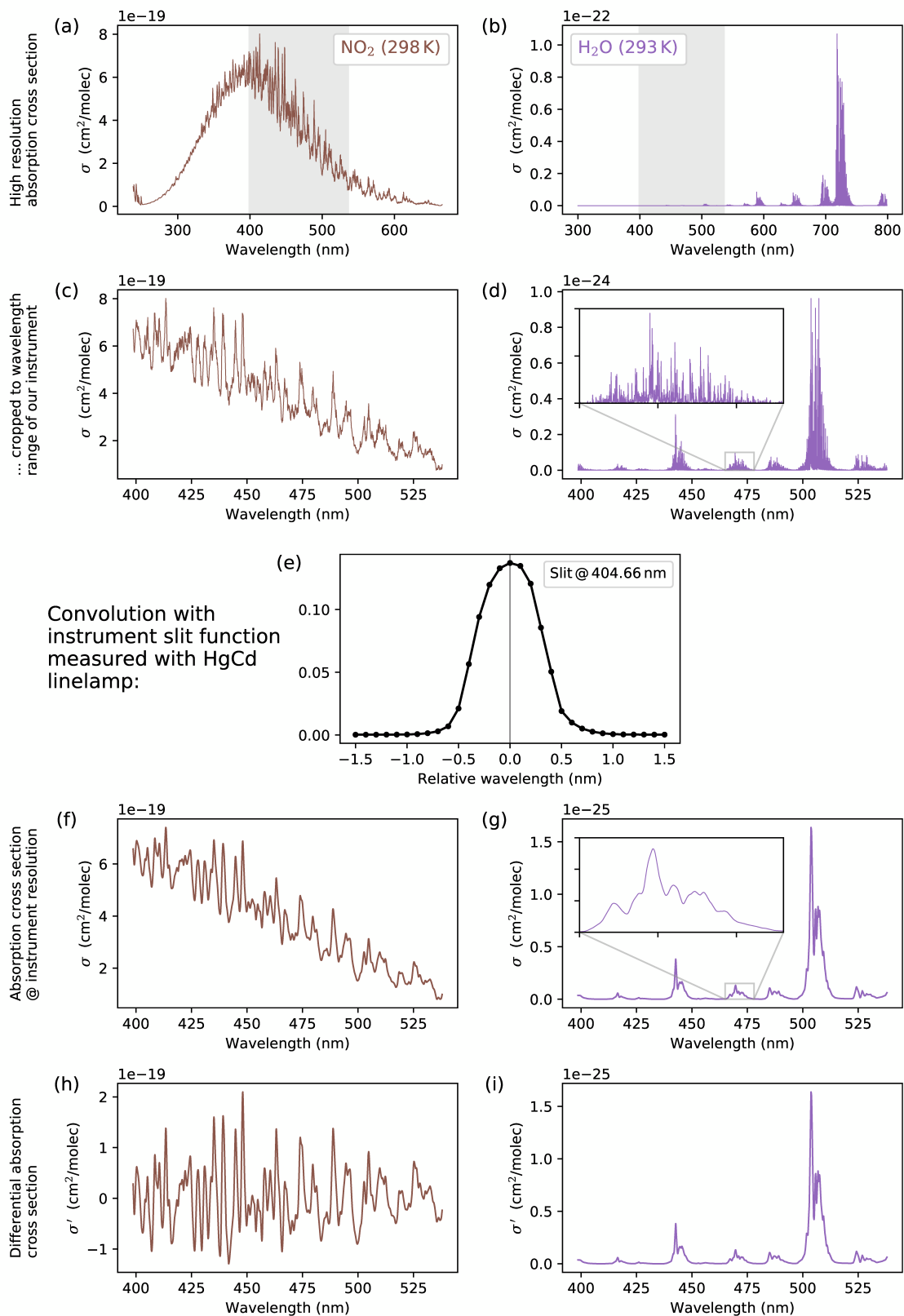


Figure 5.3.: Preparation of the absorption cross sections for the DOAS fit on the example of NO_2 and water vapor

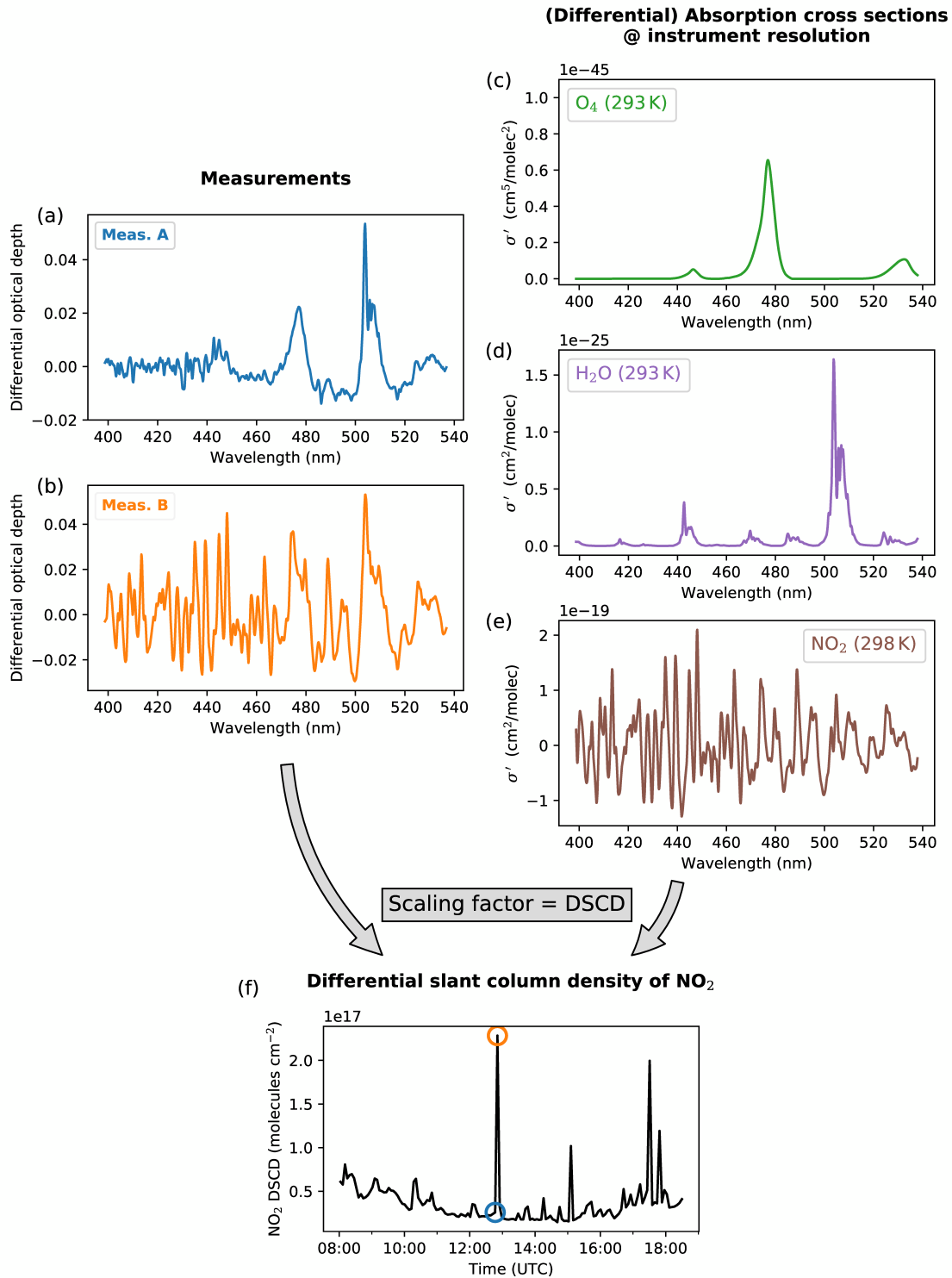


Figure 5.4.: Side-by-side comparison of the differential optical depth of the two selected measurements A and B and the differential absorption cross sections of O_4 , water vapor and NO_2

a ship's emission plume was probed by the MAX-DOAS instrument, leading to significantly enhanced NO₂ levels and a strong peak in the NO₂ time series.

5.2 The DOAS fitting routine

The DOAS fit for the measurements presented in this study has been performed with IUP Bremen's own software *NLIN_D* (Richter, 1997). Before the DOAS fit, the spectra measured by the CCD through IUP Bremen's measurement software *AMAX_OMA* have to be prepared for the further analysis. For this, in an automated daily procedure dark spectra for each CCD exposure time and HgCd line lamp spectra are measured every night. To obtain a dark spectrum, a shutter in the telescope blocks the light entrance, so that only the dark signal of the unexposed CCD is measured. This dark signal consists of the CCD's dark current, readout noise and has an artificial offset component⁴ added by the manufacturer to ensure that measured intensities are positive. It is subtracted from the measurements as well as from the line lamp spectrum.

In the next step, the raw spectra (counts vs. CCD pixel number) are wavelength-calibrated by using the HgCd line lamp spectrum and a literature atlas of spectral line positions of Mercury (Hg) and Cadmium (Cd), ending up with calibrated spectra (counts/sec vs. wavelength). These steps are performed by the software tool *nprepare*. Another tool, *resolut*, extracts the instrument's slit function from the line lamp spectrum. In the software *NLIN_D*, the absorption cross sections are then brought to the instrument's resolution by convolution with this slit function.

In the DOAS fitting routine, first the reference measurement I_0 is fine-calibrated with a high-resolution Fraunhofer atlas (Kurucz, 1984) in a non-linear fit (Levenberg-Marquart) enabling the wavelength axis to be shifted and squeezed. The main DOAS fit consists of two alternating routines: The measurement I and the absorption cross sections σ_i are calibrated onto I_0 in another non-linear fit with possible shift and squeeze. For each combination of shift and squeeze parameters, the DOAS equation (5.7) is solved in a linear least squares fit according to Eq. (5.8). The two alternating routines are iteratively repeated until convergence is reached.

5.3 DOAS measurement setups and applications

The DOAS technique has been applied to various measurement geometries and platforms, with different light path setups and various light sources. Active DOAS measurements use

⁴Usually a few hundred counts

artificial light sources like lamps or lasers and have been applied for example as long-path DOAS (e.g. Perner et al., 1976; Stutz and Platt, 1997a; Stutz and Platt, 1997b), later expanded by the use of retroreflectors to fold the light path once, tomographic DOAS, and folded-path DOAS (or cavity enhanced DOAS) (e.g. Ritz et al., 1992).

Passive DOAS measurements rely on natural light sources like the Sun, or less frequently, Moon and stars. As the light crosses the entire atmosphere, a direct computation of concentrations from the absorptions like it can be done for the active DOAS techniques is not possible for passive DOAS and can make the interpretation of the measurements challenging. The trace gas slant columns along the light path through the atmosphere can be converted to atmospheric vertical columns via geometry or radiative transfer model (RTM) calculations, though. In comparison to the active techniques, passive DOAS has the advantages of a relatively simple experimental setup, of not needing a stable artificial light source, of not needing a counterpart station with a retroreflector, and much longer light paths.

In passive DOAS, a distinction is made between direct-sun measurements, either ground-based, balloon-borne or realized as occultation measurements from satellites, measurements of scattered sunlight like ground-based zenith-sky DOAS (e.g. Noxon, 1975; Solomon et al., 1987) and multi-axis-DOAS (MAX-DOAS) (e.g. Hönninger et al., 2004; Wittrock et al., 2004), both expanded to a variety of different moving platforms like ships, airplanes, helicopters, cars or bikes, and measurements of backscattered sunlight like airborne imaging DOAS (e.g. Meier et al., 2017; Schönhardt et al., 2015) and DOAS on satellite instruments (e.g. Bovensmann et al., 1999; Burrows et al., 1995, 1999) in limb or nadir geometry.

The measurements performed for this thesis and presented in the following studies have been taken using ground-based MAX-DOAS instruments, but also measurements taken by airborne imaging DOAS and by satellite DOAS are used for validation purposes.

5.4 MAX-DOAS measurement geometry and the selection of a reference spectrum

For DOAS measurements according to Eq. (5.7), a suitable reference spectrum I_0 has to be selected. For DOAS measurements from satellites (e.g. Schönhardt et al., 2008), an extraterrestrial sun spectrum containing no terrestrial absorptions and only Fraunhofer structures from the Sun's atmosphere can be used as the reference spectrum. In this case, *absolute* slant column densities can be retrieved, i.e., the absorbers' concentrations integrated along the complete light path through the Earth's atmosphere. From a ground-based

instrument, no such pure solar spectrum without terrestrial absorbers can be measured. For ground-based measurement, in principle, one could use a high-resolution extraterrestrial satellite spectrum convoluted with the ground-based instrument's slit function as I_0 , but one would lose the advantage of the canceling out of all the instrumental effects in the division of I_0 by I which inevitably leads to errors in Eq. (5.7). Hence, to fully exploit the important advantage of the compensation of the instrumental effects and characteristics in the division of I_0 by I in the optical depth, the reference spectrum I_0 is measured with the same ground-based instrument.

Usually, a zenith measurement is used as a reference, but other viewing directions are also possible. Usually, either a daily zenith reference spectrum taken at noon, when the solar zenith angle is smallest and the light path through the upper atmosphere is shortest, or a *sequential*, close-in-time zenith measurement is used. For the latter, the reference measurement I_0 in zenith direction is performed either shortly before or shortly after the measurement I , or interpolated in time between those two. This sequential reference provides the advantage, that the compensation of instrumental effects by canceling out in the division of I_0 by I works the better, the closer in time I and I_0 are measured. A close-in-time reference guarantees the highest similarity in atmospheric conditions and avoids possible changing instrumental characteristics with time, so-called instrumental drifts.

Another possibility is the usage of a fixed reference spectrum taken at noon on one specific day with suitable conditions for a longer time series. For mobile measurements, often a fixed reference in a clean area is used for the whole trip.

The reference spectrum I_0 , when measured with a ground-based instrument, even when measured at noon at the shortest possible light path through the atmosphere, contains atmospheric absorptions, in contrast to an extraterrestrial spectrum. Due to this, the retrieved slant column densities can never be absolute but only differential values and the retrieved quantity is called the *differential* slant column density (DSCD), the difference between the SCD of the measurement and the reference:

$$\text{DSCD}_{\text{meas}} = \text{SCD}_{\text{meas}} - \text{SCD}_{\text{ref}}. \quad (5.10)$$

The light path through the atmosphere in general depends on the elevation angle (EA), i.e., the viewing angle above the horizon, the solar zenith angle (SZA), representing the height of the sun on the sky, and the solar azimuth angle (SAA), the horizontal angle between the viewing direction and the sun.

Figure 5.5 shows the principle MAX-DOAS viewing geometries for tropospheric measurements while Fig. 5.6 shows the viewing geometry for zenith sky DOAS measurement of stratospheric absorbers. For the sketched viewing geometries in both figures a single

scattering event of the photons on their way from the Sun to the instrument is assumed and the SAA-dependence is omitted.

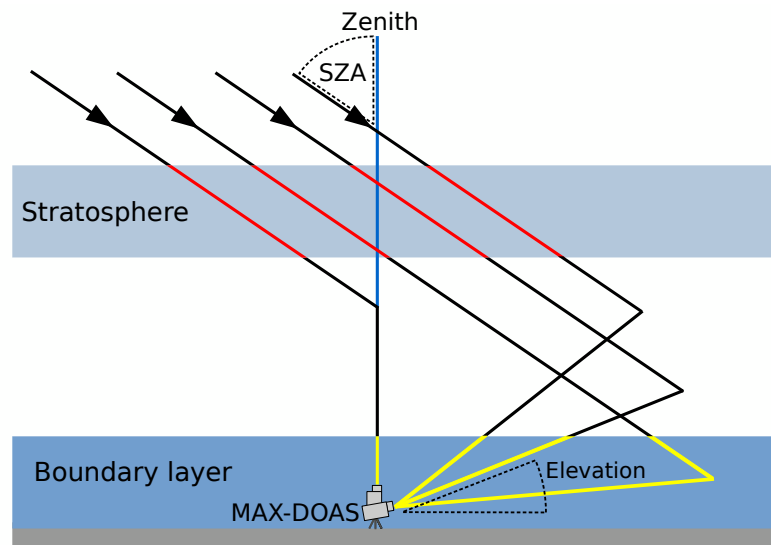


Figure 5.5.: MAX-DOAS viewing geometry (schematic) for different elevation angles and a fixed solar zenith angle (SZA)

Common MAX-DOAS measurement elevations range from low elevation angles pointing at or slightly above the horizon, to higher elevation angles of 10° , 15° or 30° , for example, to zenith sky (90°) measurements, each having different advantages and disadvantages for certain applications. The measurement elevations different from the zenith direction are often called *off-axis* directions.

A MAX-DOAS “scan” (or “vertical scan” or “elevation scan”) is a measurement sequence consisting of multiple elevation angles measured consecutively, often in an ascending order. Usually, these scans are repeated on a regular order every few minutes (depending on the integration times per direction), and in between the off-axis scans a zenith measurement is taken. Normally the elevation angle steps are chosen to be small for low elevations while larger steps can be used for the higher elevations, as the light paths do not change as much at higher elevations.

For measurements of tropospheric absorbers, like air pollution in the boundary layer, the measurement geometry is sketched in Fig. 5.5. The lower the elevation angle, the longer the light path through the boundary layer and the higher the sensitivity to absorbing trace gases in the boundary layer. As can be seen from the figure, for measurements taken at similar SZA the light path through the upper atmosphere is similar for all off-axis directions. The fact that the retrieved quantity is a *differential* slant column density thus enables to

nearly completely remove the absorptions in the upper atmosphere from the measured DSCDs, as the absorptions on the similar stratospheric light paths cancel out⁵.

For air pollution, which is often found in layers close to the ground, the last scattering point (in the simple sketch in Fig. 5.5 the only scattering point) can either lie above the absorber layer or inside the absorber layer. As each photon takes a different path through the atmosphere, only a mean effective last scattering point can be determined and the light path sketched here is only a statistical mean of an infinite number of possible light paths. A high aerosol concentration in the boundary layer increases the scattering possibilities and thus shifts the most probable scattering point towards the instrument, which can drastically shorten the light path in the lower viewing elevations.

Because of the different light paths through the troposphere, the MAX-DOAS scan, i.e., the consecutive measurements in different elevations, contains information about the vertical distribution of an absorbing trace gas. Utilizing a radiative transfer model, a MAX-DOAS scan with many small-step elevation angle changes with slightly different light paths can be used to compute a vertical trace gas profile (Bösch et al., 2018; Clémer et al., 2010; Frieß et al., 2006; Wagner et al., 2004; Wittrock, 2006).

For zenith-sky measurements on the other hand, the tropospheric light path barely depends on the SZA, while the stratospheric light path strongly depends on the SZA and can get very long for low sun, as it is sketched in Fig. 5.6. This is taken advantage of for the investigation of stratospheric absorbers. Already the first regular ozone measurements by Dobson used this simple setup (Dobson and Harrison, 1926).

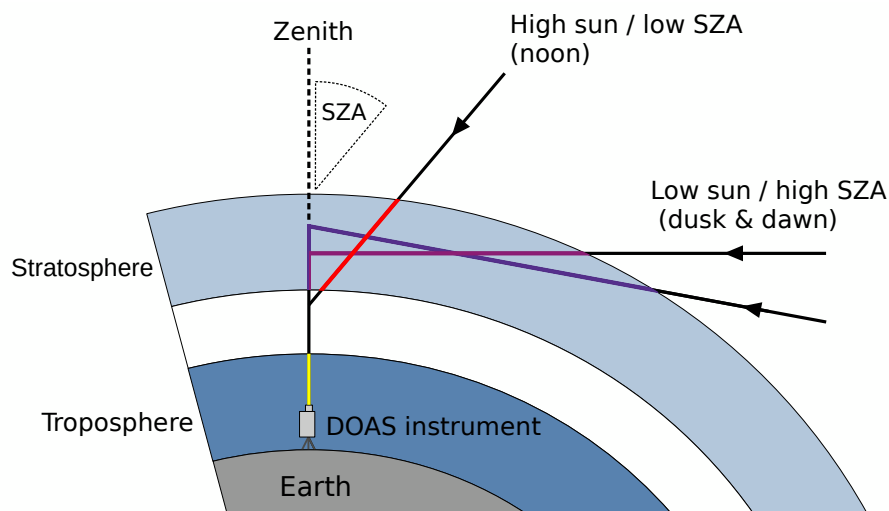


Figure 5.6.: Zenith viewing geometry (schematic) for three different solar zenith angles (SZAs)

⁵Provided that a sequential zenith reference spectrum, i.e., a zenith measurement with an as close as possible SZA, is chosen

If the MAX-DOAS instrument (or more accurately the telescope) points to the zenith, photons are measured that have been scattered downwards towards the ground in zenith direction above the instrument. As can be seen from Fig. 5.6, the distance covered by the photons along the slanted path in the stratospheric absorber layer increases with increasing SZA, giving the highest sensitivity for the detection of stratospheric absorbers for the lowest sun elevations, or even before sunrise and after sunset.

Knowing the actual scattering height of the last scattering event is impossible, as again, myriads of different photon paths are possible and thus the photons detected on the ground could originate from all different scattering heights, hence is why only a most likely scattering height can be stated. As the light is more intense in higher altitudes, more photons should be scattered there. On the other hand, the number density of air and thus possible scatterers decreases exponentially with height, so that the most likely scattering height should lie somewhere in-between. It is a function of the SZA and increases with increasing SZA. For 30° SZA it is located at approximately 5 km height, for 90° SZA at 15 km height, and for 93° SZA at about 25 km height, for light of 440 nm (Solomon et al., 1987).

For MAX-DOAS measurements in low elevation off-axis directions, the determination of the actual light paths in the troposphere is much more challenging due to additional scattering on aerosol particles and cloud droplets and the enhanced probability of multiple scattering events. Even scattering at the ground and back into the light path is possible. Usually if knowledge on the boundary layer height, absorber layers and aerosol distribution and properties are present, radiative transfer modeling (RTM) can be used for the determination of tropospheric light paths. As such knowledge from e.g. supplementary measurement techniques is not available for the measurements presented in this thesis, no RTM calculations have been applied here.

Chapter 6 on the MAX-DOAS measurements on Neuwerk presents an alternative approach to determine the horizontal effective light path in the boundary layer via the DSCD of the oxygen collision complex O_4 , which absorbs in the UV-vis region and can be retrieved simultaneously to NO_2 in the DOAS fit. Chapter 8 on the shipborne measurements on-board the RV Celtic Explorer presents a simple geometric approximation of the tropospheric light paths for the conversion of trace gas slant columns to vertical columns.

MAX-DOAS measurements of shipping emissions of NO₂ and SO₂ on Neuwerk

This chapter presents measurements of ship emissions on the island Neuwerk with the focus on coastal air quality and long term trends. First, the measurement site and the MAX-DOAS instrument is introduced and the ship emission measurement geometry is explained. In the next part, with the O₄ scaling method an approach for the retrieval of path-averaged near-surface volume mixing ratios (VMRs) from MAX-DOAS DSCDs is introduced, evaluated, and applied to measurements on Neuwerk. The retrieved NO₂ and SO₂ VMRs are compared to on-site in-situ trace gas measurements. This is followed by an analysis of the diurnal and weekly variability of NO₂, giving a hint on the influence of land-based pollution sources on the air quality on Neuwerk. The effect of the recent introduction of stricter sulfur limits for marine fuel oils on SO₂ emissions from ships and the air quality in general is investigated for in-plume SO₂ to NO₂ peak ratios and in the wind direction distribution of the VMRs. An approach to estimate the contributions of ship emissions and land-based pollution sources is presented and also investigated for the effect of the fuel sulfur content limit change. From all of this, general trends for the air quality in coastal regions with respect to NO_x and SO₂ are derived.

This chapter is in parts based on Seyler et al. (2017), where most of the presented results have been published.

6.1 Measurement site Neuwerk: Instrumentation, measurement geometry and collected data base

The measurements presented within this study were taken on Neuwerk, a small island in the German Bight in the North Sea with a size of about 3 km² and only 33 inhabitants. It is located in the Wadden Sea northwest of Cuxhaven at the mouth of the river Elbe, roughly 8–9 km off the coast, as can be seen from the map in Fig. 6.1a).

As already described in Chapter 3, the North Sea has one of the highest ship densities in the world (Matthias et al., 2016) and practically all ships headed towards the port of Hamburg

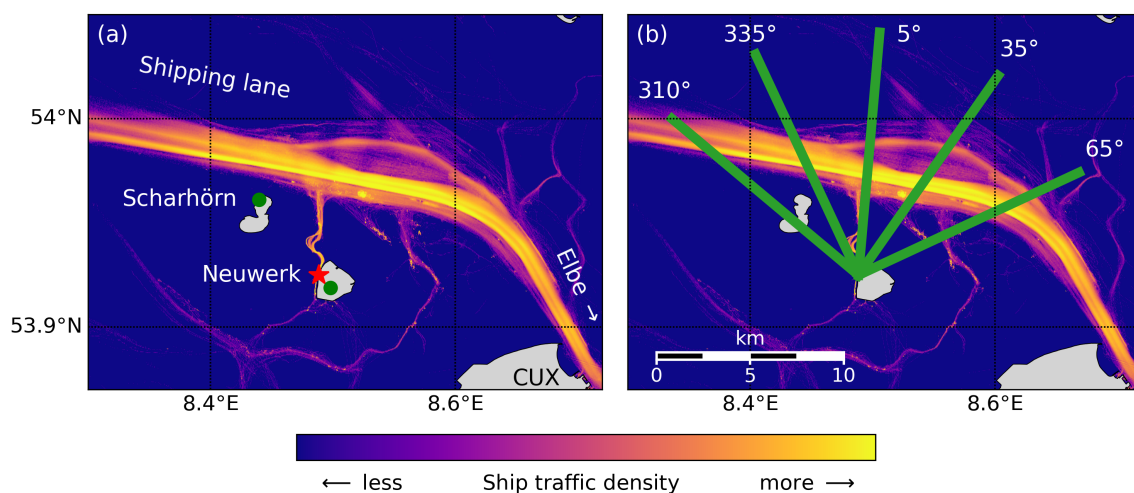


Figure 6.1.: (a) Ship traffic density map calculated from all received AIS messages (2013-2016) showing the main shipping lane from the North sea into the Elbe river close to the measurement site on the island Neuwerk's radar tower (red star). Wind measurements are available on Neuwerk as well as the neighboring island Scharhörn (green dots). (b) The five azimuthal viewing directions of the MAX-DOAS instrument: 310°, 335°, 5°, 35° and 65°, with respect to north.

or the Kiel canal, an important shortcut into the Baltic Sea, pass the island on the main shipping route into the Elbe river. Hamburg is among the top 20 container ports worldwide, and together with Rotterdam and Antwerp Hamburg is one of the three largest ports in Europe (UNCTAD, 2019), with container throughput growth rates of 13–14% in the years 2009 to 2011 (UNCTAD, 2012), but slowing down a bit in recent years, with 4–5% increase in the years 2012 to 2014 (UNCTAD, 2015), 7% increase from 2016 to 2017 (UNCTAD, 2018b) but also years of stagnation in-between. Hamburg also experiences a large increase in the number of cruise ships, with 195 ship calls in 2018 compared to 25 in the year 2005 (Statistische Ämter des Bundes und der Länder (Statistikamt Nord), 2019).

With a distance of 6–7 km, Neuwerk is located relatively close to the highly frequented main shipping lane from the North Sea into the Elbe river. Still close, but located further west are the main shipping lanes towards Bremerhaven and Bremen and to Wilhelmshaven (JadeWeserPort).

As Neuwerk is surrounded by the Hamburg Wadden Sea National Park and is a car-free island, there are no significant sources of air pollution on the island itself, making it a very suitable station for measurements of shipping emissions (Seyler et al., 2017).

The measurements presented in this study were carried out with a two-channel¹ MAX-DOAS instrument, that is described in Section 6.1.1, while the general DOAS measurement principle is explained in Chapter 5. It was set up on the main platform of the radar tower of

¹UV and visible spectral range

Neuwerk in the northwest of the island. Located in a height of about 30 m, the practically flat surroundings enable a wide visibility range.

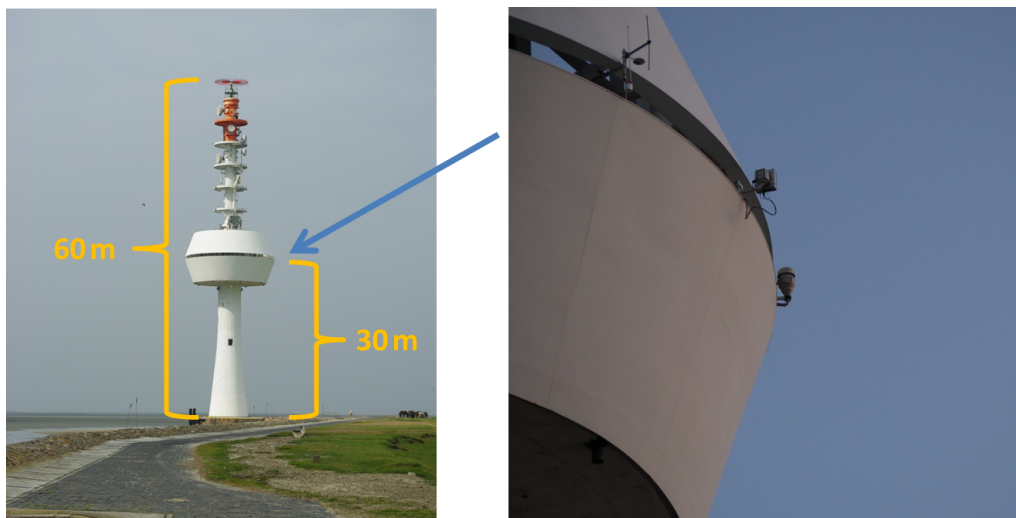


Figure 6.2.: Radar tower Neuwerk with measurement devices installed at the main platform (Seyler, 2014)

To sample a larger region, the MAX-DOAS measurement procedure was set up to point into five different azimuthal viewing directions: 310° , 335° , 5° , 35° and 65° with respect to north, each pointing towards different sections of the shipping lane (see Fig. 6.1b). The measurements are performed in a low elevation angle pointing slightly above the horizon, to probe the corresponding height range above the shipping lane, where the freshly emitted ship plumes are located. A more detailed description of the exact measurement geometry is given in the following section.

6.1.1 MAX-DOAS instrument

The MAX-DOAS instrument used in this study consists of a telescope mounted on a pan-tilt head, an Y-shaped optical fiber bundle and two spectrometers (for the UV and visible channel), each equipped with a CCD detector operated by a separate computer. The telescope, which is attached to the outer sheathing of the circular platform of the radar tower, uses a converging lens to collect the photons from a specific viewing direction and to focus the light and couple it into the optical fiber. The combination of converging lens and optical fiber (see Section 4.5.4) in use leads to a field-of-view of approximately 1° .

The pan-tilt head enables the mounted telescope to point in different azimuth angles (panning) as well as different elevation angles (tilting). Dark measurements, which are needed for the determination of the CCD's dark current signal are performed on a daily basis during nighttime using a shutter, that is included in the telescope, to lock out any remaining

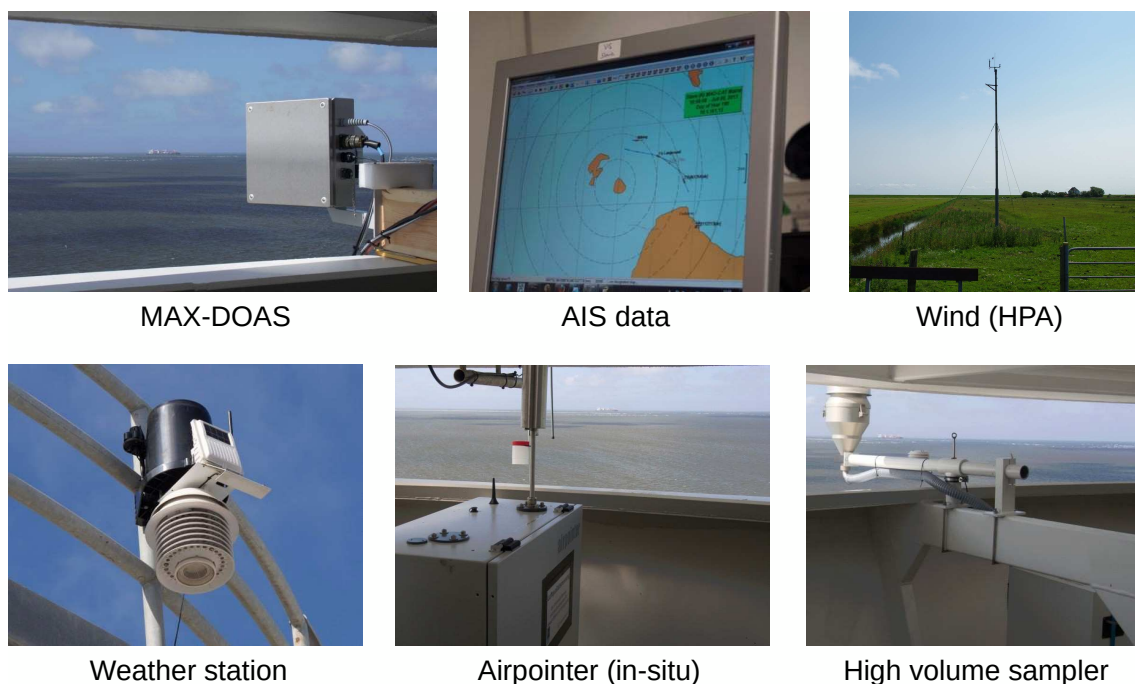


Figure 6.3.: Scientific instrumentation on Neuwerk (Seyler, 2014)

ambient light. In the same fully automatic procedure, daily line lamp measurements using an internally mounted HgCd lamp are performed for the wavelength calibration of the spectra and the determination of the slit function of the instrument (see Section 5.2). The instrument's spectral resolution, as determined by the FWHM of the slit function, is approximately 0.4 nm for the UV and 0.7 nm for the visible channel.

The Y-shaped optical fiber cable is a bundle of 2×38 cylindrical, thin and flexible quartz fibers, guiding the light over several meters and from the telescope to the two temperature-stabilized spectrometers with attached CCD detectors inside the weatherproof platform building. Each individual fiber has a diameter of $150 \mu\text{m}$ and is 20 m long (pictures of both fiber ends can be seen in Fig. 6.4).

Both the UV and visible channel instruments consist of identical Andor² Shamrock SR-303i imaging spectrographs, a grating spectrometer in "Czerny-Turner" design with a focal length of 303 mm. Although the spectrographs are identical, the used reflective gratings differ. The UV instrument is equipped with a 1200 grooves/mm, 300 nm blaze angle grating and the visible instrument with a 600 grooves/mm, 500 nm blaze angle grating. The UV instrument covers the wavelength range 304.6–371.7 nm, the visible spectrometer covers 398.8–536.7 nm.

²<https://andor.oxinst.com/>

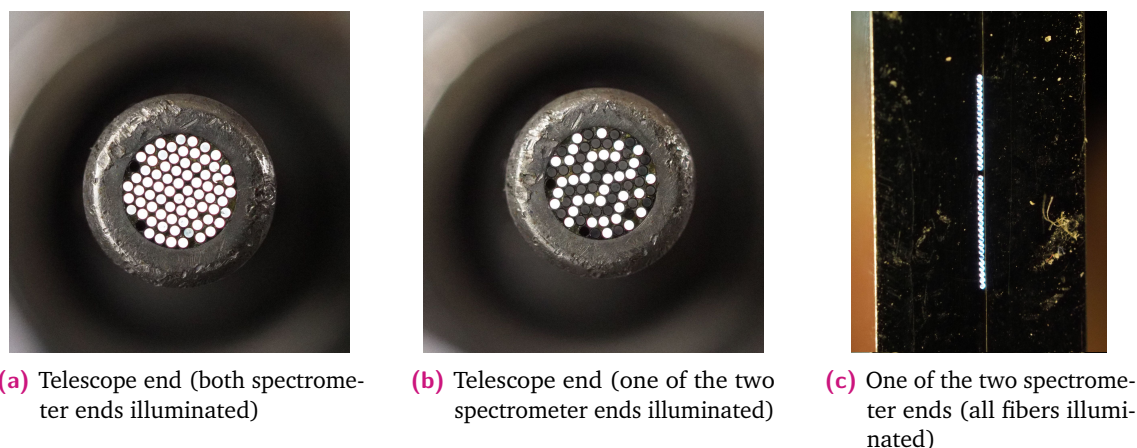


Figure 6.4.: Photographs of the end ferrules of the fully or partly illuminated fiber bundle in the Y-shaped (i.e., one telescope end, two spectrometer ends) fiber-optic cable. Dead, broken fibers are black. Photographed by the author.

Attached to the spectrometers are the CCDs, where different models are used for UV and visible channel. For the UV, a Princeton³ NTE/CCD 1340/400-EMB detector with a resolution of 1340×400 pixels and a pixel size of 20×20 microns is used, whereas for the visible spectral range, an Andor iDus DV420-BU back-illuminated CCD detector with a resolution of 1024×255 pixels and a pixel size of 26×26 microns is used. Both CCDs are cooled to -35°C to minimize the thermal dark currents and thus the dark shot noise on the spectrum.

6.1.2 Measurement geometry

The measurement geometry for MAX-DOAS measurements of ship emissions on Neuwerk is sketched in Fig. 6.5. To measure ship emissions, the MAX-DOAS instrument's telescope is pointed towards the horizon, collecting photons that passed directly through a ship's exhaust plume. A close-in-time zenith-sky measurement is used as a reference so that the retrieved tropospheric differential slant column density (DSCD) is the difference of the slant column densities (SCD) along the two paths 1 and 2 in Fig. 6.5:

$$\text{DSCD} = \text{SCD}_1 - \text{SCD}_2 \quad (6.1)$$

$$= \text{SCD}_{\text{horiz}} - \text{SCD}_{\text{zenith}} \quad (6.2)$$

Assuming that the stratospheric light path and trace gas absorption is approximately the same for both measurements 1 and 2, the stratospheric part should cancel out (see also Section 5.4). This is especially important for the trace gas NO_2 which is also present in the stratosphere.

³<https://www.princetoninstruments.com/>

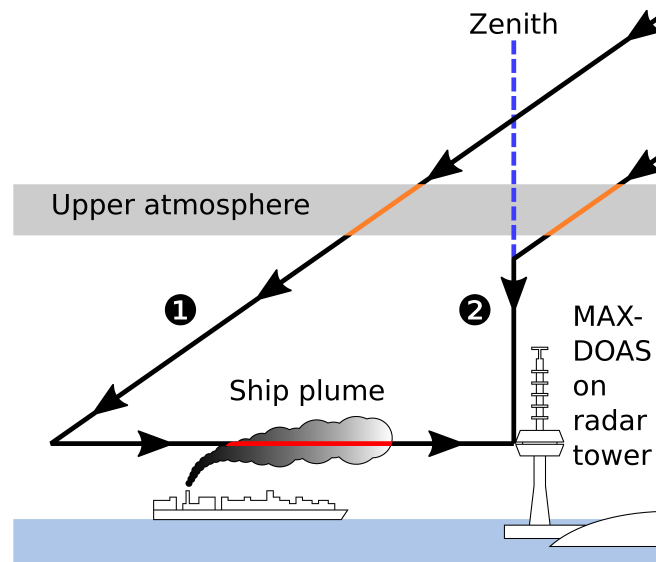


Figure 6.5.: Measurement geometry for MAX-DOAS measurements on Neuwerk with schematic light paths for off-axis (1) and zenith-sky reference measurements (2) for an exemplary solar zenith angle (SZA) of 55° (Seyler et al., 2017)

The assumption that the vertical part of the light path cancels out when taking the difference between off-axis and zenith-sky reference measurement is only valid if the NO_2 in the air above the instrument is spatially homogeneously distributed. This is usually the case for stratospheric NO_2 , but not for ship plumes. If a spatially limited pollution plume from point sources like ships or power plants is blown above the radar tower, it influences only the reference measurement and not the horizontal off-axis measurement, and more NO_2 is canceled out than desired. Hence, the mentioned assumption is violated, leading to an underestimation of the derived DSCD on the horizontal part of the light path.

The usage of such a close-in-time measured *sequential* reference spectrum also minimizes possible instrumental artifacts like wavelength drifts and avoids changes in the atmospheric state between both measurements (off-axis and reference).

6.1.3 DOAS fit settings

The DOAS fit settings for the retrieval of the trace gas slant columns of nitrogen dioxide (NO_2) in the UV and visible channel, as well as sulfur dioxide (SO_2), which is also retrieved in the UV, from the measured spectra are listed in Tables 6.1 and 6.2, respectively.

Table 6.1.: DOAS fit settings for the retrieval of NO₂ and O₄ in UV and visible spectral range

Parameter	NO ₂ (UV)	NO ₂ (visible)
Fitting window	338–370 nm	425–497 nm
Polynomial degree	4	3
Intensity offset	Constant	Constant
Zenith reference	Sequential reference spectrum*	Sequential reference spectrum*
SZA limit	Up to 85° SZA	Up to 85° SZA
O ₃	223 K & 243 K (Serdyuchenko et al., 2014)	223 K (Serdyuchenko et al., 2014)
NO ₂	298 K (Vandaele et al., 1996)	298 K (Vandaele et al., 1996)
O ₄	293 K (Thalman and Volkamer, 2013)	293 K (Thalman and Volkamer, 2013)
H ₂ O	–	293 K (Lampel et al., 2015)
HCHO	297 K (Meller and Moortgat, 2000)	–
Ring	SCIATRAN (Rozanov et al., 2014)	SCIATRAN (Rozanov et al., 2014)

* Interpolation in time between the zenith measurements directly before and after the off-axis scan

Table 6.2.: DOAS fit settings for the retrieval of SO₂

Parameter	SO ₂ (UV)
Fitting window	307.5–317.5 nm
Polynomial degree	3
Intensity offset	Constant & slope
Zenith reference	Sequential reference spectrum*
SZA limit	Up to 75° SZA
O ₃	223 K & 243 K (Serdyuchenko et al., 2014)
NO ₂	298 K (Vandaele et al., 1996)
SO ₂	293 K (Bogumil et al., 2003)
Ring	SCIATRAN (Rozanov et al., 2014)

* Interpolation in time between the zenith measurements directly before and after the off-axis scan

6.1.4 On-site in-situ instrumentation

Apart from the MAX-DOAS instrument, the on-site instrumentation for air quality assessment includes a MLU Airpointer⁴ in-situ trace gas analyzer equipped with modules for measuring CO₂, NO_x (NO and NO₂), SO₂, and O₃, a high volume filter sampler, and passive samplers for NO₂ and SO₂.

For the trace gas analyzer, a short overview of the respective measurement techniques, specified measuring ranges and detection limits is given in Table 6.3. A detailed description of the in-situ instruments, their working principle, precision and calibration procedures can be found in Kattner (2019).

⁴<http://www.mlu.eu/>

Table 6.3.: Airpointer in-situ device: measured trace gases, corresponding measuring techniques, measuring ranges and detection limits [Source: MLU (manufacturer), <http://www.mlu.eu/>]

Trace gas	CO ₂	O ₃	NO, NO ₂	SO ₂
Measuring technique	Non-dispersive IR spectroscopy LI-COR LI820	UV absorption (EN 14625)	NO Chemiluminescence (EN 14211)	UV fluorescence (EN 14212)
Detection limit	1 ppm	0.5 ppb	0.4 ppb	0.25 ppb
Measuring range	up to 20 000 ppm	up to 200 ppm	up to 20 ppm	up to 10 ppm
Measuring period	1 s	<30 s	<60 s	<90 s

6.1.5 AIS

To identify the ships that pass the island, an AIS (Automatic Identification System) receiver with an antenna is set up on the radar tower to receive and log the AIS signal broadcasted by the ships. The AIS signal contains various information like a ship's name, position (latitude and longitude), speed, heading, course, length, width, draft, ship type, status, the international registration numbers MMSI and IMO and often also the ship's destination port. These information are transmitted by a set of different classes of messages. The positional data is broadcasted with the highest frequency every few seconds, the other information are sent with lower frequencies.

Regulations from the International Maritime Organization (IMO) require AIS transponders to be fitted aboard all ships of 300 gross tonnage and upwards as a safety measure for collision avoidance, for fleet monitoring, and as a help in case of accidents and search and rescue (SAR) operations (IMO, 2003, 2004, 2015).

Analyzing and plotting the AIS ship position data received and logged during three years of measurements on Neuwerk, ship traffic density maps can be derived like the one used as a background map in Fig. 6.1, nicely illustrating the course of the various shipping lanes in the region. A detailed view onto the AIS ship traffic density map presented in Fig. 6.1 and more such maps can be seen in the appendix.

6.1.6 Wind & weather

In addition to the air quality measurements and AIS receiver, environmental parameters like temperature, pressure, humidity, solar irradiation, wind speed and wind direction are measured by a weather station. Additional wind data is available from stations maintained by the Hamburg⁵ Port Authority (HPA) on Neuwerk and the neighboring island Scharhörn,

⁵Historically, the island Neuwerk belongs to the city of Hamburg.

which are expected to give more reliable data since our weather station on the radar tower is screened to one side by the tower.

The seasonal distribution of wind directions during the three years of measurements on Neuwerk is shown in Fig. 6.6.

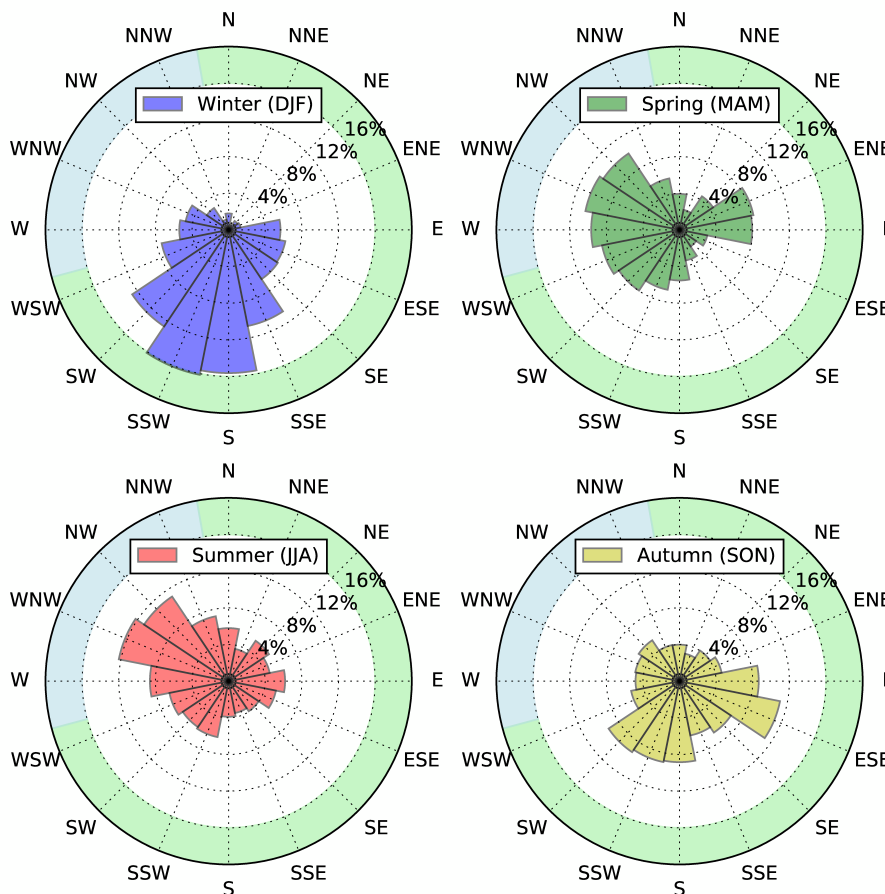


Figure 6.6.: Seasonal wind direction distribution for Neuwerk (Data from 4 July 2013 to 27 June 2016). The colored sectors show directions with wind from the coast (green) and from the open North Sea (blue). (Seyler et al., 2017)

In spring and summer, the ideal seasons for MAX-DOAS measurements, on a high percentage of days the wind blows from the open North Sea, where ships are the only significant source of local air pollution. In winter, southerly directions prevail, bringing potentially polluted air masses from land-based sources into the region and blowing the ship emission plumes away from the measurement site. Furthermore, the short days and low sun during winter results in less UV radiation reaching the surface, which means that MAX-DOAS measurements are in general sparse in winter months, especially for SO₂, which has its strong absorption features in the UV-B range.

6.1.7 Data base

Figure 6.7 presents the data availability for the different instruments during the three year period of measurements on Neuwerk. The above mentioned winter gaps in the SO₂ measurement time series can be clearly seen in the availability “bars”.

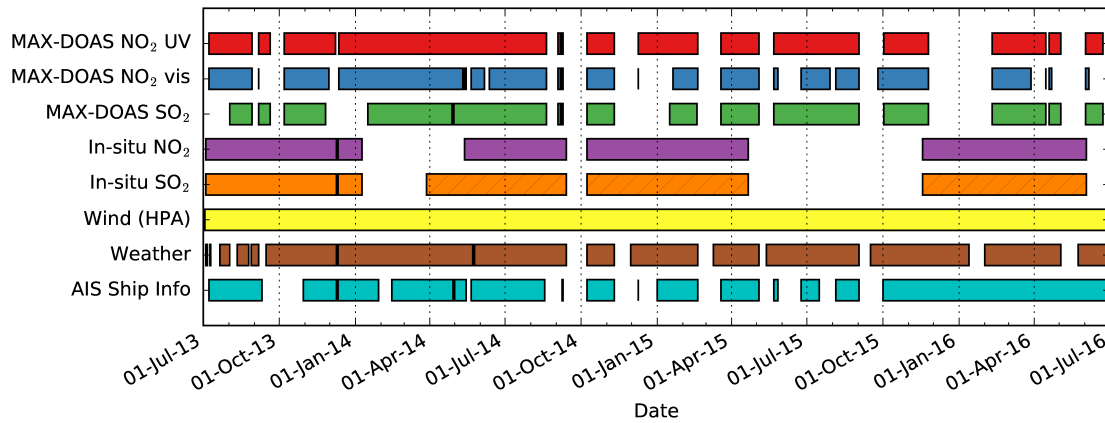


Figure 6.7.: Data base of measurements on Neuwerk showing the data availability in the analyzed measurement period between July 2013 and July 2016. From March 2014 on (hatched), there were instrumental problems with the in-situ SO₂ instrument resulting in a strong oscillation of ± 0.5 ppb superimposing the data. However, this data can still be used for the comparison of long-term averages. (Seyler et al., 2017)

6.2 O₄ scaling method – retrieval of path-averaged near-surface VMRs from MAX-DOAS DSCDs

The MAX-DOAS trace gas column density is the concentration of an absorber integrated along the light path through the atmosphere (see Section 5.1). To get from columns to concentrations or volume mixing ratios, the length of the path through the atmosphere has to be known. The path length depends on the atmospheric visibility, which is limited by scattering on air molecules and aerosols. For high elevation angles like 15° or 30°, the path through the troposphere can be estimated via a simple geometric approximation (see also Section 8.4.3 on the shipborne MAX-DOAS measurements). For low elevations, where the ship emissions are located at our site, this simple geometric approximation fails. In this case, the oxygen collision complex O₂–O₂ (often called “O₄”), which absorbs in similar wavelength ranges as NO₂ in the UV and visible spectral range, can be used as a proxy for the path length. When the near-surface concentration of O₄ is known, the effective horizontal path length L can be derived from dividing the differential slant column

density⁶ of O₄ (unit: molecules per area) by its number density n_{O_4} (unit: molecules per volume):

$$L = \frac{\text{SCD}_{O_4,\text{horiz}} - \text{SCD}_{O_4,\text{zenith}}}{n_{O_4}} = \frac{\text{DSCD}_{O_4}}{n_{O_4}} = \frac{\text{DSCD}_{O_4}}{(n_{O_2})^2}. \quad (6.3)$$

As the surface number density of O₄ is proportional to the square of the molecular oxygen concentration (Greenblatt et al., 1990; Wagner et al., 2004), it can be easily computed from the measured air temperature T and pressure p via the ideal gas law:

$$n_{O_4} = (n_{O_2})^2 = (0.20942 \cdot n_{\text{air}})^2 \quad \text{with} \quad n_{\text{air}} = \frac{p_{\text{air}} \cdot N_A}{T_{\text{air}} \cdot R}, \quad (6.4)$$

with the universal gas constant R and Avogadro's constant N_A .

Knowing the horizontal light path length L , the number density of NO₂ (unit: molecules per volume) can be computed by dividing the NO₂ DSCD (unit: molecules per area) by L (unit: length). This yields the average number density of NO₂ along the effective horizontal light path shown in Fig. 6.5. Dividing the number density of NO₂, n_{NO_2} , by the number density of air, n_{air} , yields the average NO₂ volume mixing ratio (VMR) along L :

$$\text{VMR}_{NO_2} = \frac{\text{SCD}_{NO_2,\text{horiz}} - \text{SCD}_{NO_2,\text{zenith}}}{L \cdot n_{\text{air}}} = \frac{\text{DSCD}_{NO_2}}{L \cdot n_{\text{air}}}, \quad (6.5)$$

where n_{air} can be computed from the measured temperature and pressure according to (6.4).

This method, called “O₄ scaling approach”, has been successfully applied to MAX-DOAS measurements before, for example in the urban polluted areas of Mexico City (Sinreich et al., 2013) and the city of Hefei (China) (Wang et al., 2014) or at remote high mountain sites like the Izaña Atmospheric observatory on Tenerife (Canary Islands) (Gomez et al., 2014) or the mountains Zugspitze (Germany) and Pico Espejo (Venezuela) (Schreier et al., 2016).

As the O₄ DSCD can be retrieved simultaneously to NO₂ in both DOAS fits in the UV and visible spectral range this approach can be applied to NO₂ in both fitting ranges. The O₄ scaling approach can in principal also be applied to SO₂, which is retrieved further in the UV. However, the wavelength dependence of Rayleigh scattering ($\propto \lambda^{-4}$) leads to a wavelength-dependence of atmospheric path lengths. As a result, the wavelength difference in fitting windows in the UV for O₄ and NO₂ on the one hand and SO₂ on the other hand introduces an uncertainty which has to be accounted for. Wang et al. (2014) derived an empirical formula from radiative transfer modeling (RTM) for a variety of aerosol scenarios

⁶Which is the difference between the horizontal, off-axis SCD and the zenith-sky reference SCD (see Fig. 6.5)

to account for this and to compute the path length at 310 nm (SO₂ absorption) from the path length at 360 nm (O₄ absorption):

$$L_{310} = 0.136 + 0.897 \times L_{360} - 0.023 \times L_{360}^2, \quad (6.6)$$

with path lengths L_{310} and L_{360} in km. Although this formula was derived for polluted sites, the authors state that the deviations expected for an application at other sites are small (Wang et al., 2014). This formula was used for the correction of path lengths in the retrieval of path-averaged SO₂ VMRs shown in the following.

With the scaling via O₄, this approach takes into account the variation of the atmospheric effective light path length with aerosol loading. In contrast to an often-used simple geometric approximation of the light path in the boundary layer, like it is described in Section 8.4.3 later-on, it does not require the estimation of a typical mixing layer height for the derivation of surface concentrations in a so-called box profile⁷, which approximates the pollutant distribution in a well-mixed boundary layer. It thus overcomes the disadvantages of such simple geometric light path approximations, especially for off-axis measurements at very low elevations pointing towards or slightly above the horizon, where geometric light path assumptions like the one given in Section 8.4.3 do not work well (see there).

In theory, for a well-mixed, homogeneous NO₂ field along the horizontal path, the retrieved VMR should agree with in-situ measurements taken at the same altitude. In the case of ship emission measurements, where only a small fraction of the horizontal effective path, which can be several kilometers long, probes the plumes, the retrieved path-averaged VMR will systematically underestimate the local VMR inside the plume, which would theoretically be measured by in-situ instruments in the plume (Seyler et al., 2017).

Moreover, differences in the shape of the atmospheric profiles of the trace gases of interest (NO₂ or SO₂) and the path length proxy O₄ can introduce systematic uncertainties as has been demonstrated by Sinreich et al. (2013) and Wang et al. (2014) in extensive and comprehensive RTM simulations. Pollutants like NO₂ or SO₂ are emitted and formed close to the ground, have high concentrations in low altitudes, and tend to decrease very rapidly with height above the boundary layer (often approximated as box profiles), while O₄ concentrations decrease exponentially with height. Such a difference in profile shapes violates the basic assumption that O₄ is a good proxy for the light path through the NO₂ and SO₂ layers and as a result, the retrieved near-surface VMRs might not be representative for the trace gas amount directly at the surface, but for some kind of average over a certain altitude range in the boundary layer (Seyler et al., 2017).

To account for this, Sinreich et al. (2013) and Wang et al. (2014) use correction factors derived from RTM simulations. The correction factors depend on the relative solar azimuth

⁷Box profile: constant concentration up to a certain height, zero above

angle (RSAA), solar zenith angle (SZA), aerosol optical density (AOD), vertical extent of the pollutant box profile and the extent and vertical position of the aerosol layer relative to the pollutant profile (Sinreich et al., 2013). While RSAA and SZA are well-known quantities, the AOD and the needed information on the NO₂ (or SO₂) and aerosol profile are unknown quantities which were not measured and cannot be easily approximated for the ship emission measurements presented here.

Especially for trace gas layers less than 1 km high a strong dependence of the correction factors on the height of the box profile is reported. Thus, for the application of the suggested parameterization method, additional knowledge about the trace gas layer height is needed, which would come ideally from measurements (e.g. with LIDAR) or otherwise has to be estimated. For low boundary layer heights below 500 m, the use of this method without knowing the actual boundary layer height is not recommended by the authors (Sinreich et al., 2013). At the measurement site Neuwerk, no such measurements and thus no additional knowledge of the height of the NO₂ or SO₂ layers are available.

In previous studies, a well-mixed NO₂ layer from ground up to a certain (box profile) height and absence of NO₂ above that box has been assumed. However, this assumption is not valid for the horizontally very inhomogeneous NO₂ field formed by ship emission plumes over the shipping lane. Because of the lack of additional knowledge and the invalidity of the underlying assumptions, correction factors are not considered here. Still, one has to keep in mind the possible systematic overestimation of path lengths and thus underestimation of path-averaged VMRs (Sinreich et al., 2013; Wang et al., 2014). Gomez et al. (2014) and Schreier et al. (2016) applied the approach without correction factors to their measurements on high mountain sites due to the low aerosol amounts in such heights.

Not only aerosols, but also clouds can have an impact on the path lengths the photons travel through the atmosphere. Clouds can either decrease or increase the path length and thus O₄ absorption by multiple scattering, depending on the cloud's location and its optical properties, especially the cloud's optical thickness (Wagner et al., 2014). Days with scattered or broken cloud conditions can show a strong variation in path lengths compared to a clear sky day, where path lengths are constant or slowly changing. Cloud-induced path length changes can happen even between consecutive measurements, due to having clouds in either off-axis or reference measurement or both or neither. This can make the interpretation of the measurements much more challenging.

6.3 O₄ scaling method – statistics and validity check

The O₄ scaling approach can be applied independently for both UV and visible MAX-DOAS measurements of NO₂. At the Neuwerk site, over three years of measurements, average horizontal path lengths of $L_{UV} = (9.3 \pm 2.3)$ km and $L_{vis} = (12.9 \pm 4.5)$ km [mean \pm standard deviation] were retrieved. Fig. 6.8 shows a histogram of the retrieved path lengths, clearly showing how the UV paths are shorter due to stronger Rayleigh scattering at shorter wavelengths. It also shows how the actual path lengths vary depending on the observational conditions. Under clear sky conditions, typical horizontal effective path lengths are 10 km in the UV and 15 km in the visible spectral range or longer.

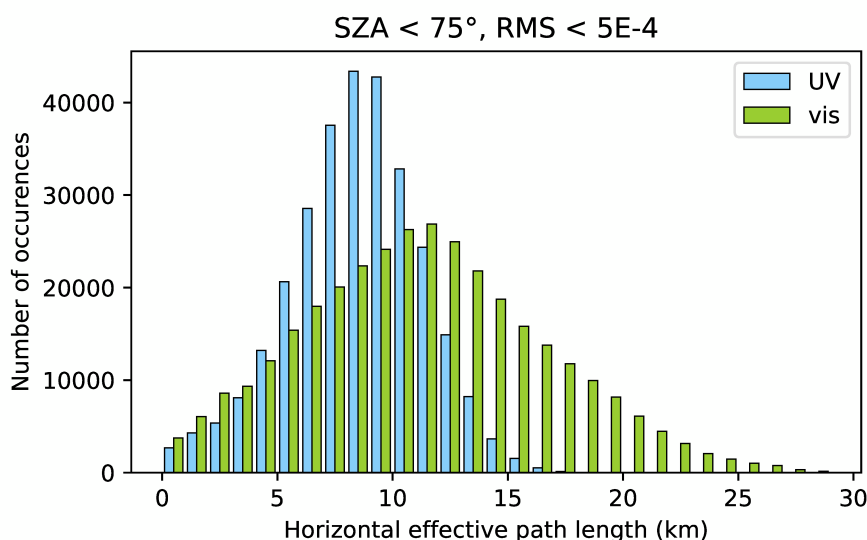


Figure 6.8.: O₄ scaling path statistic

A comparison of UV and visible DSCDs with the via O₄ scaling retrieved VMRs can serve as a validity check whether the O₄ scaling method can account for the variation of light paths. The wavelength dependence of Rayleigh scattering leads to longer light paths and thus, in the case of a homogeneous, well-mixed NO₂ field, larger DSCDs in the visible, compared to the UV. The O₄ scaling should compensate for the difference in path lengths and the resulting horizontal path-averaged UV and visible VMRs should agree. Panel a of Fig. 6.9 shows a scatter plot of all simultaneously measured pairs of UV and visible NO₂ DSCDs (quality criterion: DOAS fit RMS better than 1×10^{-3}).

The scatter plot shows that NO₂ DSCDs in UV and visible spectral range are strongly positively correlated with a Pearson correlation coefficient of 0.983. The slope of the regression line of 1.30 corresponds to on average 30% longer horizontal paths in the visible compared to the UV, due to more intense Rayleigh scattering at shorter wavelengths. The intercept of the regression line is very small, as expected, since there should not be an offset

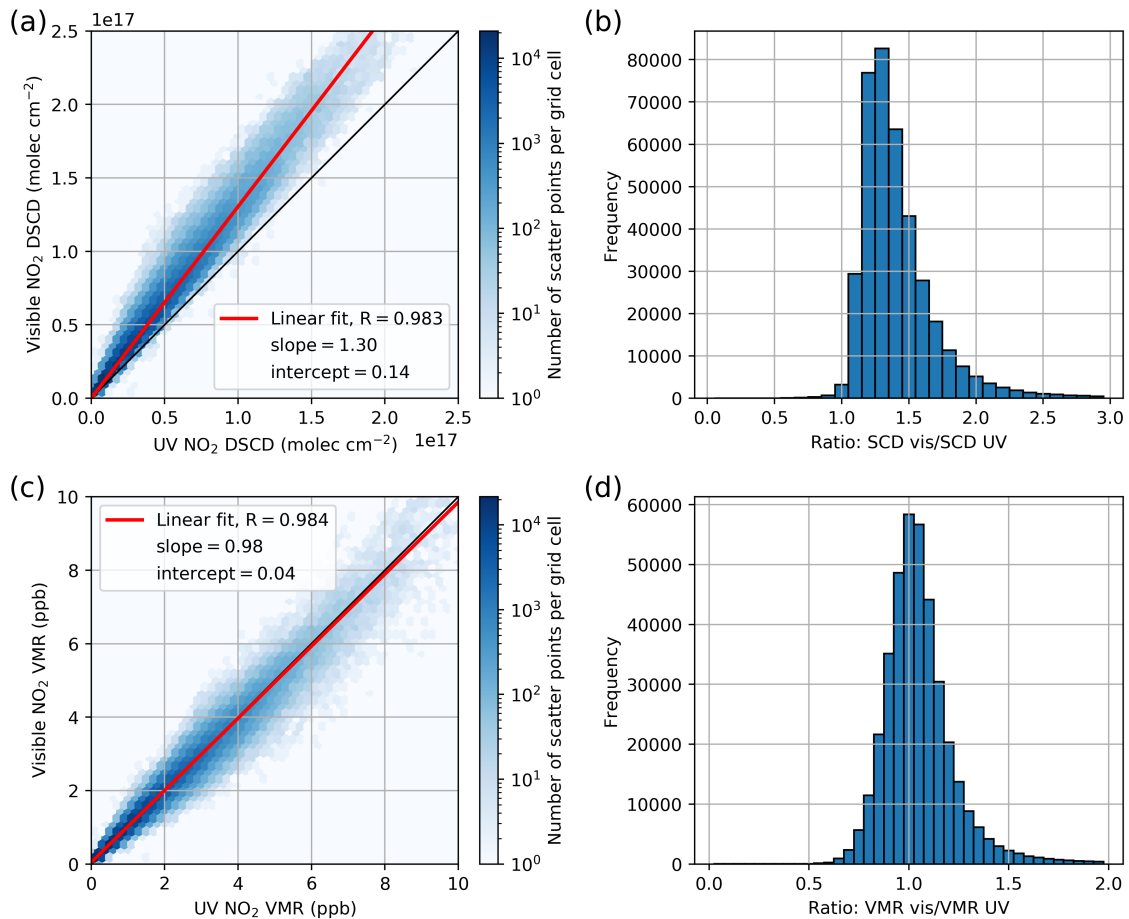


Figure 6.9.: (a) Scatter plot: NO₂ slant column density retrieved in the visible vs. UV measured in all azimuth angles at 0.5° elevation for solar zenith angles smaller than 75°. The parameters derived from the linear fit by orthogonal distance regression are also shown. (b) Histogram of the ratio of the two NO₂ slant column densities (visible/UV). (c) As (a), but for volume mixing ratios. (d) Histogram of the ratio of the two NO₂ volume mixing ratios (visible/UV). (Seyler et al., 2017)

between both. Panel b of Fig. 6.9 shows a histogram of the ratios between both DSCDs. The peak of the distribution is reached for ratios of 1.3, in good agreement with the slope of the fitted line in the scatter plot.

In panel c of Fig. 6.9 the DSCDs were converted to path averaged VMRs via the O₄ scaling method. In this scatter plot, the points scatter symmetrically along the 1:1 identity line, with a slope of 0.98, close to unity. The intercept is even smaller, negligible indeed, and the Pearson correlation coefficient has further increased to 0.984. The corresponding histogram of the ratios of both VMRs (panel d) peaks at 1.0. Comparing the VMR plots in panel c and d to the DSCD plots in panel a and b, shows that the O₄ scaling in fact can compensate for the light path differences between UV and visible measurements. This confirms the validity of the O₄ scaling approach to compute path averaged VMRs from

MAX-DOAS DSCDs. Remaining differences are most probable due to different averaging volumes in case of inhomogeneous NO₂ fields. Relatively fresh and undiluted ship plumes emitted along the shipping lane are a very prominent case for this and can create very inhomogeneous NO₂ fields in the region covered by our measurements.

6.4 O₄ scaling method – application to NO₂ measurements

Figure 6.10 shows in panel a the MAX-DOAS differential slant column densities of NO₂ measured in UV and visible spectral range in 0.5° elevation in the 335° azimuth viewing direction (with respect to north, compare Fig. 6.1) on 23 July 2014. In the plotted time series, sharp peaks in the curves originate from measured ship plumes, which were probed along the line of sight (LOS) of the MAX-DOAS instrument, characterized by rapid changes in the measured NO₂ column density between consecutive measurements of up to one order of magnitude when a plume moves in and out of the line of sight of the instrument. Between the peaks, the NO₂ levels do not go down to zero, showing that an ambient NO₂ background pollution is present, which is slightly enhanced in the morning. On this day, values reach up to more than 1.4×10^{17} molec cm⁻², which is about 1.0×10^{17} molec cm⁻² above the ambient background pollution.

The systematic difference between the NO₂ measured in the UV and the NO₂ measured in the visible spectral range, with visible being consistently higher, emerges from the above-mentioned wavelength dependence of Rayleigh scattering ($\propto \lambda^{-4}$). As the Rayleigh scattering is stronger for shorter wavelength, i.e., for photons in the UV, the effective horizontal path lengths between the mean last scattering point and the instrument, or visibility, is longer in the visible spectral range.

Panel b of Fig. 6.10 shows the horizontal path lengths derived via Eq. (6.3) (see page 89) from the simultaneously measured O₄ DSCDs in the O₄ scaling approach presented above. It shows how the horizontal path length in the visible spectral range, amounting to around 15 km, is significantly longer than the 10 km in the UV. The fact that the path lengths are almost constant over time reveals that the 23 July 2014 was a clear sky day presenting optimal weather conditions for MAX-DOAS measurements.

As discussed above, scattered or broken cloud conditions would show up as strong short term variations in the path lengths as clouds can increase or decrease light path lengths (Wagner et al., 2014) depending on a cloud's optical properties, especially its optical thickness, and on the cloud's position in relation to the line of site.

Combining the information from panels a and b via Eq. (6.5) (see page 89), the O₄ scaling method, panel c of Fig. 6.10 shows the resulting path averaged NO₂ VMRs. As

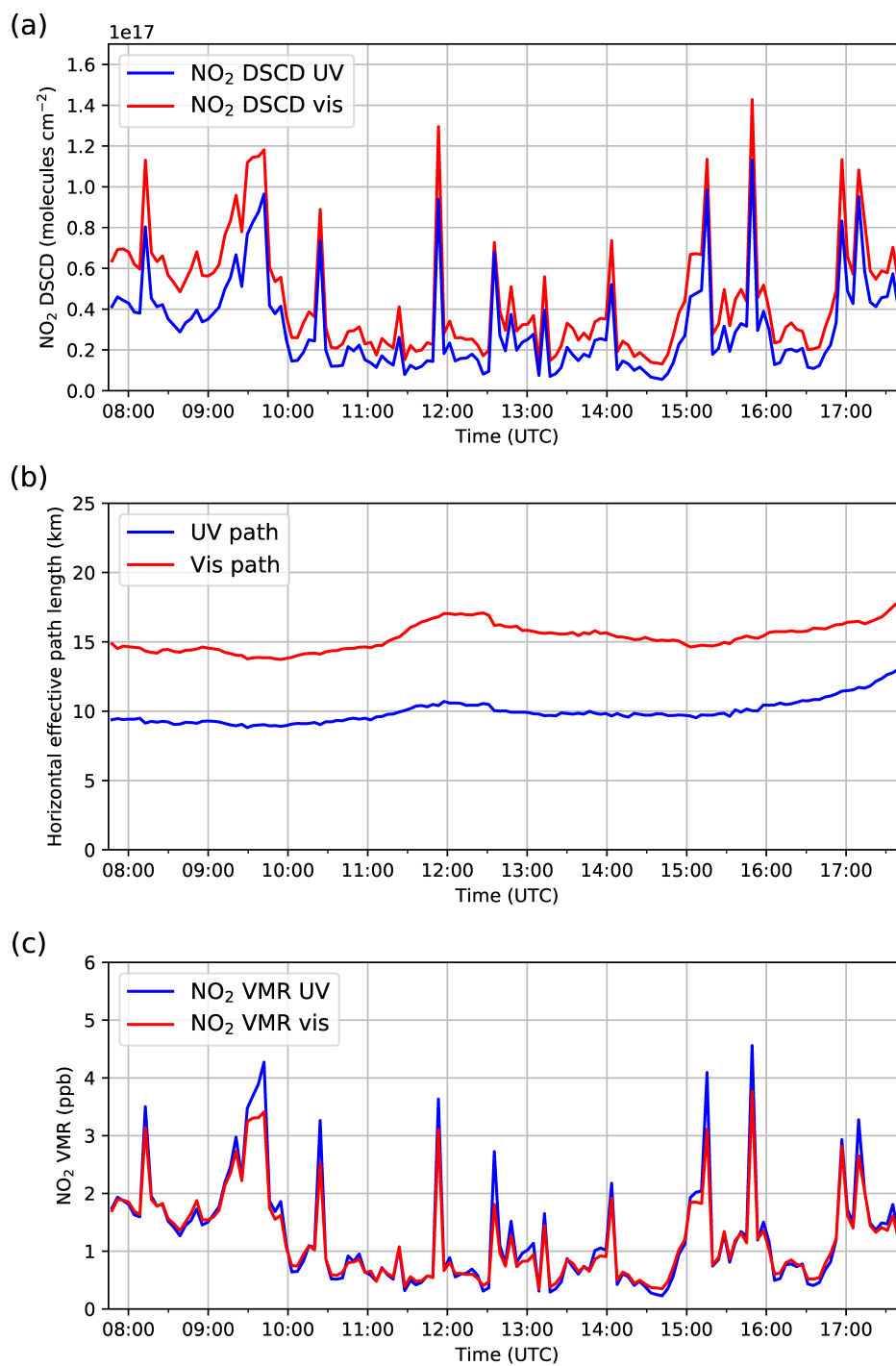


Figure 6.10.: Differential slant column densities of NO₂ (a), horizontal effective path lengths (b) and horizontal path averaged volume mixing ratios of NO₂ (c) on Wednesday, 23 July 2014 in 0.5° elevation and 335° azimuth for the UV (purple) and visible spectral range (green).

can be seen from the plot, the O_4 scaling can compensate for the light path differences as it shows a very good agreement between UV and visible NO_2 VMRs, in particular for situations characterized by well-mixed ambient background pollution, when the NO_2 is distributed homogeneously along the light paths. It also shows how for situations with an inhomogeneous NO_2 field along the LOS, which most certainly is the case for ship plumes located somewhere along the horizontal paths, the situation is different: As both paths have a different length, one can expect different values for the averages along the different paths as they probe different parts of the NO_2 field, and as the plot shows, the UV and visible curves do not agree for the peaks. While in the DSCD the visible signal was always higher for the ship emission peaks, in the VMR it is vice versa and the UV signal shows almost always higher peaks.

In general, whether UV or visible signal gives higher peaks depends on the exact location of the plume within the line of sight. In this example, the wind was blowing from northerly directions transporting the plumes from the shipping lane towards the measurement site. For such short distances of the plumes to the instrument the shorter UV path completely covers the plumes (and the longer visible path as well, of course), which leads to higher values in the UV signal as the part of the paths probing the higher NO_2 concentrations has a larger relative contribution to the average than for the longer visible path. If the plumes would be further away from the site and mainly (or only) be covered by the longer visible path, the peak in the visible VMR would be higher (or the only one). The information on the horizontal distribution of the absorber which is contained in this relationship is further investigated in Chapter 7.

6.5 Comparison of MAX-DOAS path-averaged VMRs to in-situ measurements

Perfect agreement can never be expected in a comparison of MAX-DOAS and in-situ trace gas measurements due to the inherent differences in measurement volumes. MAX-DOAS measurements probe a long light path through the atmosphere and in-situ trace gas analyzers measure the local concentration at the instrument site. The MAX-DOAS averages over a long horizontal light path, and since ship plumes usually do not cover the whole light path but rather a small fraction of it, very high concentration peaks will be underestimated in the MAX-DOAS VMR compared to the in-situ measured local VMR inside the plume.

Figure 6.11 shows as an example the comparison of the MAX-DOAS path averaged NO_2 VMRs (in an excerpt of the same data as in Fig. 6.10c from the previous section) and the on-site in-situ NO_2 measurements on Wednesday, 23 July 2014.

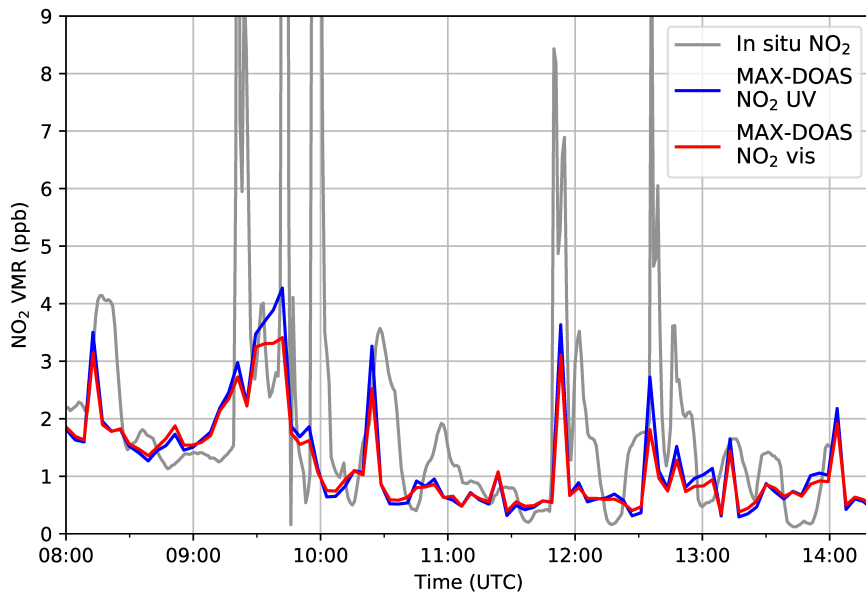


Figure 6.11.: Comparison of MAX-DOAS (UV and vis) and in-situ NO_2 VMRs on Wednesday, 23 July 2014. The MAX-DOAS measurements were taken in the 335° azimuth viewing direction in 0.5° elevation. The clipped in-situ peaks reach up to 22.3 ppb (09:20 UTC), 31.6 ppb (09:43 UTC), 20.0 ppb (09:57 UTC) and 11.2 ppb (12:35 UTC).

The plot clearly demonstrates how ship emission peaks in the in-situ measurements are both higher and broader than the corresponding peaks in the MAX-DOAS time series showing that the local VMR inside the plume is much higher than the path averaged values which can be retrieved from MAX-DOAS. The fact that the in-situ peaks are broader shows how the plumes have already been diluted in the time between emission at the shipping lane, which is more than 6 km away, and measurement on the radar tower. Due to this travel time of the plumes, which strongly depends on wind direction and speed but also on the movement direction of the ship and its position on the shipping lane, usually a time shift exists between MAX-DOAS and in-situ measurements of plumes. The in-situ instrument usually detects the plume later than the MAX-DOAS, but under certain wind conditions also the vice versa can be observed.

Between 9:00 and 10:00 UTC several ships passed Neuwerk on the shipping lane in a row and the in-situ instrument measured their plumes one after another as they reached the radar tower. The MAX-DOAS instrument, however, can not separate the multiple plumes that cross the line of sight simultaneously and, as a result, only one broad peak shows up in the measurements. For the interpretation of individual ship plume measurements and the attribution to sources (ships) it is therefore important to also consider wind data as well as the ships' positions and movements. A graphically illustrative way to investigate all these factors at once is presented in Chapter 7, which includes ship plume forward trajectories

combined with a Gaussian plume model plotted onto a map of the region-of-interest together with ships and the MAX-DOAS and in-situ NO₂ measurements.

For a homogeneous NO₂ field of well-mixed ambient background pollution along the line of sights, which can occur for polluted air masses from land as well as for residual, old, diluted ship plumes, MAX-DOAS and in-situ instrument should in theory measure similar values, like it is the case here for the background NO₂ between the peaks. How good the agreement is, varies from day to day. Often the agreement is very good, but sometimes also systematic deviations between MAX-DOAS and in-situ measured background values can be observed. As discussed in Section 6.2, correction factors would need to be applied to the MAX-DOAS VMRs to account for the different profile shapes of the investigated pollutants NO₂ and SO₂ and the light path proxy O₄. As in our case no additional measurements of the height of the NO₂ and SO₂ layers are available, only uncorrected VMRs are shown here which can be systematically underestimated due to overestimated path lengths, explaining the observed deviations on some days.

The lack of comparability between both instruments for individual measurements due to the wind-dependent time shift between MAX-DOAS and in-situ measurements as well as the different peak heights and shapes make a correlation analysis on such short time scales pointless. For a meaningful comparison, averaging over longer time spans has to be applied to the data from this station to mitigate the impact of the inherent differences of both measurement techniques.

Figure 6.12 shows a comparison of MAX-DOAS and in-situ daily mean VMRs. For NO₂ in the UV (panel a), three months of daily mean VMRs during summer 2014 are shown. For SO₂ (panel b), three months of daily mean VMRs during summer 2013 are shown. Although summer 2014 had better weather conditions for the MAX-DOAS measurements and much less data gaps caused by power outages, the in-situ SO₂ trace gas analyzer had instrumental problems from spring 2014 on and reliable in-situ SO₂ measurements are only available for 2013 and until mid of January 2014 (see Fig. 6.7 for a general overview on the acquired data set and data availability). The MAX-DOAS NO₂ measurements in the visible spectral range look very similar to the UV ones but unfortunately have some data gaps, which is why only the UV NO₂ is shown here. The shaded areas in the plots show the corresponding standard deviation of the daily means and thus indicate the variability during the individual days.

For a better comparability, the in-situ data has been filtered to include only measurements between the start of the MAX-DOAS measurements in the morning (with sunrise) and the end of measurements in the evening (with sunset), or in other words, only measurements taken under the same SZA range as the MAX-DOAS measurements (up to 85° SZA for NO₂ and up to 75° SZA for SO₂). The long gaps in the SO₂ time series were caused by power outages on the radar tower.

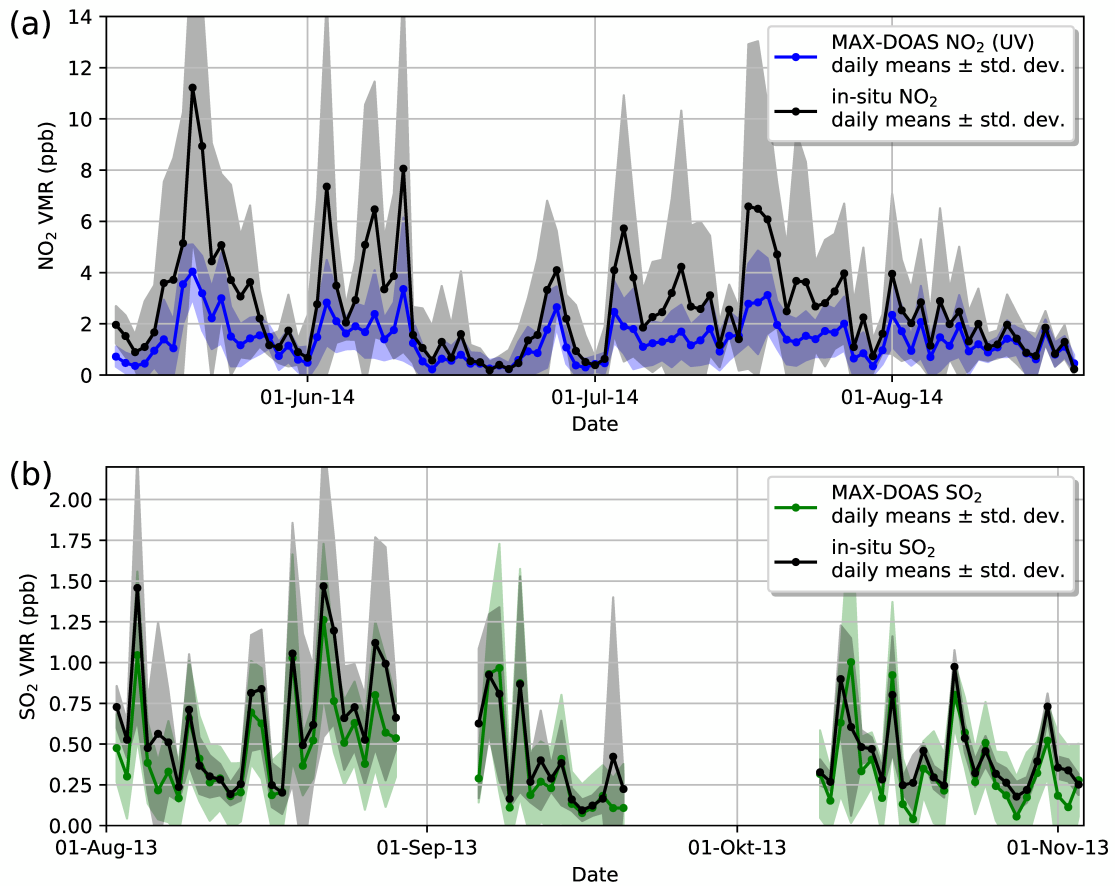


Figure 6.12.: Comparison of MAX-DOAS (UV) and in-situ daily mean VMRs of NO₂ (a) during summer 2014 and SO₂ (b) during summer 2013. Shaded areas show the standard deviation for each daily mean value.

For NO₂, the in-situ VMRs are systematically higher than the MAX-DOAS VMRs, but the day-to-day variability agrees very well. For SO₂, a similar systematic difference might be there, but it is much smaller and hardly visible. The agreement in the day-to-day variability is even better here.

A reason for the systematic differences between MAX-DOAS and in-situ instrument is certainly the non-consideration of the correction factors arising from the different profile shapes of the pollutants NO₂ or SO₂ and the oxygen collision complex O₄, which leads to a systematic underestimation of the MAX-DOAS VMRs (a detailed discussion on this can be found in Section 6.2).

As mentioned above, agreement between MAX-DOAS and in-situ trace gas measurements is only expected for well-mixed ambient background pollution, which could be from emissions on land or from old, strongly diluted ship emissions. Ship emission plumes, however, create a very inhomogeneous NO₂ field along the line of sight and the MAX-DOAS path-averaged

VMRs will systematically underestimate the plume VMR and could also cause systematic differences between MAX-DOAS and in-situ data.

For NO_2 and SO_2 , the hypothetical scaling factor which would be needed to bring the MAX-DOAS and in-situ data together is different, since the above-mentioned systematic differences are much smaller for SO_2 . This discrepancy can be attributed to plume chemistry. During combustion processes in ship engines, mainly nitric oxide (NO) is formed which has to be converted to NO_2 (titration with tropospheric ozone) before it is measurable with DOAS, whereas SO_2 is directly emitted and possible chemical conversions take time. As the MAX-DOAS – in-situ comparison for a single day in Fig. 6.11 above has shown, the MAX-DOAS instrument probes the plumes earlier than the in-situ instrument on the radar tower. The measured plume is thus in an earlier state and the fraction of NO_2 on the total NO_x in the plume should be lower than in the transport-time-delayed in-situ measurements, what could explain at least a part of this discrepancy.

Figure 6.13 shows the corresponding scatter plots to the daily mean time series plots in Fig. 6.12. The good agreement of MAX-DOAS and in-situ VMRS in the day-to-day variability for both NO_2 and SO_2 is confirmed by the good correlation. The systematic differences in the absolute values can be seen in the slopes being larger than one.

These results illustrate that a MAX-DOAS instrument can determine day-to-day trends as in-situ measurements.

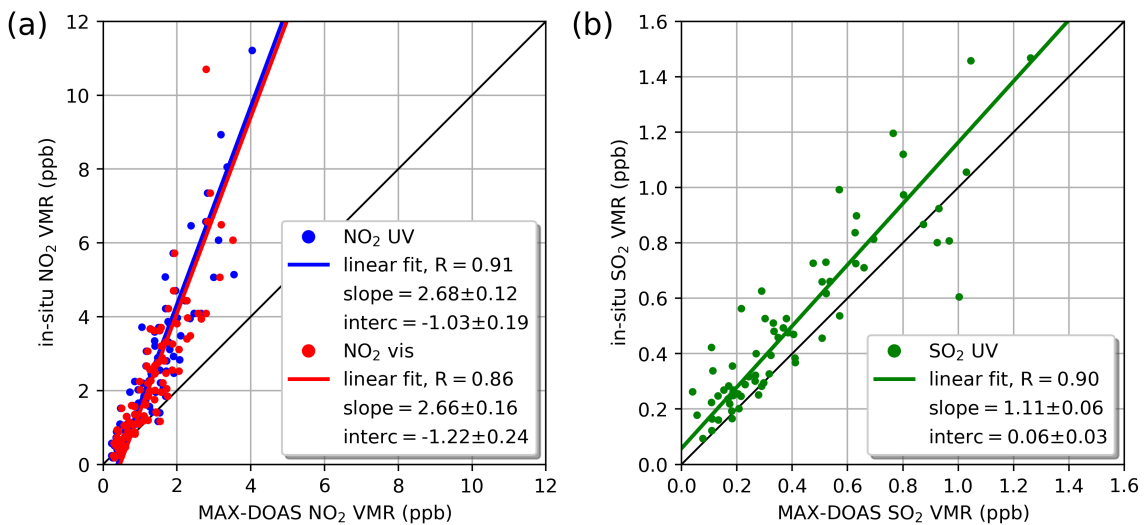


Figure 6.13.: Scatter plot of (a) NO_2 VMR and (b) SO_2 VMR from MAX-DOAS vs. in-situ. For NO_2 daily means from summer 2014, for SO_2 daily means from summer 2013 are shown. For the MAX-DOAS instrument, to get a better statistic, all measurements in all azimuth viewing directions have been averaged. For the in-situ instrument, the mean of all measurements during the daily MAX-DOAS measurement periods (sunrise till sunset) has been taken. The linear fits were calculated with orthogonal distance regression (Deming regression). The fit parameters are given in the legend.

6.6 Diurnal and weekly variability of NO₂ – Influence of coastal air masses on air quality on Neuwerk

The measurement instruments on the small island Neuwerk are located approximately 10 km off the coast. There are nearly no sources of air pollution on the island itself, as it features no car traffic and has only about 30 inhabitants. The MAX-DOAS line of sights all point in northerly directions towards the shipping lane so that the MAX-DOAS instrument measures air masses even further remote from the coast.

To detect a possible influence of coastal air masses and therefore land-based air pollution sources, the diurnal and weekly variability of air pollutants can be investigated. Apart from some pleasure crafts and small ferries with negligible contributions to pollution levels, shipping emissions in general do not depend on the time of day or the day of week. Land-based air pollution on the other hand, like road traffic, does depend on the time of day, with enhanced pollution during rush hours creating a clear diurnal cycle. Also a weekly cycle of NO₂ emissions has been detected in polluted regions before, for example by Beirle et al. (2003), Kaynak et al. (2009), Bell et al. (2009) and Ialongo et al. (2016). On Neuwerk, wind from northeasterly, easterly, southerly and southwesterly directions is expected to blow polluted air masses from the coast and hinterland towards the measurement site.

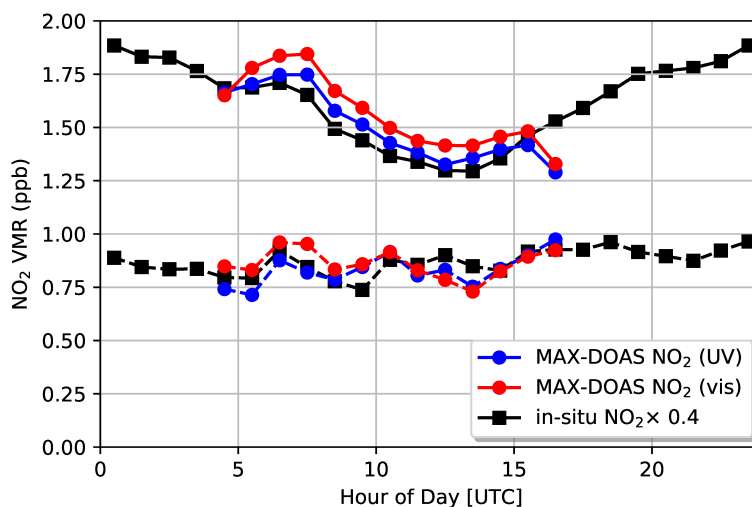


Figure 6.14.: Average diurnal cycle of MAX-DOAS (UV and visible) and in-situ NO₂ volume mixing ratios for all measurements (solid lines) and for a subset of measurements with wind from the open North Sea (dashed lines). For a better visual comparability the in-situ values are scaled by a factor of 0.4. (Seyler et al., 2017)

Figure 6.14 shows the average diurnal variation of NO₂ VMRs from the MAX-DOAS instrument and the in-situ trace gas analyzer plotted as mean values per hour of day. Solid lines show the resulting hourly means for all measurements (unfiltered), dashed lines show a

subset of measurements filtered for northwesterly wind directions representing wind from the open North Sea. The first major difference visible from the figure is the magnitude of the values: measurements filtered for wind from the open North Sea show by a factor of two lower VMRs. The diurnal evolution when including all measurements shows a prominent daily cycle typical for road-traffic-influenced air masses with enhanced values in the morning and the late afternoon during rush hours. If the data is restricted to periods with prevailing winds from the open North Sea, the diurnal cycle vanishes and values are more or less constant over the day. This shows that no road traffic emissions from land are contained in those air masses and confirms the expectation that the amount of ship traffic is nearly independent from the time of day. Remaining variations might be due to residual land-based emissions not being filtered out, unknown regularly scheduled ship traffic (e.g. from ferries), or due to noise on the measurements.

In Fig. 6.15, the mean NO₂ VMRs per weekday are plotted, including curves for all measurements (unfiltered: solid lines) as well as for winds from the open North sea (filtered: dashed lines). This figure shows in a similar way to the one for the diurnal evolution the influence of land-based road traffic emissions. Lowest values are measured on Sundays, when the least intense road traffic is expected. The subset of data measured under prevailing northwesterly winds shows very small variations from weekday to weekday and significantly lower values overall.

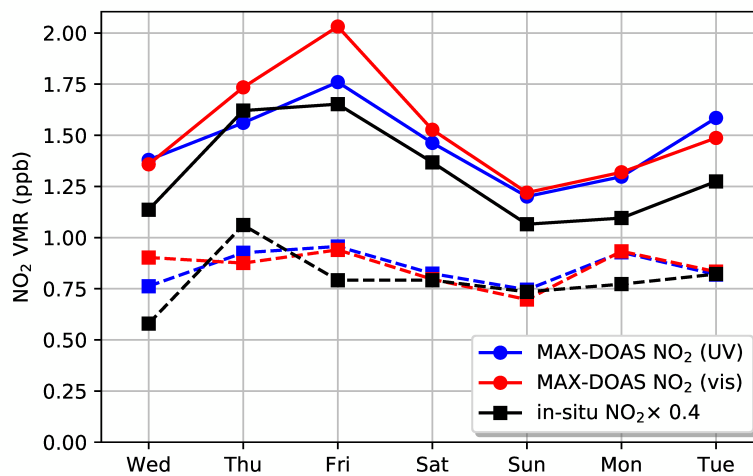


Figure 6.15.: Average weekly cycle of MAX-DOAS (UV and visible) and in-situ NO₂ volume mixing ratios for all measurements (solid lines) and for a subset of measurements with wind from the open North Sea (dashed lines). For a better visual comparability the in-situ values are scaled by a factor of 0.4. (Seyler et al., 2017)

The fact that the highest values were measured on Friday might be due to the earlier end of work time on Fridays and an earlier afternoon rush hour, which, at least in the winter season, should contribute more to the daily mean than an evening rush hour on other weekdays with too low sun for MAX-DOAS measurements anyway. The fact that air masses

containing road traffic emissions which are measured at or north of the measurement site on Neuwerk need a certain amount of time to travel there from their land sources, creating a delay between emission and measurement, would even enhance this effect.

Except for a scaling factor of 0.4 to 0.5, the shape of the diurnal and weekly cycle retrieved from MAX-DOAS and in-situ measurements agree remarkably well.

From the investigation of both the diurnal and weekly variation of NO_2 it can be seen that road traffic on land can have a strong influence on the measured NO_2 values, indicating that the measurement region is, although located in the North Sea, in fact strongly influenced by land-based ambient background pollution for certain wind directions.

6.7 Influence of recent fuel sulfur content regulations on SO_2 emissions

6.7.1 SO_2 to NO_2 ratios in ship plumes

The strength of the MAX-DOAS-measured ship plume signals, represented by the peak height (or peak area) in the measured MAX-DOAS time series, can in general not be taken as a measure for the amount of the emitted pollutants, as it also strongly depends on geometry: the higher the fraction of the horizontal light path that probes the plume, the higher the measured values. This means that high values are measured when the plume extends along the instrument's line of sight (LOS), and much lower values when the plume runs orthogonal to the LOS. The derivation of emission factors or absolute amounts (e.g. in mass units) of the pollutants emitted by individual ships thereby requires further knowledge, e.g. from modeling. If a model or auxiliary measurements provide the location and spatial extent of the plumes, in-plume pollutant concentrations or volume mixing ratios (VMRs) can be derived, as it is shown in Section 7.6.

Although emission factors cannot be measured by MAX-DOAS directly due to the plume–LOS geometry dependence, the NO_2 and SO_2 signals yield the ratio of both. By taking the ratio between UV NO_2 and SO_2 , the plume–LOS geometry dependency cancels out, and a ship emission specific value can be obtained, which can then be compared for different ships. Also a comparison to ratios of emission factors reported in other studies as well as measurements on other sites or with different instruments are possible. From a practical point of view, using the SO_2 to NO_2 ratio is better than vice versa, as the SO_2 content in the plume depends strongly on the ship's fuel sulfur content and can also be close to zero, while NO_x emissions are an integral part of high temperature combustion processes in ship engines (see Section 2.5 on the Zel'dovich mechanism) independently of the fuel, and are

not expected to decrease until NO_x emission limits are set into force. Having SO_2 values close to zero in a NO_2 to SO_2 ratio would mean a wide span of possible values without upper bound (approaching infinity), therefore defining the ratio the other way round is much more practical.

The height of the NO_2 peaks also depends on the time span between emission and measurement because of NO to NO_2 titration (see Section 2.5) and the fact that a large fraction of the emitted NO_x is emitted as NO . Using a SO_2 to NO_x ratio would avoid this, but since NO does not absorb in the UV–vis spectral range, it cannot be measured with a passive MAX-DOAS instrument. So, one has to bear in mind possible deviations due to the fact that the equilibrium in NO to NO_2 titration might not be reached.

Comparing SO_2 to NO_2 ratios from different ships makes it possible to roughly distinguish whether a ship uses fuel with high or low sulfur content. Beecken and Mellqvist from Chalmers University, Sweden, applied this relationship for airborne DOAS measurements of ship exhaust plumes on an operational basis in the CompMon project (Compliance monitoring pilot for MARPOL Annex VI) (Van Roy and Scheldeman, 2016). Following individual ships with an aircraft or helicopter and measuring downward across the emitted plume enables to discriminate between ships using low (0.1 %) or high (1 %) fuel sulfur content fuel with a probability of 80–90 % (Van Roy and Scheldeman, 2016). A more detailed measurement can then follow using in-situ trace gas analyzers by flying the aircraft inside the plume (e.g. Balzani Lööv et al., 2014; Beecken et al., 2014).

From the spectra of the UV channel of our MAX-DOAS instrument, which cover a wavelength range of 304.6 to 371.7 nm, both SO_2 and NO_2 DSCDs can be retrieved at once (see Section 6.1.3 for the exact fitting windows). The measurement time is therefore identical. As SO_2 is retrieved at shorter wavelengths, the horizontal effective path lengths along which the DSCDs are measured and thus the measurement volumes are slightly different (see Section 6.2).

Panel a and c of Fig. 6.16 show as an example the MAX-DOAS NO_2 and SO_2 DSCDs measured on 23 July 2014, before the stricter fuel sulfur content limits were introduced. Both the NO_2 and SO_2 signal display strong enhancements in the form of high and sharp peaks when ship plumes crossed the LOS of the instrument. Most of the peaks are of similar shape in NO_2 and SO_2 signal, whereas the NO_2 values are roughly three times higher than the SO_2 values. Both pollutants show an elevated level of underlying, slowly-varying ambient background pollution.

To separate ship related signals from smooth ambient background pollution⁸, first a running median filter was applied to the time series of NO_2 and SO_2 with a relatively large kernel

⁸Although the ambient background pollution can of course also contain old, diluted ship plumes, only the sharp, distinct enhancements from young emission events are essentially meant here.

size (e.g., over 21 points). Broad, smooth peaks in the time series can systematically shift this running median upwards. It is then biased to higher values than the actual baseline as it can be identified by eye. In such cases, this procedure is not sufficient and a second running median filter is applied to the values in the lower 50 % quantile with a smaller kernel size (e.g., 5). If necessary, the respective kernel sizes are varied by hand until a good approximation of the real baseline is reached.

In the next step, to remove the underlying ambient background pollution from the signal, the baseline is subtracted from the raw signal (see panel b and d in Fig. 6.16). To account for cases, where NO₂ is enhanced and SO₂ not, which would be the case for ships with very low fuel sulfur content, the identification of the peaks is based on the NO₂ time series only. For the peak identification, a simple peak detection algorithm was applied to the baseline-corrected NO₂ signal. Afterwards, the corresponding peaks in the SO₂ time series are assigned. A final manual checkup followed, where all the detected peaks were looked through and manually selected for the statistics. All cases where peaks are too close together to be separated were filtered out, and again, if necessary, a fine-tuning of the baseline detection algorithm parameters was performed. To gain a better signal-to-noise ratio, instead of the peak height, the integrated peak area was used.

In the example shown in Fig. 6.16, the measured SO₂ to NO₂ ratios range from 0.17 to 0.41. As can be seen from the figure, the SO₂ to NO₂ ratio can differ a lot for different ship plumes. The plume of the ship passing the line of sight around 12:00 UTC yields a strong NO₂ signal, but is low in SO₂, whereas the opposite is true for the plume of the ship passing the LOS at 12:30 UTC. This indicates that the latter ship was using fuel with a significantly higher sulfur content.

After the change in fuel sulfur content regulations on 1 January 2015, drastically reducing the allowed fuel sulfur content from 1 % to 0.1 %, the situation has changed fundamentally. Figure 6.17 shows as an example the NO₂ and SO₂ measurements from one day in summer 2015, but other days look similar. Compared to Fig. 6.16, the NO₂ signal again shows high, sharp peaks caused by probed ship plumes, but the SO₂ signal is rather flat and shows no clearly distinguishable peaks anymore, a result of much less sulfur in the fuel. There might still be some small collocated SO₂ enhancements to the NO₂ peaks, yet it cannot be determined if these are real signals or just random noise fluctuations. Two very small SO₂ peaks at 10:40 UTC and 14:00 UTC, only slightly enhanced above noise level, might be real SO₂ plume signals caused by ships having a higher than average fuel sulfur content.

In the example from 2015, the SO₂ to NO₂ ratios range from 0.00 to 0.09, much lower than before the stricter fuel sulfur limits.

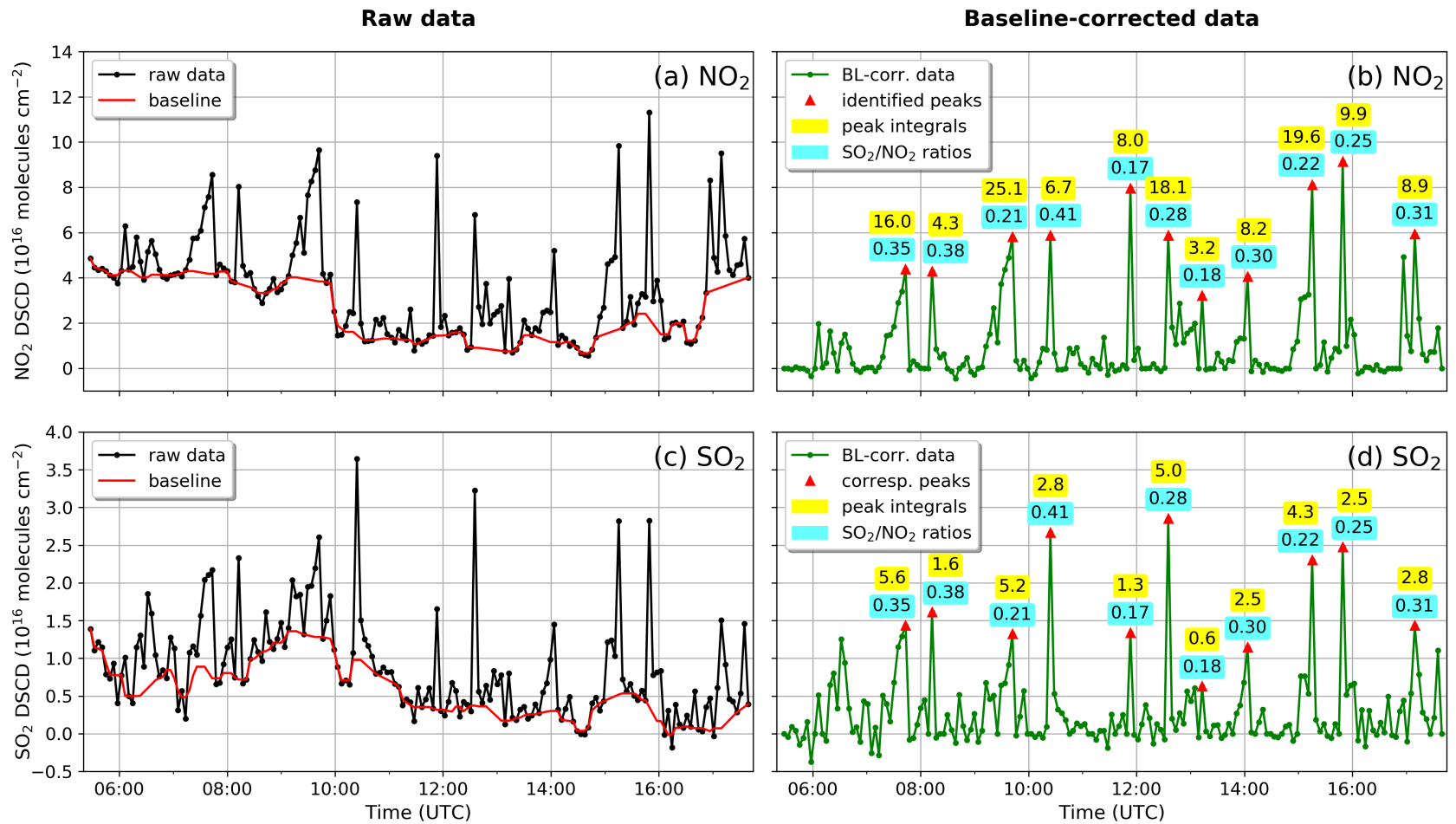


Figure 6.16.: Calculation of SO₂ to NO₂ ratios for ship emission peaks for one example day (23 July 2014) before the change in sulfur emission limits. Panel a shows the UV NO₂-DSCD raw data for 0.5° elevation and 335° azimuth and the determined baseline. Panel b shows the baseline-corrected NO₂ data for which the automatically identified peaks are highlighted with red triangles. Numbers close to the peaks denote the peak integrals in 1×10^{16} molec cm⁻² (marked in yellow) and the SO₂ to NO₂ ratios (marked in blue). Panels c and d show the corresponding plots for SO₂. (Seyler et al., 2017)

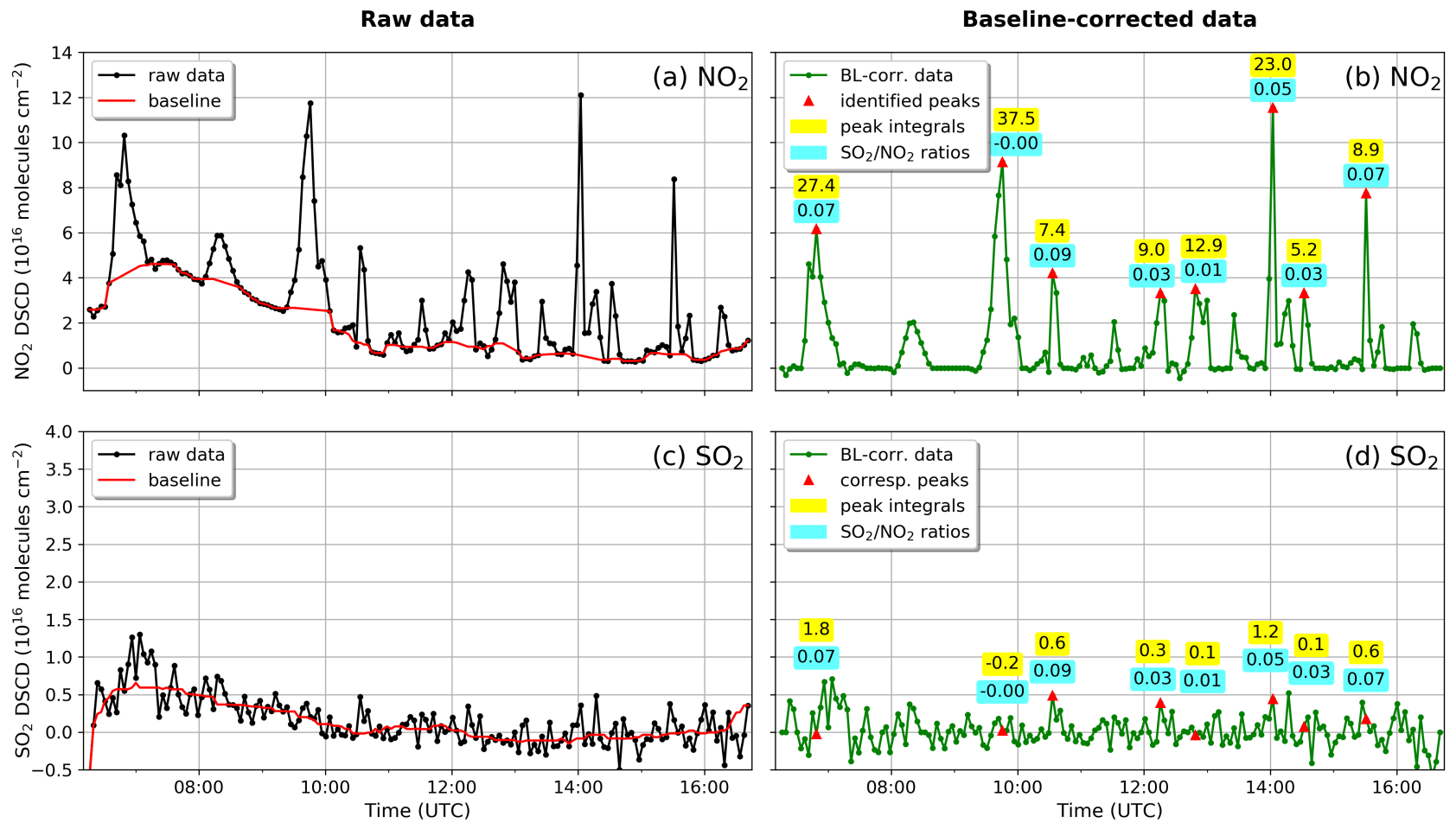


Figure 6.17.: As Fig. 6.16 but for an example day (3 July 2015) after the introduction of stricter fuel sulfur content limits. Measurements in 0.5° elevation and 65° azimuth are shown. Peak integrals are given in 10¹⁶ molec cm⁻². (Seyler et al., 2017)

To generate a sufficiently large dataset for a statistically meaningful comparison of both time periods before and after the legislation change, two representative subsets of ship emission peak samples were selected manually according to the above-mentioned procedure and analyzed in a semi-automatic way. To eliminate the influence of clouds or bad weather, days with unfavorable measurement conditions were filtered out by using solar radiation measurement data from the on-site weather station. That way, two samples of more than 1000 peaks each were selected, one from the data of 2013 and 2014 representing the state before introduction of stricter fuel sulfur content limits, and one from the data of 2015 and 2016, representing the situation afterwards. Since no attribution of the measured plume signals to the emitting ships was carried out⁹, it cannot be ruled out and is highly probable that some ships were measured repeatedly on different days and/or in multiple azimuthal viewing directions.

Figure 6.18 shows a histogram of the distribution of SO₂ to NO₂ ratios computed from peak integrals for the two samples, before and after the legislation change on 1 January 2015. The histogram shows that in the data from 2013 and 2014 the SO₂ to NO₂ ratios in ship plumes were substantially higher than in the data from 2015 and 2016.

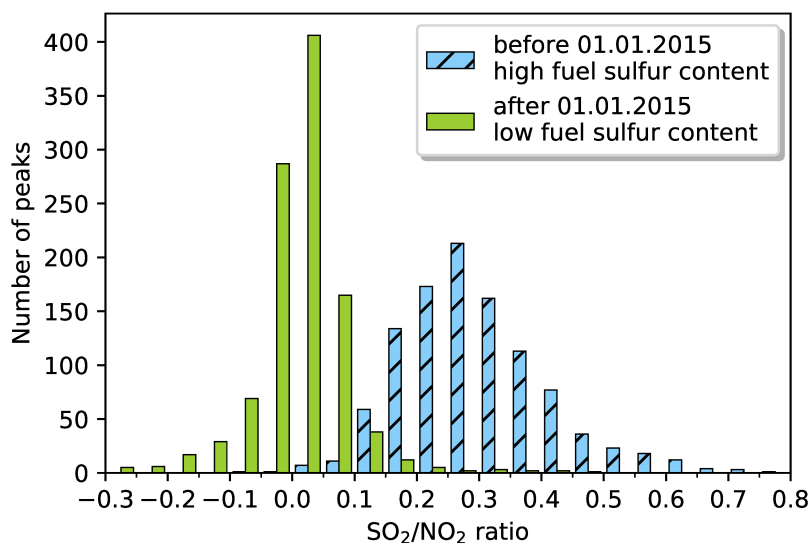


Figure 6.18.: Histogram showing the distribution of SO₂ to NO₂ ratios in two samples ($N = 1055$ for each) of ship emission peaks measured in 0.5° elevation and all azimuth angles for the time before (blue, hatched) and after (green) the change in fuel sulfur content regulation on the 1st of January 2015. (Seyler et al., 2017)

A comparison of mean values, standard deviation and median values is given in Table 6.4, confirming the drastic reduction in plume SO₂ content after the fuel sulfur limit reduction.

⁹Which can be achieved with plume forward trajectory modeling, as it is shown later on in Section 7, at reasonable expense for case studies only

Inputting the samples into a Welch's t-test, a t-test for unequal variances, shows that the observed reduction is statistically highly significant.

Table 6.4.: Mean values, standard deviations and median values of the SO₂ to NO₂ ratios for the two samples of $N = 1055$ selected peaks

Dataset	SO ₂ to NO ₂ ratio in ship plumes		
	Mean value	Std. deviation	Median value
2013/2014	0.30	0.13	0.28
2015/2016	0.007	0.089	0.013

For a plausibility check these results can be compared to those from other studies, while one has to bear in mind possible differences that can arise from different measurement techniques, measurement geometries and sites, different relative distances to the emitting ships, and thus different NO to NO₂ titration in the plumes.

McLaren et al. (2012) measured NO₂ to SO₂ emission ratios in ship plumes in the Strait of Georgia in 2005. In the analyzed sample of 17 plumes, a median molar NO₂/SO₂ ratio of 2.86 was found. Translated into a SO₂ to NO₂ ratio this yields a value of 0.35, which is in good agreement with this study's findings for the time before 2015, especially considering McLaren et al. (2012)'s relatively small sample size of 17 plumes.

Diesch et al. (2013) measured gaseous and particulate emissions from various marine vessel types and a total of 139 ships on the banks of the Elbe river in Germany in 2011. The reported SO₂ and NO₂ emission factors can be translated into SO₂ to NO₂ emission ratios, yielding a ratio of 0.13 and an average fuel sulfur content (FSC) of 0.22 ± 0.21 % for small ships (< 5 000 tons), a ratio of 0.24 and a FSC of 0.46 ± 0.40 % for medium size ships (5 000–30 000 tons) and a ratio of 0.28 and a FSC of 0.55 ± 0.20 % for large ships (> 30 000 tons). Diesch et al. (2013)'s results for large and medium size ships fit quite well to the results of this study. Small ships' plumes, however, have not been taken into account in this study's statistic because of low signal-to-noise ratio if measurable at all, so cannot be compared to Diesch et al. (2013).

Assuming that Diesch et al. (2013)'s dependency of SO₂ to NO₂ ratio and FSC can be applied to this study's dataset, a rough estimate of the ships' FSC can be derived. For the data from 2013 and 2014, this yields an average fuel sulfur content of 0.5–0.7 %, which is in good agreement with the results reported by Kattner et al. (2015) for the months before the legislation change.

Cheng et al. (2019) measured SO₂/NO₂ ratios in emission plumes from 55 ocean-going, inbound and outbound vessels at Yantian Port close to Shenzhen, China, for which the 3.5 % global fuel sulfur content limit applied. The distribution of the measured ratios has

its peak at about 0.6 to 0.9, but also ratios up to 2 and higher were frequently measured, as can be seen in Fig. 6.19, taken from their publication. Compared to the histogram of SO_2/NO_2 ratios measured on Neuwerk before 2015 (see Fig. 6.18) under a 1 % FSC limit, a factor of 3 to 4 lies between both distributions, confirming the validity of the results of both studies.

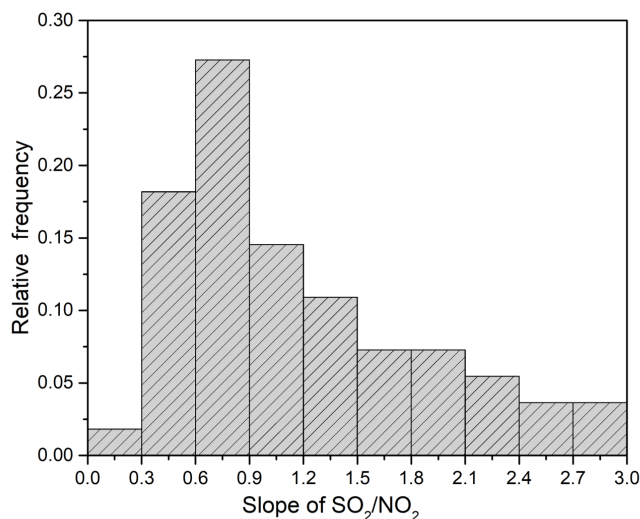


Figure 6.19.: Frequency distribution of the slope of SO_2/NO_2 from samples of 55 vessels. (Cheng et al., 2019)

The drastic reduction in SO_2 in ship plumes since the fuel sulfur content reduction on 1 January 2015 was also observed by other studies: Using in-situ measurements in Wedel at the bank of the Elbe river, a few kilometers downstream from Hamburg, Germany, Kattner et al. (2015) reported that in early 2015 95.4% of the measured ships complied with the new 0.1 % sulfur limit. Analyzing 1.5 years of SO_2 measurements at the English Channel, Yang et al. (2016) found a three-fold SO_2 reduction in 2015 compared to 2014.

6.7.2 Dependence of NO_2 and SO_2 pollution levels on wind direction

Although Neuwerk is a very small island in the German Bight, approximately 10 km off the coast, not only air pollution emitted by ships is measured here. As the measured diurnal and weekly cycle in NO_2 pollution levels (see Section 6.6) for certain wind directions have shown, land-based air pollution sources also play a role for the air quality at this site.

A map of the German Bight and the German North Sea coast is shown in Fig. 6.20. Neuwerk is located in the west of Cuxhaven, in the center point of the color-coded circular sectors overlaid on the map. As can be seen from the map, depending on the prevailing wind direction, different air masses with different pollution source contributions can reach the site. For north easterly wind directions, highlighted with a in blue sector in the map, the

wind is coming from the open North Sea, where ships are the only source of local air pollution. Section 6.6 has shown that no diurnal or weekly cycle in NO_2 was measured for wind coming from these directions. The map shows that for all other wind directions the air masses which are blown to the site are expected to contain pollution from land-based sources. For the yellow sectors in the map, a mix of shipping emissions and land-based emissions is expected, while for southeasterly wind directions, highlighted by the green sector, mainly pollution originating on land is expected with a small contribution of shipping emissions that cannot be ruled out. This classification in yellow and green sector for land-based air pollution influenced air masses gets important in the following Section 6.7.3, where the contributions from shipping and land-based emissions on the air quality in the inspected region are estimated.

A reduction of SO_2 emissions due to the lowering of the allowed marine fuel sulfur content from 1 % to 0.1 % from 1 January 2015 on, should thus be strongest in the data measured during northeasterly winds, where ships are the only local SO_2 pollution source.



Figure 6.20.: Source region classification by wind sector, distinguishing between wind coming mainly from land (green), only from sea (blue) and from directions with mixed contributions (yellow). The background map is adapted from a work by Halava, CC BY-SA 3.0, <https://commons.wikimedia.org/w/index.php?curid=11707771>.

To investigate the dependence of NO_2 and SO_2 pollution levels on wind direction, the data has been separated into 16 bins of 22.5° each, according to the prevailing wind direction. The bins are centered at 0° (N), 22.5° (NNE), 45° (NE) and so on. For each wind direction bin, the mean volume mixing ratio is computed. To evaluate the effect of the fuel sulfur reduction, data from 2013 and 2014 (“before the change”) is treated separately from the data from 2015 and 2016 (“after the change”). Two days of SO_2 measurements on 20 and 30 October 2014 that show very high SO_2 values from an Icelandic volcanic plume

(Bárðarbunga eruption 2014) transported to Neuwerk have been excluded from the SO₂ time-series to avoid the resulting bias in the wind direction dependence distribution.

Figure 6.21 shows in two polar plots the angular distribution of the mean NO₂ (panel a) and SO₂ (panel b) VMRs¹⁰ depending on the wind direction. Measurements before and after the change in fuel sulfur limit regulations are shown separately.

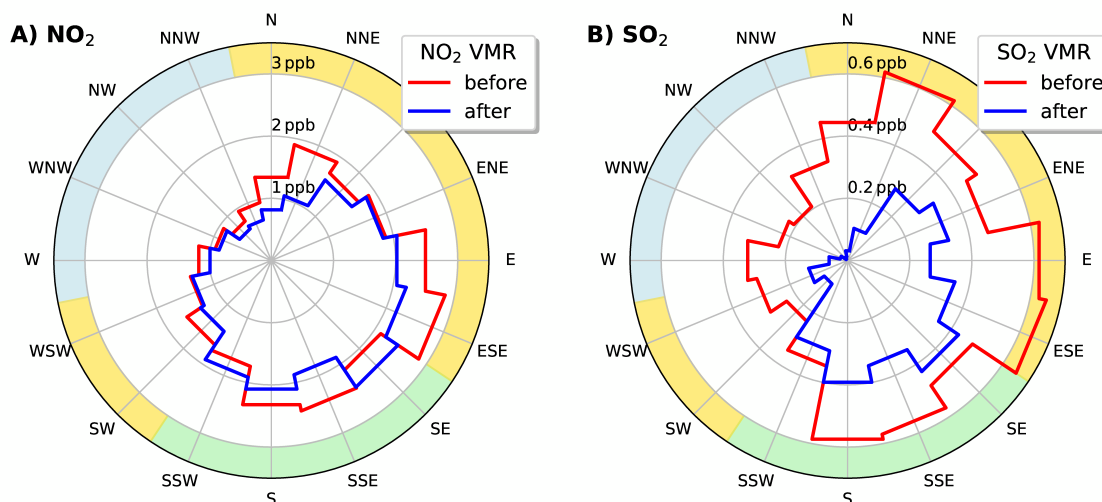


Figure 6.21.: Wind direction distribution of the measured NO₂ (A) and SO₂ (B) volume mixing ratio in 0.5° elevation before and after the change in fuel sulfur limit regulations on 1 January 2015. The colored sectors show directions with wind mainly from land (green), open North Sea (blue) and mixed origin (yellow). Note that the scale of the radial axes of both plots is different. (Seyler et al., 2017)

For SO₂, a significant reduction in the average pollution levels is found after the introduction of the stricter fuel sulfur limit for almost all wind directions. The relative decrease is strongest for wind directions from West to North representing wind from the open North Sea, where SO₂ levels go down to almost zero. This confirms the efficacy of the new and more restrictive fuel sulfur content regulation leading to a clear improvement in coastal air quality. The SO₂ decrease for other wind directions shows that not only land-based sources but also shipping emissions contribute to the air pollution in air masses from these directions. No or only a small decrease is observed for the green wind sector where the contribution of shipping is expected to be the least.

For NO₂ on the other hand, both the absolute values and the directional distribution for 2013/2014 (“before”) and 2015/2016 (“after”) are nearly identical, implying no changes in NO_x emissions between both time periods. This result meets the expectations, since NO_x emission limits for the North and Baltic Sea ECA were not yet set into force at this time.

¹⁰Derived via O₄ scaling (see Section 6.2)

For a plausibility check, the computed mean SO₂ VMRs can be compared to SO₂ concentrations measured by the German Federal Environmental Agency (Umweltbundesamt, UBA). In 2016, for rural stations in Northern Germany the typical average concentrations are in the order of 0.5 to 1 μg m⁻³ (Umweltbundesamt, 2017), which converts to 0.2 to 0.4 ppb using a conversion factor of 1 ppb ≅ 2.62 μg m⁻³ for SO₂ at standard temperature and pressure. Measurement stations in urban areas and close to industrial areas measure higher average values. At the UBA station in Bremerhaven, the closest station to the Neuwerk site, a mean concentration of 1.77 μg m⁻³ is measured, which converts to 0.67 ppb. The SO₂ VMRs measured in this study for wind directions with mainly land-based air pollution sources amount to 0.3 to 0.4 ppb, which is in good agreement with the UBA measurements at rural background stations of about 0.2 to 0.4 ppb.

The variation in NO₂ between both time periods could give a hint on the uncertainty of the retrieved VMRs, but, not unlikely, could also indicate changes in the emissions. The fact that the MAX-DOAS measurements are no point measurements at the location of the instruments, but averaged values over horizontal light paths of several kilometers reaching from the radar tower towards the shipping lane in the north and even beyond, depending on the distance to the mean last photon scattering event, can introduce uncertainties: For southerly or southeasterly wind directions, i.e., the green sector defined in Fig. 6.20, the probed air masses are expected to contain mainly pollution originating on land. Pollution plumes emitted by the ships on the shipping lane are expected to be blown northward, away from the instruments. If the horizontal light path extends beyond the shipping lane the photons reaching the MAX-DOAS instrument can have probed these ship plumes. Thus, a contribution of shipping emissions in the measured air masses for southerly or southeasterly wind directions cannot be ruled out. Since the analysis of the wind direction dependence of measured NO₂ levels is performed on UV data only¹¹, the effective paths usually extend not that far northward beyond the shipping lane. As a result, if ship emission peaks are observed in the UV data for southerly wind directions (at all), they are very small. The influence on the statistic and the thereby introduced uncertainty is considered to be very small.

6.7.3 Contributions of ships vs. land-based pollution sources on coastal air quality on Neuwerk

Revisiting the wind direction dependence of measured NO₂ and SO₂ VMRs in the previous section, the measured data can also be used to estimate and investigate the contributions of ships and land-based sources to coastal air pollution levels in the region of interest.

¹¹For the better comparability between the horizontal averaging paths and the associated measurement volumes for SO₂ and NO₂

For a northwesterly sector of wind directions ranging from 258.75° to 348.75° the wind is coming from the open North Sea and ships are the only local air pollution source (see Fig. 6.20). To trade off emissions from shipping against land-based emissions from industry, road traffic etc., in addition to this geography-defined sector of 90° , a second sector of 90° of wind directions ranging from 123.75° to 213.75° has been chosen where wind is mainly coming from land and the contribution of shipping emissions is expected to be small.

For other wind directions, air masses are expected to contain pollution both from land-based sources as well as ship emissions. For easterly wind directions, for example, the air mass was transported over the mouth of the Elbe river where there is shipping, but also over Cuxhaven or other cities further inland, right up to the city of Hamburg. These remaining wind directions, which are not included in the two representative sectors of 90° each, thus have a mixed pollution origin. Assuming that pollutant concentrations measured during periods where wind was coming from one of these sectors have their source in the according sector and ignoring any wind field curvature, the two selected sectors (blue and green) can be taken as representative sectors for the estimation of the source contributions. Measurements in all azimuth angles have been included into this analysis for the sake of getting a better statistic.

Figure 6.22 shows in pie charts the contributions of ship and land-based pollution influenced source regions to measured NO_2 and SO_2 levels on Neuwerk. For SO_2 , the data has again been separated for the time period before and after the fuel sulfur content limit change. Because of the high degree of similarity between the results for both time periods for NO_2 the total measurement time series was not split up and considered together.

The first column of pie plots in Fig. 6.22 shows the percentage of measurements with wind coming from open North Sea sector, land sector, and the directions with mixed origin for NO_2 and SO_2 , the latter split up in 2013/2014 and 2015/2016. The second column of pie plots shows the relative contribution of the sources to the total integrated volume mixing ratios of NO_2 and SO_2 . The third column of pie plots shows again the relative contribution to the total integrated NO_2 and SO_2 VMRs, but this time considering only the land and sea sector, omitting the measurements with mixed pollution origin.

With around 55 to 60%, more than half of all measurements for both NO_2 and SO_2 have been performed while wind was coming from either the assigned land or sea sector, making the use of these sectors as representative samples for land-based and shipping emission source regions a reasonable approximation.

The total number of available measurements is different for NO_2 and SO_2 , since NO_2 can be easily fitted until 85° solar zenith angle (SZA) with good results on Neuwerk, while the SO_2 fit delivers realistic values only up to 75° SZA. For higher SZAs (lower sun) the remaining shorter wavelength UV radiation reaching the MAX-DOAS instrument is not

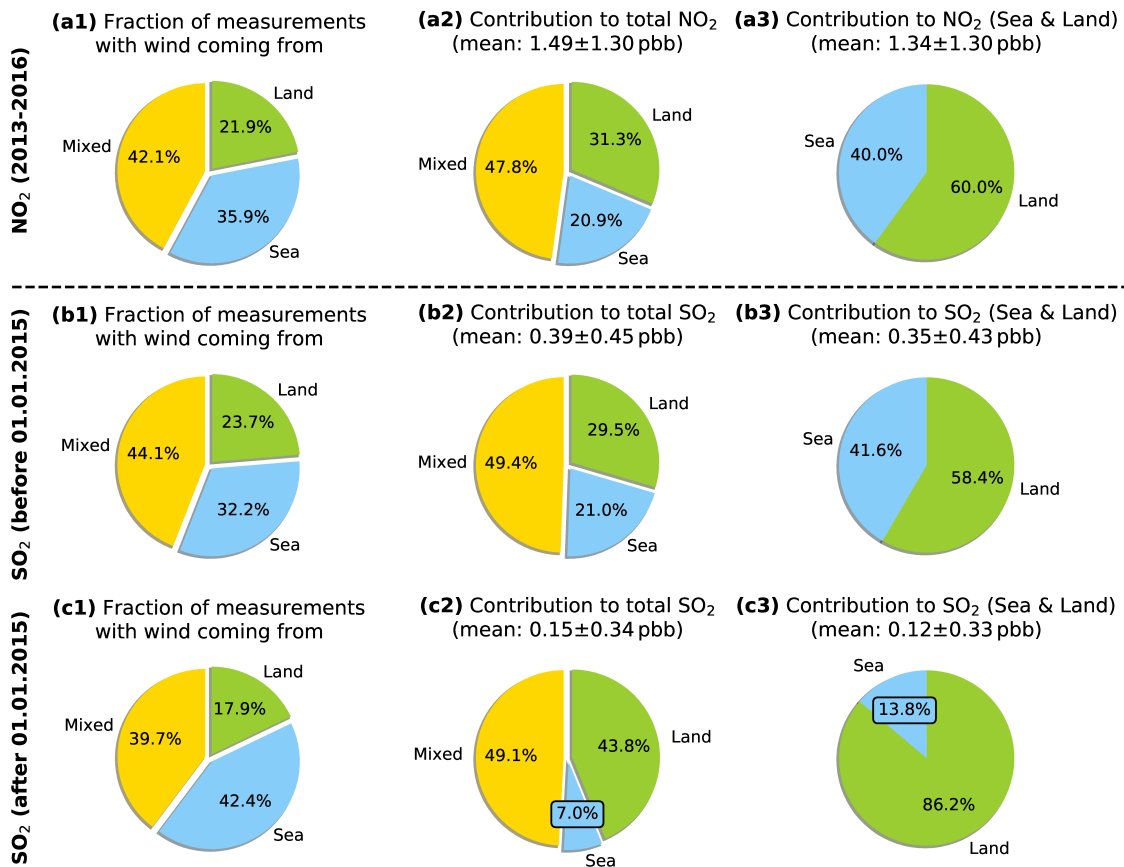


Figure 6.22.: Contributions of ships and land-based pollution sources to measured NO₂ and SO₂ levels on Neuwerk:

Panels a1, b1 and c1: Percentage of measurements with wind coming mainly from land (green), only from sea (blue) and from directions with mixed contributions (yellow) for all NO₂ data (a1), SO₂ data before (b1) and after the change in fuel sulfur content limits (c1).

Panels a2, b2 and c2: Contributions to the integrated volume mixing ratios of NO₂ (a2) and SO₂ (b2, c2) from the source regions in percent.

Panels a3, b3 and c3: Contributions to the integrated volume mixing ratios when considering only the land and sea sector. It can clearly be seen that the lower fuel sulfur limit led to a strong decrease in the SO₂ contribution from shipping since 2015. (Seyler et al., 2017)

sufficient for good fits. This leads to less measurements for SO₂ than for NO₂ and is especially pronounced in winter times, when sun is low. Despite this, the observed general wind direction frequency distribution is similar for NO₂ and SO₂, with wind coming from the sea sector for 32 to 42 % of all measurements and from the land sector 18 to 24 % of the time.

For NO₂ (upper row of pie plots in Fig. 6.22), more than half of the total integrated NO₂ was measured while the prevailing wind direction was either from the sea or land sector, with 21 % attributed to ships and 31 % attributed to land-based sources. For 48 % of the total NO₂, the source can not be attributed and could be land or ships or, most probably, both.

When ignoring the measurements with mixed (or non-attributable) origin and considering only the two sectors for which the primary source can be identified, and taking these two sectors as representative, we can say that 40 % of the NO₂ on Neuwerk is coming from ships, while 60 %, the majority, is coming from sources on land. As the island Neuwerk is located quite close to the coast, air quality on Neuwerk is apparently still strongly impacted by polluted air masses from land. Similar findings have been derived from the analysis of the diurnal and weekly variability in NO₂ (Fig. 6.14 and 6.15 in Section 6.6), showing clear road-traffic-emission-induced diurnal and weekly cycles for wind from land. This indicates that in near-coastal marine regions in Germany land-based NO_x sources like road traffic and industry can, despite the heavy ship traffic, be the strongest source of NO_x air pollution while ship emissions come in second.

For SO₂, the time periods before and after the introduction of stricter sulfur limits for marine fuels in the North Sea ECA on 1 January 2015 were analyzed separately. For the first period, one and a half years of measurements in 2013 and 2014, the resulting pie plot statistics are shown in the middle row of Fig. 6.22. The second period, after the change of the allowed fuel sulfur content, comprises of one and a half years of measurements in 2015 and 2016 and has approximately the same length as the first. The corresponding pie plots for the second period are shown in the bottom row of Fig. 6.22. In 2013/2014, 32 % of the SO₂ measurements were taken while wind was coming from the open North Sea sector and about 24 % when wind was coming from the designated land sector. In 2015/2016, wind was coming a bit more often from the open North Sea (42 % of the time) and less often from the land sector (18 % of the time), but generally the situation was quite similar.

For 2013/2014, before the introduction of stricter sulfur limits, the contributions of the three sectors (land, sea and mixed origin) to the total integrated SO₂ are very similar to those for NO₂. In 2015/2016, with less sulfur in the fuel, the relative contribution from the sea sector shrank significantly from 21 to 7 % while the relative contribution of the land sector increased from 30 to 44 %. The relative contribution from the mixed sector, where the SO₂ source can not be clearly identified, stagnated at 49 %. The increase of

the contribution of the land source sector, however, is only a relative increase and the absolute contribution decreased even slightly, as has already been observed in Fig. 6.21 in the previous section. A strong overall decrease in SO₂ from 2013/2014 to 2015/2016 – the mean SO₂ VMR decreased from 0.39 ppb to 0.15 ppb – conceals the magnitude of the reduction also for the sea sector: While the relative contribution from the open North Sea sector decreased only by a factor of 3, the absolute contribution from this sector after the introduction of stricter sulfur limits decreased by a factor of 8, even though coincidentally the wind was coming more often from the sea sector in this period, meaning that a higher fraction of measurements were taken while wind was coming from the open North Sea.

When considering only the two assigned sectors as representative for ships and land-based emissions, the relative shares changed from 42 % : 58 % from sea and land, which is very similar to the 40 % : 60 % observed for NO₂, to 14 % : 86 %, a significant reduction of SO₂ pollution.

The observed strong reduction of SO₂ pollution from shipping (by a factor of 8) shows that the stricter fuel sulfur content limits introduced on 1 January 2015 are working and significantly improved the air quality in coastal regions of the North Sea with respect to SO₂. It also indicates that no heavy fuel oil with high sulfur content is burned in the ship engines in this region any more. These results are in good agreement with other studies like Kattner et al. (2015), who reported that with around 95 % the vast majority of ships is sticking to the new limits.

According to our measurements since 2015, the vast majority of SO₂ emissions can be attributed to land sources and ships play only a negligible role, while prior to 2015 shipping emissions presented a significant SO₂ source in our coastal region.

As discussed in the previous section, in southerly wind situations with good visibility (long horizontal light paths) and low wind speeds, the MAX-DOAS line of sight can be long enough to probe ship plumes in the north of the shipping lane, which would add to the emissions of land sources south of Neuwerk. As this analysis uses UV measurements, the resulting peaks are typically very small and compared to the strongly enhanced ambient background pollution in such cases of southerly winds, the additional contribution is small, maybe negligible (for a few example days it is in the order of 2 to 4 %), but is certainly leading to a small overestimation of land sources in the designated “land sector”. For measurements in the visible spectral range with significantly longer horizontal light paths, the influence of this effect will certainly be much stronger.

6.8 Long term analysis maps

Averaging measurements over a long time period should make it possible to predict the general NO₂ distribution around the measurement site, at least for certain selected wind conditions. From the O₄ scaling approach the effective horizontal light path lengths and the average NO₂ VMRs along the light paths are known. In the approach presented in the following, the known light paths are divided into several short segments of 1 km length. The total light path length in kilometers is rounded to the nearest integer value beforehand.

Since the exact distribution of NO₂ molecules along the light path is unknown and only the total horizontal column density and the average VMR is known, in absence of a better alternative, it has to be assumed that the average VMR along the total light path is homogeneously distributed, so that the average VMR along each light path segment is the same as the average VMR along the total light path. This is equivalent to assuming that the NO₂ molecules (adding up to the total horizontal column or average VMR) are evenly distributed along the light path, and at the same time assuming that all photons traveled the whole horizontal light path length and all photons were scattered at the same distance from the instrument, which is of course not happening in reality. On the contrary, more photons are reaching the instrument from nearby and less photons from further away and the effective light path length is more like a mean path length. Still, in absence of a better alternative and further knowledge, these assumptions have to be made.

For example, one measurement gives a 10 km light path with an average NO₂ VMR of 5 ppb. In the approach described in the following, the light path is divided into ten segments of 1 km each, with 5 ppb average VMR on each segment. This is done for all measurements and, afterwards, the mean VMR for each segment, like for example for the 5 to 6 km segment in the 5° viewing direction, is calculated. Figure 6.23 shows a sketch of the procedure to help better visualizing the approach.

What is the expected result? If only well-mixed background pollution is measured, the path-averaged NO₂ VMR should be the same on short light paths as well as long light paths. If ship plumes are present, the NO₂ field above and around the shipping lane is inhomogeneous. For example for northerly wind directions, the plumes are blown from the shipping lane towards the instrument. Short light paths should now show enhanced path-averaged NO₂ VMRs compared to longer light paths. Such a case is assumed in Fig. 6.23.

The results of this approach for northerly wind directions are shown in Fig. 6.24 for the UV measurements and in Fig. 6.25 for the measurements in the visible spectral range. For this analysis, all MAX-DOAS measurements under a certain wind direction range were used. Additional quality criteria are an RMS limit of 1×10^{-3} and a maximum SZA of 85°. To

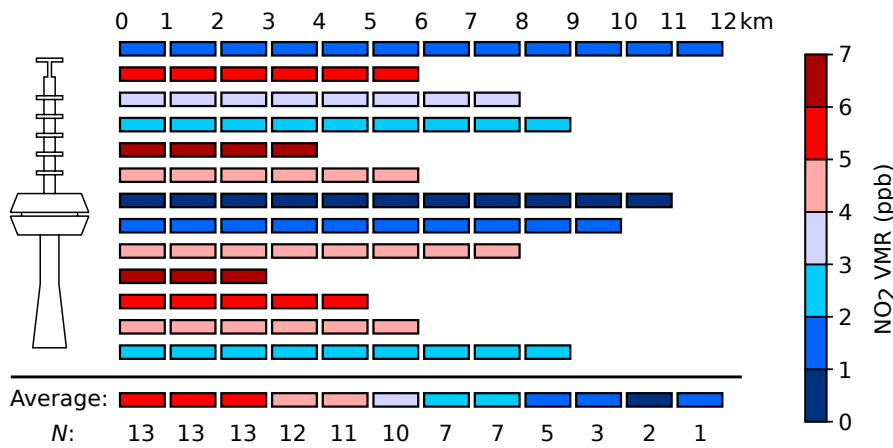


Figure 6.23.: Sketch illustrating the averaging procedure for the light path segments for the case of a plume close to the radar tower

make sure that data quality is acceptable and enough values contribute to the calculated means, only light path segments with $N = 1000$ or more averaged measurements are used.

Both pictures show enhanced NO₂ south of the shipping lane and lower values north of the shipping lane, as expected. The fact that the longer light paths with lower NO₂ also contribute to the average on all the 1 km light path segments closer to the instrument leads to a systematic underestimation closer to the instrument and the contrast between north and south is weakened and should in reality be even stronger.

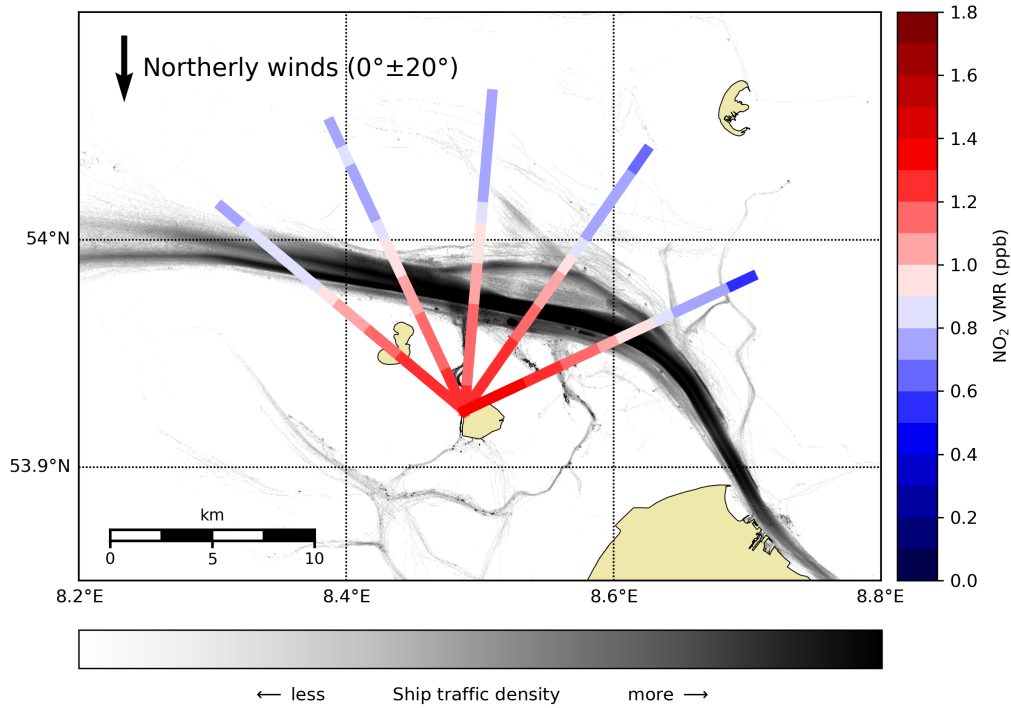


Figure 6.24.: Map showing average MAX-DOAS UV NO₂ volume mixing ratios per 1 km light path segments for northerly winds

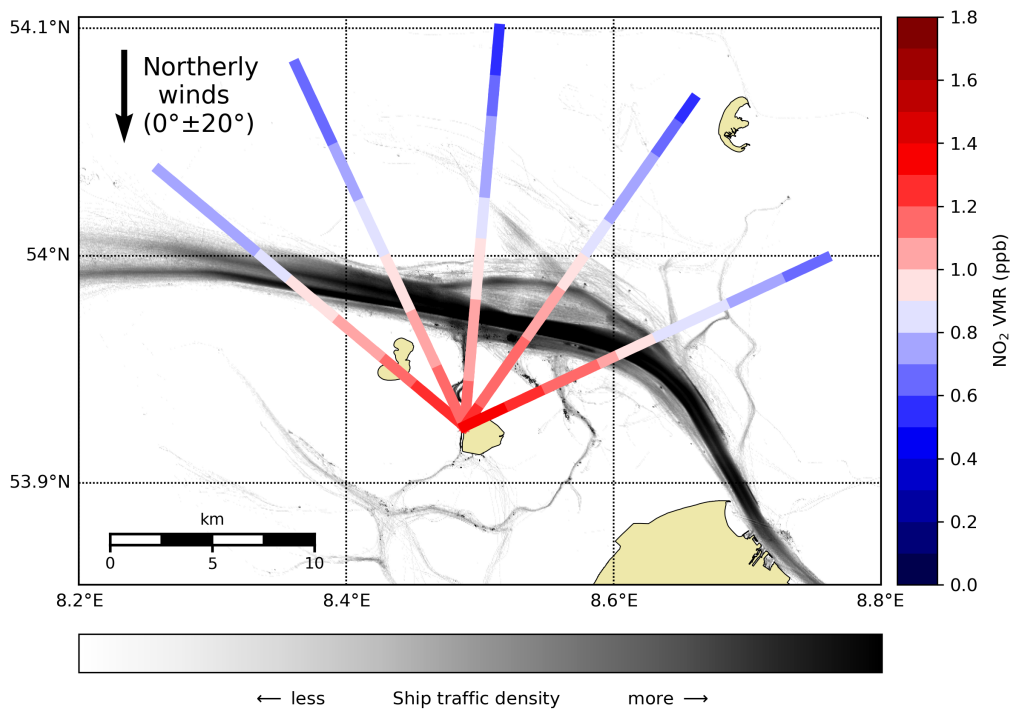


Figure 6.25.: As Fig. 6.24, but for NO₂ in the visible spectral range

6.9 Summary and conclusions

In the first study presented in this thesis, three years of MAX-DOAS observations of NO_2 and SO_2 taken on the island Neuwerk, located in the German Bight close to the main shipping lane into the Elbe river towards the port of Hamburg and the Kiel canal, were analyzed for pollution emitted from ships. Measuring at 0.5° elevation in 5 different azimuth directions, both ambient background pollution and plumes from individual ships could be identified. Using simultaneously retrieved O_4 column amounts as a light path tracer, path averaged volume mixing ratios of NO_2 and SO_2 could be determined. Comparing NO_2 measurements in the UV and visible spectral region, an excellent agreement between mixing ratios determined from the two retrievals especially for ambient background pollution was found, demonstrating consistency in the results. Deviations occurred if ship plumes were measured. The deviations between UV and visible measurements contain information about the spatial distribution of the NO_2 , that are further evaluated in the next chapter.

In a comparison of MAX-DOAS and co-located in-situ observations, high correlation was found between mixing ratios derived with the two measurement techniques on average, although in-situ measurements showed systematically larger values, especially when ship plumes were measured. These deviations can be understood by the difference in measurement volume, the MAX-DOAS averaging over light paths of several kilometers and the in-situ trace gas analyzer measuring the local concentration inside the plume, and a systematic underestimation of MAX-DOAS VMRs introduced due to different profile shapes of the light path tracer O_4 and the pollutants NO_2 and SO_2 . For NO_2 , the difference is larger than for SO_2 , most likely because of titration of NO to NO_2 with ozone after emission and during the transport from the shipping lane (MAX-DOAS measurements) to the measurement site (in-situ instrument).

The measurements on Neuwerk showed, that although the measurement site is within a few kilometers of one of the busiest shipping lanes in the North Sea, it is influenced by land-based air pollution depending on wind direction. Comparing measurements taken while wind was blowing from the shipping lane and from land, systematic differences in the diurnal and weekly evolution of the NO_2 levels were found. While NO_2 in air masses from land shows high values in the morning and evening and lower values around noon and on weekends, NO_2 from sea was found to be nearly constant over time as expected from continuous shipping operations. This effect can be seen in both MAX-DOAS and in-situ observations. Both NO_2 and SO_2 levels are often higher when wind is coming from land, indicating that land-based NO_2 and SO_2 sources contribute significantly to air pollution levels on the island in spite of its relatively remote location and its vicinity to the shipping lanes. Analyzing the wind direction dependence of the NO_2 and SO_2 signals in more detail, and excluding all data with mixed air mass origin, the contribution of shipping sources to

air pollution on Neuwerk could be estimated to be 40 % for NO₂ and 41 % for SO₂ in the years 2013 and 2014. As nearly half of the measurements were taken under conditions with wind coming from directions with mixed origin, this is only a rough estimate but is still a surprisingly small fraction.

Although MAX-DOAS measurements cannot be used to directly determine NO_x or SO₂ emissions from individual ships due to the unknown fraction of the light path probing the plume (a problem, which is addressed in the next chapter with plume modeling), the ratio of SO₂ and NO₂ column-averaged mixing ratios gives a good estimate of a ship's SO₂ to NO_x emission ratio. In the three-year time series of measurements on Neuwerk, more than 2000 individual ship emission plumes were identified in the data and the ratio of SO₂ to NO₂ was computed after subtraction of the ambient background pollution. The results varied between ships but on average yielded values of about 0.3 for the years 2013/2014, a result which is in good agreement with findings from other studies.

Since 1 January 2015, a much lower fuel sulfur content limit of 0.1 % applies in the North and Baltic Sea emission control areas, compared to the 1 % limit that was valid before. As a result, SO₂ levels in the MAX-DOAS measurements were significantly lower for wind from the shipping lanes. In fact, rarely any ship related SO₂ peaks could be found in the data since 2015. Applying the same analysis as for the period before the sulfur regulation change, as expected, no significant changes were found for NO₂ in terms of ratio between ship and land contributions (about 40 % : 60 %). For SO₂ in contrast, overall levels were reduced by two-thirds, and the relative contribution of shipping sources was reduced from 41 % to 14 %, a drastic reduction that is in good agreement with findings from other studies. Even for wind directions coming from land a reduction in SO₂ levels was observed, presumably because shipping emissions also contributed to SO₂ pollution in coastal areas.

In conclusion, long-term MAX-DOAS measurements of NO₂ and SO₂ on Neuwerk demonstrated the feasibility of monitoring pollution originating from ships remotely. It was shown that pollution signals from individual ships can be identified and path averaged mixing ratios can be determined, which on average correlate well with in-situ measurements, reproducing day-to-day trends. MAX-DOAS measurements do not provide emission estimates for individual ships but enable a statistical analysis of signals from thousands of ships at a distance and even under unfavorable wind conditions for in-situ instrumentation. A stricter sulfur limit in shipping fuels led to a large reduction in SO₂/NO_x ratios in the ships' exhausts, and to a significant reduction in SO₂ pollution levels at the German North Sea coast. As expected, the amounts of NO₂ are not impacted by the change in the fuel's sulfur content, implying that combustion temperatures were probably not significantly changed. The overall contribution of ship emissions to air pollution levels at the measurement site is large but land-based pollution sources still dominate, even in the immediate vicinity of shipping lanes.

Studies of the horizontal inhomogeneities in NO₂ concentrations above a shipping lane

This chapter describes a novel application of an “onion peeling” like approach to MAX-DOAS measurements on Neuwerk to estimate two-dimensional pollutant distributions above a shipping lane. First, the method and its application is explained theoretically. A demonstration of its potential follows in selected case studies. For validation purposes, a comparison to airborne imaging DOAS measurements during the NOSE campaign in July 2013 is included.

This chapter is in parts based on Seyler et al. (2019), where most of the presented results have been published.

7.1 “Onion peeling” MAX-DOAS approach

As described in Section 6.2, the λ^{-4} -dependence of Rayleigh scattering causes a wavelength dependence of the effective light path length after the last scattering event. Simultaneous DOAS measurements in the UV and visible spectral range therefore probe different air masses in the atmosphere. For a two channel MAX-DOAS instrument the aforementioned O₄ scaling method (see Section 6.2) delivers both a path length and a path-averaged NO₂ volume mixing ratio for each UV and visible measurement: One VMR for the shorter UV and one for the longer effective horizontal path in the visible spectral range. A third volume mixing ratio can be calculated from the difference of the two DSCDs and path lengths:

$$\text{VMR}_{@\Delta L} = \frac{\text{DSCD}_{\text{vis}} - \text{DSCD}_{\text{UV}}}{(L_{\text{vis}} - L_{\text{UV}}) \cdot n_{\text{air}}} = \frac{\Delta \text{DSCD}}{\Delta L \cdot n_{\text{air}}} \quad \text{with} \quad n_{\text{air}} = \frac{p_{\text{air}} \cdot N_A}{T_{\text{air}} \cdot R}, \quad (7.1)$$

yielding the average volume mixing ratio along the path difference ΔL .

VMR_{UV} , VMR_{vis} and $\text{VMR}_{@\Delta L}$ are not independent, because they originate from only two measurements (UV and vis). However, it is more illustrative and more intuitive to compare

VMR_{UV} and $\text{VMR}_{@ \Delta L}$ on separate horizontal path segments, than VMR_{UV} and VMR_{vis} on overlapping paths.

This enables to probe air masses at different horizontal distances to the instrument. Extending the measurement pattern to multiple azimuth directions makes a range-resolved probing of the horizontal NO_2 distribution possible. The more azimuth directions, the easier it is to recognize why the approach is called “onion peeling” MAX-DOAS: For circular measurements around the instrument (so called azimuthal scans), VMR_{UV} on L_{UV} and $\text{VMR}_{@ \Delta L}$ on ΔL represent two “onion shells” around the instrument location, as can be seen from Figure 7.1. The larger the number of azimuth directions, the better the spatial coverage. But since measurements take a certain time, a large number of different azimuth directions also means a low “refresh” frequency for each individual measurement.

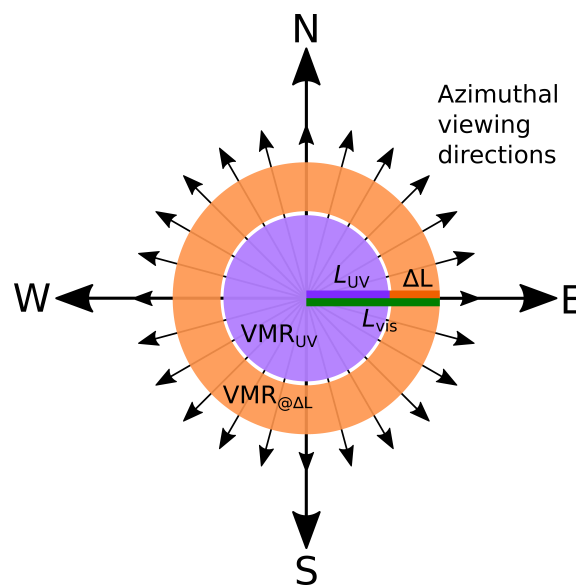


Figure 7.1.: Conceptual sketch of the “onion peeling” MAX-DOAS approach: Circular measurements of VMR_{UV} and $\text{VMR}_{@ \Delta L}$ would form two shells around the instrument. See text for more details.

Ortega et al. (2015) have applied this “onion peeling” like technique to MAX-DOAS measurements before: By applying the approach to circular azimuth scans around the instrument they measured two-dimensional NO_2 fields in Mainz, Germany, during the MAD-CAT campaign¹ in 2013. For the investigation of horizontal NO_2 gradients in a strongly polluted area – the metropolitan region of Mainz, Wiesbaden and Frankfurt (plus airport) – the authors probed a circular area by using 14 azimuthal measurement directions nearly evenly distributed over a 360° view around the instrument. This provides a good spatial resolution and a very large probed area of up to 1960 km^2 (Ortega et al., 2015) but the refresh frequency of one measurement per 7 minutes (or 14 minutes including elevation angle

¹Multi-Axis DOAS Comparison campaign for Aerosols and Trace gases

scans in one direction) (Ortega et al., 2015) in each azimuth direction would be too low for the monitoring of individual ships.

To get a higher refresh frequency or time resolution for the ship emission monitoring, in the present study the measurement pattern was restricted to 5 different azimuth directions distributed nearly evenly over a 120° angle of view. The viewing angles and resulting coverage of the shipping lane close to the island Neuwerk can be seen in the map in Fig. 7.2b, showing typical lengths of the effective horizontal paths as a purple (UV) and green line (visible) as well as the path difference as an orange line.

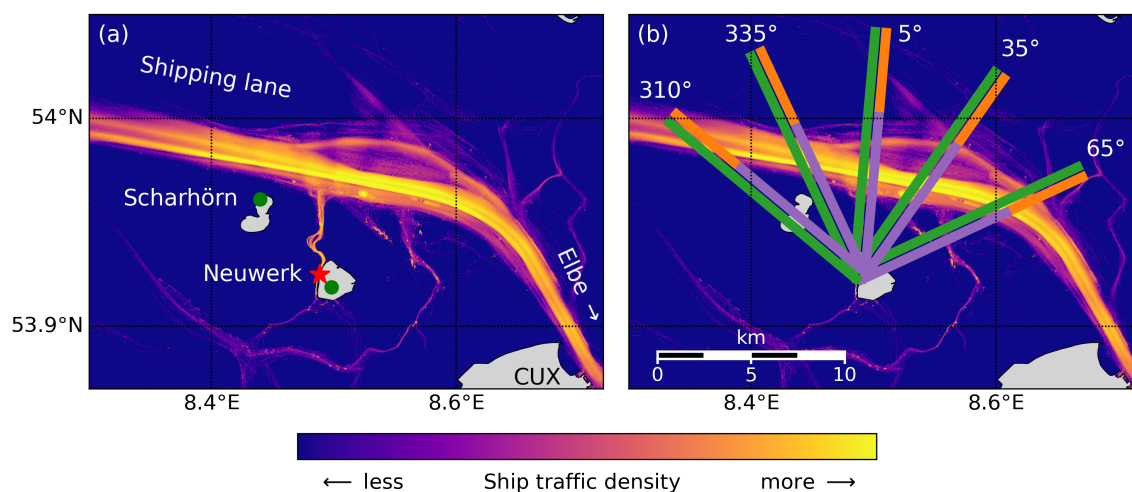


Figure 7.2.: (a) Ship traffic density map calculated from all received AIS messages (2013-2016) showing the main shipping lane from the North sea into the Elbe river close to the measurement site on a radar tower on the island Neuwerk (red star). Wind measurements are available on Neuwerk as well as the neighboring island Scharhörn (green dots). (b) Effective horizontal light paths in UV (purple line) and visible spectral range (green line) for the five azimuthal viewing directions of the MAX-DOAS instrument (310°, 335°, 5°, 35°, 65°, with respect to north), shown for typical light path lengths of 9 km (UV) and 113 km (vis), respectively. The difference between both paths, ΔL , is highlighted by the orange line. (Seyler et al., 2019)

The NO_2 field above and around the shipping lane is expected to be strongly inhomogeneous, as each individual ship is a point source of NO_x emissions, the emitting ships are (usually) moving, and the emitted plumes move with the local wind. As a result, we expect the NO_2 from shipping to not be evenly distributed along the effective horizontal paths.

The horizontal path averaged volume mixing ratios can differ substantially depending on the location of the plume in relation to the shorter UV and longer visible path. Figure 7.3 shows (in the same colors as used before) schematically the plume light path geometry for three common scenarios and illustrates the expected average NO_2 VMR on the different paths.

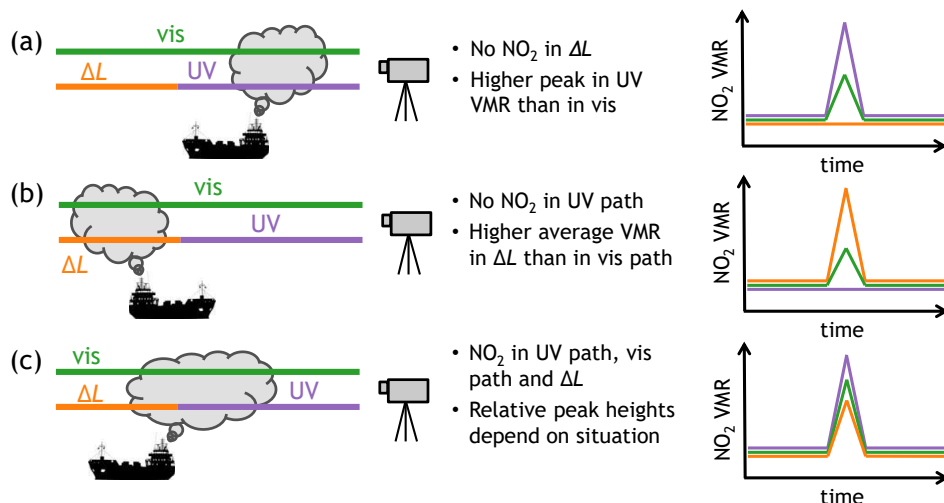


Figure 7.3.: Plume–light–path geometry and the resulting path averaged NO_2 concentrations for three possible cases: When the plume is close to the instrument and completely covered by the UV path (a), when the plume is further away from the instrument than the UV scattering point and is only covered by the visible path and thus, ΔL , (b) and when the plume is located around the UV scattering point (c). (Seyler et al., 2019)

The different scenarios can be categorized by the distance between the ship emission plume and the measurement site (and instrument).

Case a shows a scenario with a plume close to the site. The plume is closer to the instrument than the mean last scattering point in the UV and therefore completely covered by the UV path L_{UV} . As the visible path is longer, it also completely covers the plume. Both paths “contain” the same amount of NO_2 which means that the UV and visible radiation measured by the instrument experience the same NO_2 absorption. If there is no other ambient NO_2 on the paths, the measured differential slant column densities should agree. The retrieved path-averaged VMR, however, is higher for the shorter UV path because the fraction of the radiation path probing the plume has a higher relative contribution. As the plume is closer to the instrument than the mean last UV scattering point the path difference ΔL contains no plume NO_2 . The path-averaged VMR on ΔL is either zero or represents the ambient background level of NO_2 . This kind of situation predominantly occurs for northerly wind directions, as can be seen from Fig. 7.2b. The case study in Section 7.4 shows exemplarily measurement results for such a scenario.

Case b is the somehow “contrary” scenario where a plume is far away from the site. The plume is further away from the site than the mean last scattering point in the UV and therefore only probed by the visible radiation on path L_{vis} . In the UV no NO_2 signal from the ship plume can be seen while in the visible measurements an NO_2 enhancement is

recorded. As ΔL is per definition shorter than the total horizontal path in the visible L_{vis} , the path fraction probing the plume (which is the same for L_{vis} and ΔL) has a higher relative contribution on ΔL and the retrieved path-averaged NO_2 VMR is higher. On Neuwerk, such a scenario predominantly occurs for southerly winds (compare Fig. 7.2b). The case study in Section 7.5 shows exemplarily measurement results for this scenario.

Case c is the more complex intermediate scenario where a plume is close to the mean last scattering point in the UV. In this case, an NO_2 enhancement is measured on all paths, L_{UV} , L_{vis} and ΔL . The relative peak heights for VMR_{UV} , VMR_{vis} and $\text{VMR}_{\Delta L}$ depend on the plume fraction probed by the different horizontal paths and the total paths lengths. Depending on the path lengths, situations like this can occur on Neuwerk for all wind directions but will most likely occur for easterly or westerly winds.

As already discussed in Chapter 6, the measured NO_2 DSCDs and path-averaged VMRs do depend on the angle of intersection between plume and the MAX-DOAS line of sight, which is further investigated in the following, and on the time span between emission and measurement because of NO to NO_2 titration after emission.

7.2 Application to ship emission measurements on Neuwerk

The time series plotted in panel a in Fig. 7.4 shows MAX-DOAS NO_2 DSCDs measured in 0.5° elevation in a viewing direction of 335° azimuth with respect to north (compare Fig. 7.2b) on 26 May 2014. In this plot and the following ones the purple line represents measurements in the UV spectral region, the green line measurements in the visible spectral region and the orange line the difference or delta quantity. In the plotted time series, plumes emitted by ships show up as sharp peaks caused by rapid changes of NO_2 column amounts between consecutive measurements of up to one order of magnitude when the plume moves in and out of the line of sight of the instrument. An ambient NO_2 pollution background, which shows up as the low but non-zero baseline between the peaks, is also visible in the plot. It may be originating from land-based pollution sources but may also contain residual, diluted shipping emissions. The enhancement of the background in the morning might be a result of boundary layer height changes or due to the morning traffic rush hour on land. As explained above, the higher NO_2 DSCDs measured in the visible compared to the UV are mainly due to the longer horizontal path through the boundary layer. The difference column $\Delta\text{DSCD} = \text{DSCD}_{\text{vis}} - \text{DSCD}_{\text{UV}}$ shows peaks coinciding with some in the UV and visible signal, but not all. The strong enhancement at 12:50 UTC for example does not show up in the ΔDSCD , indicating that the plume is closer to the instrument than the mean last scattering point in the UV.

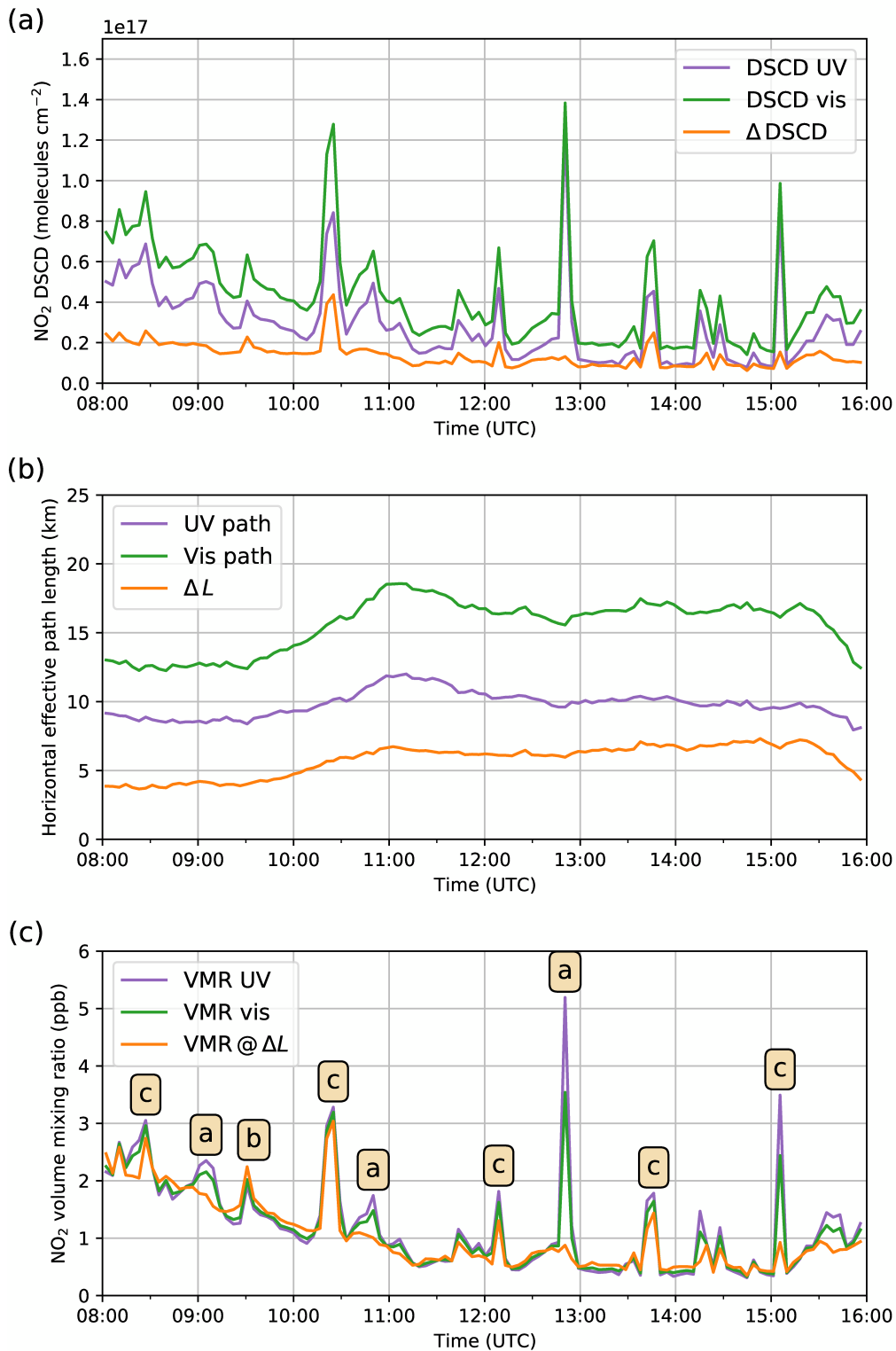


Figure 7.4.: Differential slant column densities of NO₂ (a), horizontal effective path lengths (b) and horizontal path averaged volume mixing ratios of NO₂ (c) on 26 May 2014 in 0.5° elevation and 335° azimuth for the UV (purple) and visible spectral range (green) and their difference (orange) (a & b). In panel c the orange line denotes not the VMR difference but the average VMR along the path difference ΔL . The yellow labels over the peaks in panel c indicate which scenario from Fig. 7.3 is resembled in each case. (Seyler et al., 2019)

The time series of horizontal path lengths derived via Eq. (6.3) (see page 89) from the O₄ DSCDs measured simultaneously to the NO₂ DSCDs are shown in panel b of Fig. 7.4, again in purple for UV, green for visible and orange for the difference. The fact that the horizontal path lengths are almost constant over time reveals that this was a clear sky day. A day with scattered or broken clouds will show a strong variation in path lengths² already between consecutive measurements. Having clouds in either off-axis or reference measurement or both or neither, makes the interpretation of results much more difficult. The time series shows typical values for the effective horizontal path lengths at this site with ~15 km (13 to 18 km) in the visible range, ~10 km (8 to 12 km) in the UV and ~5 km (4 to 6 km) for the difference.

Combining the O₄ scaling (Eq. (6.5) on page 89) and onion peeling MAX-DOAS approach (Eq. (7.1) on page 123), path-averaged NO₂ VMRs can be retrieved from the DSCDs in panel a and path lengths in panel b of Fig. 7.4. The resulting time series is shown in panel c of the same figure in the same colors as before. The orange line in this case is not the difference of the UV and visible VMR, but the average VMR along the path difference ΔL (see Eq. (7.1), page 123).

The baselines of the three curves agree very well, indicating that the ambient NO₂ pollution is well-mixed in the lower boundary layer and dispersed homogeneously along all the horizontal path sections. The relative heights of the sharp peaks caused by the measured ship plumes vary widely, indicating that the NO₂ field created by the emitted plumes is inhomogeneous as expected. The strong peak at 12:50 UTC already mentioned above is an example for scenario (a) in Fig. 7.3 with a ship plume located close to the site and will be further investigated in Section 7.4 below.

7.3 Plume modeling

For the interpretation of MAX-DOAS measurements of ship emission plumes it is important to know the location and orientation of the plumes in respect to the light path as well as the spatial dimensions.

Plume modeling is used to estimate the spatial extent of the pollution plumes emitted by the ships and their movement and evolution with time. The plume modeling method applied here is a combination of simple forward trajectories with a simple Gaussian plume model. In this section, first the modeling technique is explained, later a validity check

²Clouds can decrease or increase the light path length and O₄ absorption by multiple scattering. This depends on the cloud's position in relation to the line of sight and the cloud's optical properties, especially its optical thickness (Wagner et al., 2014).

of the modeled plumes is performed using airborne imaging DOAS measurements for comparison.

7.3.1 Plume forward trajectories

The plume trajectories used here are simple forward trajectories for the plume air parcels emitted from the ships. For the calculation, ship position data from the ships' AIS signal (see Section 6.1.5) is needed as well as wind data, namely wind speed and direction, in a reasonably high time resolution. Wind data from weather models with typical time resolutions of one value every few hours (often every six hours) is not sufficient considering the relatively small spatial scale used here and the high time resolution that is needed to model the plumes of individual ships. For the measurements on Neuwerk, wind data from the weather stations on Neuwerk and Scharhörn, operated by the HPA (Hamburg port authority), is used, which has a time resolution of 10 min. As the AIS messages of the different ships are broadcasted with a highly irregular frequency, the AIS ship position data is interpolated on a 10 s time grid, which is also used for the plume trajectory calculations.

For the computation of the trajectories, the ship plumes are treated as point shaped plume air parcels. Each time step on the 10 s–time grid each plume air parcel is moved from its old position to a new projected position calculated from wind speed and direction. Each time step each ship as a point source emits a new plume air parcel at its current position. Thus, a chainline-like string of plume air parcels is created. To also account for old, residual plumes of ships that already left the area of interest before the investigated time period, an initialization phase of three hours is included.

7.3.2 Gaussian plume model

A simple model for plume broadening and dispersion over time is the Gaussian plume model (Gifford, 1961; Pasquill, 1961; Sutton, 1932, 1953), which is often used to model emissions from point sources like power plants. The Gaussian plume model describes the increasing lateral and vertical dispersion of a plume with growing distance from the emission source with two Gaussian curves, assuming normal distribution of the plume material. For simplicity reasons, wind speed is assumed to be constant with height (Pasquill, 1961). The Gaussian plume model links the pollutant concentration C at the point (x, y, z) to the emission rate Q , the mean wind speed U (in x -direction) and the horizontal and vertical dispersion coefficients σ_y and σ_z :

$$C(x, y, z) = \frac{Q}{2\pi U \sigma_y \sigma_z} \exp\left(\frac{-y^2}{2\sigma_y^2}\right) \left[\exp\left(\frac{-(z-H)^2}{2\sigma_z^2}\right) + \exp\left(\frac{-(z+H)^2}{2\sigma_z^2}\right) \right], \quad (7.2)$$

where the vertical coordinate z is corrected for the effective stack height H , which is the sum of the actual stack height and the initial plume rise. H is equivalent to the effective height of the plume center line, as can be seen from Fig. 7.5. The second term in the square brackets is a mirror image source placed below ground level to take into account the effect of the ground as an assumed perfect reflector (Sutton, 1953).

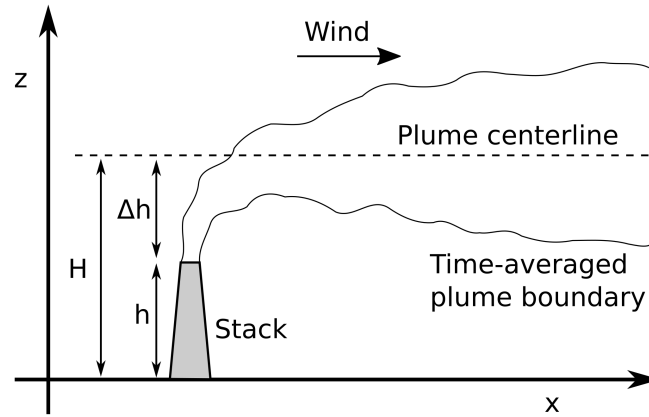


Figure 7.5.: Plume dispersion definition sketch with effective stack height H , the sum of the actual stack height h and initial plume rise Δh

The degree of dispersion is controlled by the lateral and vertical dispersion coefficients σ_y and σ_z , the standard deviations of the normal distributions in y and z direction, and depends on the atmospheric conditions, which can be stable, neutral or unstable. Table 7.1 shows a simple classification scheme for atmospheric stability based on solar insolation and wind speed defining six classes ranging from very unstable (A) to stable (F) (Pasquill, 1961). An often used estimation for σ_y and σ_z as a function of the downwind distance x are the empirical functions reported by Martin (1976):

$$\sigma_y(x) = a \cdot x^{0.894} \quad (7.3)$$

and

$$\sigma_z(x) = c \cdot x^d + f. \quad (7.4)$$

Note that σ_y and σ_z have units of meters whereas the downwind distance from the emission source x is input in kilometers. Values for the stability-dependent constants a , c , d , and f are listed in Table 7.2, with different values for $x \leq 1$ km and $x > 1$ km (Martin, 1976).

Fig. 7.6 shows the model results for a large cargo ship's typical effective stack height of 50 m (40 to 45 m stack height plus 5 to 10 m initial plume rise). The wind is set to blow along the x -axis and atmospheric conditions are set to be neutral (stability class D). As can be seen in the figure, a pollutant plume is formed downwind of the emission source. A

Table 7.1.: Atmospheric stability classification scheme (Pasquill, 1961; Turner, 1970) based on surface wind speed and solar insolation: A...very unstable, B...moderately unstable, C...slightly unstable, D...neutral. The additional stability classes E...slightly stable and F...stable (not shown here) occur only at night. For intermediate classes like A–B take average of stability parameters for A and B (see Table 7.2).

Wind speed (10 m AGL) in m/s	Solar insolation		
	Strong	Moderate	Slight
< 2	A	A–B	B
2–3	A–B	B	C
3–5	B	B–C	C
5–6	C	C–D	D
> 6	C	D	D

Table 7.2.: Empirical stability parameters for the computation of the horizontal and vertical dispersion coefficients σ_y and σ_z (Martin, 1976) for the different atmospheric stability classes according to Pasquill (1961). For intermediate stability classes like A–B, take average of parameter values for A and B.

Stability class	Description	a	$x \leq 1$ km			$x > 1$ km		
			c	d	f	c	d	f
A	Very unstable	213	440.8	1.941	9.27	459.7	2.094	–9.6
B	Moderately unstable	156	106.6	1.149	3.3	108.2	1.098	2.0
C	Slightly unstable	104	61.0	0.911	0	61.0	0.911	0
D	Neutral	68	33.2	0.725	–1.7	44.5	0.516	–13.0
E	Slightly stable	50.5	22.8	0.678	–1.3	55.4	0.305	–34.0
F	Stable	34	14.35	0.740	–0.35	62.6	0.180	–48.6

short distance (a few hundred meters) away from the emission source the plume hits the ground, leading to enhanced surface pollutant concentrations.

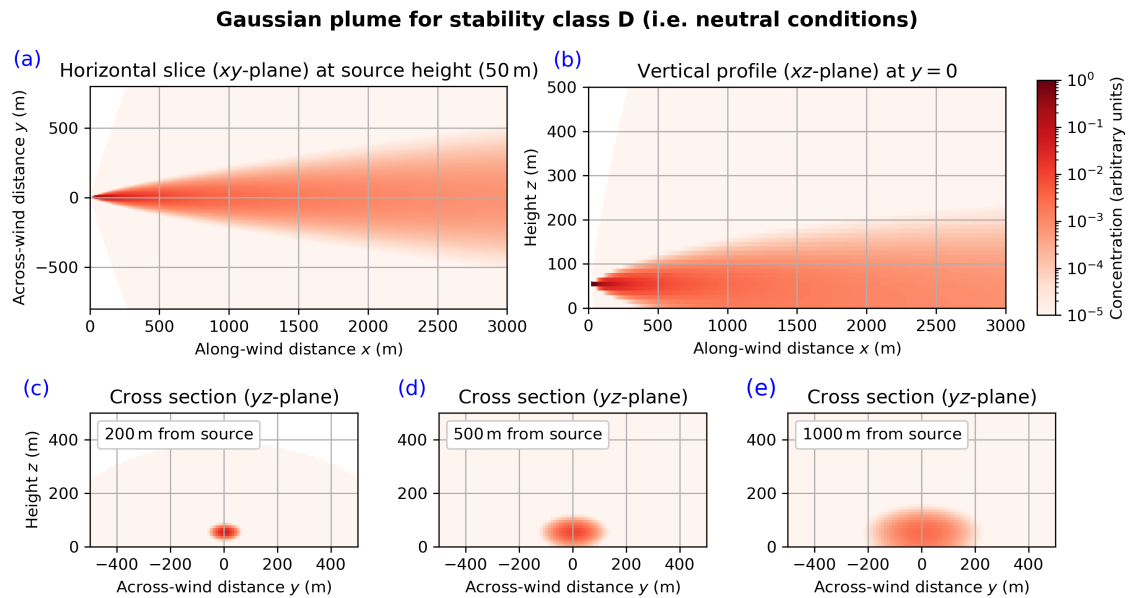


Figure 7.6.: Spread and dispersion of plume pollutant concentrations modeled with a simple Gaussian plume model for a pollutant source in 50 m height under neutral conditions (stability class D). The pollutant emission source is located at $(x = 0, y = 0, z = 50 \text{ m})$, the wind blows along the x -axis. Panel (a) shows the dispersion of the plume in the horizontal axis, panel (b) shows the vertical spread and panels (c), (d) and (e) show plume cross sections in 200 m, 500 m and 1000 m distance from the emission source.

In Fig. 7.7 and 7.8, similar model results are shown for more unstable atmospheric conditions: Fig. 7.7 shows the pollutant plume under slightly unstable atmospheric conditions (stability class C), Fig. 7.8 under moderately unstable conditions (stability class B). In comparison to Fig. 7.6, the modeling results under more unstable conditions show stronger plume dispersion and more spreading, as expected.

The plumes retrieved from the Gaussian plume model are very smooth, while real plumes, depending on conditions, can be much more irregular. Figure 7.9 shows some example photographs of real plumes for comparison. The flow pattern of a real plume is usually not laminar but governed by turbulence. The random turbulent flow creates eddies of all sizes, the flow pattern is constantly changing and there are irregularities everywhere (Warhaft, 1997). These photographs of plumes are snapshots in time. The Gaussian plume model, however, describes a time-averaged plume. Hence, an individual snap shot of a plume will in general not look like a smooth Gaussian plume, but if several snapshots are averaged over a longer time period, the resulting average flow will be much smoother and should more and more approach the typical Gaussian plume shape. The application of the Gaussian plume model to real emission sources on short time scales can therefore only be

Gaussian plume for stability class C (i.e. slightly unstable conditions)

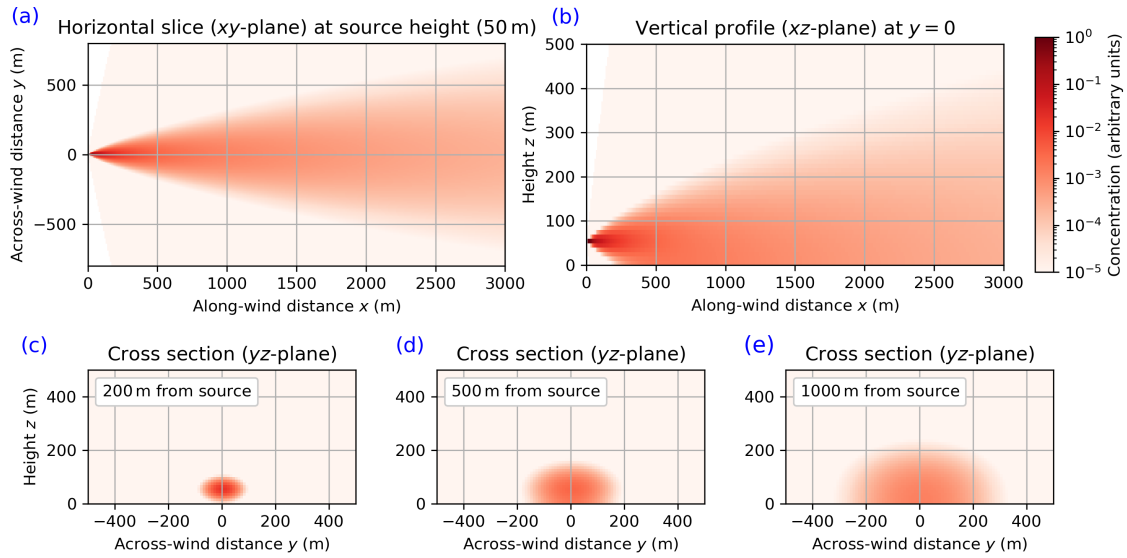


Figure 7.7.: As Fig. 7.6 but assuming slightly unstable conditions (stability class C)

Gaussian plume for stability class B (i.e. moderately unstable conditions)

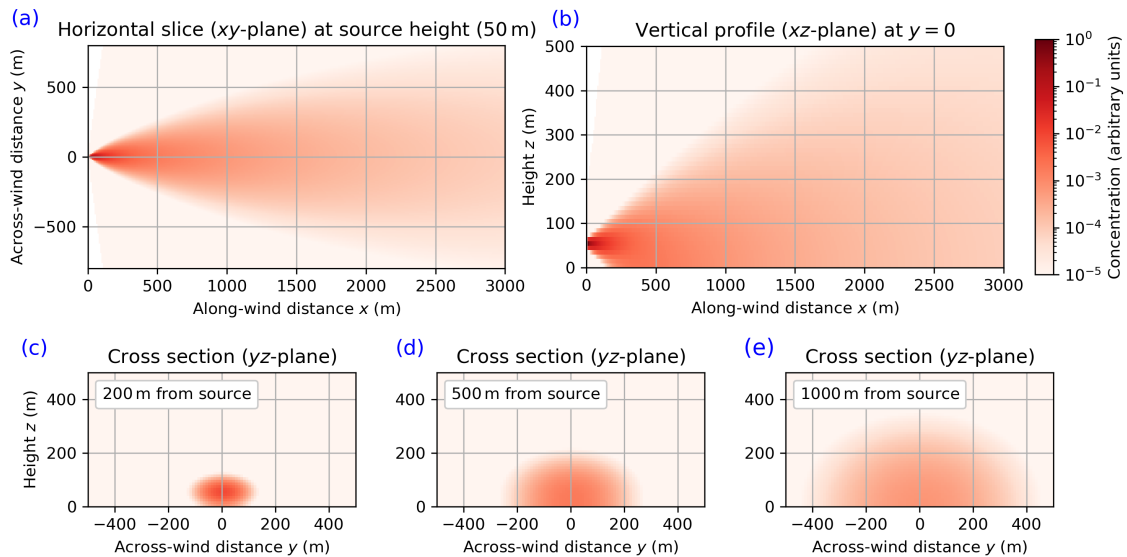


Figure 7.8.: As Fig. 7.6 but assuming moderately unstable conditions (stability class B)

an approximation. However, it is the best we have, as exact modeling of the turbulent flow is, due to its very chaotic behavior, not possible.



(a) A smoke plume from the Dunbar Cement Works chimney (Scotland), - © Walter Baxter, CC BY-SA 2.0, <https://www.geograph.org.uk/p/3220320> (b) A smoke plume from the Dunbar Cement Works chimney (Scotland), - © Walter Baxter, CC BY-SA 2.0, <https://www.geograph.org.uk/p/3765299>



(c) Smoke plumes from the chimneys of a power plant in Helsinki, Finland, photograph by Pöllö, CC BY 3.0, <https://commons.wikimedia.org/w/index.php?curid=9475382> (d) Hazelwood Power Station (Australia), photograph by Mriya, distributed under a CC BY-SA 4.0 licence, <https://commons.wikimedia.org/w/index.php?curid=57513119>

Figure 7.9.: Photographs of real plumes

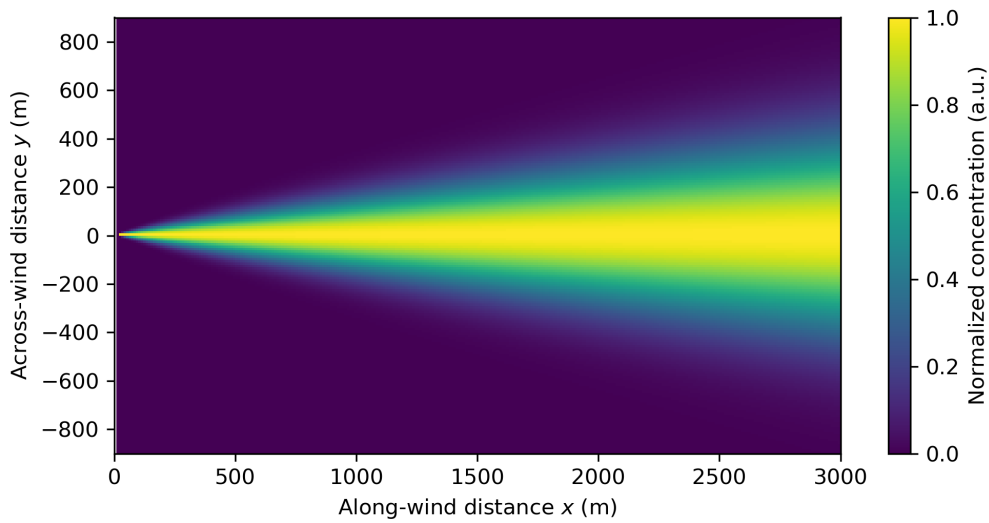
7.3.3 Merging plume forward trajectories and Gaussian plume model

If not anchoring (e.g., in the roadstead) or being moored in a harbor, ships are in general moving point source emitters. Thus, the course of the ships' plumes is not only governed by

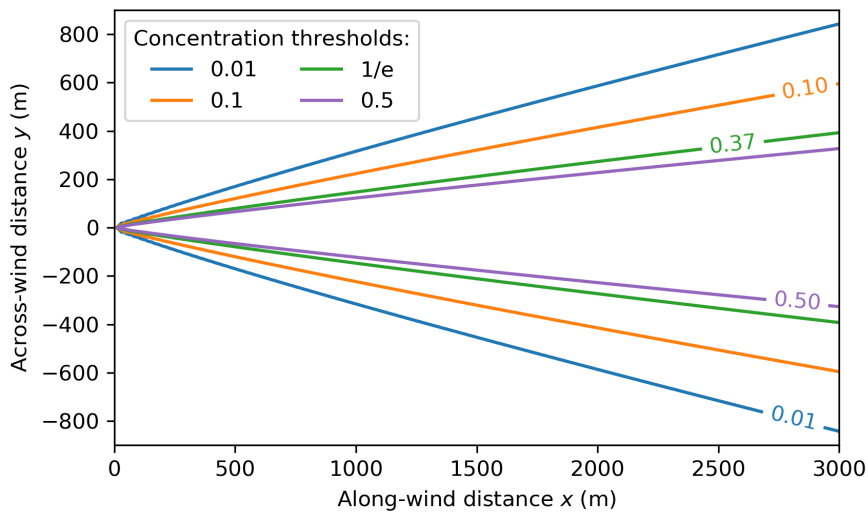
the wind direction, but also depends on the pathway on which the ship has sailed before. As the ship moves with a specific speed and direction, it creates an apparent wind (Berg et al., 2012). Running the Gaussian plume model for each ship position at each time step on the aforementioned time grid (see Section 7.3.1) is therefore not sufficient. Depending on the wind direction and the relative movement direction and path of the ship, the plume is deformed and elongated or clinched, compared to the plume of a stationary source. As each of the aforementioned plume air parcels is emitted by the ship at a different location, the Gaussian plume model has to be combined with the plume forward trajectories (see Section 7.3.1). This is accomplished by running the Gaussian plume model for the atmospheric stability class chosen for the prevailing weather conditions during the investigated time period and by building look-up-tables (LUTs) for the horizontal (lateral) and vertical plume extent as a function of the downwind distance from the point of emission. For each individual plume air parcel in the forward trajectory, the LUT is evaluated at precisely the accumulated distance it traveled since its emission to gain the modeled plume width (or height) at this location.

For the creation of the look-up-tables the Gaussian plume model is run on a 10 by 10 meter grid. At each downwind distance value in 10 m steps along the grid (in x -direction), all lateral distances (y -direction, across-wind) from the plume centerline are checked for the distance, in which the concentration drops below a threshold level (here: $1/e$) relative to the maximum concentration on the plume centerline at this respective downwind (x) distance. This is equivalent to a normalization along the lateral direction for each downwind distance slice (in 10 m steps) separately. Figure 7.10 shows a modeled plume with such a normalization, in contrast to Fig. 7.6 to 7.8.

As, through this normalization, only the relative concentration difference to the respective maximum concentration at the plume centerline plays a role, the multiplicative factors emission rate Q and wind speed U in the Gaussian plume model equation (7.2) become irrelevant for the computation of the LUTs, although the wind speed is taken into account for the calculation of the plume forward trajectories. For the lateral extent of the plume, i.e., the plume width, the thus obtained LUT can be applied to all ships regardless of size. For the vertical plume extent, however, the LUT depends on the effective stack height and therefore on the size (height) of the ship's stack. This means that, for each individual ship a separate LUT for the plume height has to be computed, as stack heights differ from ship to ship. Unfortunately, neither ship height nor stack height is contained in the received AIS data stream broadcasted by the ships, which means that the stack height has to be researched individually for each ship. Since there is no database of ship stack heights, in this study, the stack height was estimated from photographs of the ship taking the known standardized height of the loaded containers on the pictures as a height measure.



(a) Concentration map (normalized concentration)



(b) Contour lines for concentration thresholds

Figure 7.10.: Modeled Gaussian plume with normalization along the lateral direction (y) for each downwind distance (x , in 10 m steps) relative to the maximum concentration on the plume centerline at this respective downwind distance. The model was run for stability class C representing slightly unstable atmospheric conditions.

For aerial overview maps, as are shown in the following, the vertical plume extent is irrelevant for the visual representation in the maps. Nevertheless, for a detailed analysis of an individual plume of a selected ship at a specific point in time, as shown later on, the described procedure for manually determining the ship's stack height is necessary and feasible.

For the derivation of in plume NO_2 VMRs from MAX-DOAS and airborne imaging DOAS measurements it is sufficient to know the horizontal and vertical plume extent, while the fact that the unknown source emission rate is not modeled is irrelevant.

Sources of uncertainty are the approximation of the real ship plumes with a Gaussian plume model as discussed above and the neglect of plume chemistry like NO to NO_2 titration, NO_2 loss reactions, and NO_2 lifetime effects in general.

7.3.4 Validity check with airborne imaging DOAS measurements

Airborne imaging DOAS measurements can deliver spatially highly resolved NO_2 maps, which are well suited for the validation of the plume modeling approach. In the aerial view from the airplane, the NO_2 which is contained in the ship plumes, shows up as distinctive NO_2 enhancements in the data, making it possible to identify the position and course of the plumes, as well as their horizontal dimensions. Such airborne measurements have been performed with the AirMAP instrument in the vicinity of the Neuwerk site during the NOSE campaign (Meier, 2018) on 21 August 2013 aiming for a cross-comparison to the MAX-DOAS measurements on the radar tower. Further information on the AirMAP instrument, the NOSE campaign and the comparison to the MAX-DOAS measurements can be found in Section 7.6.2 below.

Figure 7.11 shows ships and modeled ship plumes on the main shipping lane in the north of Neuwerk as well as an AirMAP NO_2 vertical column density map measured on one flight track crossing the region from south to north on 21 August 2013 at 9:34 UTC (11:34 local time). The ship and plume positions are shown for 9:34:20 UTC (11:34:20 LT), the airplane position at this time is marked close to the flight track. The Gaussian plume model was run for stability class C, representing slightly unstable conditions, which was selected due to the weak to moderate insolation at that time (the day was cloudy in the morning, later clearing up) and relatively low wind speeds between 3 and 4 meters per second (for the stability classification scheme according to Martin (1976) see Table 7.2).

As can be seen from the figure, the ship plumes have a curved shape due to the combination of ship movement and wind. At this time, the airplane was located between the plume of the 277 m ship in the center of the figure and three other plumes further north, which originate from ships which have already moved out of the area shown in the map to the

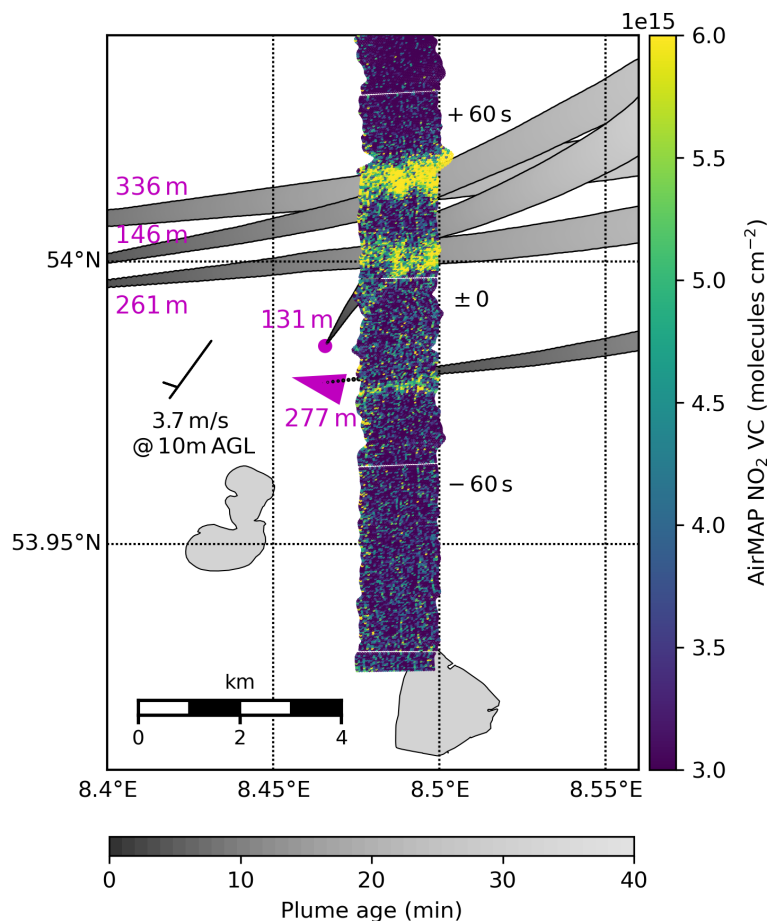


Figure 7.11.: Map showing ships and modeled ship plumes on the shipping lane in the north of Neuwerk on 21 August 2013 at 9:34:20 UTC (11:34:20 local time), in comparison with air-borne imaging DOAS measurements from the AirMAP instrument. Magenta triangles show the current ship positions and course (tip), magenta numbers denote the ship length. The modeled ship plumes are shown as gray stripes, the lightness of the gray shading representing the plume age. The flight track of the airplane and the AirMAP vertical column measurements of NO₂ are shown as a broad, color-coded image stripe. The airplane crossed the scene from south to north. The numbers close to the flight track denote the current position of the airplane (±0) at 9:34:20 UTC as well as the position one minute before (-60 s) and one minute later (+60 s). Wind direction and speed (measured on Scharhörn) is shown with a meteorological wind barb.

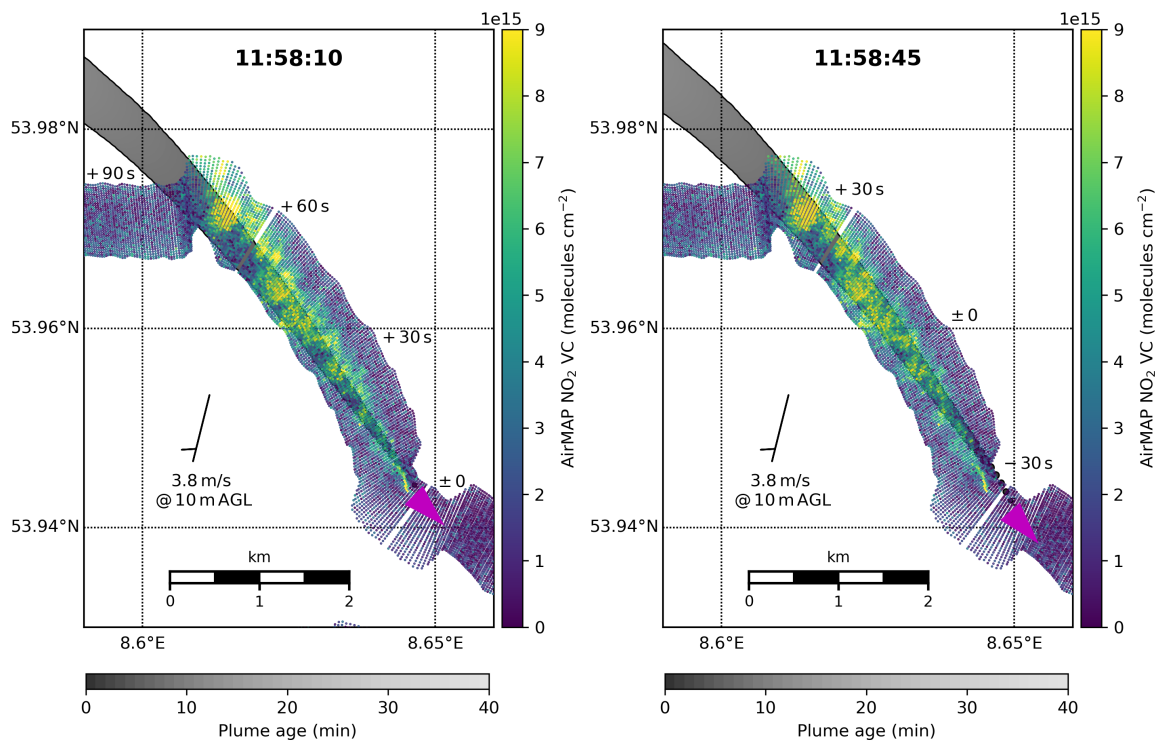
west. The AirMAP measurements show strong NO₂ enhancements crossing the flight track. As there are no other NO₂ sources around that could lead to such spatially confined NO₂ signals, this can only be ship plumes. The positions and shapes of the NO₂ enhancements agree quite well with the projected plume positions from the plume forward trajectories.

There is sometimes a small shift visible between the modeled plumes and the plume positions measured by AirMAP. The southernmost plume, for example, originating from the ship in the center of the map, is predicted to be further north than in the AirMAP measurements. Sources for such discrepancies can be the time shift between modeled plume position and AirMAP overpass – the AirMAP measurements were taken approximately 30 seconds earlier – in which the wind blows the plume further northward so that the position does not fully coincide with the modeled plume trajectory (a visualization problem), but the unknown location of the exhaust stack on the ship might also play a role. For the plume modeling, it is assumed that the stack is located at the center of the ship on the ship's position, which in reality is not the case for most ships, which have the bridge either in the rear part of the ship or in the front part, depending on the ship type.

A similar shift between modeled plume position and AirMAP measurements can be seen for the northernmost plumes of the 336 m-ship and the 146 m-ship, but in the opposite direction. In this case, the plume position is expected further south than the AirMAP measurements indicate. Again, there is a time shift, the AirMAP measurements at this location have been taken 45 seconds later than the scene shown here. In this time, the wind will have blown the plumes further northward.

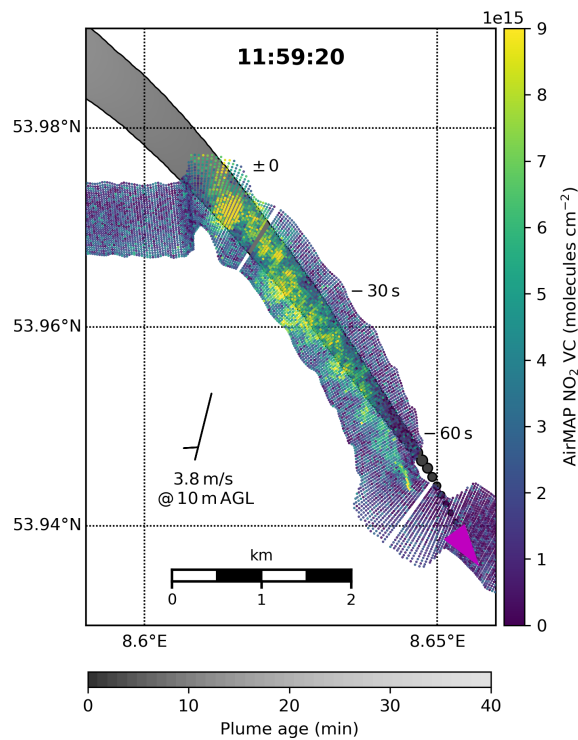
Inspecting the AirMAP measurements of the northernmost plume in detail already reveals that the real plumes do not have such a smooth shape as the modeled plumes, instead it shows turbulent flow induced irregularities and fluctuations. This is even better visible in the next example in Fig. 7.12, discussed below. Such a deviation between model and reality is expected, as the Gaussian plume model assumes a steady state and describes only a long time averaged plume, as discussed in Section 7.3.3 above. Nevertheless, the plume width from the model agrees quite well with the AirMAP measurements.

Similar conclusions can be drawn from the second example in Fig. 7.12, showing a scene on the same day, nearly two and a half hours later around 11:58 UTC (13:58 LT), where a single ship and its plume were targeted (Meier, 2018). In this scene, the airplane overpassed the ship, followed the plume and mapped the plume downwind of the ship for nearly 4 km. This flight track was performed at a lower flight level of 0.9 km (compared to 1.5 to 1.6 km before) (Meier, 2018) giving an even better ground resolution. The figure consists of three panels presenting ship and plume positions at three times during the overflight, each separated by 35 seconds.



(a) 11:58:10 UTC (13:58:10 LT)

(b) 35 seconds later



(c) 70 seconds later

Figure 7.12.: As in Fig. 7.11: Maps showing ships and modeled ship plumes on the shipping lane in the north of Neuwerk on 21 August 2013 around 11:58 UTC (13:58 local time), in comparison with AirMAP airborne imaging DOAS NO_2 VCD measurements.

At that time, the insolation was already much stronger, so the more unstable stability class B–C was chosen for the plume modeling in this scene.

In the first panel a the airplane is located over the ship. As expected, the modeled plume fits very well to the AirMAP measurements which are close in time (close to the ship and up to around one third of the observed plume) but not so well to the AirMAP measurements which have been taken one minute later, at the end of the observed plume.

In the next panel, 35 seconds later, the ship sailed further to the south east and the model projects that the plume was moved further north by the wind. At this snapshot, the measurements in the middle of the plume, where the airplane is located, fit quite well to the modeled plume.

In the last panel, the airplane has moved further along the plume, the ship has sailed further to the south east and the plume was blown further north. Here, the AirMAP measurements at the end of the observed plume fit very well to the model, while the measurements taken one minute earlier further to the south east show a clear discrepancy to the current modeled plume state, again expected due to the time difference.

This example shows even better the irregularities and random fluctuations in the plume flow due to turbulence, which cannot be represented by the model.

The comparison to the airborne imaging DOAS measurements confirms that simple forward trajectories are well suited to project and track the ship plume positions with sufficient accuracy and that the Gaussian plume model gives a reasonable estimation of the plume width.

In the next sections, the presented plume modeling approach will be used to investigate ground-based MAX-DOAS and in-situ trace gas measurements on Neuwerk in two case studies, one with northerly winds and one with southerly winds, resembling the two main scenarios from Fig. 7.3.

7.4 Northerly wind scenario

Under northerly wind conditions the exhaust plumes emitted by the passing ships are blown southwards towards the island and measurement site, as can be seen from the map in Fig. 7.2. This should result in enhanced NO_2 concentrations south of the shipping lane and lower concentrations in the north of it, as the plumes are blown the other way. As there are neither other important shipping lanes in the proximity in the north nor land sources, NO_2 values are expected to be low in the region north of the main shipping lane. Especially

for the viewing directions towards the north, the situation should resemble scenario a in Fig. 7.3.

To further investigate the strong NO₂ signal from Fig. 7.4 in Section 7.2, a 12 minute sequence of 15 consecutive MAX-DOAS measurements on 26 May 2014, starting at 12:46 UTC (14:46 local time), are plotted in the 15 maps in Fig. 7.13. Each map shows for one two-channel MAX-DOAS measurement (UV & visible spectral range) the location and length of the horizontal paths L_{UV} and ΔL as colored lines, with color representing the path averaged NO₂ mixing ratios VMR_{UV} and $VMR_{\Delta L}$. The colored dot at the location of the measurement site shows the on-site in-situ NO₂ measurements (instrument specification see Section 6.1.4), again with color representing the measured NO₂ VMR. Also shown are the positions and course of the ships (>50 m), obtained from the received AIS signal (see Section 6.1.5), the modeled plumes (see Section 7.3), and wind direction and wind speed measured by the weather station on Neuwerk. For the Gaussian plume modeling, the stability class C representing slightly unstable conditions has been selected based on the prevailing wind speeds and the strong solar insolation on this clear sky day.

In the situation shown in the map sequence, two larger ships are under way on the main shipping lane in opposite directions. The sequence starts at 12:46 UTC (14:46 local time), shortly after the two vessels passed each other. The larger ship (351 m length) moves westward towards the open North Sea. The smaller ship (151 m length) moves eastward into the river Elbe. Another small ship close to the port of Cuxhaven, to which the AIS contact is lost after the first picture, and the residual plumes further away from the site play no important role for the interpretation of the measurements and can be considered as irrelevant. The fact that the projected plume trajectories of the two larger ships have a very different shape is due to the opposite movement directions of the ships and the curved shape of the main shipping lane around the island Neuwerk (see Fig. 7.2).

Panel 1 shows the MAX-DOAS measurements at 12:46:24 UTC in the 335° azimuth viewing angle (towards NNW). The similar dark blue colors of the lines representing the paths L_{UV} and ΔL show that the path averaged NO₂ VMRs are very low (<1 ppb) and agree very well on the two path segments. The dot representing the on-site in-situ measurements has a similar color as well, showing that in-situ VMR and MAX-DOAS path averaged VMR agree well in this situation. This indicates that the ambient NO₂ background is spatially well-mixed in the boundary layer. The fact that the plume of the smaller ship, although crossing the line of sight of the MAX-DOAS in the map, shows up only slightly in the measurements might be due to low emissions from this comparatively small ship and dilution of the, at this point, already strongly dispersed plume for which the plume model predicts a vertical extent of ~400 m and a plume width of 1200 to 1300 m at this plume age of 700-800 seconds.

Panels 2 to 4 show the following measurements in 5° (N), 35° (NNE) and 65° (ENE) azimuth direction. All three maps show enhanced NO₂ VMRs up to 4 ppb along L_{UV} , close to the instrument and low NO₂ VMRs further away along ΔL . The observed enhancement close to the site is most likely due to the plume of the larger ship, which is located between the site and the mean last scattering point in the UV. From panel 2 to 4 the plume moves closer to the radar tower but has not reached it yet, therefore in-situ measured NO₂ VMRs stay low.

Panel 5 shows the next MAX-DOAS measurements towards 310° azimuth angle. The scenario is similar to panel 1. After panel 5 the azimuthal measurement pattern repeats itself.

Panels 6 to 10 show the next measurement cycle during which the plume approaches the measurement site and in-situ NO₂ values start to rise. MAX-DOAS NO₂ VMRs are still high close to the site and low in the north of the shipping lane (ambient background pollution). As can be seen from the figure, the magnitude of the MAX-DOAS path averaged VMR depends on the angle of intersection between plume and LOS of the instrument. The highest value of ~5 ppb is measured alongside the plume (panel 6) and much lower values when measuring orthogonal to it (e.g. panel 8). This high value measured at 12:50:35 UTC is the strong peak highlighted in Section 7.2.

From panel 9 on, the in-situ measurements rise even higher, exceeding 5 ppb, which, as the color scale, which extends up to 5 ppb, is saturated, is not represented in the figure. In panel 9 the measured in-situ NO₂ VMR increases to 6.1 ppb, in panel 10 and 11 it tops at 8.3 ppb and 8.9 ppb, respectively. In panel 12 the measured in-situ VMR drops to 6.3 ppb but afterwards another increase is measured caused by the second plume, where measured values reach 6.6 ppb, 6.8 ppb and 7.1 ppb through panels 13 to 15. After panel 15, the in-situ NO₂ VMR increases further to 8.8 ppb and after that decreases again to ambient background concentration levels. This pattern is a clear indication that the in-situ instrument measured two partly overlapping plumes, like it was projected from the plume modeling.

Compared to the MAX-DOAS measurements, the maximum level of the in-situ NO₂ VMRs is much higher. This discrepancy originates from the different measurement geometries: The in-situ instrument measures directly the local NO₂ VMR inside the plume while the MAX-DOAS delivers path-averaged values (averaged over several kilometers). Unless the plume fills the total horizontal effective path, a very rare case in reality, this leads to a systematic underestimation of the local VMR inside the plume.

That in this situation at least part of the plume was at some point located above the MAX-DOAS instrument is indicated by a small NO₂ enhancement in the zenith sky SCD measurements of 4×10^{15} molec cm⁻², which has been seen earlier in the MAX-DOAS than

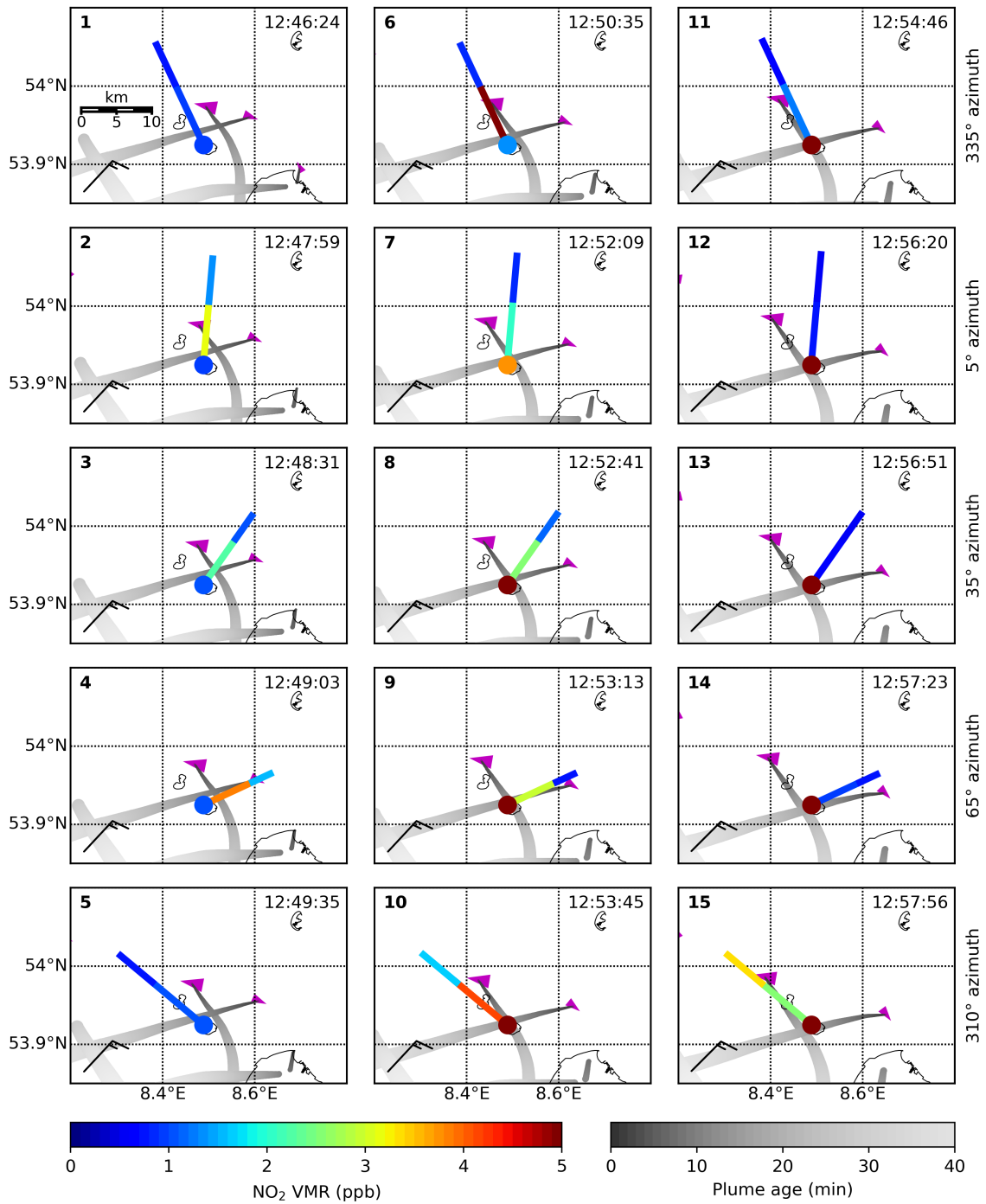


Figure 7.13.: Sequence of maps showing 15 consecutive measurements in 0.5° elevation on 26 May 2014, starting at 12:46 UTC (14:46 local time): The extent of the horizontal paths L_{UV} and ΔL and corresponding path averaged NO_2 VMRs are shown as colored lines. In-situ NO_2 VMRs are shown as a colored dot at the location of the measurement site. Magenta triangles show the ship position and course (sharp tip), with larger triangles for larger ships. Grey point clouds show forward trajectories of the emission plumes calculated from wind speed and direction for the moving ship. Wind direction and speed is shown with meteorological wind barbs. The reading direction is column-wise from top to bottom, the respective azimuth viewing angle is noted in the right margin. (Seyler et al., 2019)

in the in-situ measurements, around 12:50 UTC, which is gone at 12:55 UTC. As the zenith sky SCDs are used as a sequential reference for the off-axis ship plume measurements, this causes a small canceling effect on the resulting DSCDs. As off-axis DSCDs are two orders of magnitude larger than the enhancement in the zenith sky SCD, on the order of 1×10^{17} molec cm⁻² reaching up to 1.4×10^{17} molec cm⁻² (compare Fig. 7.4a), the overall impact on the path averaged NO₂ VMRs is very small, on the order of 2 to 4%. The time shift between the plume overpass detection by the in-situ trace gas analyzer and the MAX-DOAS zenith sky measurements, which saw the plume earlier, indicates a vertical wind speed shear with higher wind speeds at higher altitudes, causing the upper part of the plume to travel faster and to cross the radar tower earlier than the lower part which is the one that can be detected by the in-situ instrument.

Panels 11 to 14 show low MAX-DOAS NO₂ VMRs on both path segments, as the plume has been blown out of the narrow LOS of the MAX-DOAS instrument and NO₂ levels drop rapidly to ambient background concentration.

Panel 15, where the large ship has moved further westward and thereby further away from the measurement site, shows for the first time in this measurement sequence a higher NO₂ VMR far away from the instrument on ΔL than close to the site along L_{UV} . A detailed inspection of the locations of the MAX-DOAS path segments and comparison with ship and modeled plume position reveals, however, a larger intersect of the plume with L_{UV} than with ΔL . This might be an example hinting at the systematic uncertainty (overestimation) of the retrieved effective path lengths caused by the neglect of the correction factor in the application of the O₄ scaling in the approach as discussed in Section 6.2.

The measurements, ship positions, and modeled plume positions from panel 10 are shown again in more detail in Fig. 7.14. To better visualize the retrieved two-dimensional NO₂ field above and around the shipping lane, the figure shows also the four previous MAX-DOAS measurements from between 30 seconds and 3 minutes before (from panel 6 to 9 in Fig. 7.13). Wind data, ship positions, and plume trajectories, however, represent the state from panel 10. The very pronounced horizontal gradient between high NO₂ VMRs close to the instrument and low, ambient VMRs further away, to the north of the shipping lane, is clearly visible in the figure.

Summarized, in a scenario with northerly winds at this site, the NO₂ VMR_{UV} along L_{UV} is enhanced due to the ship emission plumes being blown southward towards the instrument while VMR_{@ ΔL} along ΔL stays low on background level. Panel 15 in Fig. 7.13 is an exception, because only in this north eastern viewing direction the mean last scattering point in the UV is located south of the shipping lane.

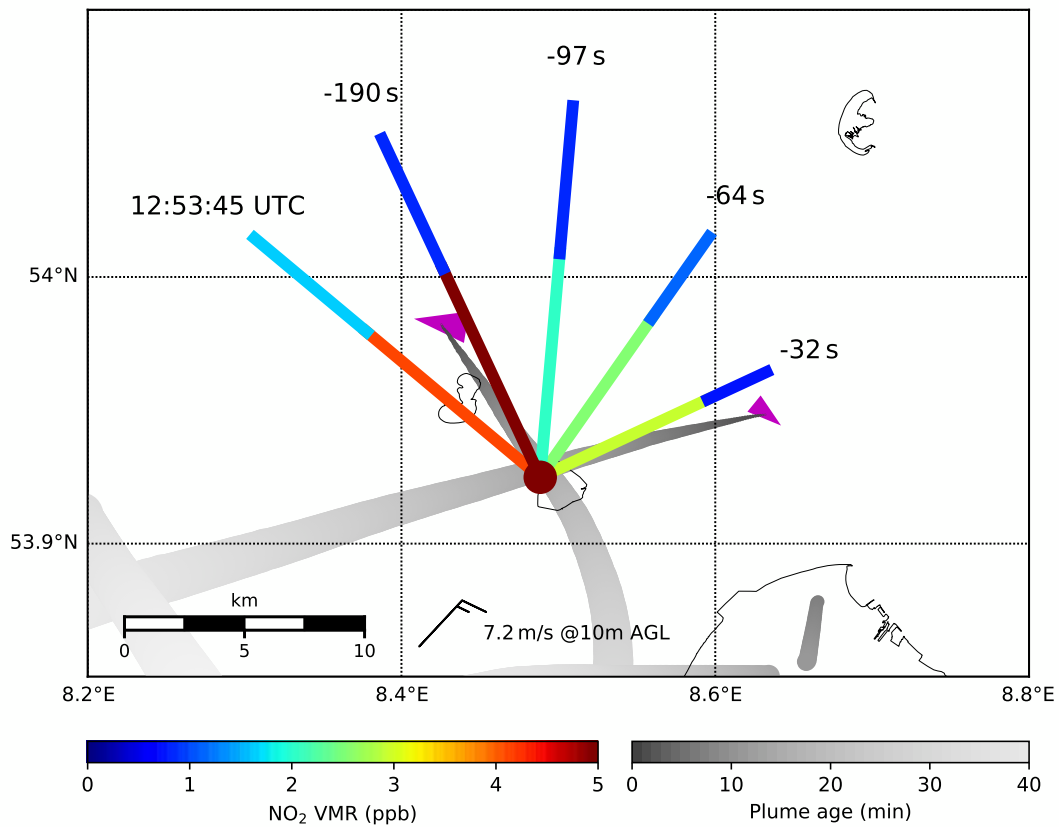


Figure 7.14.: Map showing a zoom in onto panel 10 of Fig. 7.13 and the four previous MAX-DOAS measurements between 30 seconds and 3 minutes before. Horizontal light path lengths (UV path and ΔL) and corresponding path averaged volume mixing ratios of NO_2 are shown as colored lines, in-situ NO_2 values as a colored dot at the location of the instrument. Magenta triangles show the ship position and course, with larger triangles for larger ships. Gray stripes show forward trajectories of the emission plumes calculated from wind speed and direction for the moving ship. Please keep in mind that ship and plume position were different for the past measurements. Wind direction and speed is shown with a meteorological wind barb. (Seyler et al., 2019)

7.5 Southerly wind scenario

A completely different scenario is found for southerly wind directions. In such a case, the wind blows the plumes away from the instruments towards the north of the main shipping lane, as can be seen from the map in Fig. 7.2. As a result, NO₂ levels north of the shipping lane are expected to be enhanced, while NO₂ levels south of the shipping lane, i.e., close to the site, should be low. For the northward pointing viewing directions the situation is expected to resemble the scenario b in Fig. 7.3. The in-situ trace gas analyzer on the radar tower should not be able to detect the ship emission plumes.

A 12 minute sequence of 15 consecutive MAX-DOAS measurements for such a scenario, taken on 13 August 2014 starting at 12:35 UTC (14:35 local time), is shown in the 15 maps in Fig. 7.15.

Like in the previous section, each individual map in the sequence shows the length of L_{UV} and ΔL and their path averaged NO₂ VMR as colored lines, while the colored dot on Neuwerk shows the on-site in-situ NO₂ measurements. Also shown are the positions and course of ships (with length >50 m), their modeled plumes as well as wind direction and speed from the weather station on Neuwerk. For this clear sky day, stability class C representing slightly unstable conditions has been selected for the Gaussian plume model based on the prevailing wind speeds and the strong solar insolation.

In the situation shown in the map sequence, two large ships (336 m and 365 m) and one smaller ship (100 m) are under way on the main shipping lane in eastward direction. As the ships move in the same direction on the shipping lane, the plume trajectories run in parallel. For enhanced NO₂ VMRs in northwesterly directions far away from the instrument without ship plumes in the line of sight, two coal-fired power plants in Wilhelmshaven were identified as a probable source and their modeled plume was added to the map. In the presented view, it extends from the lower left corner to the upper center and it the thickest gray line that crosses the ship plumes almost orthogonally. The two power plants are located directly adjacent at (53.57° N, 8.14° E), to the southwest of the measurement site in a distance of about 50 km. For this distance, the average wind speed of (7.5 ± 1.0) m/s measured at 10 m above ground layer (AGL) leads to a plume age of approximately 110 min, taking into account that wind speed increases with height, even shorter. Unlike the ships which are moving, this is a stationary source, so the plume trajectory should follow the wind, explaining the different plume trajectory courses.

Panel 1 shows the MAX-DOAS measurements at 12:35:31 UTC in the 310° azimuth viewing angle (towards NW). The path averaged NO₂ VMR_{UV} along L_{UV} is very low (~ 0.6 ppb), while VMR_{@ ΔL} along ΔL , further away from the site, is slightly enhanced (~ 1 ppb). This

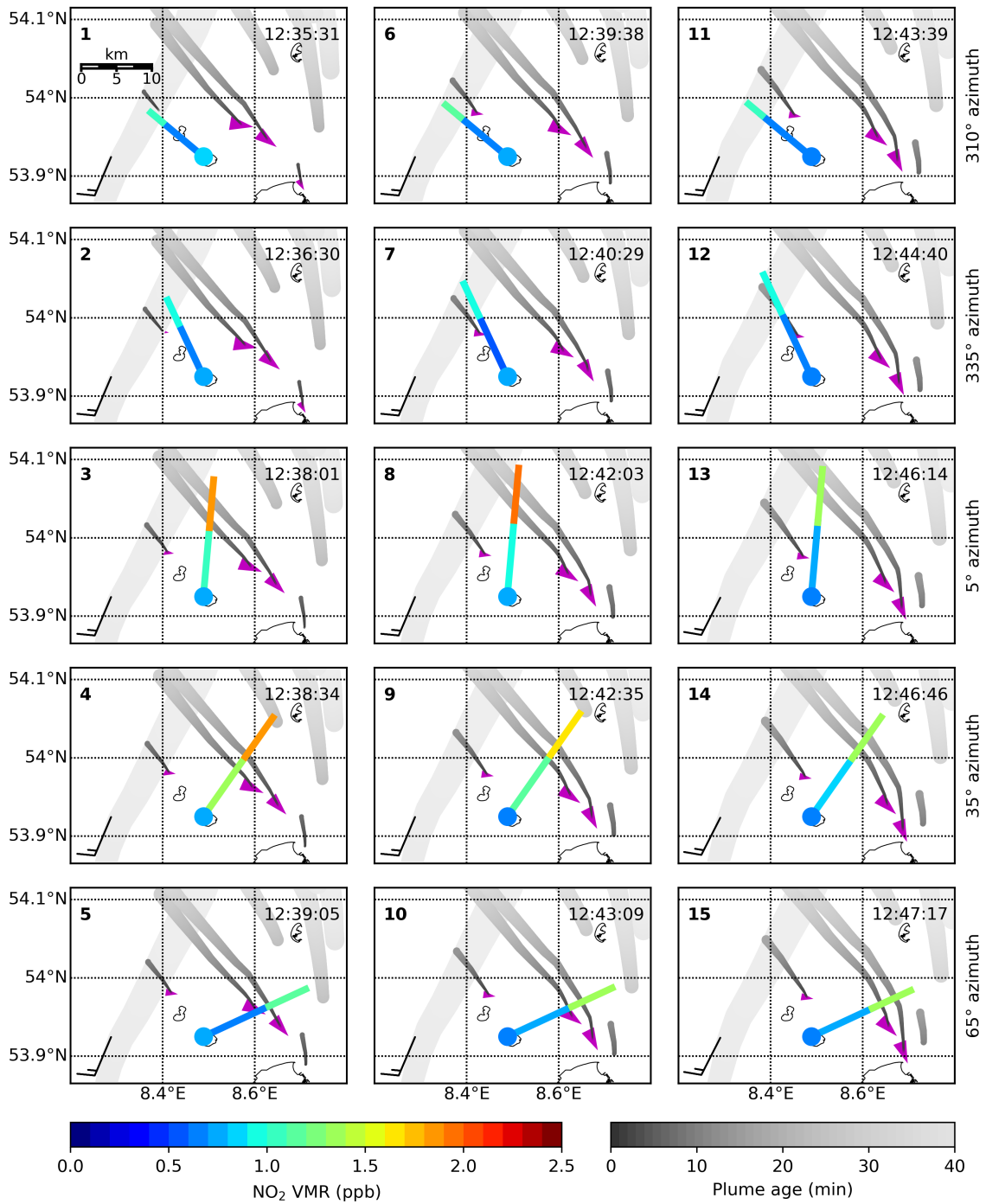


Figure 7.15.: Sequence of maps showing 15 consecutive measurements in 0.5° elevation on 13 August 2014, starting at 12:35 UTC (14:35 local time): The extent of the horizontal paths L_{UV} and ΔL and corresponding path averaged NO_2 VMRs are shown as colored lines. In-situ NO_2 VMRs are shown as a colored dot at the location of the measurement site. Magenta triangles show the ship position and course (sharp tip), with larger triangles for larger ships. Grey point clouds show forward trajectories of the emission plumes calculated from wind speed and direction for the moving ship. Wind direction and speed is shown with meteorological wind barbs. The reading direction is column-wise from top to bottom, the respective azimuth viewing angle is noted in the right margin. (Seyler et al., 2019)

slight enhancement could either be due to the small ship's plume or the plume from the power plants in Wilhelmshaven.

Panel 2 shows the next measurements in 335° azimuth (NNW), with similar results. The LOS of the MAX-DOAS instrument in this viewing direction does not probe the plume of the small ship, but the plume of the power plants, and still $\text{VMR}_{@L}$ along ΔL is enhanced. This indicates that the dominant source for the slightly enhanced NO_2 along ΔL are the more distant power plants.

Panel 3 shows MAX-DOAS measurements towards north (5° azimuth), probing the plumes of the two large ships. The rear, more southern plume is probed very close to the mean last scattering point in the UV, the other one runs further away. As a result, VMR_{UV} along L_{UV} is medium high (~1 ppb) and $\text{VMR}_{@L}$ along ΔL is twice as high, almost 2 ppb.

Panel 4 for 35° viewing azimuth angle (NNE direction) shows again high NO_2 VMR to the north of the main shipping lane and medium high values on the UV path closer by.

Panel 5 shows the next measurement, taken in the 65° viewing direction (towards ENE) where only one of the plumes of the two large ships, the one from the leading ship, is probed by the MAX-DOAS instrument on ΔL , as the second ship, slightly behind the first, has not moved far enough to the east yet. As a result, $\text{VMR}_{@L}$ along ΔL is enhanced. As L_{UV} does not probe any plume, the measured average NO_2 VMR along this path is low.

Panels 6 and 7 resemble panels 1 and 2, indicating that the situation in these azimuthal viewing directions has not changed much over the four minutes.

Panel 8, showing measurements four minutes after panel 3 in the same viewing direction, has an even more pronounced gradient between $\text{VMR}_{@L}$ and VMR_{UV} , because the plumes have been blown northward and behind the mean last scattering point in the UV.

Panels 10 to 12 show similar measurement results than panels 5 to 7.

Panels 13 to 15 present a situation where the plumes of the two big ships are now clearly further away from the site than the last scattering point in the UV and therefore only probed by the photons in the visible, leading to enhanced NO_2 levels along ΔL and low NO_2 VMRs along L_{UV} representing the ambient NO_2 background pollution level.

During the whole time period of MAX-DOAS measurements shown here the in-situ instrument measured constantly low values and could not detect any ship emission plumes, confirming the expectation that for southerly wind scenarios at this measurement site in-situ instruments are not able to detect ship plumes. The magnitude of the in-situ NO_2 VMRs agrees very well with the path averaged ambient background pollution retrieved with the MAX-DOAS instrument, confirming the validity of the onion peeling MAX-DOAS approach.

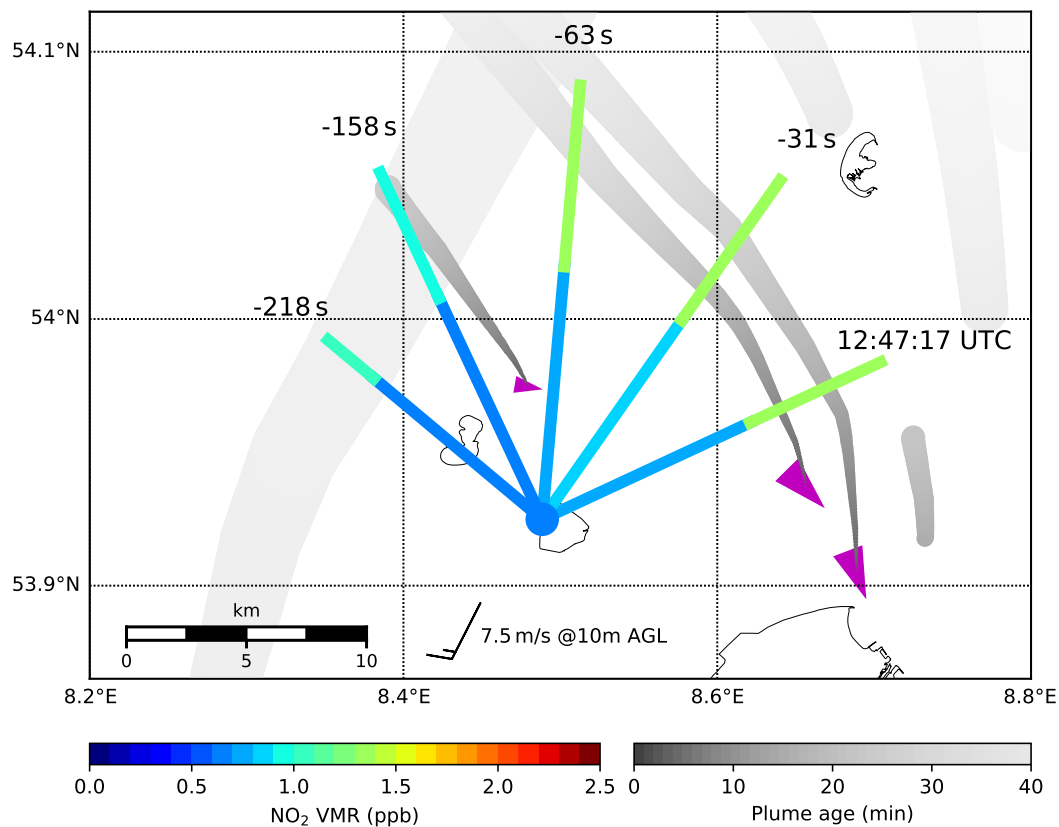


Figure 7.16.: Map showing a zoom in onto panel 15 of Fig. 7.15 and the four previous MAX-DOAS measurements between 30 seconds and 3.5 minutes before. Horizontal light path lengths (UV path and ΔL) and corresponding path averaged volume mixing ratios of NO_2 are shown as colored lines, in-situ NO_2 values as a colored dot at the location of the instrument. Magenta triangles show the ship position and course, with larger triangles for larger ships. Gray stripes show forward trajectories of the emission plumes calculated from wind speed and direction for the moving ship. Please keep in mind that ship and plume position were different for the past measurements. Wind direction and speed is shown with a meteorological wind barb. (Seyler et al., 2019)

As in the previous section, the two-dimensional NO₂ field above and around the shipping lane can be visualized best by plotting multiple MAX-DOAS measurements into a single map. In Fig. 7.16, the MAX-DOAS measurements from panel 15 are plotted as well as the four previous measurements from 30 seconds until up to 3.5 minutes before (from panels 11 to 14 in Fig. 7.15). The ship and plume positions as well as wind data is drawn for the time of the measurements in panel 15.

The horizontal gradient between the low NO₂ levels close to the site and enhanced values further away from the instruments, to the north of the shipping lane, is clearly visible in the MAX-DOAS measurements in the figure.

This example shows how MAX-DOAS measurements can be used to estimate the NO₂ distribution above the shipping lane and to identify inhomogeneities and local gradients in the NO₂ field. It also demonstrates how a MAX-DOAS is feasible to measure ship emissions even when the wind conditions are unfavorable for on-site in-situ measurements, and how the in-situ instruments cannot.

7.6 Computation of in-plume NO₂ volume mixing ratios from MAX-DOAS measurements and validation with airborne imaging DOAS measurements

One shortcoming of the onion peeling MAX-DOAS approach for ship emission measurements is, that only path-averaged VMRs can be retrieved which underestimate the local NO₂ VMR inside the plumes. As already shown in Section 7.4 and 7.5, the onion peeling approach makes it possible to get a very broad estimate of the plume position and to distinguish between plumes which are close to the instrument and those which are further away, but it gives neither information on the actual position of the plume inside the paths nor on the fraction of the paths that actually probe the plume, which would be important for the derivation of in-plume concentrations or VMRs. This shortcoming can be overcome with the plume modeling approach described in Section 7.3 above, which fills the knowledge gap by projecting the plume position and giving an estimate of the plume width. Thus, if the position of the sources (ships) is known (like in this study from AIS data), plume modeling enables us to retrieve in-plume NO₂ VMRs from MAX-DOAS measurements, which is demonstrated in the following. For a validation of the MAX-DOAS in-plume NO₂ VMRs and the plume modeling results, a comparison to airborne imaging DOAS measurements is included.

7.6.1 Computation of in-plume NO₂ VMRs from MAX-DOAS measurements

If the plume width and thus the fraction of the path probing the plume is known, the local VMR inside the plume can be retrieved from MAX-DOAS measurements. To get an estimate of the plume width, plume modeling (see Section 7.3) is used.

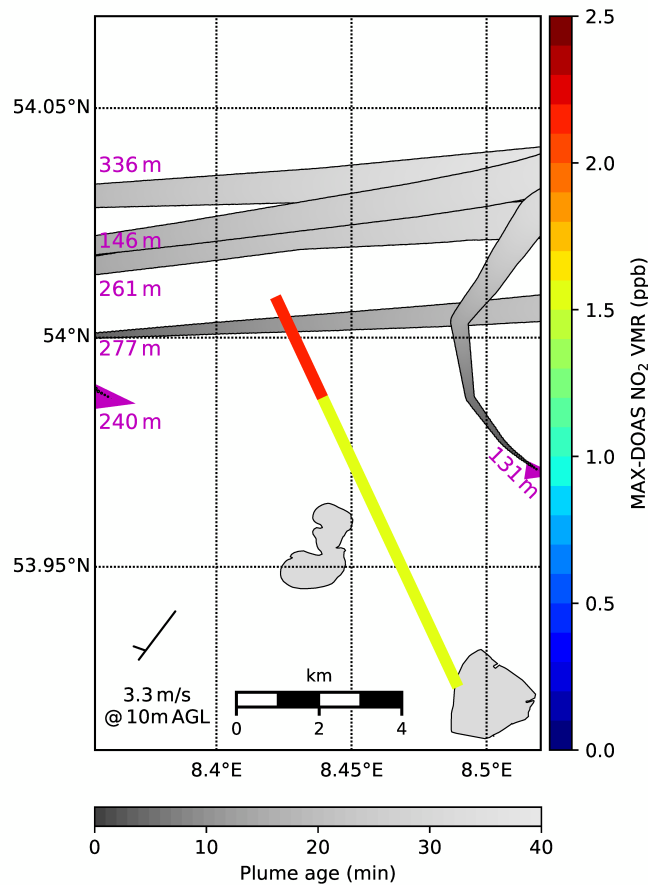


Figure 7.17.: Map showing the MAX-DOAS path averaged VMRs of NO₂ (colored lines) on 21 August 2013 at 9:53 UTC (11:53 local time). Magenta triangles show current ship positions and course. Modeled ship plumes are shown in gray, the lightness of the gray shading representing the plume age. Wind direction and speed is shown with a meteorological wind barb.

Figure 7.17 shows MAX-DOAS path averaged NO₂ VMRs along L_{UV} and ΔL measured on Neuwerk on 21 August 2013 at about 9:53 UTC (11:53 local time) in the 335° viewing direction at 0.5° elevation, plotted, as before, as colored lines on a map. Ship positions at this time and modeled plumes are also shown on the map. For the Gaussian plume model the stability class C, representing slightly unstable conditions, was selected because of wind speeds between 3 and 4 meters per second and the weak insolation due to clouds in the

morning, as discussed in Section 7.3.4. Wind speed and direction were measured at the weather station on the neighboring island Scharhörn.

The map shows four plumes of ships of different sizes that crossed the area of interest before and already left the mapped area to the west, a fifth plume is located in the east of the map area. The southernmost plume of the four, originating from a ship of 277 m length, was probed by the MAX-DOAS instrument's farther-reaching measurements in the visible spectral range, but not in the UV. As a result, the NO_2 $\text{VMR}_{@ \Delta L}$ along ΔL is enhanced, the VMR_{UV} along L_{UV} shows a lower, ambient background NO_2 concentration.

In other words, the onion peeling MAX-DOAS detected enhanced NO_2 and gives us an approximate localization of a plume somewhere along the ΔL path, limiting the possible distance of the ship plume to the radar tower to a range of 7.8 to 10.1 km. This is confirmed by the plume modeling, which provides a more detailed projected localization of the plume.

For the plume state at the intersection of plume and MAX-DOAS line of sight, according to the plume trajectory model, the plume air parcels have traveled a distance of (2180 ± 30) m in (660 ± 10) s since emission. The Gaussian plume model yields a plume width of (580 ± 20) m at this point. The error margin of ± 20 m is clearly set too small, as the selection of the stability class has a strong influence on the modeled plume width. For the more unstable class B–C a plume width of (720 ± 20) m is obtained and the more stable class C–D yields (480 ± 20) m. This span of values gives a much more realistic error estimate for the plume width. The MAX-DOAS LOS probed the plume not orthogonally, but under an angle of about 70° , giving an effective plume width of (610 ± 130) m.

For the computation of the average NO_2 VMR inside the plume, the partial horizontal NO_2 column inside the plume needs to be determined, as just scaling the path averaged $\text{VMR}_{@ \Delta L}$ to the effective plume width does not take the ambient background signal into account. To estimate the underlying background signal along ΔL , the UV DSCD can be used, since there is no plume along L_{UV} .

Figure 7.18 shows the MAX-DOAS NO_2 DSCDs in the lowest five elevation angles in three panels for UV, visible spectral range, and their difference, ΔDSCD . At 9:53 UTC, the MAX-DOAS measured a ΔDSCD of 1.35×10^{16} molec cm^{-2} (see panel c) along a ΔL path of 2.3 km. In the UV, a column density of 3.0×10^{16} molec cm^{-2} was measured along a L_{UV} path of 7.8 km.

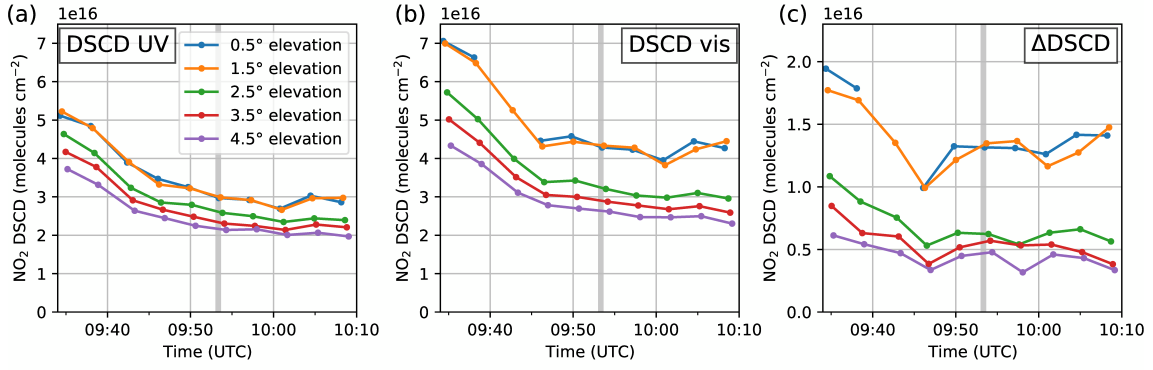


Figure 17.18.: MAX-DOAS differential slant column densities of NO_2 in the UV (a) and visible (b) spectral range as well as their difference ΔDSCD (c) for the five lowest elevation angles for the azimuthal viewing direction of 335° on 21 August 2013. The vertical gray line indicates the AirMAP plume overpass time (see Section 7.6.2). The gap in the 0.5° elevation time series in the visible channel is due to an instrumental problem. (Seyler et al., 2019)

Using the modeled effective plume width of $b = (610 \pm 130) \text{ m} = (61\,000 \pm 13\,000) \text{ cm}$, the horizontal column inside the plume can be calculated via:

$$\text{DSCD}_{\text{plume}} = \Delta\text{DSCD} - \text{DSCD}_{\text{background}} \quad (7.5)$$

$$= \Delta\text{DSCD} - \text{DSCD}_{\text{UV}} \cdot \frac{\Delta L}{L_{\text{UV}}} \quad (7.6)$$

$$= (4.7 \pm 2.5) \times 10^{15} \text{ molec cm}^{-2}, \quad (7.7)$$

where the error margin has been computed with Gaussian error propagation from the uncertainties of the measured DSCDs ($\pm 10\%$), retrieved path lengths ($\pm 20\%$) and the modeled plume width ($\pm 130 \text{ m}$), assuming independent random uncertainties in the individual variables.

This yields for the average VMR inside the plume:

$$\text{VMR}_{\text{plume}} = \frac{\text{DSCD}_{\text{plume}}}{b \cdot n_{\text{air}}} = (3.1 \pm 1.5) \times 10^{-9} = (3.1 \pm 1.5) \text{ ppb}, \quad (7.8)$$

with $n_{\text{air}} = 2.54 \times 10^{19} \text{ molec cm}^{-3}$, the number density of air, computed from the measured temperature of 19.2°C and air pressure of 1025.2 hPa . Again, Gaussian error propagation was used for the computation of the total uncertainty margin.

7.6.2 Validation with airborne imaging DOAS measurements

As already indicated in Sections 7.4 and 7.5, a validation of the onion peeling MAX-DOAS results with on-site in-situ trace gas analyzers is only feasible for ambient background NO_2

concentrations. For ship plumes, the inherent differences in both measurement techniques make a direct comparison of in-plume concentrations difficult. Moreover, for unfavorable wind conditions like southerly winds blowing the plumes away from the site, the in-situ instrument cannot detect any plumes. Satellite instruments, on the other hand, do not have enough spatial resolution to observe individual ship plumes with the needed accuracy, even with the newest Sentinel 5 precursor satellite instrument and its $3.5 \times 5.5 \text{ km}^2$ resolution (Veefkind et al., 2012), although the detection of individual ship plumes seems possible according to a new study from Georgoulias et al. (2020).

Airborne imaging DOAS measurements are available only on campaign basis, but can provide NO_2 maps of the plumes with a much higher spatial resolution, representing the middle ground between observations from ground and satellites. These high resolution NO_2 VCD maps of the plumes can be used to validate both the plume positions projected with simple forward trajectories and the plume width computed from the Gaussian plume model, as it has been shown in Section 7.3.4, and the approximate plume positions derived from the onion peeling MAX-DOAS approach. When incorporating vertical plume extent information from the plume modeling, the airborne measurements can also be used to validate the in-plume NO_2 VMRs from MAX-DOAS, as it is shown in Section 7.6.2 below. Such airborne imaging DOAS measurements have been performed by the AirMAP instrument during the NOSE campaign in August 2013 (Meier, 2018), which will be discussed in the following.

AirMAP instrument

The Airborne imaging Differential Optical Absorption Spectroscopy instrument for Measurements of Atmospheric Pollution (AirMAP) is a push-broom³ imaging DOAS instrument. A wide-angle objective, embedded in the bottom plate of the aircraft, collects scattered sunlight from below the aircraft which is then coupled into a sorted optical fiber bundle consisting of 35 individual fibers. An imaging grating spectrometer is used to disperse the image of the 35 vertically stacked fibers and to map it onto a frame-transfer-CCD, so that each fiber represents a different across track viewing direction. The total field of view of about 52° leads to a ground swath width similar to the flight altitude. Using this set-up, 35 across track pixels can be measured simultaneously at an exposure time of 0.5 seconds. This leads to a spatial ground resolution better than 50 m when the aircraft is flying at 1.5 to 1.6 km altitude. A more detailed description of the AirMAP instrument can be found in Schönhardt et al. (2015) and Meier et al. (2017).

For the NOSE campaign, the AirMAP instrument was installed in a Cessna 207 Turbo from the Freie Universität Berlin, Institut für Weltraumwissenschaften. Both the AirMAP instrument and the airplane are shown in Fig. 7.19.

³As opposed to a whisk-broom scanner. A push-broom (or along track) scanner measures a line of pixels, oriented perpendicular to the flight direction, simultaneously. A whisk-broom (or across track) scanner typically uses a moving mirror to scan across the ground track.

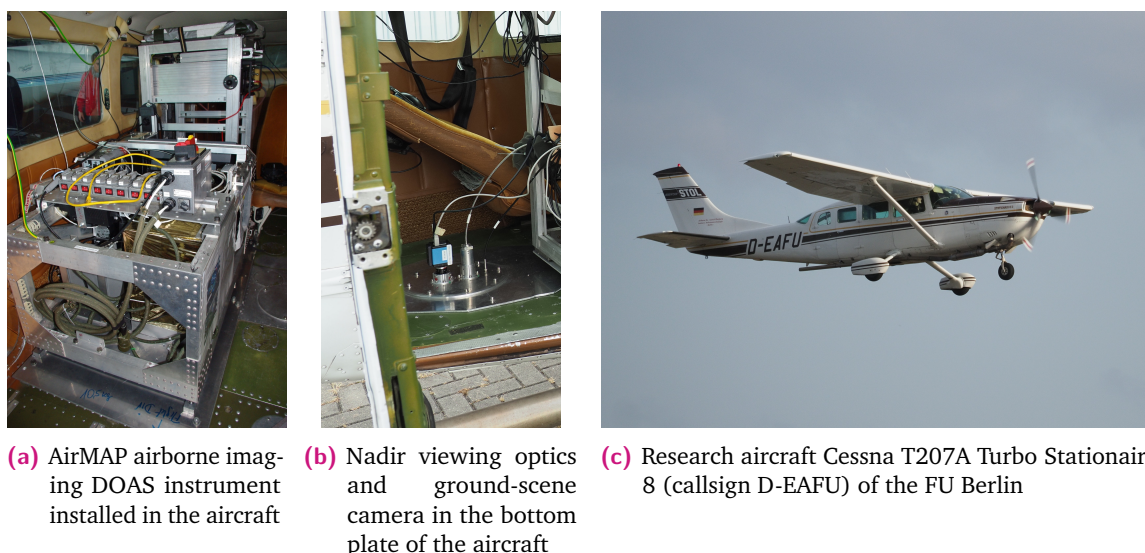


Figure 7.19.: Pictures of the AirMAP instrument and the Cessna research aircraft, photographed by the author

For the retrieval of NO_2 DSCDs a fitting window of 425 to 450 nm has been chosen using the settings described in Meier et al. (2017). The air mass factors for the conversion of slant column densities to vertical column densities were calculated using a NO_2 box profile in the lowest 500 m for an aerosol-free atmosphere and a constant surface reflectance of 0.05. The chosen box profile height represents an educated guess on an upper limit for the vertical plume extent of typical middle-aged ship plumes, which is consistent with the Gaussian plume model results.

NOSE campaign 2013

The NOSE (for German "Nord-Ost-See-Experiment") campaign took place in August 2013 in northern Germany at the North Sea coast and along the Elbe river, covering among others the MESMART measurement stations on Neuwerk and in Wedel. Its aim was the airborne measurement of ship emissions in support of the MESMART project (Meier, 2018). On 21 August between 9:00 and 12:30 UTC (11:00 and 14:30 local time), a flight over the Neuwerk region was performed. The flight pattern included flight tracks along the of the MAX-DOAS instrument's line of sight (LOS) for the five different azimuthal viewing directions shown in Fig. 7.2. It also included an overpass over an individual ship and its plume in a low height. More detailed information on the NOSE campaign can be found in Meier (2018).

Mapping of the MAX-DOAS instrument's LOS, as has been performed during the NOSE campaign, is very well suited for the validation of the onion peeling MAX-DOAS results. It enables to compare the broad estimates on the approximate plume position yielded from the onion peeling MAX-DOAS approach to the real plume position measured by AirMAP

and, in a similar manner, to validate the plume modeling results, as was already shown in Section 7.3.4 above.

Validation

Figure 7.20 is similar to Fig. 7.17, but shows additionally the AirMAP NO₂ VCDs along a flight track from southeast to northwest, mapping the MAX-DOAS 335° line of sight on 21 August 2013 around 9:53 UTC (11:53 local time). On this flight track, AirMAP overpassed multiple plumes, which show up in the measurements as strongly enhanced NO₂ VCDs that reveal the location and course of the plumes as well as the width of the plumes. The southernmost of the four plumes crossing the flight track is the plume that was also probed by the MAX-DOAS instrument and for which the average in-plume NO₂ VMR was determined in Section 7.6.1. The AirMAP measurements validate the MAX-DOAS instrument's detection and approximate localization of a plume somewhere along ΔL . Furthermore, it can be seen that AirMAP measured low NO₂ VCDs all along the UV path, L_{UV} , which confirms the assumption of ambient background pollution along this path.

The time shift between MAX-DOAS measurement and the different parts of the flight track in Fig. 7.20 are indicated close to the flight track. The MAX-DOAS and AirMAP measurements of said plume (the southernmost one) have a small time difference of less than 20 seconds, even less when considering the total integration time of the MAX-DOAS measurement of 10 seconds. Location of the plume and plume width, computed with the plume modeling approach described in Section 7.3 that combines forward trajectories and a simple Gaussian plume model, fit very well to the AirMAP measurements of the plume. The other mapped plumes further to the north were measured by the AirMAP instrument about 1 minute later, enough time for the south westerly wind to blow the plumes northward causing the measured plume positions to not fully coincide with the modeled plumes, an expected behavior, as the plume location and state were modeled for the earlier time of the MAX-DOAS measurement.

As discussed in Section 7.3.4, inspecting the AirMAP measurements in Fig. 7.20 in detail reveals that the real plumes show signs of turbulent flow induced irregularities and random fluctuations and are not as smooth as the modeled plumes, since the Gaussian plume model only describes a steady state of a long time averaged plume and cannot cover turbulent eddies and irregularities. Still, the plume width measured by AirMAP and the modeled one agree quite well, providing confidence in the applied plume modeling approach.

For the validation of the retrieved MAX-DOAS in-plume NO₂ VMR with the AirMAP instrument, the crucial differences in the viewing geometries of ground-based MAX-DOAS and airborne imaging DOAS measurements have to be considered, which are schematically shown in Fig. 7.21.

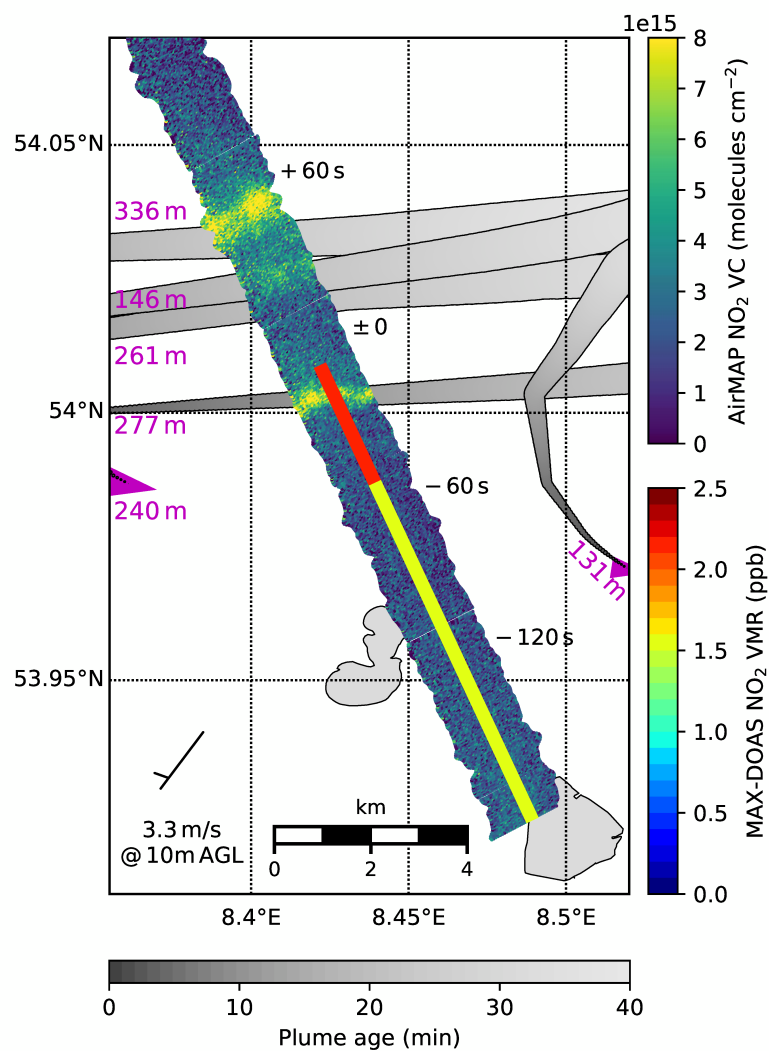


Figure 7.20.: Map showing the MAX-DOAS path averaged VMRs (colored lines) and AirMAP vertical columns of NO₂ (broad image stripe beneath) on 21 August 2013 around 9:53 UTC (11:53 local time). As the plotted physical quantities are entirely different (VMRs and columns), color scale agreements are not expected (and completely random). Magenta triangles show current ship positions and course. Modeled ship plumes are shown in gray, the lightness of the gray shading representing the plume age. The time difference between AirMAP and MAX-DOAS measurements is indicated in the map at specific parts of the flight track. Wind direction and speed is shown with a meteorological wind barb. (Seyler et al., 2019)

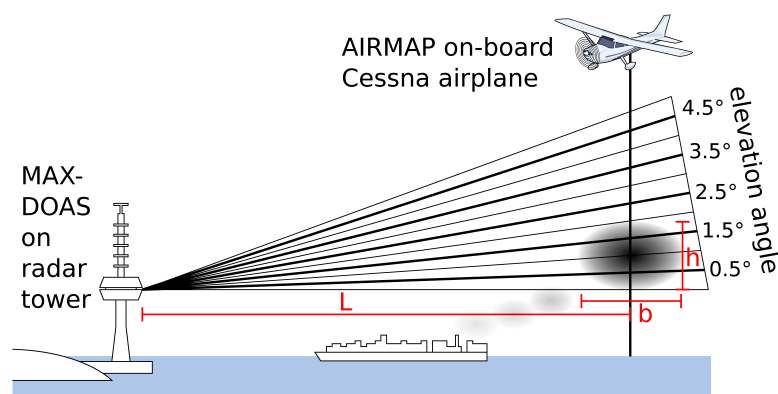


Figure 7.21.: Sketch of the different measurement geometries of ground-based MAX-DOAS and airborne imaging DOAS instrument when measuring a ship plume. While the MAX-DOAS instrument scans the plume vertically, the AirMAP instrument measures in nadir direction sunlight scattered on the ground and on air molecules in the atmosphere below the aircraft. Distances, heights and sizes are not to scale. (Seyler et al., 2019)

While the MAX-DOAS instrument probes (very slightly slanted) horizontal transects of the plume, the AirMAP instrument, pointing in nadir direction downward from the airplane, measures vertical transects of the plume. Measuring in different elevation angles enables the MAX-DOAS instrument to scan the plume vertically, while AirMAP “scans” the plume via the forward movement of the airplane. The AirMAP measurements provide vertical columns of NO_2 between aircraft and ground, but contain no information about the distribution of the NO_2 inside the column, i.e., about the vertical location of the NO_2 molecules inside the column. Indeed, concentrations or VMRs can be derived from the vertical columns by assuming a box profile for the near-ground NO_2 layer, but for an accurate retrieval of the in-plume VMR, the fraction of the light path probing the plume and thereby the vertical plume extent has to be known. This plume height h can either be computed via the Gaussian plume model, or be estimated roughly from the MAX-DOAS instrument’s vertical elevation scan, given that the distance from plume to the MAX-DOAS instrument is known. This distance can be easily derived from the AirMAP measurements, as it is shown below.

For the selected stability class C (see Section 7.6.1), an exhaust stack height of 40 m, estimated from photographs of the ship (for an explanation of the method see Section 7.3.3), and an assumed initial plume rise of 10 m, the Gaussian plume model delivers a vertical plume extent from the ground to a height of (320 ± 20) m. As for the modeled plume width (see Section 7.6.1), the modeled plume height does depend on the selection of the stability class and again, we can derive a more realistic uncertainty estimate from this. For the more unstable class B–C a plume height of (420 ± 20) m is retrieved and for the more stable class C–D a value of (230 ± 20) m, the span giving an idea on the uncertainty introduced by the stability class selection.

As mentioned above, investigating the relative ratios of the DSCDs in the different elevation angles in the MAX-DOAS vertical scan can give a hint on the vertical distribution of the NO₂ in the boundary layer and therefore on the plume height. For this we need to reconsider Fig. 7.18, which shows MAX-DOAS UV and visible NO₂ DSCDs as well as their difference, Δ DSCD, for the five lowest elevation angles each.

In panel a, the measured UV DSCDs show the typical, well-known elevation angle dependency for tropospheric absorbers featuring the longest light paths and largest DSCDs at the lowest elevation angles, and decreasing DSCDs for higher elevation angles due to shorter light path lengths through the troposphere. This behavior, also known as “separation” of the DSCDs, can, albeit being larger in general due to the longer light path lengths for longer wavelengths, also be observed in the measurements from the visible spectral range in panel b. However, the visible DSCDs show a larger “gap” between the lower elevations (0.5°, 1.5°) and higher elevations (2.5°, 3.5°, 4.5°), indicating even more additional NO₂ in the lower elevations’ light paths than is expected from the longer light path effect. In the DSCD difference, Δ DSCD, shown in panel c, this gap is even more pronounced. This additional NO₂ in the boundary layer close to the ground can only be the ship plume.

An upper boundary for the plume height h can be estimated by assuming that the plume fills the total vertical field of view (FOV) of the two lowest scan directions, the 0.5° and 1.5° elevation angle. Taking into account the total FOV of the MAX-DOAS instrument of 1°, the plume is observed from the measurement site in a solid angle of 2°, like it is depicted schematically in Fig. 7.21. Further below, it is derived that the instrument is around 9.6 km away from the plume. A solid angle of 2° at this distance corresponds to a plume height of $h = 9.6 \text{ km} \cdot \tan 2^\circ \approx 335 \text{ m}$, which fits well to the plume height computed with the Gaussian plume model of $(320 \pm 90) \text{ m}$.

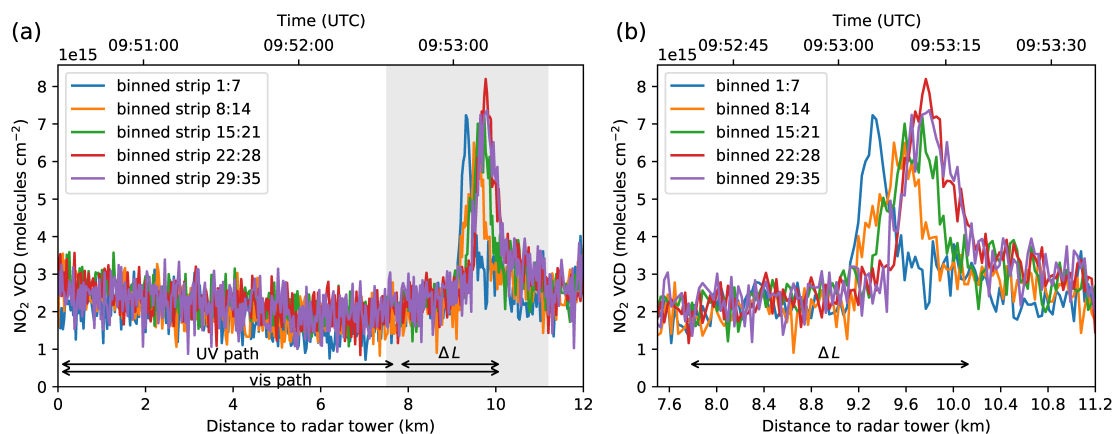


Figure 7.22.: AirMAP vertical columns of NO₂ as a function of distance (lower axis) or time (upper axis) for the flight track section shown in Fig. 7.20. The right plot is a zoom in on the gray shaded area. Black horizontal arrows below the measurements denote the horizontal effective light paths of the MAX-DOAS. (Seyler et al., 2019)

Figure 7.22a shows vertical columns of NO₂ measured by AirMAP on the flight track shown in Fig. 7.20 as a function of distance to the radar tower (on the bottom axis) or time (on the top axis). To reduce the noise on the measurements, the 35 individual viewing directions of AirMAP are binned to 5 (line 1:7, 8:14, 15:21, 22:28 and 29:35). Further binning would have reduced the noise on the measurements even further, but would also have smeared out the plume signal, because the plume crosses the flight track not perpendicular, but at an angle of about 70°. As the figure shows, binning to 5 lines seems like a reasonable compromise between better signal to noise and stronger horizontal blurring of the plume signal.

The AirMAP measurements show a strong NO₂ enhancement at a distance of 9.1 to 10.2 km to the radar tower, confirming the approximate plume distance estimation retrieved from the onion peeling MAX-DOAS, which gave a range of 7.8 to 10.1 km (see Section 7.6). As indicated by the annotated arrows in the plot showing the MAX-DOAS effective horizontal paths, the AirMAP measurements confirm that the plume's NO₂ enhancement is further away than the mean last scattering point in the UV and therefore only probed on the visible light path and hence ΔL , but not on the shorter L_{UV} . This fits very well together with the onion peeling MAX-DOAS results showing a strong NO₂ signal along ΔL while along L_{UV} the measured AirMAP NO₂ VCDs are much lower, representing an ambient NO₂ background. From Fig. 7.22a it can also be seen that the background signal is not entirely constant, but shows a slight decrease along L_{UV} from the site towards the mean last UV scattering point, which the MAX-DOAS inherently cannot resolve.

The AirMAP measurements of the plume are shown again in more detail in Fig. 7.22b. The 5 binned viewing directions represent 5 parallel slices through the plume. The plume NO₂ enhancement is nearly Gaussian-shaped for all 5 slices, providing confidence that the Gaussian plume model gives a good approximation of a real plume's shape. The deviations from the ideal Gaussian shape and the differences in peak maximums and peak widths might be either noise or, more likely, turbulent flow induced random fluctuations and irregularities in the plume. The above-mentioned non-perpendicular angle between flight track and ship plume leads to a slight shift between the slices, so that the respective NO₂ maximum as well as plume edges were overpassed at slightly different times and have a slightly different distance to the radar tower.

The vertical columns of NO₂ measured by AirMAP are total columns between ground level and flight altitude. To isolate the local NO₂ enhancement of the plume from the ambient background NO₂, the background column has to be subtracted from the total column:

$$VC_{\text{plume}} = VC_{\text{total}} - VC_{\text{background}} \quad (7.9)$$

$$= (6.9 \pm 1.0) \times 10^{15} \text{ molec cm}^{-2} - (3.2 \pm 1.0) \times 10^{15} \text{ molec cm}^{-2} \quad (7.10)$$

$$= (3.7 \pm 2.0) \times 10^{15} \text{ molec cm}^{-2}. \quad (7.11)$$

Potential error sources in the AirMAP NO₂ measurements are fitting uncertainties on the retrieved DSCDs, uncertainties on the assumed profile shape, on the surface reflectance, and aerosols, whereas uncertainties on the NO₂ amount in the reference spectrum cancel out when subtracting the background, yielding a maximum overall uncertainty on the NO₂ VCDs of about 30 % (Meier et al., 2017).

The NO₂ columns measured horizontally (MAX-DOAS) and vertically (AirMAP) through the plume differ, with $(4.7 \pm 2.5) \times 10^{15}$ molec cm⁻² and $(3.7 \pm 2.0) \times 10^{15}$ molec cm⁻², respectively. Such a disagreement is expected, as the horizontal and vertical extent of the plume differ, as the plume is roughly twice as wide as high. Therefore, for a quantitative comparison, the measured NO₂ columns inside the plume needs to be converted to an average in-plume mixing ratio:

$$\text{VMR}_{\text{plume}} = \frac{\text{VC}_{\text{plume}}}{h \cdot n_{\text{air}}} \quad (7.12)$$

yielding (4.6 ± 2.7) ppb for $h = 320$ m (from Gaussian plume model) or (4.3 ± 2.5) ppb for $h = 335$ m (estimated from MAX-DOAS vertical scan), with the respective overall uncertainty range computed via error propagation. These values are in reasonable good agreement with the in-plume NO₂ VMR of (3.1 ± 1.5) ppb derived from the MAX-DOAS measurements with help of the Gaussian plume model.

Another opportunity to check the validity of the plume modeling is to compare the AirMAP's measured plume width with the model result from Section 7.6.1. From Fig. 7.22, using the same threshold of $1/e$ as for the modeling, a plume width b of 400–500 m, or an effective plume width of $b_{\text{eff}} = (480 \pm 53)$ m due to the 70° angle between plume and flight direction, can be derived. The plume width computed by the model is quite a bit higher, with $b = (580 \pm 120)$ m and $b_{\text{eff}} = (610 \pm 130)$ m, respectively, but agrees with the AirMAP measurements within the error margins. Using the more accurate plume width measured by AirMAP instead of the modeled one, the MAX-DOAS in-plume VMR increases to a value of (3.9 ± 1.8) ppb, giving a better agreement with the AirMAP results.

There are different possible explanations for the remaining deviation between the in-plume NO₂ VMRs from MAX-DOAS and AirMAP. Inspecting the AirMAP measurements along the UV path of the MAX-DOAS in detail reveals a slight decrease of ambient NO₂ background pollution levels along L_{UV} from the radar tower towards the mean last UV scattering point and towards the plume. Taking the UV DSCD as a measure for the ambient background pollution in the scene and along ΔL could therefore lead to a small bias in the local background correction along ΔL . If too much NO₂ is subtracted as the background along ΔL , where the ambient NO₂ background is lower than along L_{UV} , as the AirMAP measurements revealed, the MAX-DOAS in-plume DSCD and VMR might both be slightly

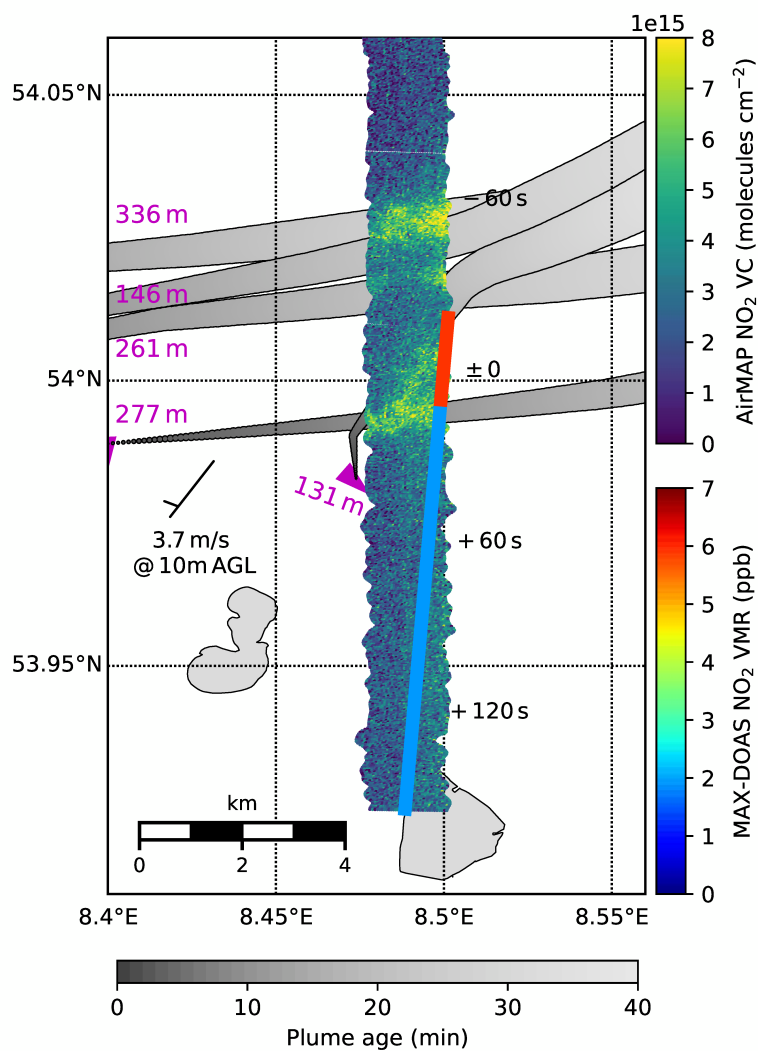


Figure 7.23.: Map showing the MAX-DOAS path averaged VMRs (colored lines) and AirMAP vertical columns of NO₂ (broad image stripe beneath) on 21 August 2013 around 9:43 UTC (11:43 local time). As the plotted physical quantities are entirely different (VMRs and columns), color scale agreements are not expected (and completely random). Magenta triangles show current ship positions and course. Modeled ship plumes are shown in gray, the lightness of the gray shading representing the plume age. The time difference between AirMAP and MAX-DOAS measurements is indicated in the map at specific parts of the flight track. Wind direction and speed is shown with a meteorological wind barb. (Seyler et al., 2019)

underestimated, which could be a possible explanation for the lower MAX-DOAS value compared to the AirMAP result.

Another potential explanation might be the systematic underestimation of the retrieved path lengths in the O_4 scaling due to the negligence of the correction factor.

In Fig. 7.23, another MAX-DOAS – AirMAP comparison plot is shown for a different flight track from ten minutes earlier. This example shows an even better agreement between modeled plume positions and the measured plume positions from the AirMAP instrument, confirming the validity of the selected plume modeling approach. It also shows again, how the onion peeling MAX-DOAS can be used to derive a rough estimate of the plume position. But this example also shows a limitation of the approach, because in cases like this, where two plumes are located along ΔL which are also not fully covered by this path segment, a computation of in-plume NO_2 VMRs is not possible.

7.7 Summary and conclusions

This study describes a novel application of the “onion peeling” MAX-DOAS approach to measurements of shipping emissions to estimate the two-dimensional pollutant distribution in the strongly inhomogeneous NO_2 field above a shipping lane. The ability to probe air masses at different horizontal distances to the instrument to derive the approximate positions of the ship plumes in the measurement area has been shown on the basis of selected case studies out of three years of measurements on the island Neuwerk. Located 6–7 km south of the main shipping lane from the North Sea into the Elbe river in the German Bight close to Cuxhaven, the island was selected as an ideal site for the application of the onion peeling MAX-DOAS approach as the distance to the shipping lane is optimal for exploiting the horizontal light path differences between UV and visible radiation to probe the emission plumes released from passing ships.

To determine the horizontal light path lengths for the onion peeling, the O_4 scaling approach, that uses the trace gas column of the oxygen collision complex O_4 as a light path tracer, has been applied, as for the long term study presented in Chapter 6. Using the O_4 scaling, path-averaged volume mixing ratios (VMRs) have been derived from the measured column amounts of NO_2 , enabling to compare the simultaneously acquired measurements along the shorter UV path and the longer visible path. For the eponymous “onion peeling”, a separate NO_2 VMR along the path difference, usually located above or close to the shipping lane and therefore several kilometers away from the instrument, has been computed from UV and visible measurements to easily compare NO_2 pollution levels close to the instrument (along the UV path) and several kilometers away (along the path difference).

Two case studies were selected to demonstrate the abilities of the onion peeling MAX-DOAS approach: The first one for northerly winds, that blow the plumes towards the island and the measurement site, shows how the MAX-DOAS instrument can reliably detect enhanced NO_2 concentrations close to the instrument (south of the shipping lane) and low NO_2 concentrations north of the shipping lane. In the contrary situation of southerly winds, that blow the plumes northward and thus further away from the island, low NO_2 values were measured close to the site (south of the shipping lane) and enhanced NO_2 values were detected in the north of the shipping lane, demonstrating that a MAX-DOAS instrument can detect pollution several kilometers away from the instrument even under wind conditions unfavorable for on-site in-situ instruments.

To compute in-plume NO_2 volume mixing ratios from the MAX-DOAS measurements, the fraction of the light path probing the plume has to be determined, which is accomplished by a combination of simple plume parcel forward trajectories and a Gaussian plume model, making it possible to model the location, movement and spatial extent of the ships' plumes. The combination of MAX-DOAS measurements and plume model enables to compute in-plume NO_2 volume mixing ratios from MAX-DOAS measurements, demonstrated exemplarily for a plume measured on 21 August 2013.

To validate both the plume model results and the MAX-DOAS in-plume VMRs, airborne imaging DOAS measurements taken by the AirMAP instrument during the NOSE campaign on this very same day have been used. AirMAP's measured plume positions agree well with the ones estimated with the onion peeling MAX-DOAS approach, showing that MAX-DOAS measurements can in fact be used to derive the approximate position of ship emission plumes in such an inhomogeneous pollution field. The good agreement of plume positions, shapes, and the plume width in the model and the AirMAP measurements shows that simple forward trajectories combined with a Gaussian plume model look-up-table approach provide sufficient accuracy to model the two-dimensional NO_2 field above the shipping lane.

By incorporating additional information about the vertical plume extent from either plume model or MAX-DOAS vertical scans, an independent measurements of the in-plume NO_2 VMR can be derived from AirMAP's vertical column measurements. The retrieved AirMAP and MAX-DOAS in-plume NO_2 VMRs agree well within their error margins, confirming the validity of both the onion peeling MAX-DOAS approach and the presented method for the retrieval of in-plume NO_2 VMRs from MAX-DOAS measurements.

Investigation of marine air pollution with shipborne MAX-DOAS measurements in North and Baltic Sea

Shipborne measurements provide the opportunity to investigate marine air quality on the open sea further away from the coast, and to investigate emissions of other possible marine air pollution sources like oil and gas rigs. The collaboration with the German Federal Maritime and Hydrographic Agency (Bundesamt für Seeschifffahrt und Hydrographie, BSH) in the framework of the MESMART project allowed for the installation of air quality measurement devices on board the research vessel Celtic Explorer during several regular BSH survey cruises in North and Baltic Sea.

Table 8.1 lists all BSH survey cruises, where a MAX-DOAS instrument and in-situ instruments (trace gas analyzers, high volume filter sampler) have been installed campaign-wise on the Irish research vessel Celtic Explorer. Because of the large amount of data gathered, this chapter is focusing only on selected results of four of these cruises, which are the 5 to 6 week long summer survey cruises from 2013, 2015, 2016 and 2017. During the 2013 and 2015 summer survey cruises, the author was part of the scientific crew.

Table 8.1.: Overview of the shipborne MAX-DOAS campaigns on RV Celtic Explorer

Cruise ID	Time period	Duration	Investigated regions		Addendum
			North Sea (German EEZ/all)	Baltic Sea (German part)	
CE12015	Nov. 2012	1 week	✓/ X	X	X
CE13005	Mar. 2013	1 week	✓/ X	X	X
CE13012	Aug./Sep. 2013	6 weeks	✓/ ✓	✓	English Channel
CE14013 [†]	Aug./Sep. 2014	5 weeks	✓/ ✓	✓	Skagerrak
CE15012	Aug./Sep. 2015	5 weeks	✓/ ✓	✓	North Minch
CE16011	Aug./Sep. 2016	5 weeks	✓/ ✓	✓	English Channel
CE17013	Aug./Sep. 2017	5 weeks	✓/ ✓	✓	Skagerrak

* German exclusive economic zone (EEZ) of the North Sea. For an overview of the North Sea area and the EEZs of the bordering countries see Fig. 8.1.

[†] Only in-situ instrumentation (trace gas analyzers, high volume filter sampler), no MAX-DOAS



Figure 8.1.: Map of the North Sea with sea depths and exclusive economic zones (EEZs) of the bordering countries. Created by Halava under CC BY-SA 3.0, <https://commons.wikimedia.org/w/index.php?curid=1170771>.

8.1 Shipborne MAX-DOAS: Setup, measurement geometry and data analysis

The Irish research vessel Celtic Explorer (picture in Fig. 8.2, technical specifications in Table 8.2) has been chartered by the German Federal Maritime and Hydrographic Agency (Bundesamt für Seeschifffahrt und Hydrographie, BSH) for regular survey cruises in North and Baltic Sea from 2011 until 2019/2020 (Arndt, 2018, 2019).

Between 2012 and 2017, during the IUP–BSH collaboration in the MESMART project, air quality measurements have been performed on several cruises in addition to the routinely conducted oceanographic measurements, measurements of the marine chemistry and radionuclides in the water body. A list of the cruises is given in Table 8.1. During these cruises, a single-channel MAX-DOAS instrument as well as in-situ instruments comprising of trace gas analyzers and a high volume filter sampler have been set up at the crow’s nest of the ship, two levels above the wheelhouse top. Figures 8.3a and 8.3b show photographs of the installed instruments.

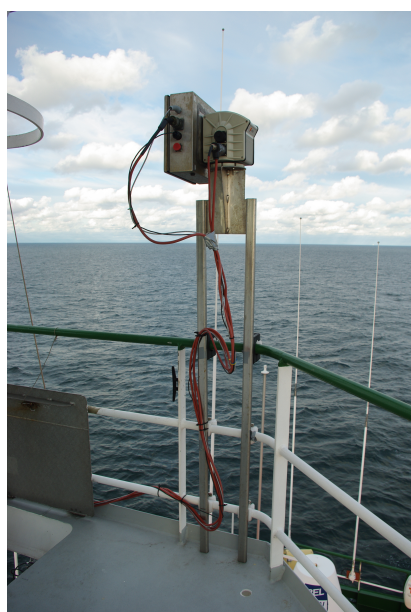
In the following subsections, the MAX-DOAS instrument’s setup, measurement geometry and data analysis are presented.



Figure 8.2.: RV Celtic Explorer in the Byfjorden close to Bergen, Norway. MAX-DOAS instrument and in-situ instruments are installed at the crow’s nest, two levels above the wheelhouse top. Photographed by the author in 2015.

Table 8.2.: Technical specifications of RV Celtic Explorer (Marine Institute, 2015)

Length o.a.	65.5 m
Beam	15 m
Draft	5.8 m
Gross tonnage	2425 t
Net tonnage	727 t
Engines	2 × 1620 kW + 1 × 1080 kW
Maximum speed	16 kn
Service speed	10 kn
Crew	13–15
Accommodation	20–22 scientists
Endurance	35 days
GPS	2 × Simrad MX500 DGPS
AIS	Foruno FA-150
Gyro compass	Robertson RGC 12
Motion reference system	Kongsberg Simrad Seapath 330+



(a) MAX-DOAS telescope with pan-tilt-head fixed to the railing



(b) In-situ instruments: high volume filter sampler (left) and Airpointer trace gas analyzer (right)

Figure 8.3.: Air quality measurement devices set up at the crow's nest of the RV Celtic Explorer, photographed by the author.

8.1.1 MAX-DOAS onboard the RV Celtic Explorer

The MAX-DOAS instrument, which was installed campaign-wise on the RV Celtic Explorer, consists of a telescope unit with a pan-tilt-head, which is fixed to the railing at the crew's nest of the ship (see Fig. 8.3a and 8.4a), and a spectrometer with attached CCD camera down on the bridge level, connected with an optical light fiber of 20 m length. Unlike the two-channel MAX-DOAS instrument on Neuwerk which comprises of separate spectrometers for the UV and visible channels, it has only one channel – one spectrometer with a broader spectral range – covering the UV range and to some extent also the visible. Spectrometer and CCD are installed in a compact 19-inch rack box in the wheelhouse (see Fig. 8.4b), together with the spectrometer's temperature stabilization unit, the telescope's control and power supply, the power supply for the HgCd calibration lamp and video camera as well as a UPS. On top of the rack box, a laptop computer for the data acquisition is set up. A second laptop computer on the bridge is recording the AIS data stream from the ship's AIS receiver and various ship motion and position related data streams like pitch & roll, GPS and speed as well as weather data.



(a) MAX-DOAS telescope attached to pan-tilt-head, seen from below



(b) 19-inch rack box on the bridge housing spectrometer and CCD, measurement computer on top

Figure 8.4.: Pictures of the MAX-DOAS telescope (a) at the Crew's nest and the spectrometer box (b) on the bridge level, photographed by the author

The spectrometer is an Andor Shamrock SR-303i imaging spectrograph, a grating spectrometer of "Czerny-Turner" design with a focal length of 303 mm. It includes a grating turret equipped with three different gratings. The grating in use is a 600 grooves/mm, 300 nm blaze angle grating, covering a wavelength range of 305 to 450 nm. To avoid thermal expansion-induced wavelength shifts, the spectrometer is located in an isolated box and actively stabilized at a temperature of $(35.0 \pm 0.1) ^\circ\text{C}$.

For the acquisition of the spectra, the spectrograph is connected to an Andor Newton 940 USB CCD detector with a resolution of 2048×512 pixels and a pixel size of 13.5×13.5 microns, thermoelectrically cooled to -35 °C.

8.1.2 Measurement geometry

The telescope was mounted to the railing at the crow's nest of the ship, pointing orthogonal to the ship's heading towards portside, as it is sketched in Fig. 8.5. In the ship's angular reference system this is equivalent to 270° , whereas the ship's heading is defined as 0° . Outside of harbors, during sailing or anchoring, this is the only azimuthal viewing direction in use. When the ship is moored in harbor, additional or other viewing directions can be used to cover possible emission sources or other regions-of-interest. In this main viewing direction of 270° , vertical (elevation) scans are performed, like it is sketched in Fig. 8.6. The scan sequence starts at -2° elevation, pointing slightly below the horizon onto the sea surface and continues going up in 1° steps until 10° elevation, followed by 15° , 30° and a zenith-sky reference measurement in 90° elevation.

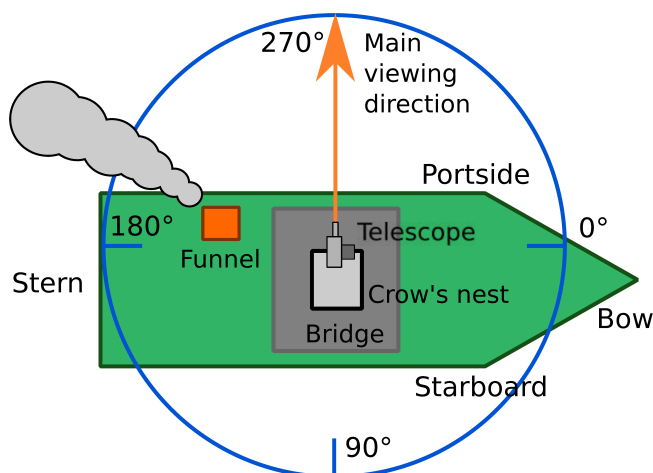


Figure 8.5.: Schematic bird's eye view of the vessel, showing the MAX-DOAS telescope's viewing direction as an orange arrow and marking the approximate position of the ship's funnel with respect to the instrument. The reference system for azimuthal viewing directions is indicated by the stated angle specifications. Provided that the direction of the ship's heading is defined as 0° , the main viewing direction pointing orthogonally to the ship towards portside counts as 270° azimuth.

As a ship is not a stable platform and is moved by the waves, the set value for the elevation angle of the pan-tilt-head can deviate from the real viewing elevation, depending on the respective tilting angle of the ship. Since the telescope points orthogonally to the ship's longitudinal axis, especially the ship's roll movement (see Fig. 8.7) plays an important role here. To avoid any significant changes in the pointing direction during the measurements,

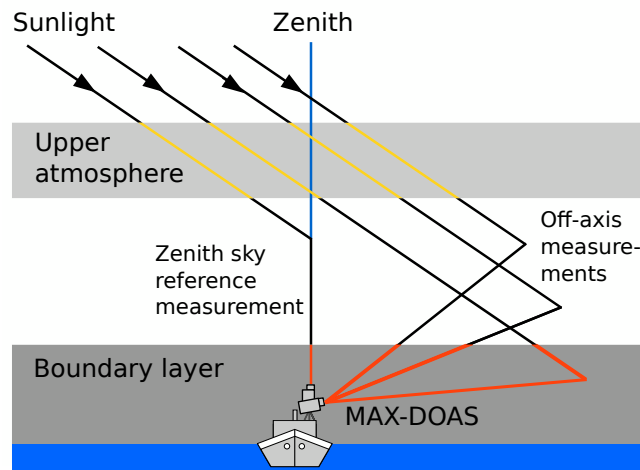


Figure 8.6.: shipborne MAX-DOAS measurement geometry for an example SZA of 55° . The lower the elevation angle, the longer the light path through the boundary layer. The photon path through the stratosphere is approximately the same for all, so that by taking a zenith-sky measurement as a reference, the absorptions in the upper atmosphere cancel out.

the individual measurements are taken with a very short exposure (or integration) time of 0.1 s. At each elevation angle, this is done repeatedly for 5 seconds and each individual measured spectrum is saved. After that, the pan-tilt-head moves to the next elevation angle. In the zenith direction, the total acquisition time is 15 seconds. The ship's movement is also the reason for the selection of negative elevations in the measurement sequence, which work as a safety margin.

Hence, the elevation angle recorded as metadata to each individual spectrum can be way off and does not reflect the real measurement elevation. The correction and sorting of viewing directions is applied in the data analysis afterwards, the procedure is described in Section 8.1.5.

Opposed to the stationary MAX-DOAS measurements on Neuwerk, where the measurement sequence was restricted to very low elevation angles pointing nearly horizontally towards the horizon to capture ship emissions up to 15, maybe 20 kilometers away from the instrument in five different azimuth directions with a high frequency and, therefore, time resolution, the aims of the shipborne measurements are more widespread. Possible emitters, like other ships, could pass at any distance and are not restricted to a certain pathway several kilometers away, like on Neuwerk. For closer emitters, higher elevation angles are needed. Pollution plumes above the ship could be missed by too shallow light paths from too low elevation angles.

For the comparison of ground-based MAX-DOAS measurements, or ship-based in this case, with satellite measurements, the slant column densities of both methods have to

be converted to vertical trace gas columns through the atmosphere. For higher elevation angles like 10° or 15° or 30°, the calculation of the necessary air mass factors (AMFs) is much easier, and can even be done approximately in a simple geometric way.

This means that a large spread of elevation angles is aimed for, lower ones for the enhanced sensitivity to the boundary layer (see Section 5.4) as well as higher ones for elevated plumes or satellite comparisons. This is sketched in Fig. 8.6 as compared to Fig. 6.5 (page 84) for the Neuwerk measurements. To have a reliable measurement sequence given the possible ship-movement-induced deviations of a few degree, the vertical scan on the ship includes even more angles in smaller steps, to have enough measured spectra to be sorted into each angle category afterwards. The procedure is described in detail in Section 8.1.5.

8.1.3 DOAS fit settings

The DOAS fit settings for the retrieval of the trace gas slant columns of nitrogen dioxide (NO₂) and sulfur dioxide (SO₂) from the measured spectra are listed in Table 8.3 and 8.4, respectively.

Table 8.3.: DOAS fit settings for the retrieval of NO₂

Parameter	NO ₂ fit
Fitting window	338–370 nm
Polynomial degree	4
Intensity offset	Constant
Zenith reference	Sequential [*] / noon [†] / fixed [‡]
SZA limit	Up to 80° SZA
O ₃	223 K & 243 K (Serdyuchenko et al., 2014)
NO ₂	298 K (Vandaele et al., 1996)
O ₄	293 K (Thalman and Volkamer, 2013)
HCHO	297 K (Meller and Moortgat, 2000)
Ring	SCIATRAN (Rozanov et al., 2014)

^{*} Interpolation in time between the zenith measurements directly before and after the off-axis scan

[†] Daily zenith spectrum with lowest SZA (highest sun)

[‡] One fixed zenith spectrum for a longer time series over several days (e.g., one cruise)

Table 8.4.: DOAS fit settings for the retrieval of SO₂

Parameter	SO ₂ fit
Fitting window	307.5–317.5 nm (2016 data: 307.85–317.5 nm)
Polynomial degree	3
Intensity offset	Constant & slope
Zenith reference	Sequential [*] / noon [†] / fixed [‡]
SZA range	Up to 65° SZA
O ₃	223 K & 243 K (Serdyuchenko et al., 2014)
NO ₂	298 K (Vandaele et al., 1996)
SO ₂	293 K (Bogumil et al., 2003)
Ring	SCIATRAN (Rozanov et al., 2014)

^{*} Interpolation in time between the zenith measurements directly before and after the off-axis scan

[†] Daily zenith spectrum with lowest SZA (highest sun)

[‡] One fixed zenith spectrum for a longer time series over several days (e.g., one cruise)

8.1.4 Auxiliary data: RV Celtic Explorer’s onboard sensor data logging and AIS

Logging of the ship’s onboard sensor information data is crucial for the DOAS data analysis and the interpretation of the measurement results. Without an automatic balancing system to keep the telescope level, the ship’s motion reference unit data, especially the roll angle data (see Fig. 8.7), is essential for the viewing angle correction and assignment of the “true” elevation angles to the measured spectra, which is described in Section 8.1.5.

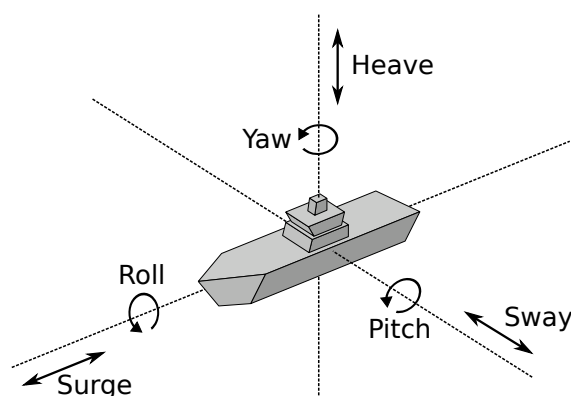


Figure 8.7.: The 6 degrees of freedom for a ship’s movement along the 3 principal axes: 3 rotational modes include pitch (rotation along the transverse axis), roll (rotation along the longitudinal axis) and yaw (rotation along the vertical axis), 3 translational modes include sway (translation along the transverse axis), surge (translation along the longitudinal axis) and heave (translation along the vertical axis)

The ship's gyro compass provides the ship's heading, from which the viewing azimuth angle can be derived to know the viewing direction of the measurements, but also to compute the correct relative azimuth angle (RAA) to the sun. For this, also the sun's absolute position or more specifically the solar zenith angle (SZA) and the solar azimuth angle (SAA) has to be known, which can only be computed if the ship's location (longitude & latitude) is known, which is provided by the ship's GPS. To enable the MAX-DOAS measurement software to start and stop the measurements at the right times during dusk and dawn, the measurement software has to be connected to the GPS data stream, or the position has to be set and updated manually in the software with a sufficient frequency. The ship's location is, of course, also very important for the interpretation of the measurements afterwards.

Wind information is not only important for the interpretation of the measurements, but also if under certain wind directions the air pollution measurements might be contaminated by the ship's own exhaust gases from its funnel (compare Fig. 8.5) and thus affected measurements would have to be filtered out. For this, knowledge about the relative wind direction and wind speed on the vessel due to the interaction of wind and ship movement is essential, but also the ship's speed log giving hints on the machine's load might help. For a definition of the relative or apparent wind see Fig. 8.8. In Section 8.1.7, a possible influence of such a contamination on the MAX-DOAS and in-situ measurements is investigated.

Not only wind data, but also weather information like temperature, pressure and humidity is provided by the RV Celtic Explorer during the cruise, which is also helpful for the data analysis. There is even more information available on the Celtic Explorer, for example course, ground speed, water depth and water temperature.

All the mentioned data is logged by the ship's technician and available after each cruise. With support of the ship's technician it is also possible to read and record¹ the various data streams via custom made cables on a computer's RS232 communication port² on our measurement computers on the bridge. This is especially helpful for the GPS data stream which is fed directly into the measurement software.

For the reception of the automatic identification systems (AIS, see Section 6.1.5) signal broadcasted by the ships, on the first cruises (see Table 8.1 for a list of all campaigns) an own AIS antenna was installed at the crew's nest in combination with an own AIS-receiver similar to the system used on Neuwerk. However, it proved to be more feasible to directly read the ship's AIS data stream from the ship's own AIS receiver into the AIS-logging software "Shipplotter", as the ship's antenna has a much better reception characteristic and receives AIS messages broadcasted from much more distant ships. On the later cruises,

¹E.g. with the "Putty" software, or the "ExtraPutty" software if no timestamp is included in the data stream and has to be logged simultaneously

²One RS232 port for each data stream

therefore the ship's AIS data stream was read into our computers³ instead of our own system, which was merely held available as an emergency backup.

Due to the collaboration of IUP Bremen and the BSH, in theory also the water body analysis and oceanographic data captured by the BSH is available for the support of the measurement analysis if needed.

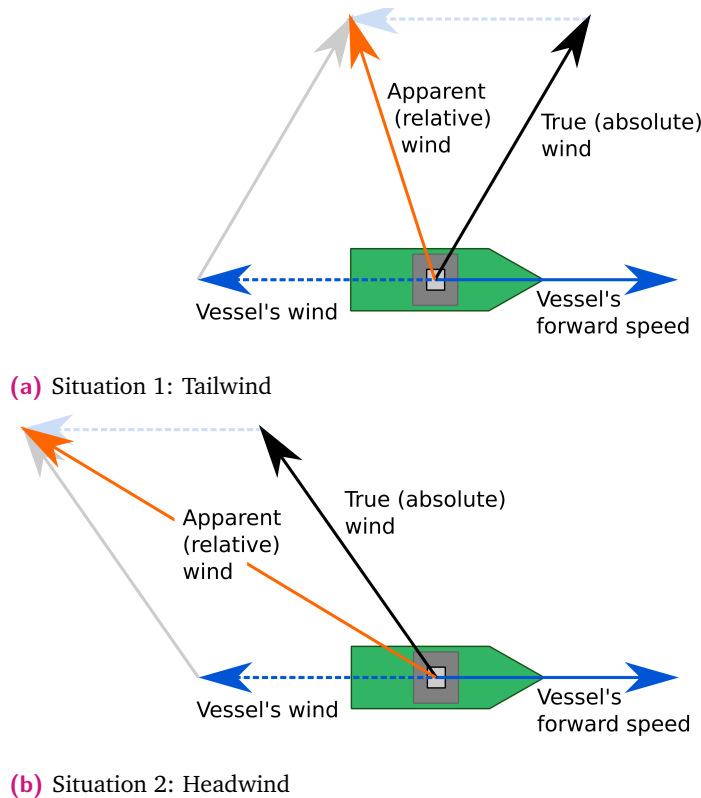


Figure 8.8.: Apparent (relative) wind as the vector sum of the absolute (true) wind and the ship's wind created by the ship's movement. The apparent wind is the perceived wind on the moving ship, which has a different wind direction and speed as the absolute (true) wind field. Subfigure a shows how even if the true (absolute) wind is a tailwind the perceived (apparent) wind can still be a headwind, depending on the relative speeds. Subfigure b shows how true headwind is enhanced by the ship's wind (and shifted in direction).

8.1.5 Ship movement correction (roll angle correction)

As already mentioned in Section 8.1.2, the ship's movement due to the waves leads to a deviation between the angular position to which the pan-tilt-head was set and the "true" viewing direction at which the MAX-DOAS telescope points at, which can be several degrees. Figure 8.7 shows the 6 degrees of freedom for a ship's movement along its principal axes.

³Also via an RS232 port

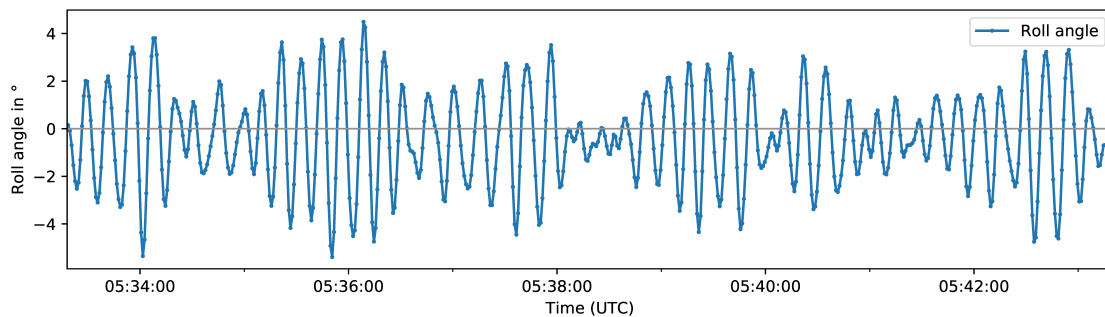
Since the MAX-DOAS telescope is measuring orthogonally to the ship's longitudinal axis towards portside (see Fig. 8.5 in Section 8.1.2) and performs only vertical (elevation) scans (i.e., no azimuthal movement) during cruising, the ship's roll angle has the strongest influence on the elevation angle uncertainty, while the contributions of the other movement modes are expected to be small and therefore negligible.

As mentioned in Section 8.1.2, the individual spectra are measured with an exposure time (or integration time) of 0.1 seconds. At first, the metadata of the spectra contains the elevation angle how it was set in the pan-tilt-head control. If these spectra were to be simply co-added like it is normally done for ground-based MAX-DOAS stations, measurements in different "true" elevation angles would mix and lead to false results. Such an example can be seen in Fig. 8.10a. The plotted DSCD of the oxygen collision complex O_4 depends only on the oxygen molecule concentration and is therefore an ideal proxy for the light path length, with longer light paths in lower elevations resulting in larger O_4 DSCDs.

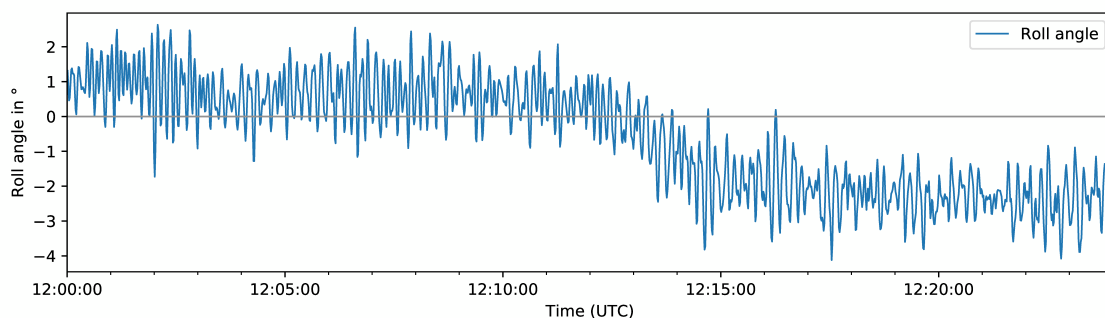
To correct for the elevation angle deviation, the roll angle data from the ship's motion reference unit (MRU) is used, a Kongsberg Seapath 330+ with a roll and pitch accuracy of $\pm 0.01^\circ$ (for $\pm 5^\circ$ amplitude) and a maximum output data rate of 200 Hz (Kongsberg Maritime, 2020). For the scientific crew, the roll and pitch data is only available with a frequency of 1 Hz, which, due to the harmonic nature of the oscillation, is still sufficient to capture the ship's motion. Figure 8.9 provides examples of some roll angle data from 2015.

In the correction algorithm, before the co-adding of the spectra, to each individual 0.1 s-spectrum's elevation angle the mean roll angle between start and end time of the measurement is added. Depending on the direction into which the ship is tilted, this correction is either positive or negative. The resulting value for the corrected elevation is a fractional number. To limit the final number of elevation angles in the data to a reasonable, manageable number, the co-adding of the spectra to the final elevations is performed with a safety margin $\Delta\alpha$, whose size depends on the elevation: For all elevation angles up to 8° , $\Delta\alpha$ is $\pm 0.5^\circ$ (equivalent to simply rounding the values), for 10° elevation it is $\pm 1^\circ$, for 15° elevation it is $\pm 2.5^\circ$, for 30° elevation it is $\pm 5^\circ$ and for 90° (zenith direction) it is $\pm 10^\circ$. This means, that, for example, all spectra with corrected, true elevations between 12.5° and 17.5° are co-added and counted as 15° elevation. In the procedure of co-adding, also the location is updated from the ship's GPS data and the location from the spectrum in the center of the co-adding period is taken as representative for the final co-added (integrated) spectrum.

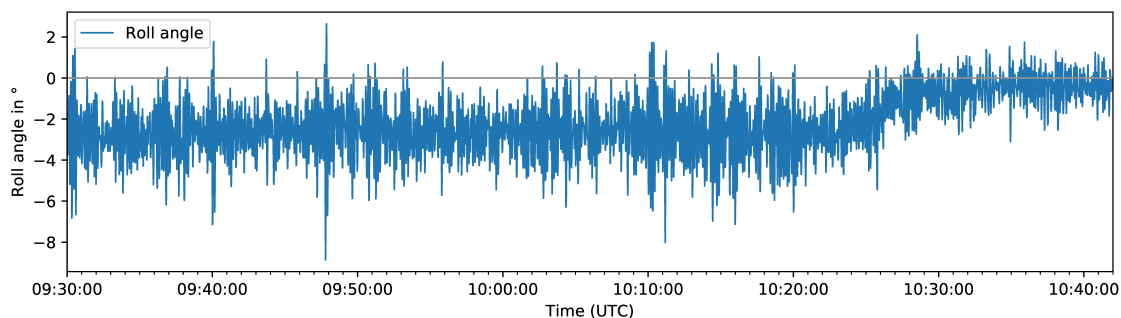
The result is shown in Fig. 8.10b, where, as opposed to Fig. 8.10a, the separation of the elevation angles due to the light path differences is clearly visible. Although still quite noisy due to the short integration time, the roll correction algorithm clearly assigned the correct elevation angles to the spectra.



- (a) 10 minutes of roll data on 18 August 2015, showing the harmonic motion of the ship triggered by the waves, with a main frequency of approximately 5 min^{-1} ($\sim 0.2 \text{ Hz}$) and a maximum amplitude of about 5° . The visible interference pattern reveals that the ship's movement is a superposition of multiple harmonic motions with different frequencies.



- (b) 25 minutes of roll data on 23 August 2015, illustrating how the ship having list due to the wind introduces a systematic bias or shift of the equilibrium position of the oscillating roll movement to one side. In this example, at first the ship is tilted approximately 1° to one side on average. Around 12:13 UTC the ship turns by 135° while its course is changed from west to northeast (compare the ship's track in Fig. 8.21, in the north of Scotland at 60° N). This drastically changes the direction from which the wind hits the vessel, leading to the ship being tilted to the other side by about 2.5° on average.



- (c) 70 minutes of roll data on 23 August 2015, showing how both the amplitude and systematic bias of the equilibrium position of the oscillating roll movement are reduced after the ship stopped at 10:25 UTC and was turned into the wind.

Figure 8.9.: Examples of roll angle data measured by the RV Celtic Explorer's motion reference unit on the 2015 summer survey cruise

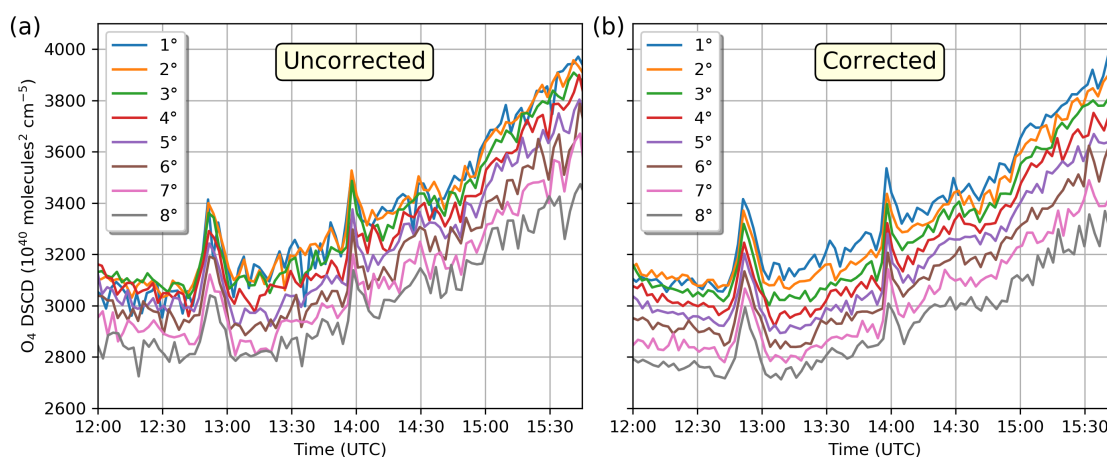


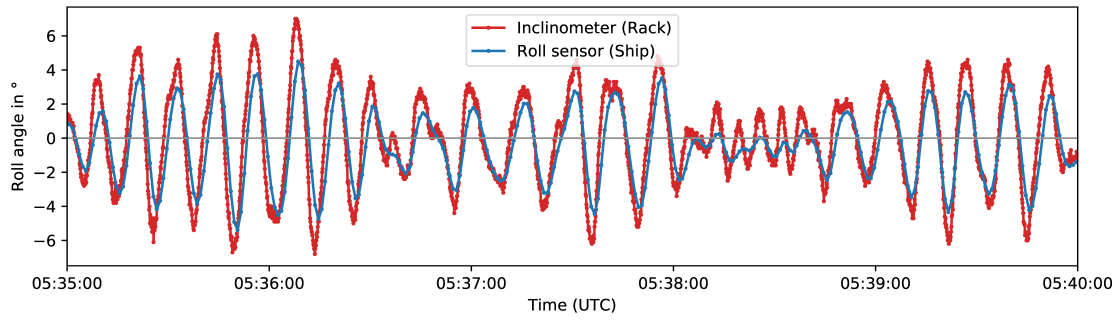
Figure 8.10.: O₄ DSCDs in elevation angles 1° to 8° in the afternoon of 24 August 2015 for uncorrected (a) and roll corrected (b) data. The uncorrected data in panel a shows a mix up of the different elevation angles, especially for the lower angles, due to the ship's roll movement in the waves. The elevation angles shown here are clearly wrong and mixed up. This is caused by the co-adding of spectra from different elevations into one. Whereas the roll-corrected data in panel b shows the expected separation of the elevation angles with higher O₄ DSCDs in the lower elevations due to longer light paths.

8.1.6 Inclinometer sensor evaluation

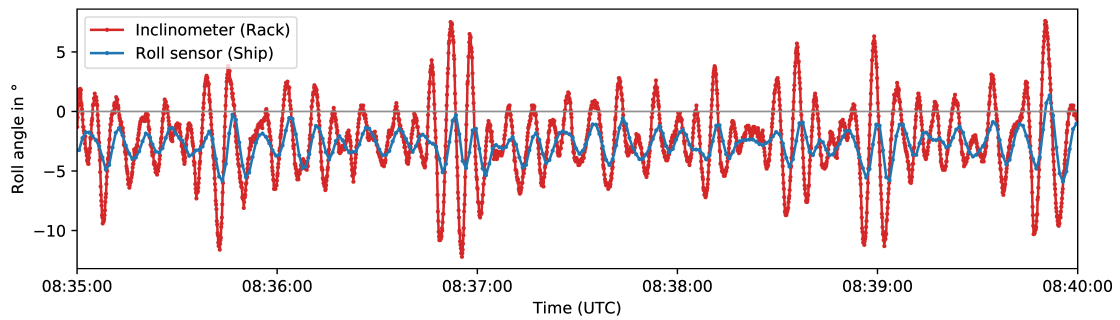
During the Celtic Explorer cruises, a small dual-axis semiconductor-based inclinometer⁴ using the open-loop MEMS (micro-electro-mechanical systems) technology has been tested as a backup system for the ship's roll angle sensor. It was installed in the DOAS rack box on the bridge. Compared to the ship's sensor data which is only available at 1 Hz, the advantage it could provide is a higher roll angle measurement frequency due to the short readout time. This would even allow to smooth the roll angle measurement curves, e.g. by averaging of values.

Figure 8.11 shows example time series of inclinometer data in comparison with the ship's roll angle readings from the ship's motion reference unit. The first two panels show data from the summer cruise in 2015, the other two panels show data from 2016. In panel a, although the agreement between both curves is quite good, the inclinometer shows systematically slightly higher values than the ship's roll sensor. The degree of agreement is very variable during the cruise. For example in panel b, showing roll angle data from three days later with a much higher roll movement (oscillation) frequency, the agreement is much worse. Maxima and minima of the measured oscillating signal fit well together, but the amplitude of the inclinometer signal is much higher than the roll sensor's readings.

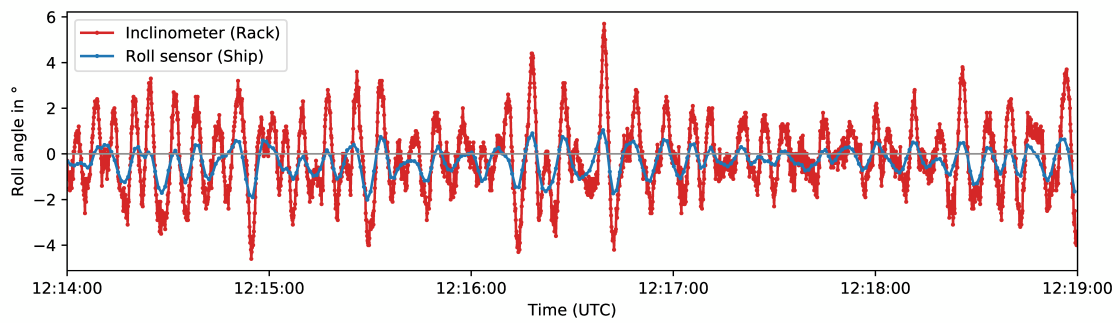
⁴AIT-720-001-30 inclinometer, manufacturer: Althen GmbH Mess- und Sensortechnik (www.althensensors.com), measurement range: ±30°, analogue output signal proportional to the sine of the angle, non-linearity < 0.5%, 10 Hz



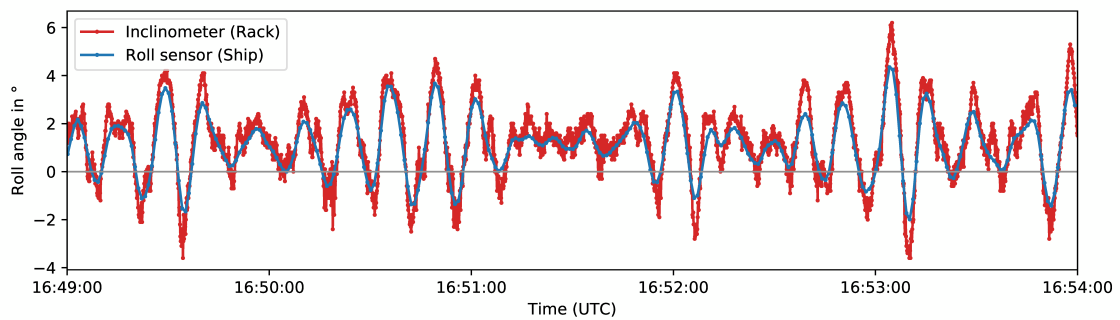
(a) 18 August 2015, 5:35 – 5:40 UTC



(b) 21 August 2015, 8:35 – 8:40 UTC



(c) 13 August 2016, 12:14 – 12:19 UTC

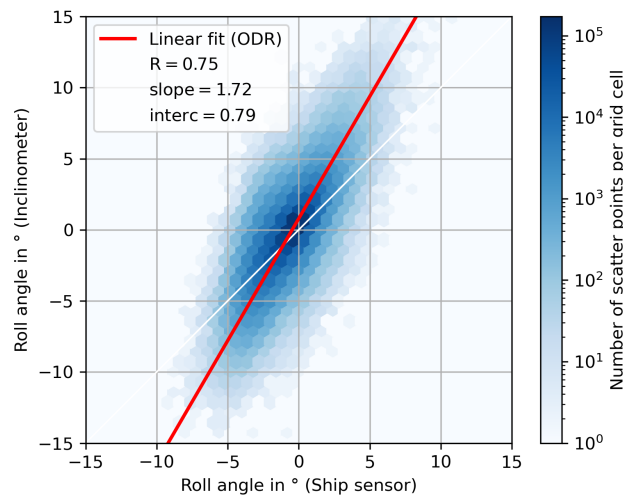


(d) 13 August 2016, 16:49 – 16:54 UTC

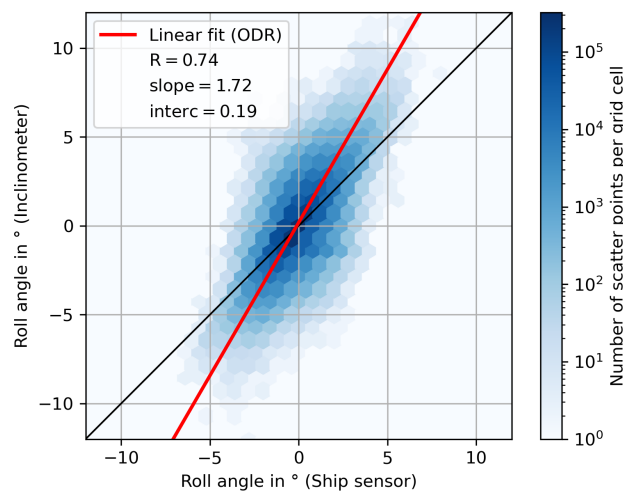
Figure 8.11.: Four examples of 5 minutes of roll angle measurements from the inclinometer compared to the ship's motion reference unit's roll data.

The scaling factor needed to bring both signals together varies between 2 and 4, maybe 5 times the amplitude.

In the data from 2016, the behavior is similar. The degree of agreement can also vary strongly over the day. Just a few hours elapsed between the situation in panel c, where again the phase and the general pattern agree well but the amplitude is way off, and panel d, where the agreement is very good, with the inclinometer's roll amplitude being only very slightly higher. The changing level of agreement can both be seen in the data from 2015 and 2016.



(a) Data from the first leg of the 2015 summer survey cruise: 10 – 25 August 2015



(b) Data from the first leg of the 2016 summer survey cruise: 5 – 23 August 2016

Figure 8.12.: Scatter plot: Roll angle measurements from the inclinometer in the rack box on the bridge vs. the ship's motion reference unit's roll sensor for 2015 (a) and 2016 (b).

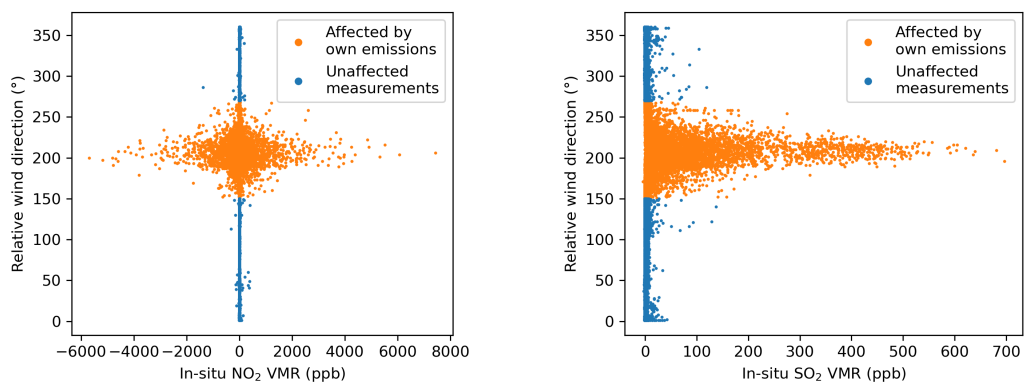
Figure 8.12 shows the corresponding scatter plots for the 2015 and 2016 cruises. The correlation between inclinometer and the ship's roll sensor is quite good but also some scatter is visible. The slope is clearly deviating from unity, giving 1.72 for both cruises, confirming the presumed systematic overestimation by the inclinometer. The spread of the values indicates how variable this factor is.

Several possible error sources for the observed overshooting come to mind. The fact that periods with very good agreement exist eliminates the possibility of a bad calibration of the inclinometer's analogue output signal via offset and scale. In contrast to the ship's MRU, the inclinometer is only an accelerometer and contains no additional gyroscope, and might be prone to overshooting for some movement intensities and frequencies. An earlier investigation in Seyler (2011), also discussed in Peters (2013), showed that the inclinometer is in fact susceptible to shock. It is also possible that the inclinometer, the 19 inch rack shelf where it is mounted or the rack box itself are not completely fixed and move a bit with the wave movement of the ship. It is also very probable, that the inclinometer was not perfectly aligned in parallel to the ship's transverse and longitudinal axes. This would result in a cross-talk and interference of the roll movement with the pitch movement of the vessel (see Fig. 8.7 for the rotational degrees of freedom of a ship).

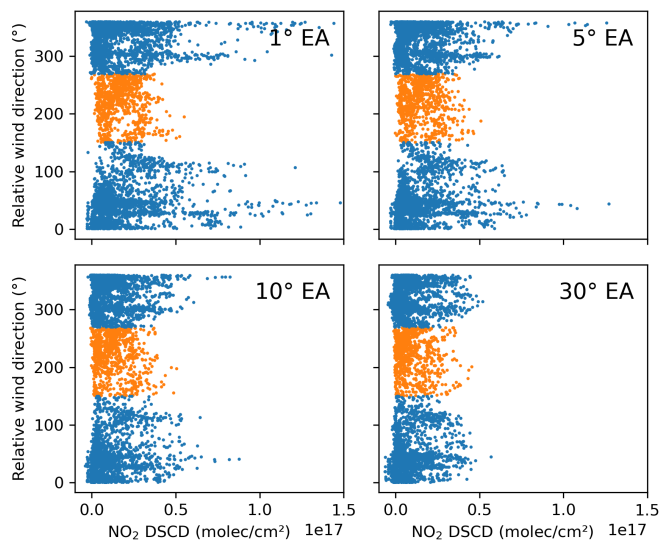
As a result, the ship's MRU data is used for the roll angle correction due to the much higher precision of its sensor.

8.1.7 Possible contamination of measurements by the ship's own exhaust emissions?

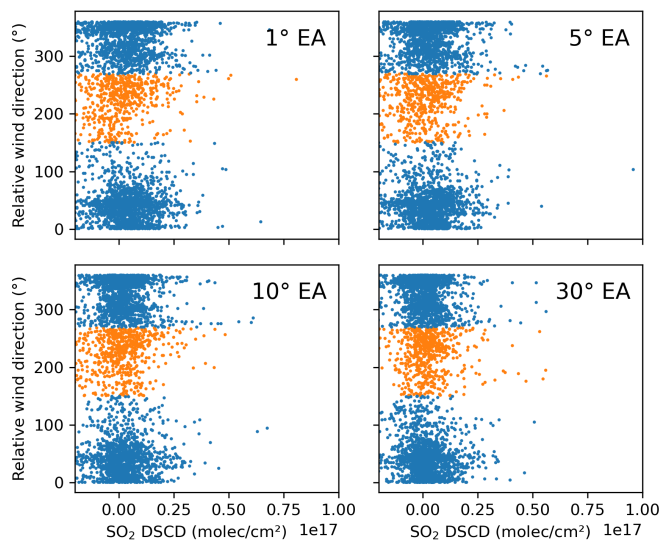
A possible contamination of the air quality measurements by exhaust gases from the ship's own stack under certain apparent (relative) wind directions is investigated in Fig. 8.13 for the 2015 summer survey cruise. As can be seen from the figure, the measurements of the in-situ trace gas analyzers for NO₂ and SO₂ are strongly impacted by the ship's own exhaust under relative wind directions between 150° and 270° (see Fig. 8.5 for the angle definition). Measuring the undiluted plume, in-situ SO₂ volume mixing ratios from this angular range are much higher than from any other relative wind direction, while NO₂ mixing ratios show unrealistically high positive but also strongly negative NO₂ mixing ratios indicating instrumental problems at such high concentrations. In the MAX-DOAS measurements, neither the NO₂ DSCDs nor the SO₂ DSCDs seem to be significantly enhanced when the wind is coming from the specified angular range or any other direction, which is the case at all elevation angles and regardless whether a fixed reference spectrum was used or a close-in-time sequential reference spectrum. This indicates, that the MAX-DOAS measurements are not affected that much from the ship's own exhaust gas plume and the contribution of the ship's plume NO₂ or SO₂ to the integrated column amounts is small.



(a) In-situ NO₂ volume mixing ratios (b) In-situ SO₂ volume mixing ratios



(c) MAX-DOAS NO₂ DSCDs at different elevation angles (EAs) using a fixed reference spectrum



(d) MAX-DOAS SO₂ DSCDs at different elevation angles (EAs) using a sequential reference spectrum

Figure 8.13.: Relative wind direction dependence of the measured in-situ NO₂ and SO₂ VMRs and MAX-DOAS NO₂ and SO₂ DSCDs during the Celtic Explorer 2015 summer survey cruise. The angular range of apparent wind directions where in-situ measured air is contaminated by the ship's own exhaust plume is highlighted in orange.

Hence, while filtering out data with specific relative wind directions is crucial in the in-situ data analysis (see Kattner, 2019), for the MAX-DOAS measurements, in the following no filtering for relative wind directions will be applied. For most parts of the investigated cruises, the dominant apparent wind direction is a headwind anyhow.

8.1.8 Overview on previous studies

Shipborne MAX-DOAS measurements of NO₂ and SO₂ have been conducted in various regions all over the world:

Takashima et al. (2012) performed shipborne MAX-DOAS measurements of NO₂ during two ocean cruises around Japan over the western Pacific and Indian Ocean, finding a clear land-ocean contrast in NO₂ amounts. The authors applied a profile retrieval algorithm to their measurements to retrieve boundary layer concentrations.

Peters et al. (2012) conducted shipborne MAX-DOAS measurements of formaldehyde and NO₂ during the TransBrom campaign over the western remote Pacific for satellite validation purposes.

Schreier et al. (2015) presents shipborne MAX-DOAS measurements of NO₂ and SO₂ in the South China and Sulu Sea from the SHIVA campaign, and also retrieved vertical pollutant profiles and compared the results to satellite measurements.

Tan et al. (2018) performed shipborne MAX-DOAS measurements of NO₂, SO₂, and formaldehyde (HCHO) in the East China Sea area in June 2017 and compared their data to satellite measurements.

8.2 Celtic Explorer 2013: SO₂ and NO₂ from ships

As the MAX-DOAS measurements on Neuwerk already showed, to find a clear SO₂ signal from ships in passive MAX-DOAS measurements in the North Sea emission control area (ECA), one needs to go back to the years before 2015, before the stricter fuel sulfur content limits were introduced. This is even more relevant for the shipborne MAX-DOAS measurements presented here, which have a worse signal-to-noise-ratio than the stationary two-channel instrument on Neuwerk due to the instrument's broader wavelength range and much shorter integration time. In this section, MAX-DOAS measurements of SO₂ and NO₂ taken on the first leg of the Celtic Explorer Summer Survey Cruise 2013 are presented showing both SO₂ and NO₂ signals from individual ships.

8.2.1 The Celtic Explorer Summer Survey Cruise 2013

The first leg of the Celtic Explorer Summer Cruise 2013 (see Table 8.1 for an overview of all shipborne campaigns on the RV Celtic Explorer) started in Hamburg and ended in Bergen, Norway. After the setup of the instruments on 10 August 2013 in the port of Hamburg, the ship left the port in the evening of the same day.

After a 21 day cruise in the North Sea with a detour/side-trip down through the English Channel into the Bay of Biscay, the ship reached the city of Bergen on 31 August 2013. The cruise track, which meanders serpentine-like from south to north through the North Sea covering all BSH measurement points located on a 1°-latitude-grid, is plotted in Fig. 8.14.

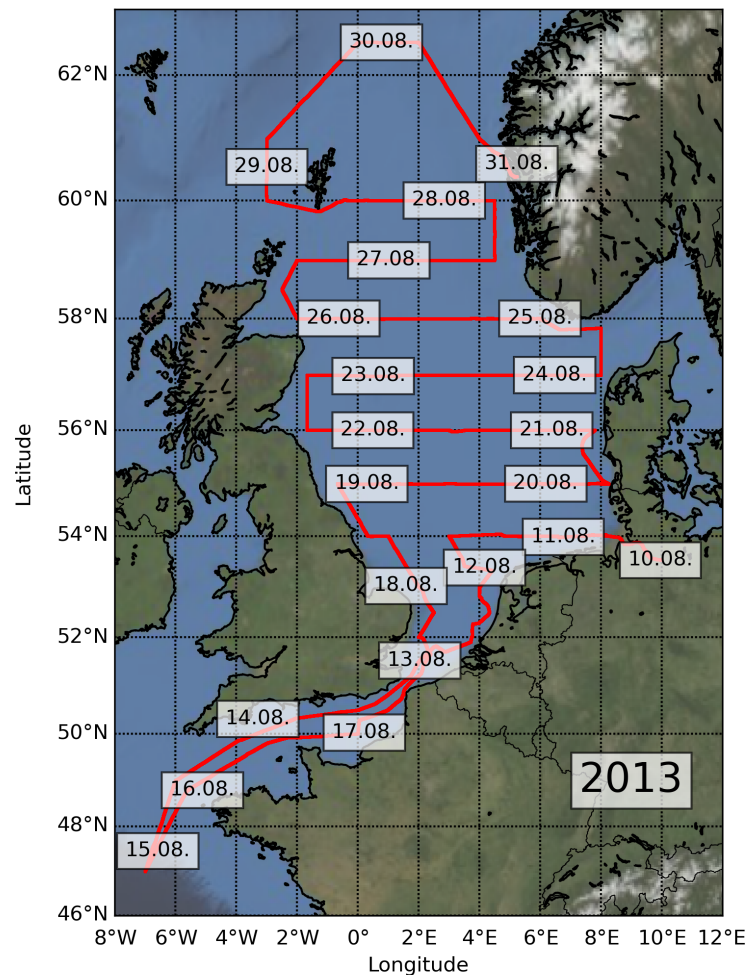


Figure 8.14.: Cruise track of the first leg of the Celtic Explorer Summer Survey 2013. The date labels for each day are centered at the respective position of the ship at 12:00 UTC.

In Bergen, both the ship's and the scientific crew was exchanged for the second leg of the cruise, which began on 5 September 2013. The second leg covered the German part of the North Sea in more detail and finally the German part of the Baltic Sea, ending in Kiel on 17 September 2013. The cruise track of the second leg is shown in Fig. 8.15. As an exception, on this cruise the air quality measurement devices including the MAX-DOAS instrument stayed on-board fully operational even after the official end of the BSH summer survey on the Celtic Explorer's way back to its home port in Galway, Ireland. The ship's track on this addendum to the cruise is plotted in Fig. 8.16.

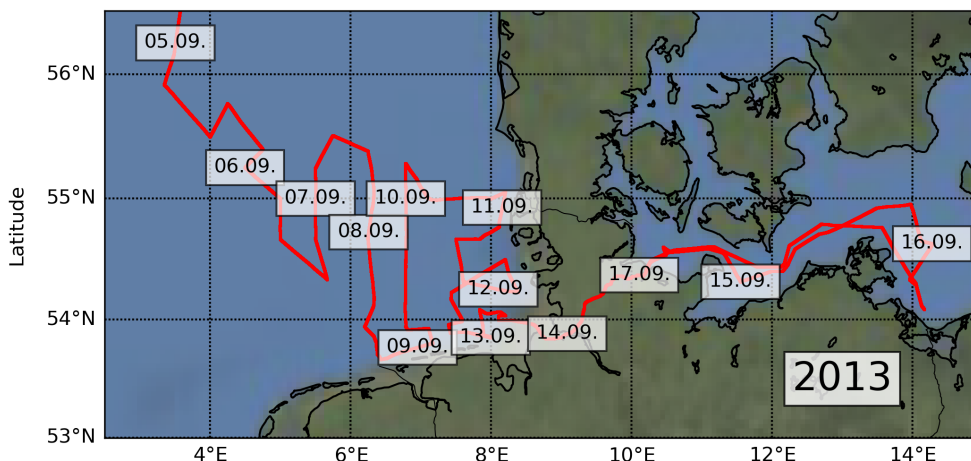


Figure 8.15.: Cruise track of the second leg of the Celtic Explorer Summer Survey 2013. The date labels for each day are centered at the respective position of the ship at 12:00 UTC.

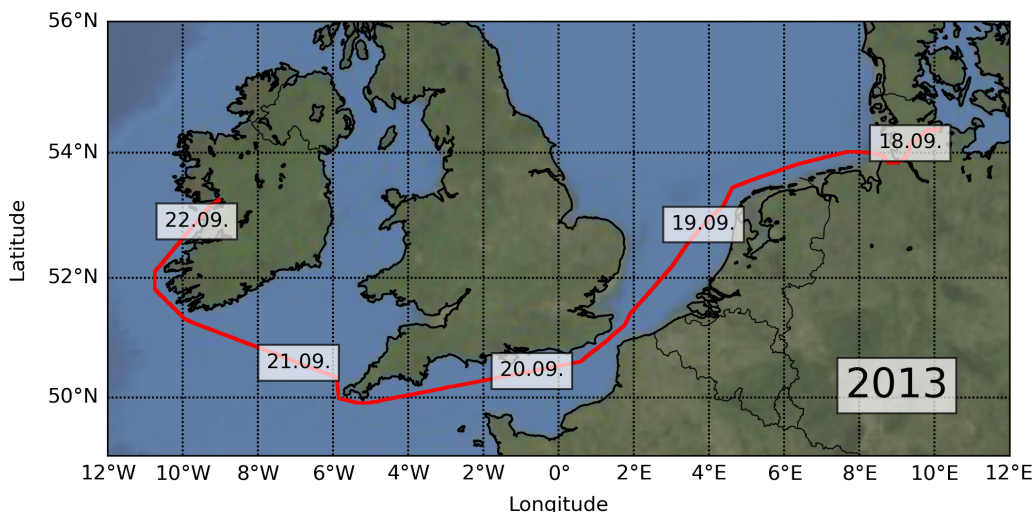


Figure 8.16.: Cruise track of the addendum of the Celtic Explorer Summer Survey 2013. The date labels for each day are centered at the respective position of the ship at 12:00 UTC.

8.2.2 SO₂ and NO₂ emissions from individual ships

21 August 2013 was one of the days with the best weather conditions for MAX-DOAS measurements during the summer cruise 2013, a sunny day with mostly clear sky conditions. Figure 8.17a, showing this day's ship track as well as the MAX-DOAS SO₂ DSCDs measured in 4° elevation (10-min means), reveals that as the Celtic Explorer sailed westward several ships crossed its path on this day. The size of these ships ranged from 133 m to 293 m (see Table 8.5), the largest being a cruise ship which was in AIS reception range between 10:39 and 10:45 UTC. Small ships <50 m like pleasure crafts or sailing boats are omitted, as they are not expected to emit enough SO₂ to cause an enhanced signal in the MAX-DOAS measurements.

Table 8.5.: Ship encounters on 21 August 2013 (only ships ≥ 50 m)

Time* (UTC)	Longitude†	Length (m)	Ship type	Speed† (kn)	Heading†
9:18 – 9:36	7.09°E	133 m	Cargo ship	15.9	209°
9:22 – 9:38	7.05°E	140 m	Cargo ship	10.7	215°
9:46 – 10:06	7.00°E	199 m	Cargo ship	16.5	27°
9:50 – 9:56	6.91°E	180 m	Cargo ship	12.6	24°
10:17 – 10:31	6.80°E	145 m	Tanker	10.3	31°
10:39 – 10:45	6.68°E	293 m	Cruise ship	18.5	37°
11:50 – 12:08	6.36°E	169 m	Cargo ship	15.0	335°

* Time span, in which the ship was in the reception range of our AIS antenna

† Mean value over the encounter

The MAX-DOAS measurements show SO₂ enhancements of up to 3×10^{16} molec cm⁻² in an ambient background SO₂ level of less than 5×10^{15} molec cm⁻². Comparing the SO₂ signal and the ship positions in Fig. 8.17a, one can see that for most SO₂ enhancements another ship was in the vicinity of the Celtic Explorer. There is a relatively broad SO₂ enhancement around 13:00 UTC with no ship in the immediate surrounding. Looking at the plotted wind vectors pointing in northeasterly direction implying a southwesterly wind direction the source for the elevated SO₂ DSCDs is most probable southwestward of the ships position. It could either be another unidentified ship which is further south and out of reach of our AIS antenna⁵ or another probable SO₂ emitter like one of the oil rigs to the southwest. The fact, that the enhancement is relatively broad speaks for an older, more diluted and dispersed plume, which would confirm the theory of a more distant emitter southwestward of the Celtic Explorer.

⁵Which is very probable, considering the very short reception range, as the short ship tracks show. The AIS antenna of the ship with a much better reception characteristic and much larger transmission reception range was first used on a later cruise.

Figure 8.17b shows a zoom into the most interesting period between 9 and 12 UTC, where several ships crossed the Celtic Explorer's path. As the ship moved westward, between 7.1°E and 7.0°E longitude it first came close to three cargo ships of 133 m, 140 m and 199 m length (see Table 8.5). SO₂ levels are clearly enhanced, the 5-min mean DSCDs go up to 2.7×10^{16} molec cm⁻². Only two separate SO₂ enhancements are visible in the data. The exact assignment to the individual ships is complicated by the short distance between the encounters which could have led to overlapping plumes. It could also be that one of the ships emitted less SO₂, either because of different sulfur contents in the fuel or due to slow steaming leading to reduced overall emissions (Cariou, 2011; Maloni et al., 2013). As the second one sailed at a much slower speed of 10 kn compared to the 16 kn of the other two, this could be a probable explanation. But like on Neuwerk, also the geometry of the MAX-DOAS instrument's line of sight (LOS) and the angle to the plume could play a role.

The next ship crossed the Celtic Explorer's path at 6.91°E longitude around 9:53 UTC. This cargo ship of 180 m length emitted apparently much less SO₂, as the highest measured DSCD values are only slightly elevated above the ambient background DSCD, reaching 1×10^{16} molec cm⁻² (5-min mean) at the maximum. The next ship, a tanker of 145 m length encountered at 6.8°E longitude around 10:20 UTC, apparently emitted even less SO₂, as no enhancement is visible in the measured DSCDs. Again, this ship was cruising at a relatively slow speed, but could also have had fuel with a very low sulfur content. The next ship encounter was with a very fast (18.5 kn) and large (293 m) cruise ship at 6.68°E longitude around 10:40 UTC. In the SO₂ time series, a very strong enhancement can be seen, with 5-min mean DSCDs going up to 4.5×10^{16} molec cm⁻², not even represented for in the colormap as the colorbar is saturated, indicating that the cruise ship is a larger SO₂ emitter than all the other ships encountered on this day. More than one hour later the Celtic Explorer came close to another cargo ship of 169 m length with apparently very moderate SO₂ emissions as the DSCDs are only slightly elevated above background.

To collect more hints on the question whether the lower emissions are a result of a lower fuel sulfur content, are due to steaming at a reduced speed to save fuel or simply are plume–light path geometry related, it helps to take a look into the simultaneous NO₂ measurements, as NO₂ emissions do not really depend on the fuel, but on the temperature and operating conditions of the ship's engine.

Figure 8.18 shows in a very similar way to Fig. 8.17 the NO₂ DSCDs measured in 4° elevation on this day. Comparing the number of measurements along the Celtic Explorer's cruise track on this day in Fig. 8.18a and Fig. 8.17a, one can see the longer diurnal measurement period for NO₂ due to more light at longer wavelengths at low sun conditions and thus different SZA limits for the SO₂ (here: SZA < 65°) and NO₂ (here: SZA < 80°) measurements to ensure an acceptable fit quality.

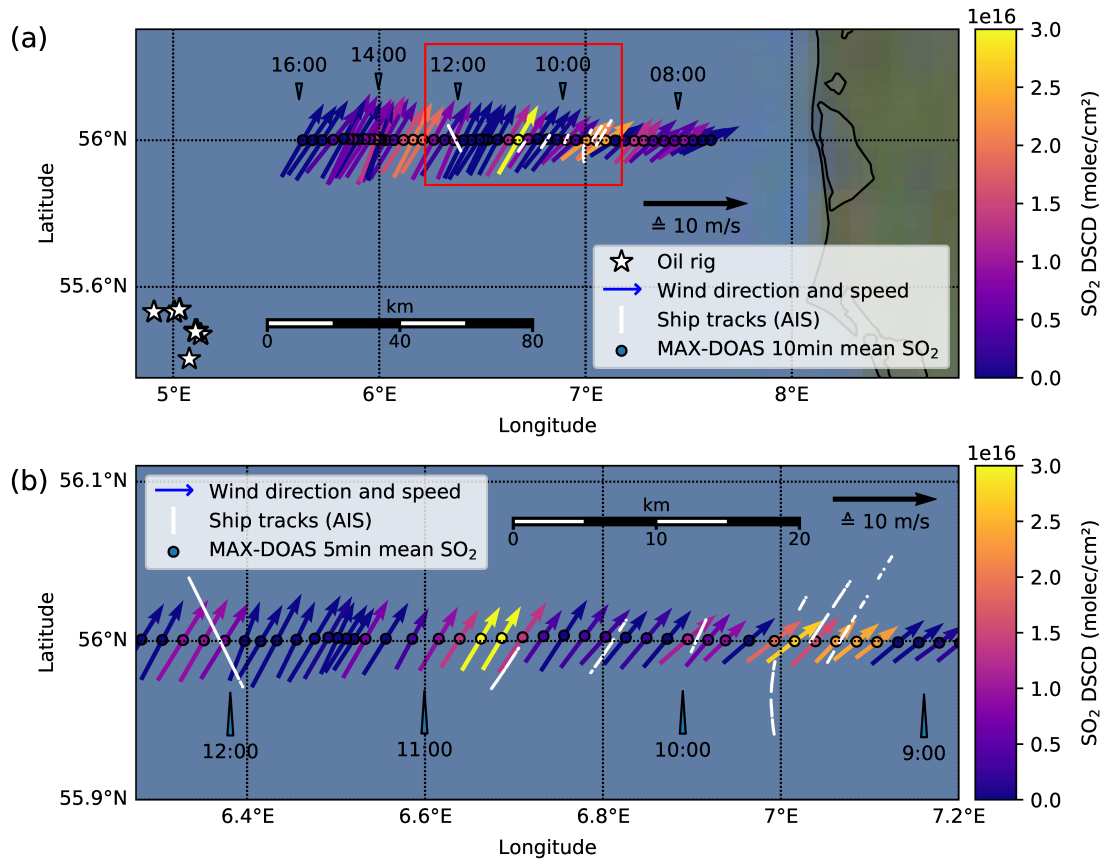


Figure 8.17.: Map showing MAX-DOAS SO₂ DSCDs measured in 4° elevation on 21 August 2013 in the North Sea at 56°N, close to the Danish coast (see Fig. 8.14 for the cruise track). The MAX-DOAS measurements are shown as colored circles at the respective position of the ship, the more yellowish the color, the higher the SO₂ DSCD (see colorbar). For source attribution, the absolute (or “true”) wind vectors are plotted in the same color as the MAX-DOAS DSCD “points”. For the assessment of the wind speed, a reference arrow which length represents a wind speed of 10 m/s is shown. White dots and lines show tracks of other ships (≥ 50 m) taken from AIS data. Operational oil rigs according to the OSPAR 2013 database are shown as white stars. Time labels denoting the ship position are in UTC. In panel a, 10-min mean DSCDs are plotted, in panel b, showing a zoom into the region marked with a red box, 5-min mean DSCDs are plotted.

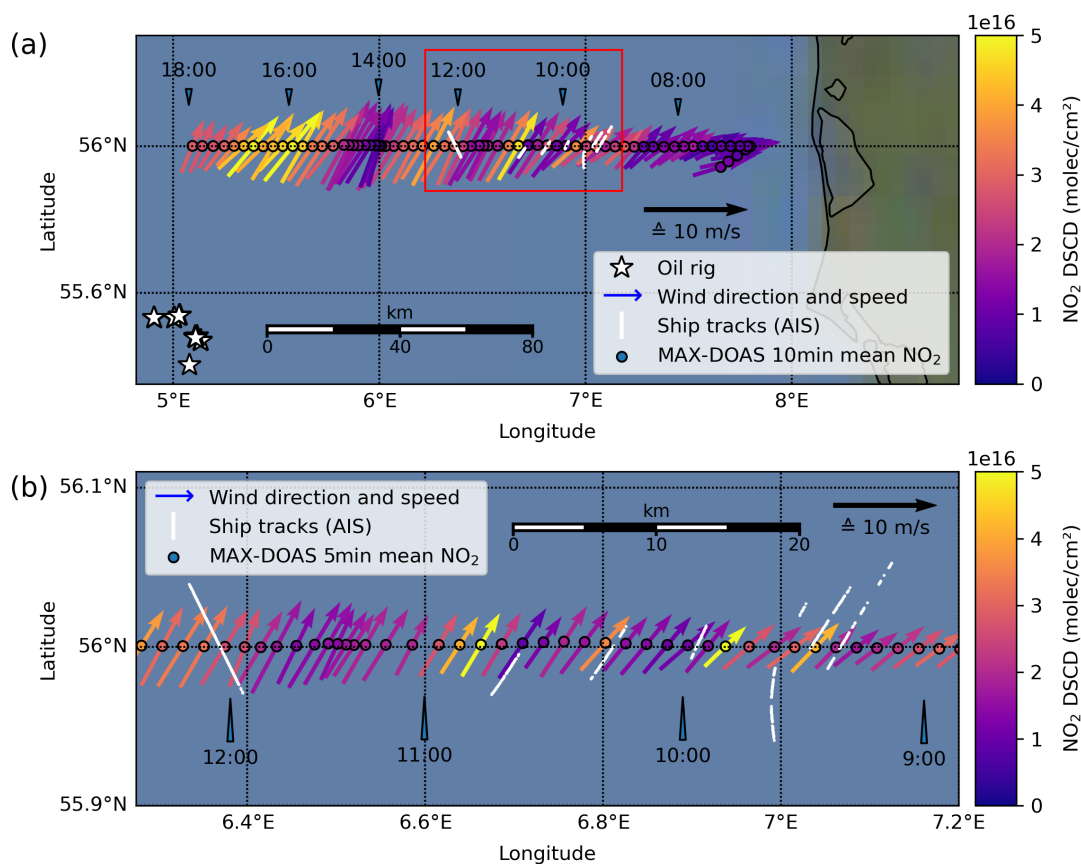


Figure 8.18.: As Fig. 8.17, but for NO₂

What strikes the eye in the NO₂ measurements is that the relative difference between elevated plume signals and background signal is much smaller because of an ambient background NO₂ pollution, while in the SO₂ measurements the values practically go down to zero (or zero ± noise) between the elevated signals. The amount of ambient background NO₂ varies over the day, with a minimum of 1×10^{16} molec cm⁻² in the morning and 1.5×10^{16} molec cm⁻² or even up to 2×10^{16} molec cm⁻² in the afternoon. Another striking difference is clearly visible in the overview over all measurements on this day in Fig. 8.17a and Fig. 8.18a: a broad, strongly elevated signal in the NO₂ measurements around 16:00 UTC, which is not there in the SO₂ measurements. The wind direction suggests that this might be a big NO₂ plume coming from the oil rigs in the southwest.

With respect to the ship related signals, comparing the corresponding SO₂ and NO₂ measurements in Fig. 8.17b and Fig. 8.18b reveals some similarities. At most ship encounters, elevated NO₂ levels from the ship's emission plumes have been measured. The two afore-

mentioned ships that crossed the path of the Celtic Explorer at 09:53 UTC at a longitude of 6.91°E (cargo ship, 180 m length) and at 10:20 UTC around 6.8°E (tanker, 145 m length), that both had very low SO₂ signals, show a clear NO₂ signal sticking out from the background, with NO₂ DSCDs going up to 5.1×10^{16} molec cm⁻² and 3.6×10^{16} molec cm⁻² in the 5-min means. Hence, a plume–LOS geometry-related effect or in general lower emissions due to slow-steaming can be excluded and the most probable explanation for the low SO₂ signals of these ships is the usage of a fuel with a much lower sulfur content compared to the other ships. Again the strongest plume signal was caused by the fast-traveling cruise ship encountered at 6.68°E longitude around 10:40 UTC, with a 5-min mean NO₂ DSCD of 7.1×10^{16} molec cm⁻². This peak's NO₂ and SO₂ values widely exceed the saturated colorscales of both the NO₂ and SO₂ plot. This and some other signals in this day's measurement time series will be further investigated in the following by examining the measurements in other elevation angles than the 4° angle shown here.

Vertical scanning of the MAX-DOAS instrument, i.e., performing a measurement sequence with a variety of different elevation angles, enables us to gather knowledge about the height-distribution of the measured pollutants. Figure 8.19 shows all individual SO₂ (panel a) and NO₂ (panel b) measurements of this day in 4 different elevation angles: 1°, 2°, 4° and 6°. In panel c, all individual measurements of SO₂ and NO₂ again in the 4° elevation angle are plotted into the same figure for a direct comparison between the SO₂ and NO₂ time series as well as to compare to Fig. 8.17 and Fig. 8.18. All panels feature a magnified view of the gray shaded part of the time series on the right. The time period in the unmagnified views on the left comprises primarily the SO₂ measurement period, i.e. the time with solar zenith angles smaller than 65°. This means, that the first (morning) and latest (evening) measurements of NO₂ are omitted to retain enough details in the presented time period. The magnified view to the right shows the time between 09:15 and 11:15 UTC, incorporating the most interesting sharp and distinct ship emission peaks.

Comparing SO₂ and NO₂ measurements, it can be seen how much noisier the SO₂ DSCDs are than the NO₂ DSCDs. While the absorption structures of NO₂ and SO₂ are in the same order of magnitude, with the differential absorption cross section of NO₂ being in the order of 1×10^{-19} cm² molecule⁻¹ and for SO₂ in the order of 2×10^{-19} cm² molecule⁻¹ (Seyler et al., 2017), the wavelength difference of the two fit windows in the UV, 307.5 to 317.5 nm for SO₂ and 338 to 370 nm for NO₂, is enough to have much less light intensity in the shorter wavelength SO₂ fit window due to ozone absorption in the atmosphere. Less photons mean worse signal-to-noise ratio, which can clearly be seen in the figure. It is even more pronounced here because of the very short integration times for the spectra compared to for example the Neuwerk measurements in the previous chapters. The one SO₂ peak that clearly stands out of the noise is the measurements of the plume of the large cruise ship around 10:45 UTC. There is some smaller peaks visible in the SO₂ time series and two broader enhancements around 9:20 UTC and 12:40 UTC, but with a much

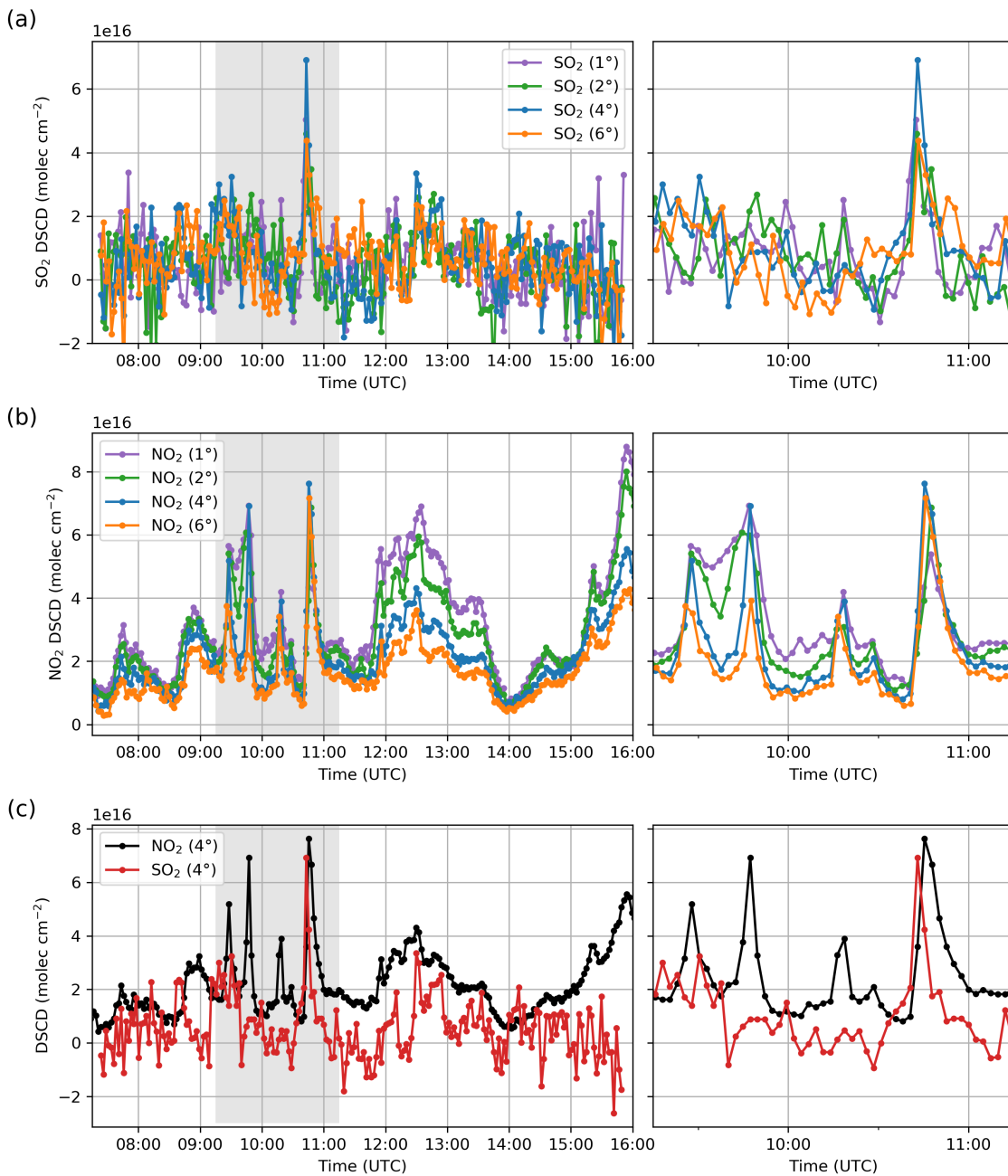


Figure 8.19.: SO₂ (a) and NO₂ DSCDs (b) measured at 1°, 2°, 4° and 6° elevation on 21 August 2013 close to the Danish coast (see Fig. 8.17 and 8.18), with a zoom into the gray shaded area on the right. Panel (c) directly compares the SO₂ and NO₂ DSCDs in 4° elevation, where the strongest signals were measured.

worse signal-to-noise ratio than for the high peak. Of course, it is expected that less SO₂ is emitted than NO₂, depending on the kind of pollution source, and for ships, the fuel's sulfur content. It is also expected, that the ambient SO₂ background pollution at sea is low, as it can be seen here.

In the NO₂ time series, more kinds of signals can be clearly identified. Sharp and distinct ship emission peaks from relatively fresh plumes can be seen, particularly in the gray shaded phase. Broader NO₂ enhancements can also be seen, especially pronounced between 12:00 and 13:30 UTC and after 15:00 UTC. As can be seen from Fig. 8.19b, these broad enhancements show the typical elevation angle separation for MAX-DOAS measurements of an absorber which is well-mixed in the boundary layer, with highest values in the lowest elevation angle. With increasing elevation, the light path through the boundary layer gets shorter thus decreasing the sensitivity to the boundary layer leading to lower NO₂ DSCDs. This suggests that these NO₂ enhancements are older, more diluted and dispersed plumes, maybe originating from more distant ships or the oil rigs visible in Fig. 8.17 and Fig. 8.18.

Inspecting the gray shaded time period in more detail as it is shown in the right panels, reveals that also for the sharper peaks the measurements in the 4 different elevation angles show deviations. The shapes of the first two NO₂ peaks measured around 9:30 and 9:50 UTC vary depending on the measurement elevation. In the higher elevations, namely 4° and 6°, both peaks can be easily separated. In the 2° elevation, the peak flanks overlap while in 1° elevation the peaks nearly merge to one broader peak. This reveals that the horizontal dispersion of the plumes of the ships is stronger at lower altitudes, where both plumes begin to mix, than at higher altitudes. The highest NO₂ DSCDs were measured in the lower angles going up to 5.7×10^{16} molec cm⁻² for the first and 7×10^{16} molec cm⁻² for the second peak with not much difference between the 1°, 2° and 4° angle, while in 6° elevation the peak values are much smaller. The next peak around 10:20 UTC is smaller, going up to 4.2×10^{16} molec cm⁻² at maximum.

In the SO₂ time series, the presence of corresponding SO₂ enhancements for these three NO₂ peaks can only be guessed. For the first peak, the measurements especially in the 4° elevation show some elevated SO₂ levels, for the second peak the 2° elevation might show a small SO₂ enhancement above background. For the third ship peak, the lowest 2 elevations, namely 1° and 2°, show a small SO₂ peak, while no enhancement is visible in the higher elevations.

Very prominent especially in the SO₂ is the fourth peak, which very probably originates from the plume of the above-mentioned large, fast-traveling cruise ship. In the NO₂ DSCDs, but even more pronounced in the SO₂ DSCDs it can be seen that the highest values were measured in the 4° elevation angle, revealing an elevated plume. This might indicate that the ship's stack was quite high and/or the ship was quite close to the Celtic Explorer.

For NO_2 , the 2° , 4° and 6° DSCDs are nearly identical and the 1° DSCD is about 30 to 35 % lower. For SO_2 , the 4° DSCD is clearly the highest, all other directions are at least 30 % lower. This also tells us that NO_2 and SO_2 are not distributed the same way in the plume.

The direct comparison of the SO_2 and NO_2 DSCDs measured in 4° elevation in the magnified view in panel c (left) reveals, that SO_2 peak and NO_2 peak were not measured at exactly the same time. There is a small time shift visible, with the SO_2 peak being measured first. At the time when the NO_2 DSCD reaches its peak values the SO_2 DSCD is already declining. Beyond that, the NO_2 peak is a bit broader than the SO_2 peak. As both trace gas DSCDs are retrieved from the same spectra in the UV, both measurements are taken at the exact same time and the photons reached the instrument on roughly the same path through the atmosphere and the plume⁶, this can only mean that SO_2 and NO_2 are unequally distributed in the measured ship plume.

To check whether the cruise ship identified via the AIS data is really the source of the measured pollution, the image of the video camera included in the MAX-DOAS telescope, from which at each measured spectrum a frame is grabbed, can be examined. In Fig. 8.20, two images captured by the video camera around the time of the highest SO_2 peak are shown. The field-of-view of the camera is much larger than the $\sim 1^\circ$ field-of-view of the MAX-DOAS, which covers only a small center fraction of the images.

The images definitely show a large cruise ship relatively close to the Celtic Explorer and confirm that the high NO_2 and SO_2 values measured definitely originate from this ship's plume, which apparently contains substantial amounts of NO_x and SO_2 .

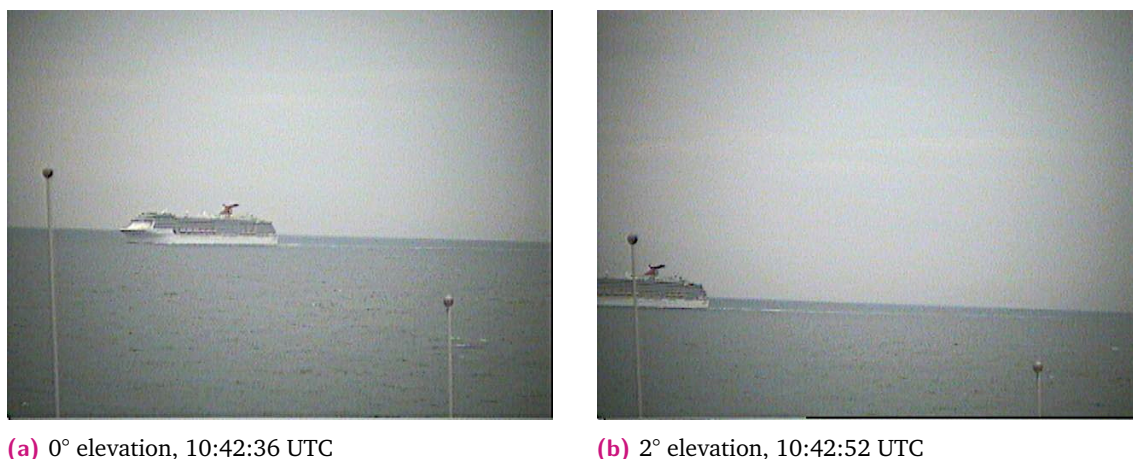


Figure 8.20.: Image frames grabbed from the in-built video camera in the MAX-DOAS telescope on 21 August 2013 during the MAX-DOAS measurements around 10:42 UTC.

How large the measured SO_2 emissions of this ship are becomes clear when examining the magnitude of the SO_2 and NO_2 columns relative to each other by computing

⁶The light path in the shorter wavelength fit window of SO_2 is a bit shorter, though.

the SO₂-to-NO₂ ratio of the plume, as it has been carried out for Neuwerk data in Section 6.7.1. In this case of the cruise ship's plume, the maximum measured SO₂ DSCD amounts to 6.9×10^{16} molec cm⁻² (see Fig. A.1c in the appendix for the DOAS fit result) above practically zero background in the 4° elevation. For NO₂, the maximum DSCD amounts to 7.6×10^{16} molec cm⁻² (see Fig. A.1b in the appendix for the DOAS fit result) above approximately 1.5×10^{16} molec cm⁻² background (1×10^{16} molec cm⁻² before and 2×10^{16} molec cm⁻² after the peak). The resulting SO₂-to-NO₂ ratio is 1.13. Taking the integrated peak area instead of the peak values gives a very similar ratio of 1.12.

Compared to the statistics of SO₂-to-NO₂ ratios of more than 1000 ship plumes measured on Neuwerk before 2015, this value is on the upper end of the scale. The mean SO₂-to-NO₂ ratio in the mentioned statistics is 0.3. In Fig. 6.18 from Section 6.7.1 (see page 108), the ratio gained for this cruise ship is outside of the plotted range, which means it is relatively rare. Of course, the plume measured here is apparently a very fresh one, but the histogram for Neuwerk also contains plumes of very different ages including young ones.

This all indicates that the investigated cruise ship burned a fuel with an unusually high sulfur content, probably exceeding the limit of 1.0% valid at that time.

8.3 Celtic Explorer 2015: Impact of emission regulations

The impact of the introduction of a stricter fuel sulfur content (FSC) limit in the North and Baltic Sea emission control area (ECA) can be clearly seen in the multi-year time series of MAX-DOAS measurements on Neuwerk: From 1 January 2015 on, emitted amounts of SO₂ from ships decreased significantly. While in the 2013 and 2014 data SO₂ peaks from ship plumes can be easily found in the time series and almost all ships have a corresponding SO₂ peak to their plumes' NO₂ peak, in the 2015 and 2016 data it is hard to find any ship-related SO₂ signals.

This section compares the shipborne MAX-DOAS measurements of SO₂ taken in 2013, before the introduction of stricter fuel sulfur limits, with the measurements from 2015, after the legislation change, to provide an additional off-shore perspective to the near-coastal measurements on Neuwerk.

8.3.1 The Celtic Explorer Summer Survey Cruise 2015

After the initial setup of the instruments in the port of Stade (Elbe) on 7 August 2015, the first leg of the Celtic Explorer Summer Cruise 2015 started on the next day, 8 August 2015. After sailing first downstream and then out of the river Elbe, the ship sailed on the

North sea for 19 days until reaching the port of Bergen, Norway, on 26 August 2015. The cruise track of the first leg is plotted in Fig. 8.21. It shows a similar serpentine-like behavior meandering from south to north through the North Sea as the track from 2013, covering all BSH measurement points located more or less on a 1°-latitude-grid.

2015's addendum to the track is a detour/side-trip to the North Minch, the inner sea off the north-west coast of Scotland, which is framed by the Outer Hebrides, the Isle of Skye (Inner Hebrides) and the Scottish coast. The second addendum is the inclusion of BSH measurement stations at 62.5°N, outside of the North Sea, off the edge of the continental shelf, where the water is deeper than 1000 m.

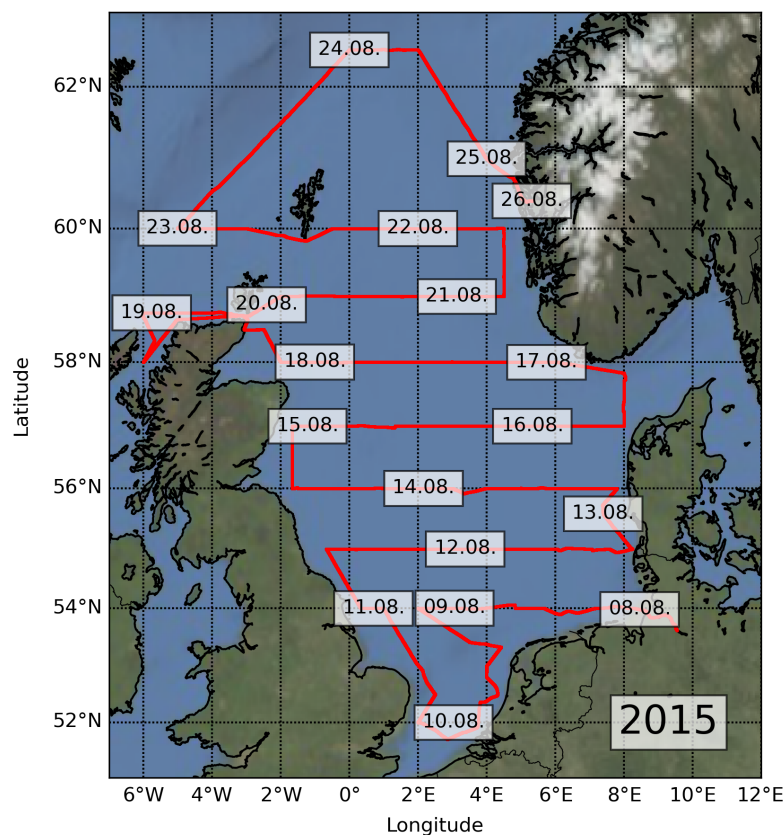


Figure 8.21.: Cruise track of the first leg of the Celtic Explorer Summer Survey 2015. The date labels for each day are centered at the respective position of the ship at 12:00 UTC.

After the arrival in Bergen, the ship's crew and the scientific crew were exchanged and the second leg of 2015's summer cruise started on 30 August 2015 and ended in Kiel on 13 September 2015. The cruise track of the second leg, covering the German part of the North Sea in more detail and the German part of the Baltic Sea, is plotted in Fig. 8.22.

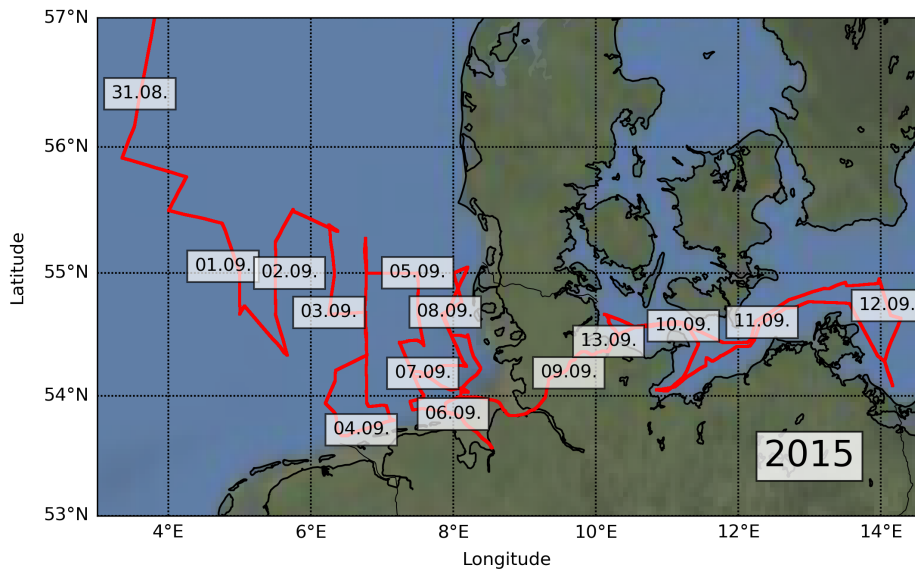


Figure 8.22.: Cruise track of the second leg of the Celtic Explorer Summer Survey 2015. The date labels for each day are centered at the respective position of the ship at 12:00 UTC.

8.3.2 2013 vs. 2015 – impact of a stricter fuel sulfur content limit on SO₂ pollution levels

Figures 8.23 and 8.24 present a map with the hourly mean MAX-DOAS SO₂ DSCD measurements in 2° elevation plotted along the Celtic Explorer’s ship track in 2013 and 2015, respectively. Both plots use an identical color scale for the SO₂. Comparing both figures, in the first general impression the difference in colors of the little circles representing the MAX-DOAS measurements is easily visible. In the map showing the measurements from 2013, colors range from blue (zero) to yellow (2×10^{16} molec cm⁻²), with the values often exceeding the saturation level of the colorscale. Also medium-high measurements, shown with orange-like colors, are present a lot.

In the map from 2015, colors are mostly blueish or purple (i.e. less than 1×10^{16} molec cm⁻²) with a few orange points. This indicates that the off-shore SO₂ levels in North and Baltic Sea in general decreased quite substantially from 2013 to 2015. Admittedly, the sampling areas are a bit different as the cruise tracks do not agree and in 2013 the ship sailed three times through the English Channel, an area which is known for having stronger air pollution. In 2015 this area was not probed at all and instead the cruise track extended further into the cleaner northern part of the North Sea and the transition region to the northern Atlantic. But still, when comparing only regions where measurements were taken on both cruises in Fig. 8.23 and 8.24, the measured SO₂ DSCDs are visibly lower in 2015.

The measured NO₂ levels in comparison can give a hint on the question whether shipping is the main reason for the measured reduction in SO₂ levels, or different probing regions,

or different wind conditions, as NO_x emissions from shipping can be assumed to be nearly constant over this time period, as the measurements on Neuwerk (see Section 6.7) have shown. Quantitatively, when comparing only the overlapping regions⁷ of both cruises, the mean SO_2 DSCD (up to 60° SZA) dropped by about 80 % from 4.9×10^{15} molec cm^{-2} in 2013 to 1.1×10^{15} molec cm^{-2} in 2015, while the mean NO_2 DSCD (up to 75° SZA) decreased only by about 20 % from 11.8×10^{15} molec cm^{-2} to 9.3×10^{15} molec cm^{-2} , a clear indication that this strong reduction is at least in parts due to the ship's lower fuel sulfur content.

On the 2017 summer cruise, discussed in Section 8.5 later on, the mean SO_2 DSCD increased to 3.3×10^{15} molec cm^{-2} , still staying clearly below the 2013 level, but also the mean NO_2 DSCD increased to 15.8×10^{15} molec cm^{-2} . As discussed later, due to prevailing off shore wind conditions several strong signals of land-based SO_2 and NO_x emitters like oil refineries and power plants were measured in 2017, explaining the higher relative SO_2 contribution as the introduced sulfur content limits and expected SO_2 emission reductions are only valid for ships.

8.4 Celtic Explorer 2016: NO_2 overview and comparison to satellite measurements

Taking the Celtic Explorer 2016 Summer Survey as an example, this section is focusing on the general distribution of NO_2 in the North Sea region. During such a several weeks long ship campaign the shipborne MAX-DOAS “maps” a large area covering the whole North Sea. As other, independent measurements on the open sea to compare to are sparse, DOAS measurements from satellite instruments provide an opportunity for data validation at least on a basis of monthly averages.

While MAX-DOAS measurements in low elevation angles feature a long light path through the boundary layer and thus give high sensitivity to pollution close the ground, satellite measurements' sensitivity to the lowest layers is limited. For the comparison to satellite measurements, which provide vertical trace gas columns through the atmosphere, MAX-DOAS measurements in higher elevation angles are more feasible, as the slant column density for such measurements can be converted into a vertical column density (VCD) using an so-called air mass factor (AMF), that can be computed via a radiative transfer model or, under certain assumptions, can be approximated in a simple geometrical way

⁷The region between 52°N and 60°N (excluding the heavy polluted English Channel), and restricted to measurements from the first legs of both cruises (as the second legs tend to be very close to the German coasts and include passages through the Kiel Canal which can be strongly influenced by land-based air pollution, especially for NO_x)

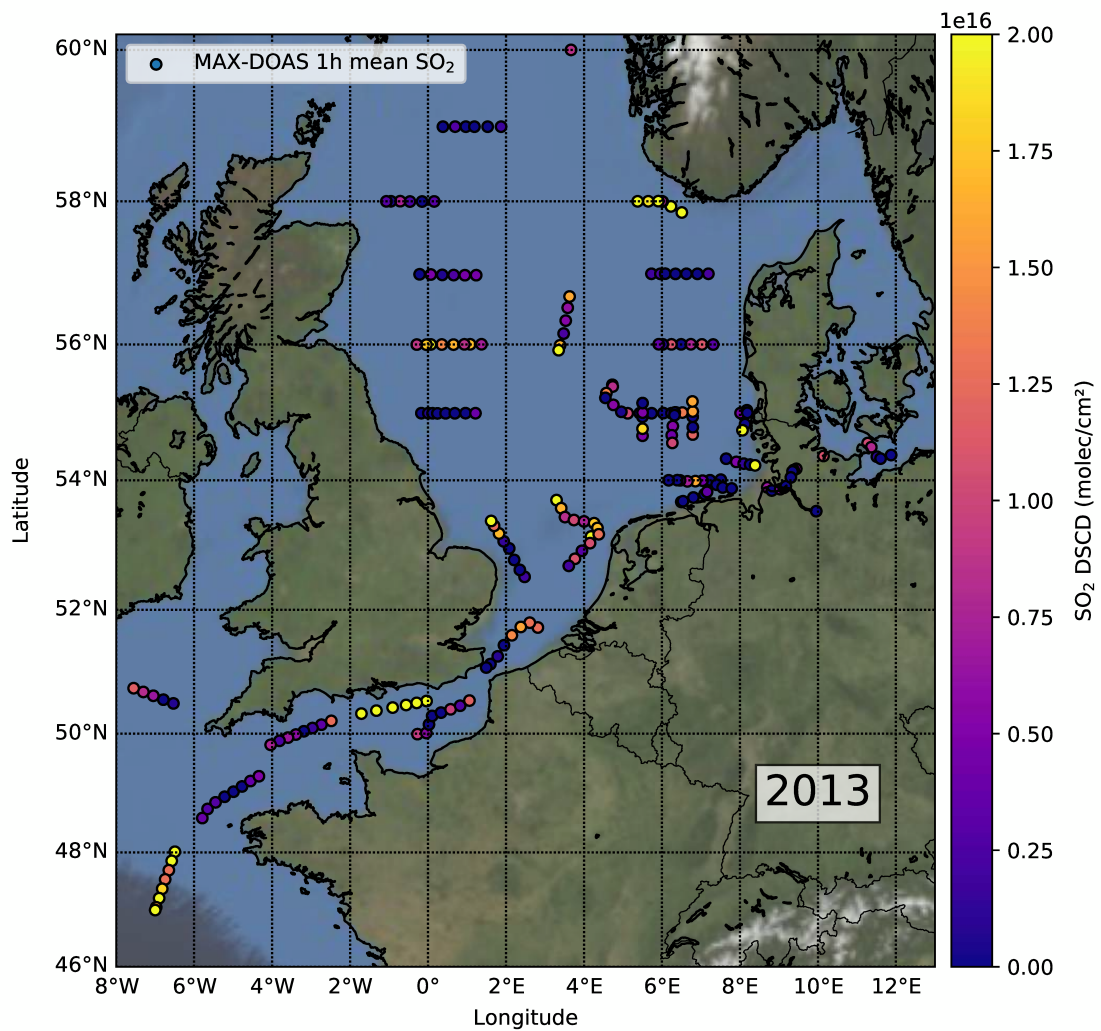


Figure 8.23.: Map showing hourly mean MAX-DOAS SO₂ DSCDs measured in 2° elevation on the Celtic Explorer Summer Survey 2013 (see Fig. 8.14, 8.15 and 8.16 for an overview of the cruise track). The MAX-DOAS measurements are shown as colored circles at the respective position of the ship, the more yellowish the color, the higher the SO₂ DSCD (see colorbar).

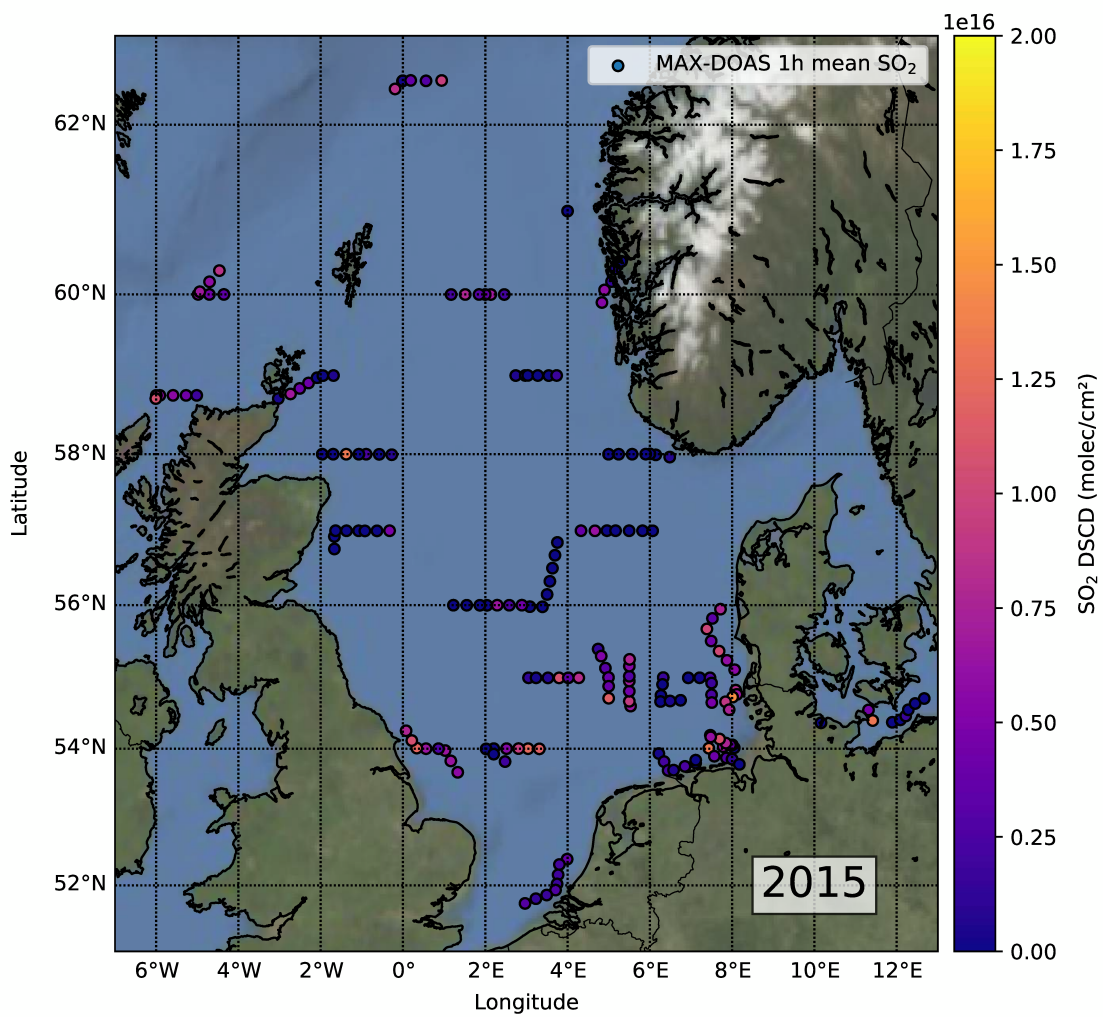


Figure 8.24.: As Fig. 8.23, but for 2015.

(e.g. Hönninger and Platt, 2002). Thus, in this section first MAX-DOAS NO₂ DSCDs in 2° elevation are compared to MAX-DOAS VCDs from 30° elevation, which in a second step are then compared to satellite measurements.

8.4.1 The Celtic Explorer Summer Survey Cruise 2016 (first leg)

For the summer survey cruise in 2016, the RV Celtic Explorer departed from Hamburg in the morning of 4 August 2016, after the instruments have been set up on the day before. After 20 days at sea, the ship arrived in Aberdeen, Scotland, on 24 August 2016. The cruise track, plotted in Fig. 8.25, is to a great extent similar to the one from 2013, again with an addendum into the English Channel, but this time not as far south into the Bay of Biscay as before. Also the northern part of the cruise track deviates from 2013, carrying the ship not as far to the north but instead further westward of the Orkney and Shetland Islands and then back south to Aberdeen. The second leg with an exchanged crew from Aberdeen to Kiel will not be further considered here.

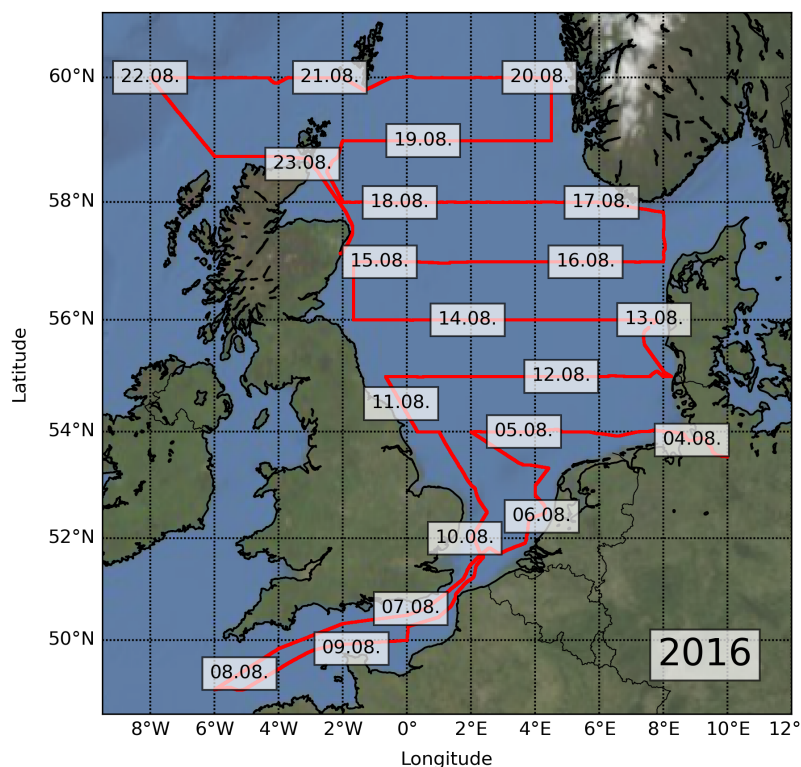


Figure 8.25.: Cruise track of the first leg of the Celtic Explorer Summer Survey 2016. The date labels for each day are centered at the respective position of the ship at 12:00 UTC.

8.4.2 MAX-DOAS NO₂ DSCDs

As the most important anthropogenic source of NO_x is combustion of fossil fuels in traffic, energy production and industry (see Section 2.5), we expect enhanced values of NO₂ close to the coast as well as in regions with intense ship traffic. High values of NO₂ are expected close to industrialized shore regions and when directly measuring the plumes of passing ships.

The map in Fig. 8.26 shows the hourly mean MAX-DOAS NO₂ DSCD measured in 2° elevation on the first leg of the Celtic Explorer Summer Survey 2016, combined with wind information. As expected, the highest NO₂ DSCDs were measured close to the coasts and in the English Channel, where there is a lot of industry on both shores. Especially high NO₂ pollution is measured when the wind is blowing from land and transporting polluted air masses to the sea, like it can be seen in Fig. 8.26 along the British coast, or when the ship was not far from land and the MAX-DOAS instrument pointed towards the shore, like it can be seen in the figure along the Dutch coast close to Rotterdam. In the open North Sea, NO₂ enhancements are most probably due to emissions from ships or due to oil rigs flaring unwanted or unused natural gas. On the open sea, apart from those spatially limited NO₂ enhancements, the measured values are quite low, especially in regions with sparse ship traffic. This is the case in the central part of the North Sea and for the measurements taken on 22 August 2016 in the north west of Scotland at 60°N, 8°W, showing very low ambient background NO₂.

8.4.3 Conversion to VCDs

For the comparison to satellite measurements, the MAX-DOAS slant column densities retrieved from the measured spectra in the DOAS fit have to be converted to tropospheric vertical column densities (VCDs) by applying a so-called air mass factor (AMF), a dimensionless number that corrects for the longer light path length:

$$\text{VCD} = \frac{\text{SCD}}{\text{AMF}} \quad (8.1)$$

As the measurement result after the subtraction of the reference measurement from the off-axis measurement in elevation α is a differential SCD (DSCD), also the AMF is a differential AMF (DAMF):

$$\text{VCD} = \frac{\text{SCD}_\alpha - \text{SCD}_{90^\circ}}{\text{AMF}_\alpha - \text{AMF}_{90^\circ}} = \frac{\text{DSCD}_\alpha}{\text{DAMF}_\alpha} \quad (8.2)$$

As each elevation angle has a different light path through the troposphere, with the lowest elevations showing the longest (nearly horizontal) light paths and thus the highest

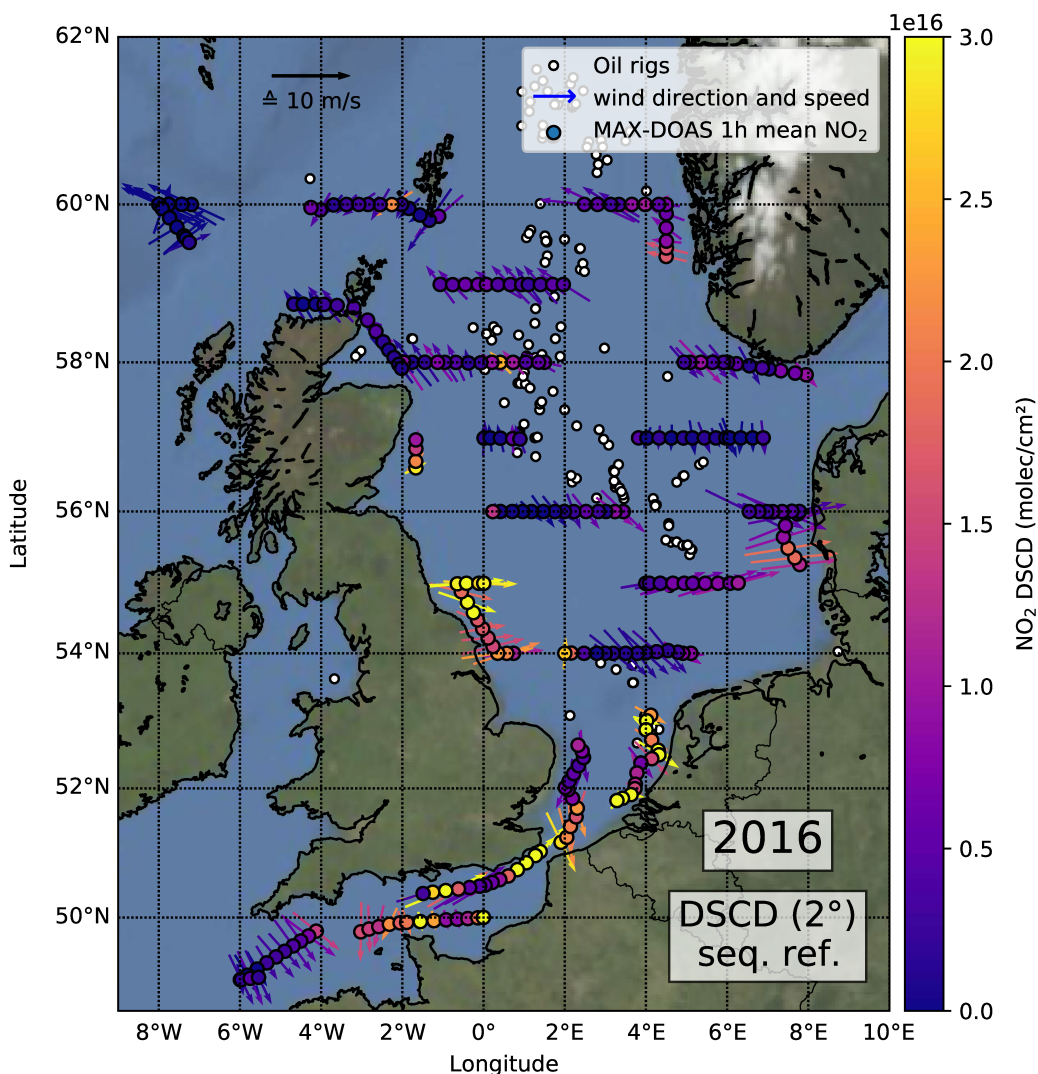


Figure 8.26.: Map showing hourly mean MAX-DOAS NO₂ DSCDs measured in 2° elevation on the Celtic Explorer Summer Survey 2016 (see Fig. 8.25 for an overview of the cruise track). The MAX-DOAS measurements are shown as colored circles at the respective position of the ship, the more yellowish the color, the higher the measured NO₂ DSCD (see colorbar). For source attribution, the absolute (or “true”) wind vectors are plotted in the same color as the MAX-DOAS DSCD “points”. For the assessment of the wind speed, a reference arrow which length represents a wind speed of 10 m s⁻¹ is shown. Operational oil rigs according to the OSPAR 2015 database are shown as white dots.

sensitivity to the boundary layer, each elevation needs a different AMF to correct for the light path length. In general, as the light path lengths are not constant also the AMFs are not constant but change with the weather and aerosol conditions.

The AMF can either be computed via an radiative transfer model solving the radiative transfer equation or can be approximated in a simple geometric way. In the latter case, the AMF or, more specifically differential AMF (DAMF) is given by

$$\text{DAMF}_{\text{geom},\alpha} = \text{AMF}_{\text{geom},\alpha} - \text{AMF}_{\text{geom},90^\circ} = \frac{1}{\sin \alpha} - 1, \quad (8.3)$$

using the fact that $\sin(90^\circ) = 1$. The geometric AMF for well-mixed tropospheric absorbers is simply $1/\sin \alpha$ (compare Fig. 5.5, page 76). This geometric approximation only holds for the troposphere and only for reasonably high elevation angles, as this AMF definition approaches infinity when $\alpha \rightarrow 0$. For an elevation angle of 30° , the DAMF equals 1, which means the DSCDs in 30° elevation are equivalent to geometric VCDs.

As no additional information about the aerosol content, distribution and properties is available for the measurements on the RV Celtic Explorer, approaches to model the AMF would face rather large uncertainties, meaning that the simple geometric approximation can be used just as well. For higher elevations such as 15° or 30° , the difference to the modeled air mass factors is often reasonably small, as the light paths in these elevations do not vary as much. The reduced sensitivity to the lowermost boundary layer by selecting a higher elevation is not so problematic as the satellite also has very limited sensitivity to the lowest layer close to the ground.

A second point is the selection of the reference spectrum. All the measurements presented and discussed above focused on pollution measurements in the boundary layer, i.e., the lower troposphere and were thus taken with a sequential reference spectrum using a close-in-time zenith-sky spectrum⁸ as a reference to cancel out absorptions higher up in the atmosphere. This is especially important for NO_2 to avoid the typical U-shaped diurnal NO_2 curve caused by strongly enhanced stratospheric absorptions at low sun in the morning and evening, when the light path through the stratosphere gets very long. This selection of a sequential reference, which also avoids problems with instrumental drifts when the instrument is not stable over longer times, has one significant drawback: If a pollution plume is located above the instrument, the reference spectrum, which then contains the absorption of the pollutant in the plume, gets subtracted from the off-axis measurements, which can have two implications: If the plume is not probed by the off-axis measurement, which could be the case for low elevations' line of sights looking beneath the plume, the measured DSCD can have a dip or even get negative, which is still a physically valid result,

⁸Either from the same scan, or like in this case: a time interpolated spectrum from the scan before and after the off-axis measurement

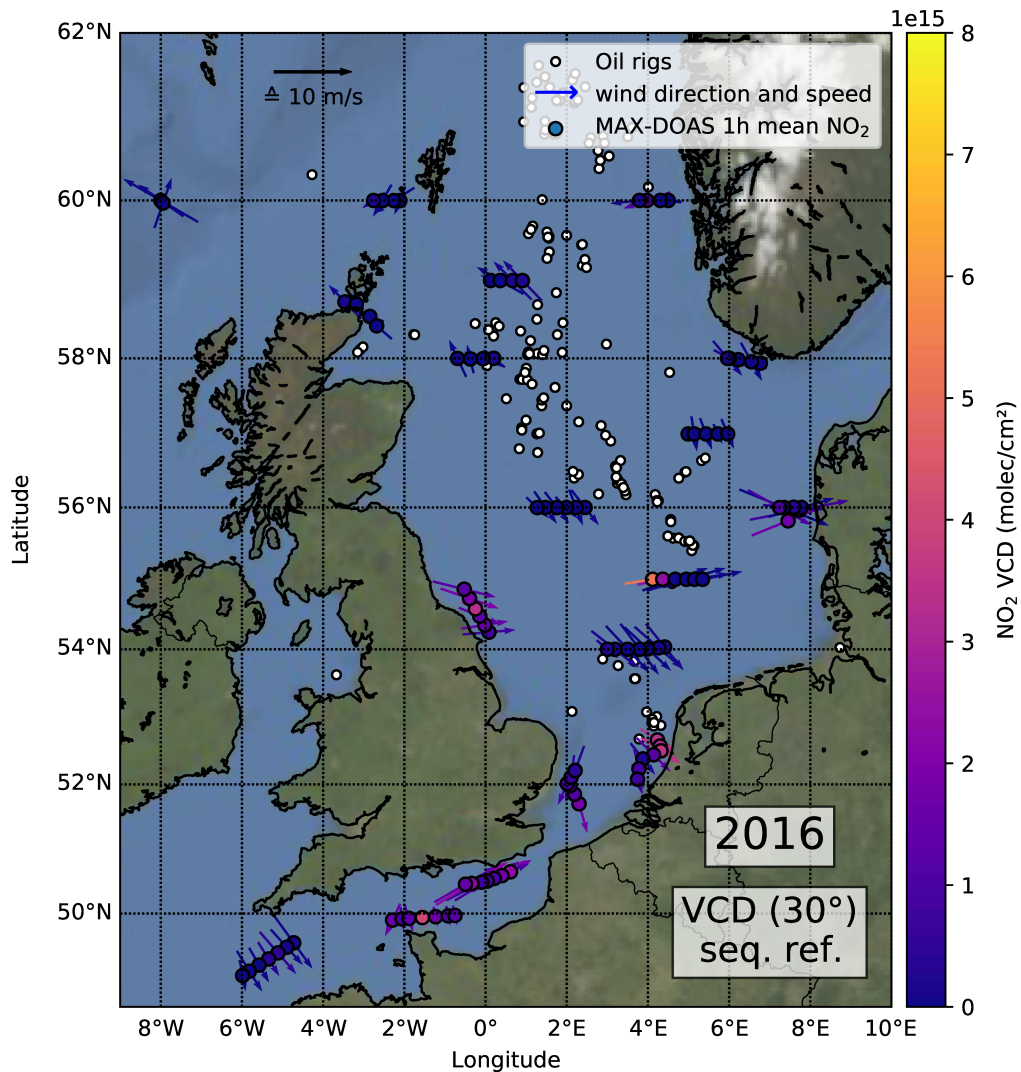


Figure 8.27.: Map showing hourly mean MAX-DOAS NO₂ VCDs (from DSCDs in 30° elevation) on the Celtic Explorer Summer Survey 2016, taken with a sequential reference spectrum. The MAX-DOAS measurements are shown as colored circles at the respective position of the ship, the more yellowish the color, the higher the measured NO₂ VCD (see colorbar). For source attribution, the absolute (or “true”) wind vectors are plotted in the same color as the MAX-DOAS VCD “points”. For the assessment of the wind speed, a reference arrow which length represents a wind speed of 10 m/s is shown. Operational oil rigs according to the OSPAR 2015 database are shown as white dots.

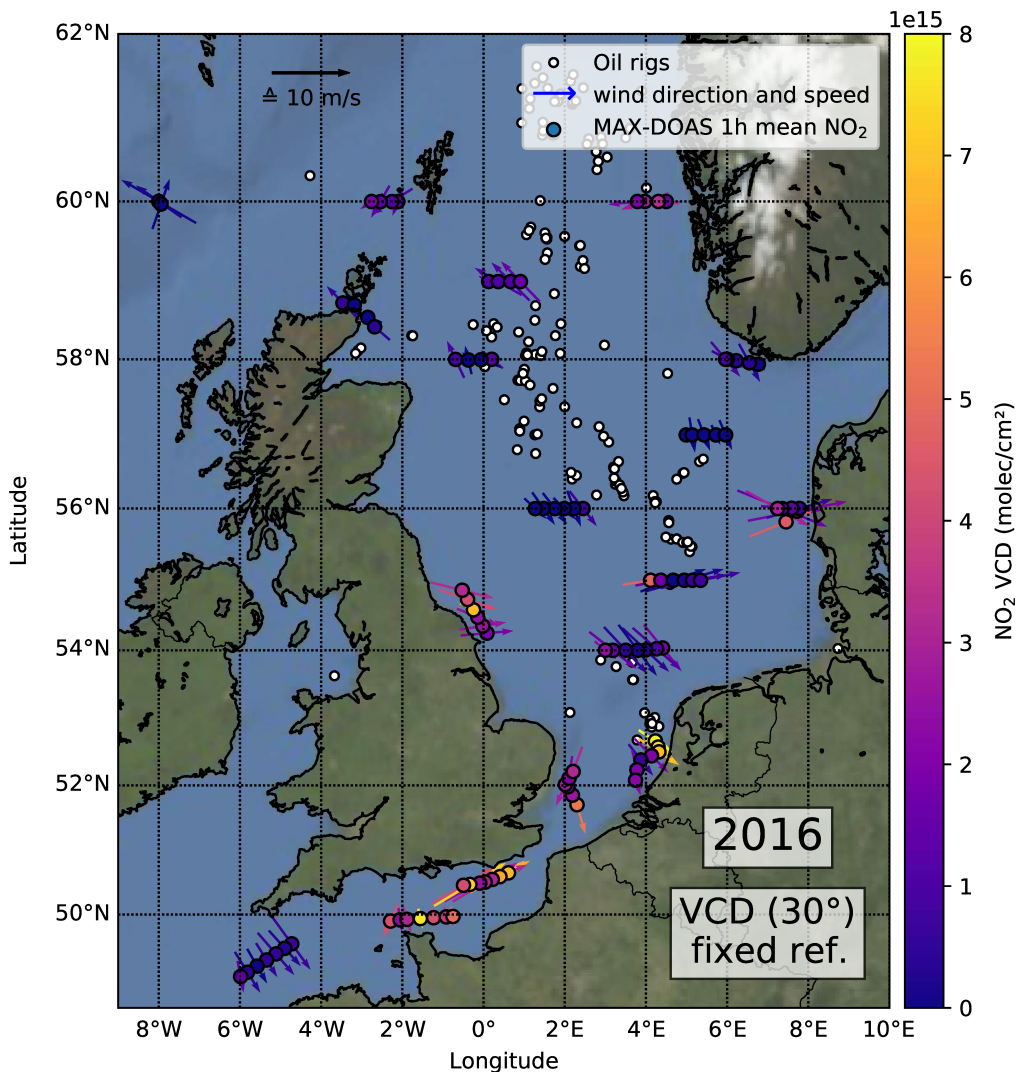


Figure 8.28.: As Fig. 8.27, but for a fixed reference spectrum taken at approximately 56°N and 2°E at noon on 14 August 2016 (see Fig. 8.25 for an overview of the cruise track).

as it just shows that more pollutant absorption is contained in the reference measurement than in the off-axis measurement. The other possible implication, if both the off-axis measurement (for example in 30° elevation) and the zenith-sky reference measurement probe the same plume, is that the elevated plume mostly cancels out and is not detected.

For a comparison to satellite measurements, missing out on such elevated pollution plumes above the ship, which the satellite’s vertical trace gas column does indeed contain, reduces the validity of the comparison. Two often used alternatives to a sequential reference spectrum are a daily noon reference, which is not applicable here as there could be a plume over the instrument at noon, or a fixed reference spectrum for a longer time period, in this case, the whole cruise. This fixed reference spectrum is taken from a part of the cruise with

very clean air, to contain as little tropospheric absorption as possible. To correct for the remaining tropospheric absorption in the reference, which negatively biases the resulting VCDs, a “clean air” tropospheric column taken from the satellite measurement can be added to the VCDs. However, for NO₂, taking a daily noon or fixed reference spectrum has again the drawback of not correcting for the stratospheric NO₂ absorption which will dominate the measurements in the morning and evening and lead to the typical U-shape of the diurnal NO₂ curve. To get rid of most of the stratospheric influence, here the measurements were restricted with an SZA limit of 50° to the time around noon.

To illustrate the differences between the VCDs with sequential and fixed reference spectrum, Fig. 8.27 and 8.28 show the respective resulting hourly mean VCDs for the 30° elevation on the 2016 summer cruise. For a better visual comparability, both the measurements with sequential (Fig. 8.27) and fixed reference (Fig. 8.28) have been limited to SZAs < 50°. As a fixed reference the zenith spectrum measured at noon on 14 August 2016 at roughly 56°N and 2°E has been selected.

Comparing both plots which share the same colorscale, two main points come to mind: On days with clean air, both VCD plots show consistently low values. Deviations can be seen in the polluted regions and along the coasts. Especially in the English channel the VCD with a fixed reference shows significantly higher NO₂ columns than the sequential reference. Most probable, this is due to elevated pollution plumes being transported over the sea from shore- or land-based sources in this highly industrialized region, which are also probed in zenith direction above the instrument and thus cannot be detected with sequential reference due to canceling out.

As a result, for the comparison to satellite measurements the MAX-DOAS VCDs with fixed reference are clearly more suitable.

8.4.4 Comparison to satellite measurements

Figure 8.29 shows a comparison of the hourly mean MAX-DOAS NO₂ VCDs to monthly mean tropospheric NO₂ VCDs from the OMI satellite DOAS instrument for August 2016 (see Boersma et al. (2011) for more information on this data product). To account for the remaining NO₂ in the fixed reference spectrum and to remove the resulting negative bias, a tropospheric column of 1.5×10^{15} molec cm⁻² has been added to the MAX-DOAS VCDs, estimated from the satellite’s monthly mean values in clean parts of the investigated region.

The satellite data clearly shows high values of NO₂ over industrial regions and densely populated areas and low values over the northern part of the North Sea. The more south the higher the NO₂ values in the North Sea get even over the open sea. Sources for the

enhanced NO_2 pollution in the southern part of the North Sea might be the intense ship traffic but also pollution plumes from land transported over the sea by the wind.

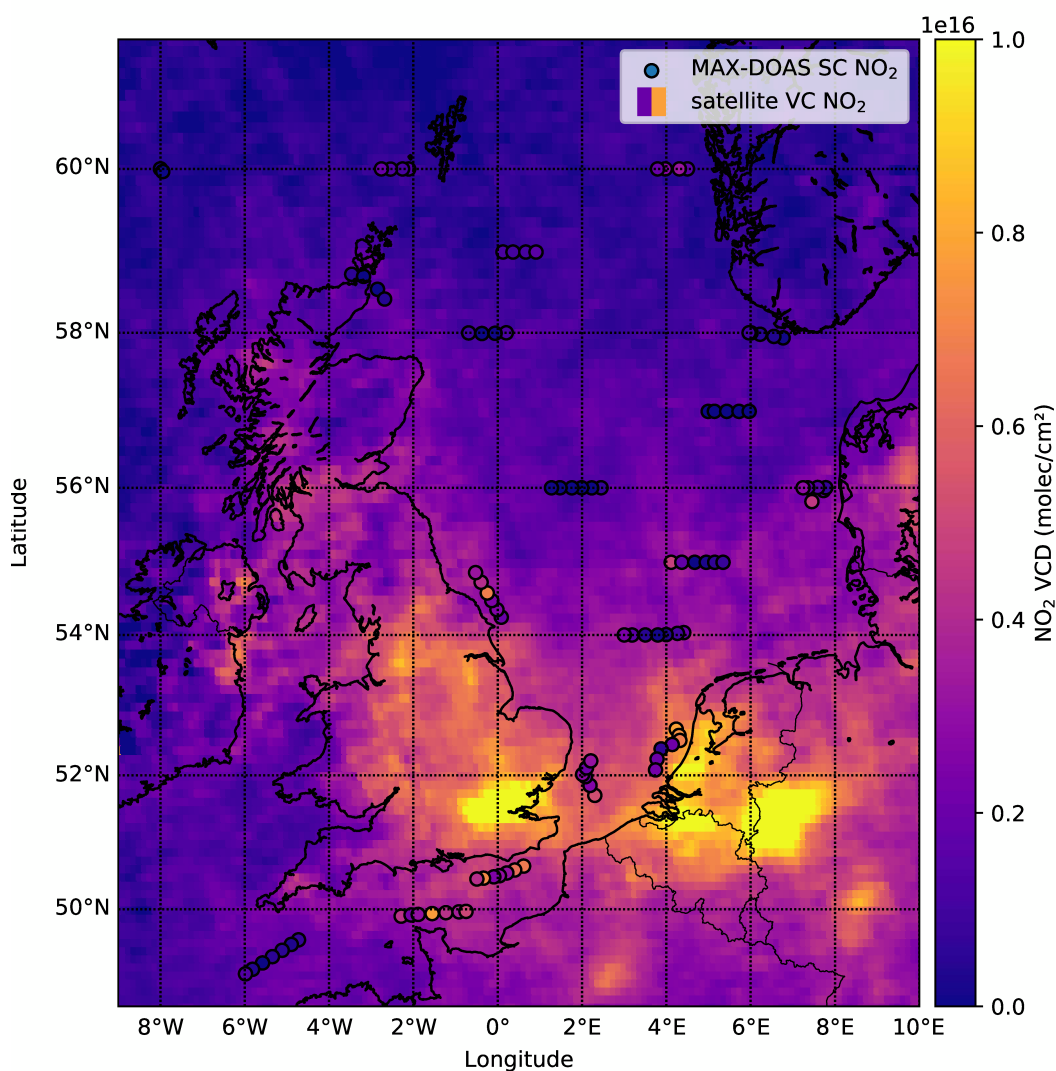


Figure 8.29.: Map showing hourly mean MAX-DOAS NO_2 VCDs (from DSCDs in 30° elevation) on the Celtic Explorer Summer Survey 2016 as colored circles compared to OMI NO_2 monthly mean satellite VCDs for August 2016 (Boersma et al., 2011; TEMIS, 2020) shown in the gridded background image.

Comparing hourly mean values on a ship track of several weeks with a monthly mean value from satellite, perfect agreement cannot be expected. Short time NO_2 enhancement events like the emissions of individual ships passing the Celtic Explorer, which can be seen in the MAX-DOAS data, will be averaged out in a monthly mean. Already in the MAX-DOAS hourly means, the averaging smooths a lot of these smaller signals out.

On the other hand, enhanced NO₂ over the sea due to transport events in the satellite data might not have been there on the day the Celtic Explorer was there, for example due to different wind conditions.

Although the general comparability is limited, the overall pattern is in good agreement. The measured absolute VCD values are in the same order of magnitude and the agreement with low values in clean regions of 0 to 2×10^{15} molec cm⁻² and high values in polluted regions of 6 to 10×10^{15} molec cm⁻² or more is quite good.

8.5 Celtic Explorer 2017: SO₂ and NO₂ pollution from shore-based emitters and NO₂ lifetime estimation

As discussed above, hardly any SO₂ emission signals from individual ship could be measured after the introduction of stricter fuel sulfur limits on 1 January 2015, drastically reducing the SO₂ pollution levels on the open North Sea. Apart from ships, however, there is other emission sources for SO₂ in the marine environment, especially close to the coasts. A good information source on air pollution emitters is the European Pollutant Release and Transfer Register (E-PRTR) which provides information on the annual emissions and pollutant releases to air, water, and land of about 30 000 industrial facilities in the European Union and EFTA. For sulfur oxides (“SO_x/SO₂”), all facilities emitting more than 150 t per year have to report their annual emissions to the register. For NO_x, the threshold is 100 t per year. This means that at least all the larger emitters should be listed in this database.

In the E-PRTR database, for SO₂ in the North Sea region, several kinds of emitters can be found: refineries, power plants, chemical industrial facilities on shore, as well as a few offshore oil rigs. For NO_x, which is produced in all industrial combustion processes, both the variety of facilities and the total number of emitters registered is much larger.

To investigate the impact of such shore-based SO₂ emitters on air quality in the North Sea, the 2017 summer survey cruise had the best conditions of all the conducted cruises: not only did the cruise track contain several passages along the coasts of the littoral states during daylight, but also the frequent occurrence of offshore wind conditions transporting pollution from shore-based emitters to the sea make this cruise interesting.

In this section, after an overview map on the cruise track and the hourly mean SO₂ DSCD measurements, the SO₂ emissions from a selection of shore-based emitters identified via the E-PRTR database are examined. After that, the local SO₂ enhancements are compared to the NO₂ measurements to investigate differences and similarities in the emission patterns. Finally, a particularly suitable route on the 2017 cruise track is utilized to estimate the NO₂ lifetime.

8.5.1 The Celtic Explorer Summer Survey Cruise 2017 (first leg)

After the installation and setup of the measurement equipment on 11 August 2017 in the port of Hamburg, the cruise started on the next day, 12 August 2017. After 19 days at sea, the Celtic Explorer arrived in Aberdeen on the evening of 30 August 2017. The cruise track, plotted in Fig. 8.30, carried the ship as usually in a meandering way from south to north through the North Sea, mostly along serpentine-like tracks in 1° latitude steps. In 2017, as an addendum the cruise track was extended into the Skagerrak and, like in 2015, the North Minch. The second leg with an exchanged crew from Aberdeen to Kiel will not be further considered here.

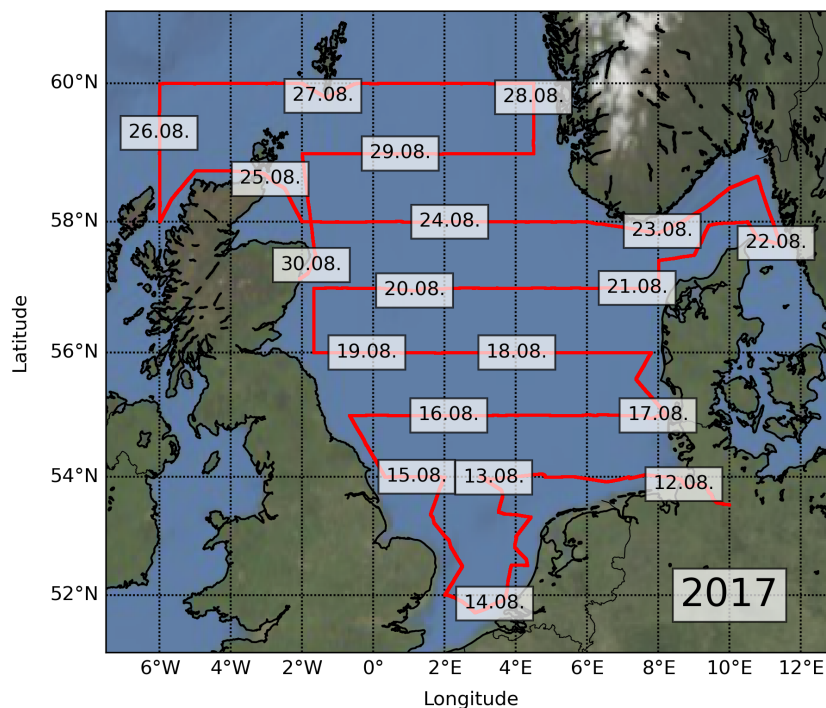


Figure 8.30.: Cruise track of the first leg of the Celtic Explorer Summer Survey 2017. The date labels for each day are centered at the respective position of the ship at 12:00 UTC.

8.5.2 SO₂ measurement overview and source allocation

Figure 8.31 gives an overview on the hourly mean MAX-DOAS SO₂ DSCDs measured in 2° elevation on the Celtic Explorer Summer Survey 2017. In the vicinity of land, several SO₂ enhancements can be seen. The elevated SO₂ levels in the regions close to Rotterdam (Netherlands), Hull (UK), Gothenburg (Sweden), and Aberdeen (UK), that are highlighted with red boxes in the map in Fig. 8.31, will be exemplary investigated in detail in the

following. For the source allocation, the measured DSCDs will be brought together with wind data and the locations of SO₂ emitters registered in the E-PRTR database.

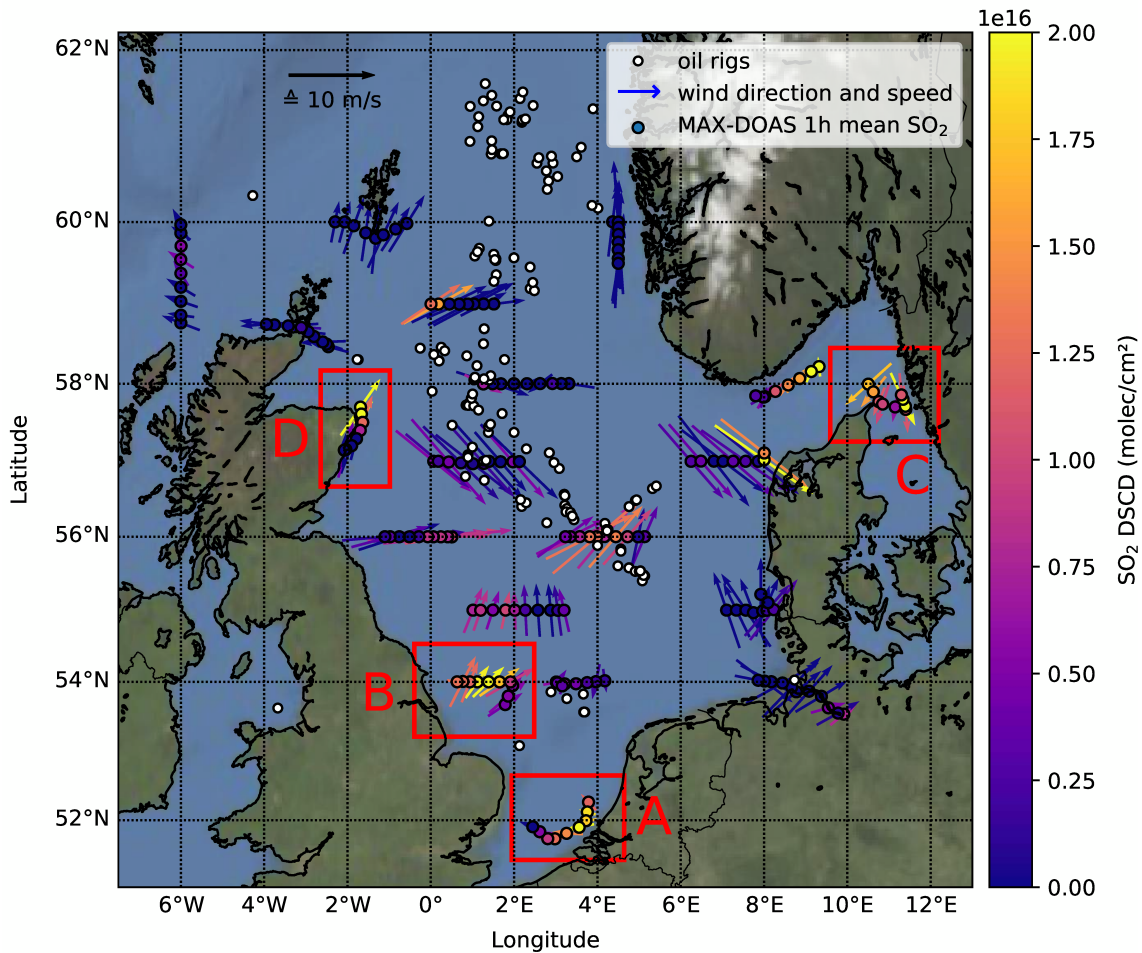


Figure 8.31.: Map showing hourly mean MAX-DOAS SO₂ DSCDs measured in 2° elevation on the Celtic Explorer Summer Survey 2017 (see Fig. 8.30 for an overview of the cruise track). The MAX-DOAS measurements are shown as colored circles at the respective position of the ship, the more yellowish the color, the higher the measured SO₂ DSCD (see colorbar). For source attribution, the absolute (or “true”) wind vectors are plotted in the same color as the MAX-DOAS DSCD “points”. For the assessment of the wind speed, a reference arrow which length represents a wind speed of 10 m/s is shown. Operational oil rigs according to the OSPAR 2017 database are shown as white dots. The red boxes highlight regions, which will be further investigated in detail in the following.

Rotterdam

Rotterdam (Netherlands) and Antwerp (Belgium) are the largest container ports in Europe, with 14.5 and 11.1 million TEU (twenty-foot equivalent units) handled in 2018 (UNCTAD, 2019), and eleventh-largest and thirteenth-largest in the world. The port of Rotterdam is the major crude oil hub in Northwest Europe and one of the world's major centers for petrochemical industry featuring 4 world-scale oil refineries and a vast number of (petro-) chemical companies and facilities (ECSPP, 2020; Havenbedrijf Rotterdam N.V., 2016). With one additional oil refinery close to Vissingen/Middelburg (NL) and three more in the port of Antwerp, the Dutch and Belgium coastal region around Rotterdam and Antwerp is a petrochemical hotspot. Most of these facilities are registered as SO₂/SO_x emitters in the E-PRTR database, meaning that they emit more than 150 t of SO₂ per year.

Figure 8.32 shows the 15 min-mean MAX-DOAS SO₂ DSCDs measured in 2° elevation while the Celtic Explorer passed along this section of the Dutch and Belgium coast near Den Haag, Rotterdam and Antwerp on 14 August 2017. The chainline of MAX-DOAS measurement points in the figure indicates this day's cruise track during the time when the sun was more than 35° above the horizon, i.e., for SZAs < 65°. At first, the Celtic Explorer headed south, sailing along the Dutch coast close to Den Haag and Rotterdam from north to south, later it turned to southwest and finally changed the course to northwest, away from the shore. This means, that the MAX-DOAS telescope, which measures towards portside, pointed towards the coast the whole time until the ship turned northwestward in the afternoon.

The largest SO₂ emitters in the area according to E-PRTR, comprising of several oil refineries, power plants, and (petro)chemical facilities, are marked in the map with different symbols. As discussed above, the highest density of these facilities can be found in the port of Rotterdam located between the shore-line and the city. Figure 8.32 shows that strongly enhanced SO₂ DSCDs were measured by the MAX-DOAS while the ship passed the Rotterdam harbor region. Comparing the location of the elevated SO₂ levels with the positions of the emitters marked in the map, and taking into account the wind arrows plotted along the measurements showing the true (or absolute) wind vector at the time of the MAX-DOAS measurements, the measured SO₂ enhancements can clearly be traced back to the port of Rotterdam.

Checking the E-PRTR database, the four large refineries in the port of Rotterdam reported annual sulfur oxide (SO_x/SO₂) emissions of 3350 t, 2860 t, 2430 t and 354 t for 2017. The older coal-fired power plant at the entrance of the harbor reported sulfur oxide emissions of 1450 t, the younger one of 165 t for 2017. The chemical facilities in the port of Rotterdam reported SO_x/SO₂ emissions of 787 t, 536 t, 171 t and 152 t, the last one being only slightly above the threshold for mandatory submission of emission data. Facilities with lower emissions are not registered in the E-PRTR database. With such massive annual SO_x/SO₂

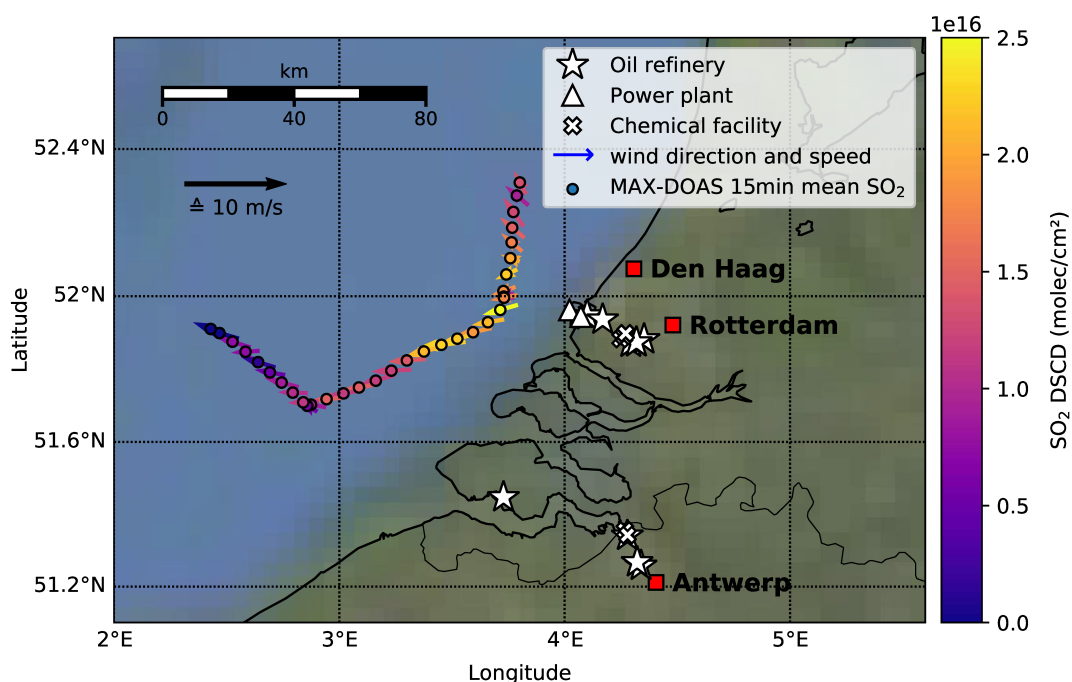


Figure 8.32.: Map showing 15-min mean MAX-DOAS SO₂ DSCDs measured in 2° elevation close to Rotterdam on 14 August 2017. The MAX-DOAS measurements are shown as colored circles at the respective position of the ship, the more yellowish the color, the higher the measured SO₂ DSCD (see colorbar). For source attribution, the absolute (or “true”) wind vectors are plotted in the same color as the MAX-DOAS DSCD “points”. For assessment of the wind speed, a reference arrow which length represents a wind speed of 10 m/s is shown. Symbols mark the locations of refineries, power plants and chemical facilities with reported SO₂ emissions in the E-PRTR database for 2017.

emissions, these facilities are a very probable source for the SO₂ plume which was observed by the MAX-DOAS offshore the port of Rotterdam. Another possible source, the intense ship traffic in the region, is expected to emit comparably much less SO₂, especially after the introduction of the stricter 0.1 % fuel sulfur content limit in the North Sea emission control area (ECA) since 1 January 2015 and is therefore less likely to be the source of the measured SO₂ enhancement.

The fact that the enhancement is quite localized offshore the port of Rotterdam and not equally distributed along the very busy shipping lane contradicts the shipping theory and confirms that the source is most probably the petrochemical industry in the harbor.

Hull

On the following day, the RV Celtic Explorer sailed northward along the English coast close to the mouth of the river Humber and the city of Hull⁹. The MAX-DOAS 15-min mean SO₂ DSCDs measured in 2° elevation on this day are plotted in Fig. 8.33. Like for Rotterdam, also on this day enhanced SO₂ DSCDs of up to 2.5×10^{16} molec cm⁻² (15-min mean) can be seen offshore of an industrial area, which could be from a SO₂ plume emitted on land.

Along the mouth of the river Humber close to the city of Hull, two large oil refineries, one power plant and one oil terminal are located. For the oil refineries, the E-PRTR database lists a reported annual SO_x/SO₂ emission of 4190 t and 2570 t for 2017, the former emitting even more than the strongest emitter in the port of Rotterdam. These two massive SO₂ emitters are very likely the source of the observed SO₂ plume, also the wind direction blowing off shore fits.

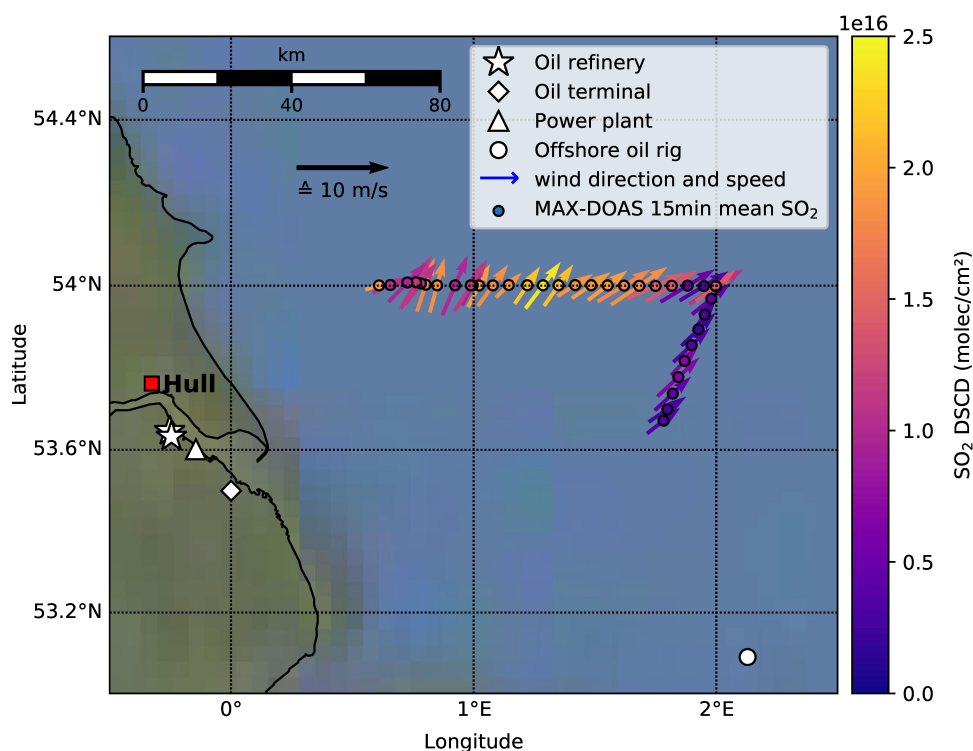


Figure 8.33.: As Fig. 8.32, but showing the 15-min mean MAX-DOAS SO₂ DSCDs measured in 2° elevation close to Hull and the mouth of the river Humber on 15 August 2017.

⁹Short for Kingston upon Hull

Gothenburg

For the MAX-DOAS measurements in the Skagerrak close to the Danish and Swedish coast near Gothenburg on 22 August 2017, the situation is not as clear. The 15-min mean MAX-DOAS SO₂ DSCDs measured in 2° elevation plotted in Fig. 8.34 are elevated in this region, and with three oil refineries on the Swedish coast and one chemical factory, there are possible emission sources. According to the wind direction, only the northernmost refinery is a possible candidate for being the emitter of the measured SO₂, but the allocation is not as compelling as for the situations discussed above. Therefore also another, unidentified source is imaginable.

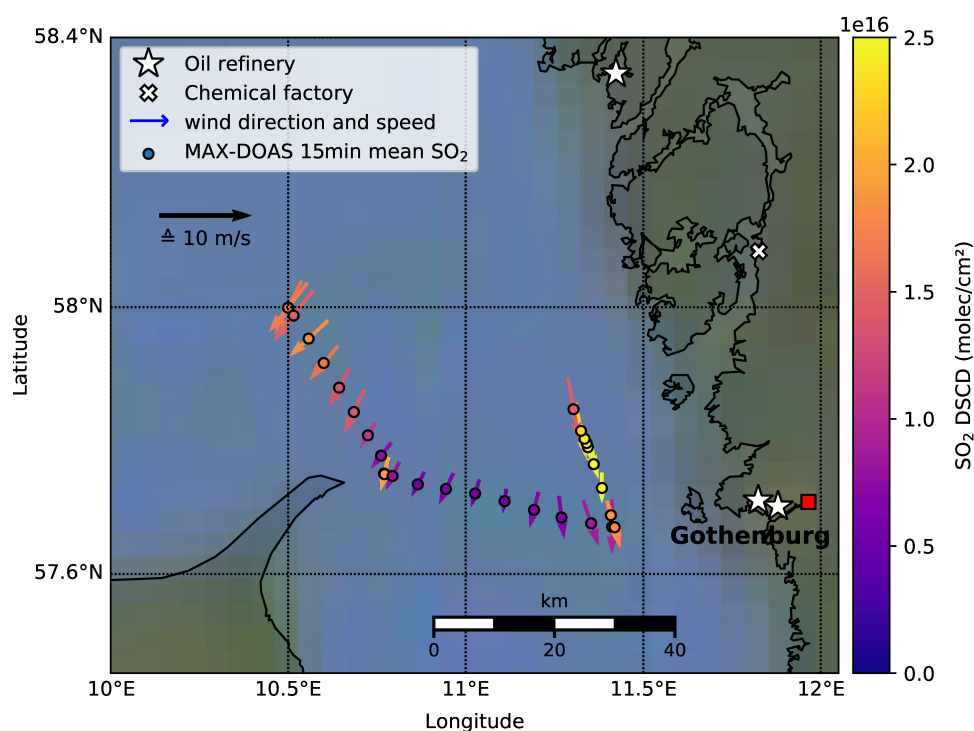


Figure 8.34.: As Fig. 8.32, but showing the 15-min mean MAX-DOAS SO₂ DSCDs measured in 2° elevation in the Skagerrak strait close to Gothenburg on 22 August 2017.

Aberdeen

On 30 August 2017, the last day of the first leg of the Celtic Explorer Summer Survey Cruise 2017, the ship sailed southward the Scottish coast to Aberdeen, where the first leg ended. As can be seen from Fig. 8.35, the 15-min mean MAX-DOAS SO₂ DSCDs measured in 2° elevation along this day's cruise track were strongly enhanced while the ship passed the headland in the north of Aberdeen, close to Peterhead. The wind blowing off shore suggests

that the gas terminals, or, more likely, the power plant is the source of the measured SO₂ plume.

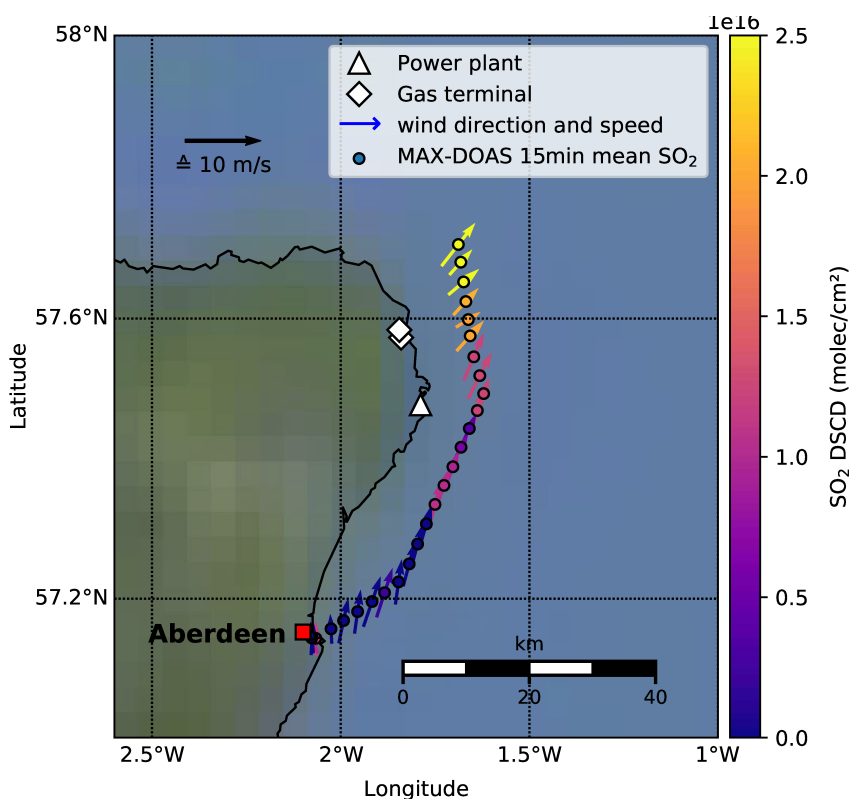


Figure 8.35.: As Fig. 8.32, but showing the 15-min mean MAX-DOAS SO₂ DSCDs measured in 2° elevation along the Scottish coast north of Aberdeen on the final day of the first leg of the 2017 summer cruise on 30 August 2017.

8.5.3 Comparison to NO₂ measurements

As a comparison to the SO₂ measurements, Fig. 8.36 gives an overview of the NO₂ measurements on the first leg of the Celtic Explorer Summer Survey 2017. The figure shows the hourly mean MAX-DOAS NO₂ DSCDs measured in 2° elevation. Compared to Fig. 8.31, the longer diurnal measurement period for NO₂, which is measured for solar zenith angles up to 80°, can be seen. As for 2016 (see Fig. 8.26), the highest NO₂ DSCDs were measured close to land and much lower values on the open sea, with the exception of some short time NO₂ enhancements caused by encountered ships. Examining the same selected regions as for SO₂, marked by the red boxes in the figure, on the first view, the NO₂ measurements close to Rotterdam (A) and close to Aberdeen (C) show a similar pattern for NO₂ than for SO₂ and will be investigated in detail in the following. The region close to the mouth of the river Humber and the city of Hull on the English coast (B) shows a different pattern, with high values in the morning and afternoon, and low values around noon, contrary to

the situation in the SO₂ measurements with enhanced values due to a SO₂ plume measured around noon. This situation, suggesting completely different sources for NO₂ and SO₂, will be analyzed in the next subsection combined with a lifetime estimation for NO₂ utilizing the special shape of that day's cruise track. For NO₂, the Skagerrak region close to Gothenburg shows no enhancement and DSCDs are comparatively low. Hence, a more detailed investigation of this region is pointless. As most oil refineries looked up in the E-PRTR database reported significantly lower NO_x than SO_x emissions, observing lower NO₂ than SO₂ values is not surprising.

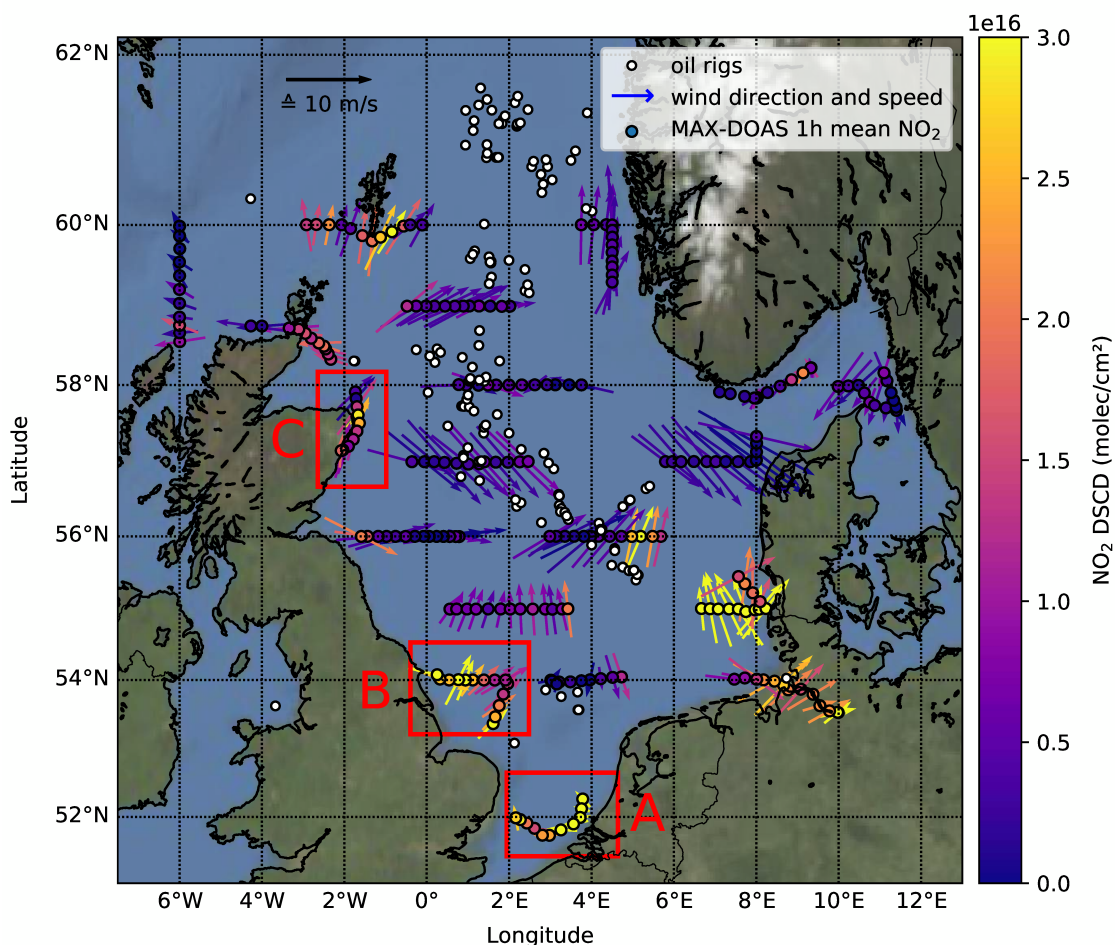


Figure 8.36.: Map showing hourly mean MAX-DOAS NO₂ DSCDs measured in 2° elevation on the Celtic Explorer Summer Survey 2017 (see Fig. 8.30 for an overview of the cruise track). The MAX-DOAS measurements are shown as colored circles at the respective position of the ship, the more yellowish the color, the higher the measured NO₂ DSCD (see colorbar). For source attribution, the absolute (or “true”) wind vectors are plotted in the same color as the MAX-DOAS DSCD “points”. For the assessment of the wind speed, a reference arrow which length represents a wind speed of 10 m/s is shown. Operational oil rigs according to the OSPAR 2017 database are shown as white dots. The regions in the red boxes are investigated in detail in the following.

Rotterdam

The Map in Fig. 8.37 shows again a magnified view of the cruise track on 14 August 2017 along the Dutch coast close to Rotterdam with the MAX-DOAS 15-min mean NO_2 DSCDs measured in 2° elevation plotted onto the map. Compared to the SO_2 measurements in Fig. 8.32, which showed a more or less localized pollution plume offshore the Rotterdam harbor entrance, the NO_2 measurements show a much broader enhancement and are elevated all the time while the ship sailed from north to south along the Dutch coast. This deviation in the SO_2 and NO_2 patterns is expected, as on land in such an industrialized region NO_x emitters like road traffic and all kinds of industries are much more frequent and widely scattered in the region compared to the few significant SO_2 emitters, which are very localized in the port area. Furthermore, even if SO_2 emissions from ships are regulated and have gone down significantly since 2015, the NO_x emissions of ships are still high, as no regulation has been in place in 2017. Thus, also the intense ship traffic on the very busy shipping lane along the coast in this region can be an additional source of NO_2 pollution.

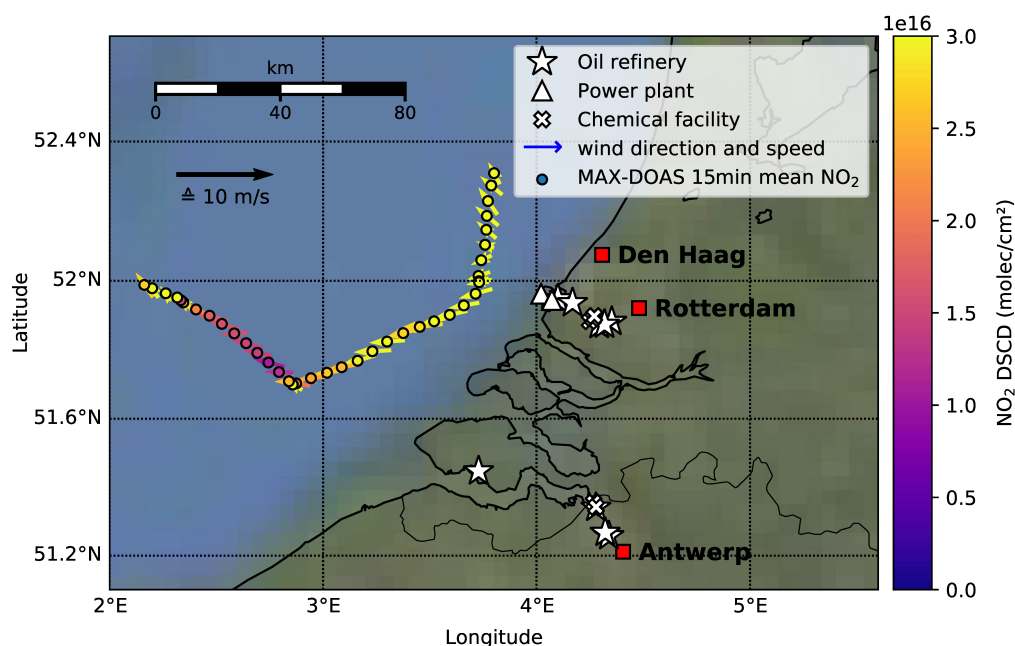


Figure 8.37.: Map showing 15-min mean MAX-DOAS NO_2 DSCDs measured in 2° elevation close to Rotterdam on 14 August 2017. The MAX-DOAS measurements are shown as colored circles at the respective position of the ship, the more yellowish the color, the higher the measured NO_2 DSCD. For source attribution, the absolute (or “true”) wind vectors are plotted in the same color as the MAX-DOAS DSCD “points”. For assessment of the wind speed, a reference arrow which length represents a wind speed of 10 m/s is shown. Symbols mark the locations of refineries, power plants and chemical facilities with reported SO_x emissions in the E-PRTR database for 2017.

After the ship turned away from the coast in the afternoon, setting course for the British coast in northwest direction, the NO₂ values decrease. At the end of the day, after the ship stopped on a waterbody measurement station, NO₂ values increase again. This second increase is most likely due to emissions of another ship.

Aberdeen

As the Scottish coast north of Aberdeen is a rural area, air pollution sources are much more localized than in the heavily industrialized Rotterdam-Antwerp area and are confined to individual facilities. Consequently, the MAX-DOAS measurements in Fig. 8.38 show the same pattern as the SO₂ measurements in Fig. 8.35 above, with mostly low values, but a strong enhancement while passing the headland north of Aberdeen close to Peterhead (approx. 19 000 inhabitants, Aberdeenshire Council (2019)). In this rural area, the only possible larger pollution sources are the power plant close to Peterhead, “one of the largest power stations in Scotland” (Scottish and Southern Energy (SSE), 2020) with E-PRTR-reported annual NO_x emissions of 794 t, and the two gas terminals with reported NO_x emissions of 784 t and 194 t for the year 2017. Most probably, the measured NO₂ emissions originate from these emitters.

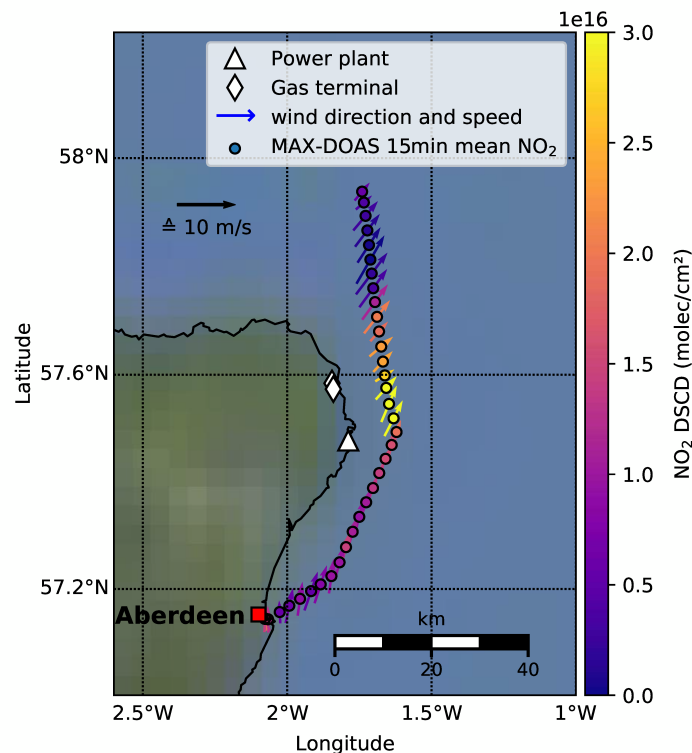


Figure 8.38.: As Fig. 8.37, but showing the 15-min mean MAX-DOAS NO₂ DSCDs measured in 2° elevation along the Scottish coast north of Aberdeen on the final day of the first leg of the 2017 summer cruise on 30 August 2017.

8.5.4 NO₂ lifetime estimation

The map in Fig. 8.39 shows the MAX-DOAS 15-min mean NO₂ DSCDs measured in 2° elevation on the V-shaped cruise track along the English coast close to the mouth of the river Humber and the city of Hull on 15 August 2017. Compared to the SO₂ measurements shown in Fig. 8.33, which featured elevated SO₂ levels in the afternoon, shortly after the ship turned from a northeasterly course receding from the coast to a northwesterly course approaching the coast again, the NO₂ measurements provide a completely different picture with high values in the morning and evening. For NO₂, the measured DSCDs are decreasing with increasing distance from the coast.

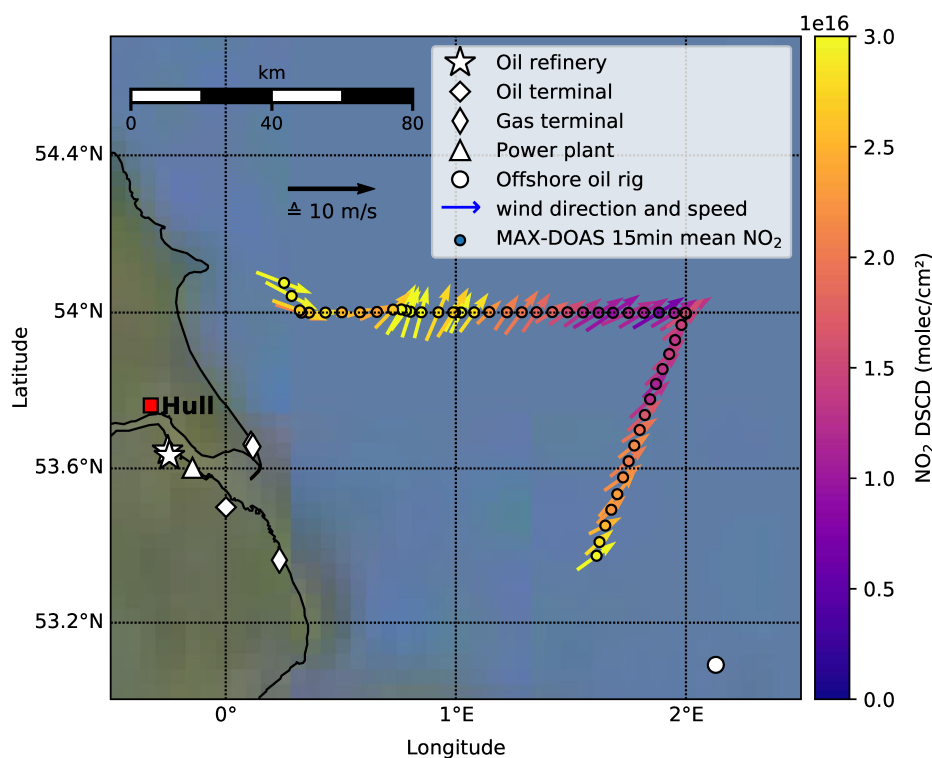


Figure 8.39.: As Fig. 8.37, but showing the 15-min mean MAX-DOAS NO₂ DSCDs measured in 2° elevation close to Hull and the mouth of the river Humber on 15 August 2017.

As the investigated coastal area close to Hull is an industrialized region, several NO_x emitters are present and listed in the E-PRTR database. As the offshore wind is blowing any pollution onto the open sea, the observed effect might very probably be an NO₂ lifetime effect. Assuming that the NO₂ is emitted more or less constantly from the several identified emitters along the coast, the NO₂ concentration is expected to rapidly increase shortly after emission, when the emitted NO is converted to NO₂ by titration with ozone, and to decrease exponentially afterwards with the NO₂ lifetime as a constant of decay. To observe

the former process, the minimal distance of the ship track to the emitters is way too large, but the latter process, the exponential decay, could theoretically be observed.

The NO₂ decrease pattern looks similar on both sides of the V-shaped cruise track. On both sides, the NO₂ decreased from approximately 3×10^{16} molec cm⁻² (at the begin of the measurements and at 54°N 1°E) to approximately 1×10^{16} molec cm⁻² (at the tip of the V at 54°N 2°E) over a distance of roughly 80 km. This is a reduction to about 1/3 or 1/e over 80 km. Taking into account the average wind speed of (10.5 ± 1.4) kn [mean \pm standard deviation] being equivalent to (5.4 ± 0.7) m/s, the estimated NO₂ lifetime ranges from 3.6 h to 4.7 h, with a mean estimate of 4.1 h.

This rough estimate agrees very well with the results of other studies: Beirle et al. (2011) investigated the NO_x lifetime from satellite DOAS measurements of NO₂ for several isolated megacities around the globe and found that daytime lifetimes are approximately 4 hours at low and mid-latitudes. For Ryadh, the study gives a result of (4.0 ± 0.4) h. In a more recent study, Liu et al. (2016) improved the methodology of Beirle et al. (2011) and derived lifetimes of (3.8 ± 1.0) h for 70 non-mountainous sites.

8.6 Summary and conclusion

Seven ship campaigns for assessment of marine air quality, six of that with a MAX-DOAS on-board, have been performed in the greater North and Baltic Sea area in a cooperation with the BSH on their regular survey cruises on the research vessel Celtic Explorer. For the shipborne measurements, the MAX-DOAS instrument has been installed up on the crow's nest, pointing towards portside and doing vertical elevation scans during cruising.

For an analysis of the measurement data, first a roll-angle correction had to be applied to the raw data to correct for the wave-induced movement of the ship. For this, a simple two-axis inclinometer has been compared to the ship's own motion reference unit's data, the latter turned out to be more accurate and was preferred for the data analysis. The inclinometer, which appeared to be very sensitive to angular misalignment, was only being used as a backup.

This study shows that shipborne MAX-DOAS measurements are well feasible to detect individual ship emission plumes from other ships that pass the own vessel. For an exemplarily selected day from the 2013 summer survey cruise, several ships were identified as sources of the measured NO₂ and SO₂ enhancements. For the largest of those ships, a fast traveling cruise ship of 293 m length, an SO₂ to NO₂ ratio of about 1.1, a very high value, was found. This means that this ship apparently emitted huge amounts of SO₂ indicating a high fuel sulfur content, maybe exceeding the 1 % limit valid at that time. The highest concentration

of NO₂ and SO₂ were found in the 4° viewing elevation, indicating an elevated plume. It is interesting to note that the NO₂ and SO₂ maximum peak values were measured at slightly different times although both were retrieved from the same spectra in the UV, showing that both pollutants were obviously not distributed equally in the exhaust plume.

However, for regular ship emission monitoring, the benefit of such measurements on these survey cruises is limited, as away from the shipping lanes, the number of encountered ships per day can be quite small. Kattner (2019), by analyzing the simultaneous on-board in-situ trace gas analyzer measurements, came to a similar conclusion.

Like for the stationary measurements on Neuwerk (see Chapter 6), after the introduction of a stricter fuel sulfur content limit of 0.1 % on 1 January 2015, no clear SO₂ signals could be measured from passing ships. The effect of the sulfur content regulation can also be seen when comparing all measurements taken in North and Baltic Sea on the 2013 and 2015 summer survey cruises, the latter showing significantly lower SO₂ pollution levels.

A comparison of NO₂ measurements in the North Sea and the English channel taken on the 2016 summer cruise in 2° and 30° elevation demonstrated the different sensitivity for the lowest part of the boundary layer. Comparing MAX-DOAS vertical column densities (VCDs) of NO₂ retrieved with sequential reference spectrum or fixed reference for the whole campaign, it can be seen that especially close to land and in the English channel elevated NO₂ pollution is present, very probably originating from land-based sources and transported over the sea. A comparison of NO₂ VCDs from MAX-DOAS (hourly mean values) and the OMI satellite instrument (monthly mean values) shows good agreement in the general picture, that is low NO₂ over the open sea, higher values close to the coasts and in the English channel, and in the magnitude of the measured columns, but also demonstrates that the comparison of hourly mean values (MAX-DOAS) to monthly means (satellite) has a limited conclusiveness.

For the evaluation of the impact of land-based pollution sources on air quality on the sea the first leg of the 2017 summer survey cruise was selected because of promising, prevailing offshore wind conditions. Although practically no SO₂ signals from other ships could be found, several strong SO₂ plumes were crossed close to the coasts. But not only SO₂ was enhanced there, also NO₂ was contained in the measured pollution plumes. A detailed analysis for the sea areas close to Rotterdam/Antwerp (NL, BE), Hull (UK), Gothenburg (SE) and Aberdeen (UK) was performed including the identification of possible sources with help of the European Pollutant Release and Transfer Register (E-PRTR), where facilities have to report their annual emissions. For both SO₂ and NO₂, several strong emitters were identified in near-coastal power plants, oil refineries, and other shore-based industrial facilities, with reported SO₂ emissions of up to 4200 t per year. For SO₂, where emissions from shipping decreased significantly since 2015, which can be seen in this study, in the measurements on Neuwerk (Chapter 6), and in various other studies, shore-based emitters

might now provide an even more substantial fraction of the SO₂ pollution in the North Sea area as before.

This study includes also a lifetime estimation for NO₂ in the marine boundary layer, giving a range from 3.6 h to 4.7 h, with a mean estimate of 4.1 h. This estimate is in good agreement with other satellite-based studies on the NO₂ lifetime in the boundary layer.

In conclusion, the shipborne MAX-DOAS measurements taken on six ship campaigns in the greater North and Baltic Sea area have shown that emissions of SO₂ and NO₂ from other ships as well as land-based emitters can be detected. The shipborne measurements on the BSH survey cruises also turned out to be very helpful to get a general overview picture of the distribution of air pollutants like NO₂ and SO₂ in the North and Baltic Sea, and thus to assess the air quality in a much larger region than possible with a stationary site like on Neuwerk, with the downside of sacrificing temporal resolution. As an addition to stationary long term measurements, shipborne campaigns have shown to be a worthwhile additional information source for air quality assessment.

Summary and conclusions

Air pollution is a major environmental health risk and affects not only human health but also plants and ecosystems. Over the last decades, there has been a strong increase in ship traffic and shipping emissions of gas phase air pollutants. At the same time, a reduction in their land sources in much of Europe occurred, which has led to an increasing contribution of shipping emissions to air pollution in coastal regions. Consequently, emission reduction measures have been enacted by the International Maritime Organization (IMO) in the International Convention for the Prevention of Pollution from Ships (MARPOL 73/78 Annex VI) globally as well as, more stringent, locally in so-called emission control areas (ECAs) like the North and Baltic Sea, which are the main areas-of-interest of the presented studies. Especially important for this thesis is the ECA-related reduction of the allowed sulfur content in marine fuels from 1 % to 0.1 %, that was set into force on 1 January 2015. In order to monitor the effectiveness of these measures as well as the overall impact of ship emissions on air quality, measurements of air pollution from ships are of crucial importance.

Long term trends on Neuwerk

The first part of this thesis presents a three-year long time series of ground-based MAX-DOAS measurements of the air pollutants NO_2 and SO_2 on the island Neuwerk, which has been analyzed for contributions from shipping emissions.

Being located in the German Bight close to Cuxhaven in a distance of 6 to 7 km to the main shipping lane into the Elbe river towards the port of Hamburg, both individual ship exhaust plumes and ambient background pollution can be measured, the latter either coming from old, diluted ship plumes, or land-based pollution sources, depending on the wind direction.

A simple approach using the measured column amounts of the oxygen collision complex O_4 for the determination of the horizontal light path lengths has been applied to retrieve path-averaged pollutant volume mixing ratios (VMRs). An excellent agreement is found between mixing ratios determined from NO_2 retrievals in the UV and visible parts of the spectrum, especially for ambient background pollution, demonstrating the validity of the approach. Obtained mixing ratios of NO_2 and SO_2 have been compared to co-located in-situ measurements from an on-site trace gas analyzer, showing good correlation on

average, especially in the day-to-day trends, but also a systematic underestimation by the MAX-DOAS O_4 -scaling approach due to the long averaging path.

Comparing data from before and after the introduction of the more stringent fuel sulfur content limit in the North Sea ECA in 2015, a significant reduction in SO_2 levels has been observed. For situations with wind from the open North Sea, where ships are the only local source of air pollution, the average mixing ratio of SO_2 decreased by a factor of eight, while for NO_2 no significant change in concentrations has been observed, confirming the expectations, as the NO_x emission limits were not set into force yet. The strong reduction in SO_2 emissions from the ships can be seen in the database of more than 2000 identified individual ship emission plumes, that were analyzed for the emission ratio of SO_2 to NO_2 . For the years 2013/2014, an average ratio of 0.3 was found, that decreased significantly in 2015/2016. The observed strong decrease in SO_2 emissions after the sulfur limit change is in good agreement with other studies.

By sorting measurements according to the prevailing wind direction and selecting two angular reference sectors representative for wind from open North Sea and coast excluding data with mixed air mass origin, relative contributions of ships and land-based sources to air pollution levels in a coastal region close to a main shipping lane have been estimated to be around 40 % : 60 % for NO_2 as well as SO_2 in 2013/2014, dropping to 14 % : 86 % for SO_2 in 2015/2016.

Onion peeling MAX-DOAS approach

Utilizing the fact that the effective light path length in the atmosphere depends systematically on wavelength, simultaneous measurements and DOAS retrievals in the UV and visible spectral range have been used to probe air masses at different horizontal distances to the instrument. As shown, this so-called onion peeling MAX-DOAS approach can be used to estimate two-dimensional pollutant distributions over a shipping lane.

Two case-studies have been selected to demonstrate the ability to derive the approximate plume positions in the observed area: A situation with northerly wind shows high NO_2 concentrations close to the measurement site and low values in the north of the shipping lane. The opposite situation with southerly wind, unfavorable for the on-site in-situ instrumentation, demonstrates the ability to detect enhanced NO_2 concentrations several kilometers away from the instrument.

Simple plume forward trajectories were combined with a Gaussian plume model look-up-table approach to project the ships' plume locations and spatial extent. For the modeled plumes' locations and shape, a good agreement with airborne imaging DOAS measurements was found.

Using this Gaussian plume model approach, in-plume NO₂ volume mixing ratios could be derived from the MAX-DOAS measurements.

For validation, a comparison to airborne imaging DOAS measurements and retrievals during the NOSE campaign in July 2013 has been performed, showing good agreement between the approximate plume position derived from the onion peeling MAX-DOAS and the airborne measurements as well as between the derived in-plume NO₂ VMRs.

In conclusion, the presented measurements provide a real world demonstration that the onion peeling approach works for MAX-DOAS measurements and can successfully be applied to investigate air pollution by ships and to derive in-plume NO₂ volume mixing ratios for ships passing the instrument in a distance of several km, considerably increasing the information that can be gained from MAX-DOAS measurements.

Shipborne measurements in North and Baltic Sea

In cooperation with the Federal Maritime and Hydrographic Agency of Germany (Bundesamt für Seeschifffahrt und Hydrographie, BSH), six¹ shipborne MAX-DOAS measurement campaigns have been performed on-board the research vessel Celtic Explorer on the BSH's routinely conducted survey cruises, expanding the research area from the German North Sea coast to the entire greater North Sea area and the German part of the Baltic Sea. The presented study shows exemplarily results from four of these six campaigns, two of them with the author on-board.

From the 2013 summer survey cruise, measurements of NO₂ and SO₂ in pollutant plumes emitted from individual passing ships are presented. This includes the encounter with an 293 m-long, fast traveling cruise ship with exceptionally large SO₂ emission and a large SO₂ to NO₂ ratio of 1.1, compared to the 0.3 found on average for the time before 2015 at Neuwerk, pointing at a probable sulfur limit regulation violation. The fact that the NO₂ and SO₂ maximum peak were measured at slightly different times although both were retrieved from the same spectra in the UV, shows that both pollutants were obviously not distributed equally in the exhaust plume, an assumption which is often taken.

Comparing all SO₂ measurements in the North and Baltic Sea area from the 2013 and 2015 summer survey cruise, the latter being after the introduction of the 0.1 % sulfur limit (down from 1 % before), shows significantly lower overall SO₂ pollution levels, especially on the open sea, although the probed areas slightly differed.

NO₂ measurements from the 2016 summer survey cruise show that especially in the English channel elevated NO₂ pollution is present, probably originating from the industrialized, highly populated surrounding. For the same cruise, a comparison of NO₂ vertical columns

¹And a seventh one with only in-situ air quality measurement devices on board

from MAX-DOAS and the OMI satellite instrument shows good agreement in the general picture, i.e., low NO₂ over the open sea, higher values close to the coasts and in the English channel, and in the magnitude of the measured columns, but also demonstrates that the comparison of hourly mean values (MAX-DOAS) to monthly means (satellite) has a limited conclusiveness.

Prevailing off-shore wind conditions on the 2017 summer survey cruise allowed to investigate several strong SO₂ and NO₂ signals close to the coast and to identify the respective sources with help of the European Pollutant Release and Transfer Register (E-PRTR), where facilities have to report their annual emissions. Strong SO₂ emitters were identified in near-coastal power plants, oil refineries and other shore-based industrial facilities with reported SO₂ emissions of up to 4200 t per year, while no ship-related SO₂ signals could be measured due to the much lower sulfur content of the fuel since 2015, similarly to the situation on Neuwerk. Thus, the influence and relative contribution of such shore-based industrial emitters on SO₂ air pollution in coastal regions and on the sea close to the coast has substantially increased compared to the years before.

From the shipborne measurements, the lifetime of NO₂ in the marine boundary layer was estimated to be around 4 hours, which is in good agreement with other studies.

Overall conclusion

As the presented studies have shown, ships contribute substantially to air pollution in coastal regions, but emission regulations like the introduced fuel sulfur content limit can be very effective in cleaning up the exhaust, significantly reducing the pollutant emissions and improving air quality in the marine environment. As both the ground-based and shipborne measurements have shown, land-based pollution sources like traffic for NO_x, and power plants and oil refineries for SO₂, contribute significantly to air pollution along the coasts, the latter with increasing contribution as not being concerned by the MARPOL sulfur limits.

In contrast to the situation for road traffic, air quality measurement stations for ship emissions are sparse, and especially on the open sea, non-existent. For the analysis of the general compliance and the impact of regulations on coastal and marine air quality, measurements of shipping emissions are crucial and long term measurement studies like the ones shown here are especially important to identify trends and to estimate source contributions.

Shipborne measurements vastly expand the probed area, and, as has been shown, allow for the assessment of air quality on the open sea and along the coasts. Although it has been shown that measurements of individual ships' exhausts are feasible on such survey

cruise campaigns, the number of ships encountered on the open sea, away from the main shipping lanes, turned out to be quite small.

Overcoming one of the main challenges in the interpretation of passive DOAS type observations, the derivation of the atmospheric light path lengths, this thesis presents newly developed approaches as well as first applications of existing methods to measurements of shipping emissions, that improve the feasibility and expand the possibilities for remote sensing measurements of individual ships' emission plumes with the MAX-DOAS technique. One of the main step-ups is the possibility to remotely detect emission plumes in a distance of several kilometers and to derive their approximate position under wind conditions unfavorable for on-site in-situ measurements, even when wind is blowing the plumes away from the measurement site. Combined with a simple model, which has been shown to predict the ship plumes' locations and spatial extent with sufficient accuracy, the retrieval of in-plume pollutant concentrations becomes possible, which is demonstrated for the first time for both ground-based MAX-DOAS measurements and air-borne nadir-looking imaging DOAS measurements.

Although most measurements of air pollution are performed with in-situ instrumentation like trace gas analyzers, including the few existing ship emission monitoring studies and stations, the studies presented show that MAX-DOAS measurements can provide both a complementary approach and an alternative to in-situ trace gas measurements at sites, where the ships are several kilometers away from the instrument and interpretation of in-situ measurements is challenging due to dilution and broadening of the plume during the travel time from the ships to the measurement site, and even under wind conditions unfavorable for in-situ measurements.

Outlook

With respect to the instruments, measurements, and data analysis, several options for further improvements exist.

For stationary measurements of shipping emissions like on Neuwerk, especially the SO₂ measurements, where the signals of the ships since 2015 are below the detection limit of the instrument and hardly distinguishable from noise, would benefit from a better signal-to-noise ratio. This could be achieved by longer integration times and thus co-adding of more spectra, by enhancing the light throughput in the UV for example with a shorter light fiber (as the Rayleigh-scattering-induced light attenuation in the fiber is much stronger in the UV) or with a different spectrometer. As longer measurement times (integration times) per azimuthal viewing direction mean less time resolution, the measurement sequence, the regularly repeated schedule of viewing directions, could be optimized and stripped of unnecessary directions to gain measurement time. With respect to the light fiber, on the radar tower on Neuwerk its length was fixed due to the distance between telescope and

spectrometer unit, but on potential other stations the usage of a shorter light fiber could be tested.

As the measurements on Neuwerk have shown, a permanent network (internet) connection from the institute to the on-site instruments should have a high priority, to avoid large data gaps due to instrumental problems remaining unnoticed until the next visit, which is even more important on such remote, difficult-to-access measurement sites.

For the onion-peeling approach, a third wavelength window further in the visible spectral range above 500 nm would enable to gain even more information on the spatial distribution of the NO_2 field above the shipping lane and at even further distances from the instrument. An intensive model study with accompanying measurements on the aerosol conditions in the marine environment of the North Sea close to Neuwerk could improve the O_4 scaling and onion-peeling results by introducing correction factors for the retrieved light path lengths, helping to quantify and to reduce the systematic underestimation bias.

For the shipborne MAX-DOAS measurements, a smaller and lighter (plastics instead of stainless steel) telescope could be designed to enable autotracking of the viewing elevation angle under the wave-induced roll-angle movement of the ship, in combination with a higher-spec inclinometer including a gyroscope sensor in addition to the accelerometer.

The new approaches presented here can be applied to other sites with suitable distance (at least a few kilometers) between the MAX-DOAS instrument and the ships. An especially interesting site for this method might be Ny-Ålesund (Svalbard), a remote location with many cruise ship calls and nearly no land-based pollution (only one small power plant at the harbor).

An unidentified trace gas featuring absorption structures in the short-wavelength UV region around 300 nm which has been measured by both a (passive) MAX-DOAS system and an active longpath-DOAS instrument at the other MESMART measurement site in Wedel should be further explored. Transport modeling approaches could help to determine its source.

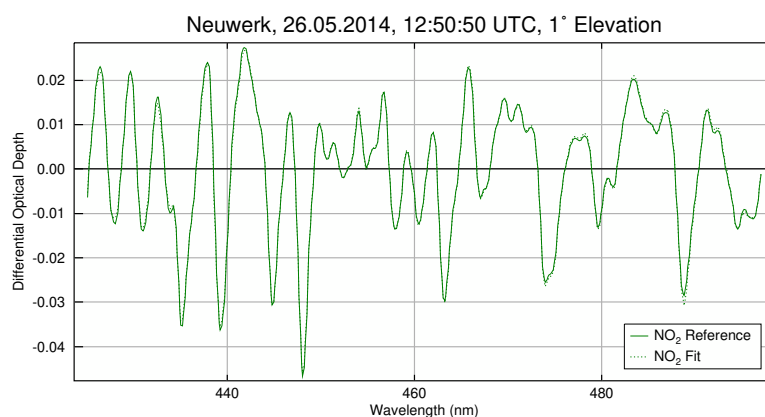
In the future, measurements of NO_x will become even more important, especially when the NO_x emissions limits are set into force in the North and Baltic Sea in 2021.

For a regular compliance monitoring of ship emissions, the development of a CO_2 retrieval technique for DOAS type measurements would be a big step forward. DOAS type CO_2 measurements would enable to remotely determine the ships' fuel sulfur content and to remotely retrieve emission factors NO_x and SO_2 . Emission factors would not only be important for ship emission monitoring, especially in consideration of the new NO_x emission limits in North and Baltic Sea and the new global 0.5 % fuel sulfur cap, but could also provide a valuable input for air pollution modeling.

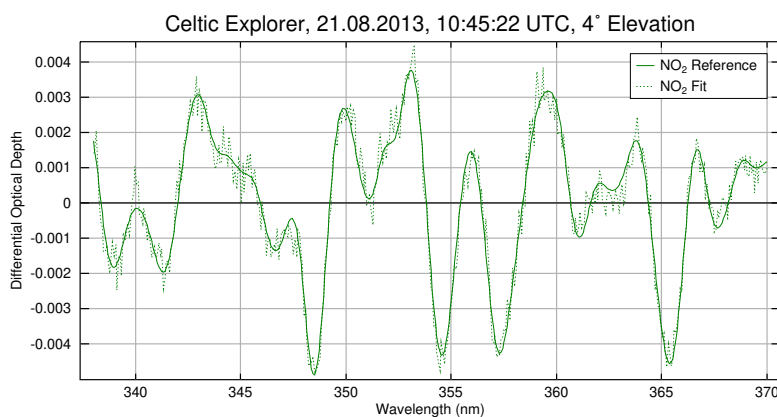
Appendix

A

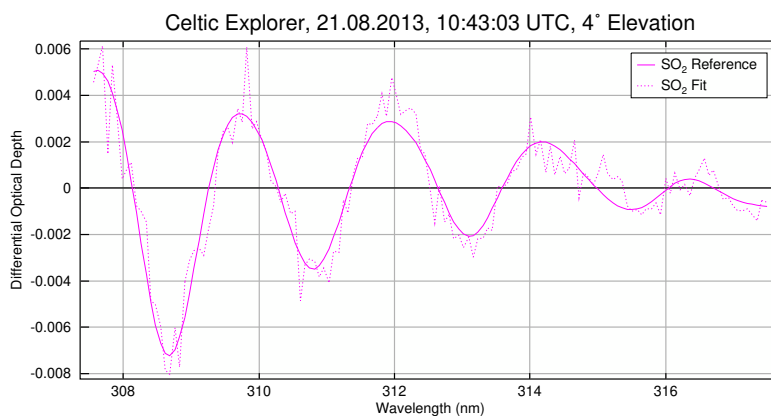
A.1 DOAS fit examples



(a) NO₂ fit in the visible region (Neuwerk, see Section 5.1), DSCD = 2.3×10^{17} molec cm⁻², Fit error = 0.2 %



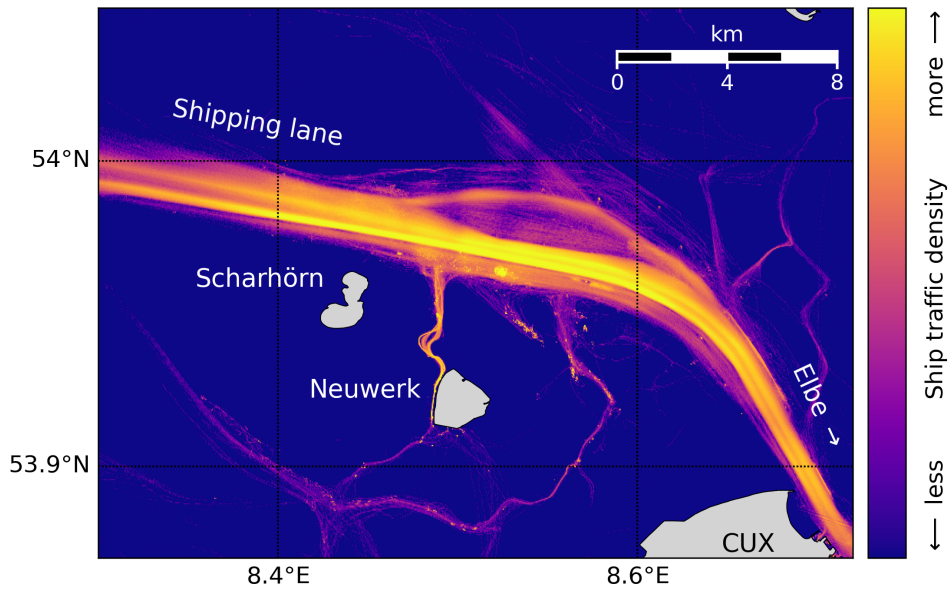
(b) NO₂ fit in the UV (cruise ship emission, see Section 8.2), DSCD = 7.6×10^{16} molec cm⁻², Fit error = 1.1 %



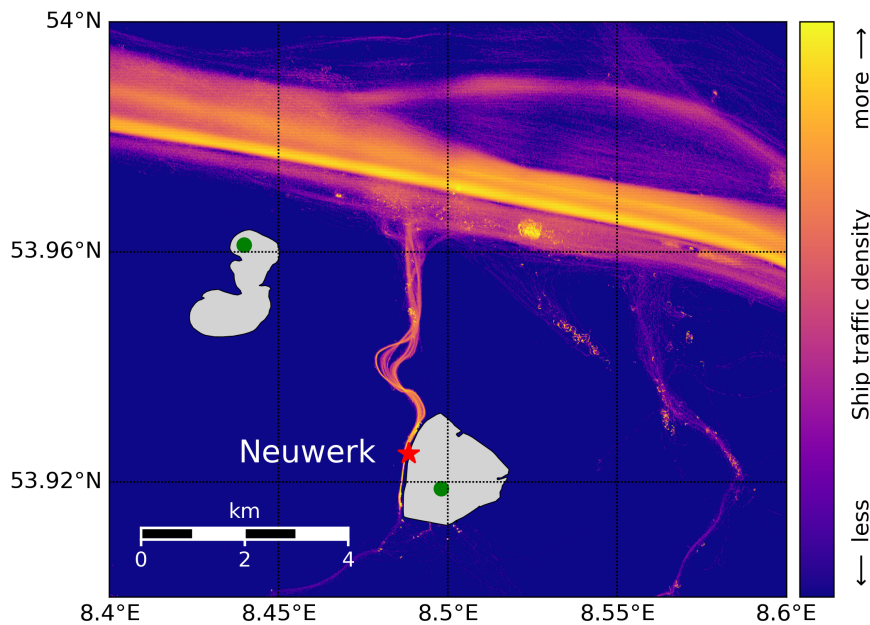
(c) SO₂ fit (cruise ship emission, see Section 8.2), DSCD = 6.9×10^{16} molec cm⁻², Fit error = 5.3 %

Figure A.1.: DOAS fit examples for NO₂ in the visible region (a), UV (b) and for SO₂ (c).

A.2 AIS ship traffic density maps

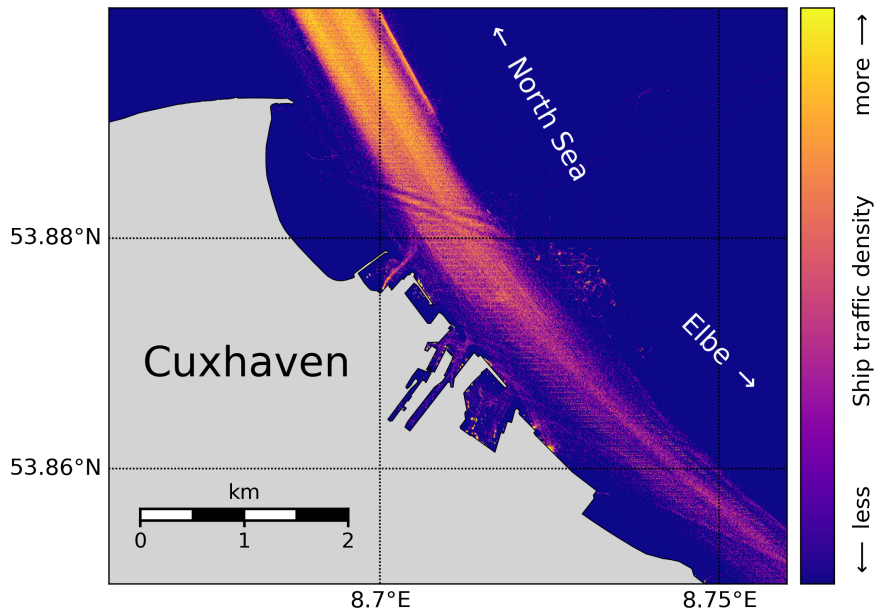


(a) Ship traffic density map showing the main shipping lane from the North Sea into the Elbe river close to the islands Neuwerk and Scharhörn.

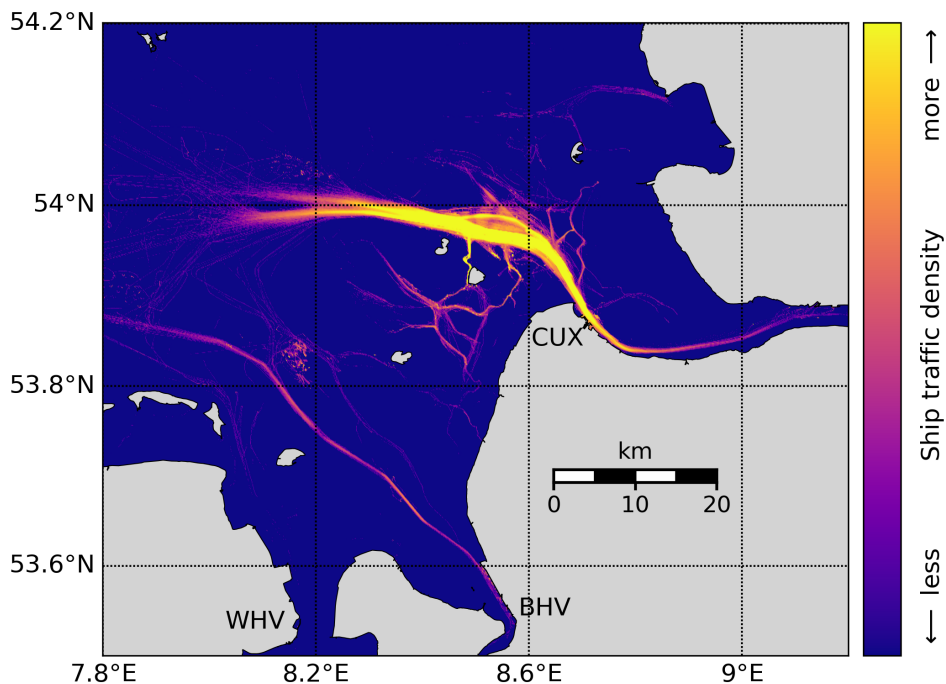


(b) Enlarged view of the island Neuwerk and part of the main shipping lane in the North of the island. The location of the MAX-DOAS instrument on the radar tower on Neuwerk is marked with a red star, the wind measurement stations on Neuwerk and the neighboring island Scharhörn are marked with green dots. As can be seen from the figure, the narrow shipping lane to the island, which is mainly used by a passenger ferry and maintenance ships of the Hamburg Port Authority (HPA), changed its pathway several times due to the highly-dynamic nature of the wadden sea. On the southern edge of the main shipping lane in the North, the Neuwerk roadstead can be seen, where idle ships anchor.

Figure A.2.: Ship traffic density maps calculated from all received AIS (Automatic Identification System, see Section 6.1.5) messages on Neuwerk from 2013 to 2016. Plotted is the number of AIS ship position messages per grid cell on a logarithmic colorscale.



(c) Enlarged view of the main shipping lane in the mouth of the Elbe river close to the city of Cuxhaven. Towards the southeast, with increasing distance to our AIS antenna and with increasing land coverage the AIS signal reception rate decreases and only the position messages of very high ships reach our AIS receiver. The ripple-like structures in the upper center of the figure at 53.88°N and 8.71°E are very probably caused by three high buildings in Cuxhaven blocking our reception of the ships' AIS signal.



(d) Overview map on the southeastern part of the German Bight showing not only the main shipping lane into the Elbe river, but also the more distant shipping lane towards Bremerhaven (BHV). North of Wilhelmshaven (WHV) and the small island of Mellum (M) at 53.8°N and 8.2°E an offshore wind farm can be identified by its busy ship traffic. Again on this map, the decreasing AIS reception rate with increasing distance from our antenna on the radar tower can be seen.

Figure A.2.: Ship traffic density maps calculated from all received AIS (Automatic Identification System, see Section 6.1.5) messages on Neuwerk from 2013 to 2016. Plotted is the number of AIS ship position messages per grid cell on a logarithmic colorscale.

List of abbreviations

AA Azimuth angle

AirMAP Airborne imaging Differential Optical Absorption Spectroscopy instrument for Measurements of Atmospheric Pollution

AIS Automatic Identification System, see Section 6.1.5

AMF Air mass factor

BSH Bundesamt für Seeschifffahrt und Hydrographie

CCD Charge-coupled device

CE Celtic Explorer

DOAS Differential Optical Absorption Spectroscopy

DSCD Differential slant column density

EA Elevation angle

ECA Emission control area

FOV Field of view

GPS Global positioning system

HFO Heavy fuel oil

IMO International Maritime Organization

IUP Institut für Umweltphysik

LOS Line of sight

MAX-DOAS Multi-axis Differential Optical Absorption Spectroscopy

MDO Marine diesel oil

MESMART Measurements of shipping emissions in the marine troposphere (project)

MFO Marine fuel oil, same as HFO

MGO Marine gas oil

MRU Motion reference unit

NECA Nitrous oxide emission control area

NOSE Nord-Ost-See-Experiment (campaign)

ppb Parts per billion (1 ppb = 1×10^{-9})

ppm Parts per million (1 ppm = 1×10^{-6})

ppt Parts per trillion (1 ppt = 1×10^{-12})

RAA Relative azimuth angle

RV Research vessel

SAA Solar azimuth angle

SC Slant column

SCD Slant column density

SECA Sulfur emission control area

SZA Solar zenith angle

TEU Twenty-foot equivalent unit

UPS Uninterruptible power supply

VC Vertical column

VCD Vertical column density

VMR Volume mixing ratio

References

- Aberdeenshire Council (2019). *Population*. URL: <https://www.aberdeenshire.gov.uk/council-and-democracy/statistics/population/> (visited on 05/01/2020) (cit. on p. 220).
- Adamchak, F. and Adede, A. (2014). “LNG as Marine Fuel”. In: *LNG 17 Proceedings*. 17th International Conference & Exhibition on Liquefied Natural Gas. URL: https://www.gti.energy/wp-content/uploads/2018/12/7-1-Frederick_Adamchak-LNG17-Paper.pdf (visited on 10/06/2020) (cit. on p. 35).
- Ahrens, C. and Henson, R. (2015). *Meteorology Today*. 11th ed. Boston: Cengage Learning Custom Publishing (cit. on pp. 15, 44).
- Alföldy, B., Lööv, J. B., Lagler, F., Mellqvist, J., Berg, N., Beecken, J., Weststrate, H., Duyzer, J., Bencs, L., Horemans, B., Cavalli, F., Putaud, J. P., Janssens-Maenhout, G., Csordás, A. P., Van Grieken, R., Borowiak, A., and Hjorth, J. (2013). “Measurements of Air Pollution Emission Factors for Marine Transportation in SECA”. In: *Atmos. Meas. Tech.* 6(7), 1777–1791. DOI: 10.5194/amt-6-1777-2013 (cit. on pp. 31, 32).
- Aliwell, S. R., Van Roozendaal, M., Johnston, P. V., Richter, A., Wagner, T., Arlander, D. W., Burrows, J. P., Fish, D. J., Jones, R. L., Tørnkvist, K. K., Lambert, J.-C., Pfeilsticker, K., and Pundt, I. (2002). “Analysis for BrO in Zenith-Sky Spectra: An Intercomparison Exercise for Analysis Improvement”. In: *J. Geophys. Res.* 107(D14), ACH 10-1-ACH 10–20. DOI: 10.1029/2001JD000329 (cit. on p. 67).
- Andersson, K., Brynolf, S., Lindgren, F., and Wilewska-Bien, M. (2016). *Shipping and the Environment. Improving Environmental Performance in Marine Transportation*. Berlin: Springer (cit. on p. 32).
- Arndt, E.-H. (2018). “Grünes Schiff im Dienste des Klimaschutzes”. In: *Täglicher Hafenbericht (THB - Deutsche Schifffahrts-Zeitung)* (cit. on p. 169).
- Arndt, E.-H. (2019). “Irische Seemannschaft, deutsche Forscher”. In: *Täglicher Hafenbericht (THB - Deutsche Schifffahrts-Zeitung)* (cit. on p. 169).
- Arndt, N. T. and Nisbet, E. G. (2012). “Processes on the Young Earth and the Habitats of Early Life”. In: *Annu. Rev. Earth Planet. Sci.* 40(1), 521–549. DOI: 10.1146/annurev-earth-042711-105316 (cit. on p. 5).
- Aspect, A. (2017). “From Huygens’ Waves to Einstein’s Photons: Weird Light”. In: *Comptes Rendus Phys.* 18(9-10), 498–503. DOI: 10.1016/j.crhy.2017.11.005 (cit. on p. 43).
- Aulinger, A., Matthias, V., Zeretzke, M., Bieser, J., Quante, M., and Backes, A. (2016). “The Impact of Shipping Emissions on Air Pollution in the Greater North Sea Region – Part 1: Current Emissions and Concentrations”. In: *Atmos. Chem. Phys.* 16(2), 739–758. DOI: 10.5194/acp-16-739-2016 (cit. on pp. 31, 33).

- Azzara, A., Rutherford, D., and Wang, H. (2014). “Feasibility of IMO Annex VI Tier III Implementation Using Selective Catalytic Reduction”. In: *The International Council on Clean Transportation* 4, 1–9 (cit. on p. 36).
- Bada, J. L. (2004). “How Life Began on Earth: A Status Report”. In: *Earth Planet. Sci. Lett.* 226(1-2), 1–15. DOI: 10.1016/j.epsl.2004.07.036 (cit. on p. 5).
- Balzani Lööv, J. M., Alföldy, B., Gast, L. F. L., Hjorth, J., Lagler, F., Mellqvist, J., Beecken, J., Berg, N., Duyzer, J., Westrate, H., Swart, D. P. J., Berkhout, A. J. C., Jalkanen, J. P., Prata, A. J., Van Der Hoff, G. R., and Borowiak, A. (2014). “Field Test of Available Methods to Measure Remotely SO_x and NO_x Emissions from Ships”. In: *Atmos. Meas. Tech.* 7(8), 2597–2613. DOI: 10.5194/amt-7-2597-2014 (cit. on pp. 31, 39, 104).
- Beecken, J., Mellqvist, J., Salo, K., Ekholm, J., Jalkanen, J. P., Johansson, L., Litvinenko, V., Volodin, K., and Frank-Kamenetsky, D. A. (2015). “Emission Factors of SO₂, NO_x and Particles from Ships in Neva Bay from Ground-Based and Helicopter-Borne Measurements and AIS-Based Modeling”. In: *Atmos. Chem. Phys.* 15(9), 5229–5241. DOI: 10.5194/acp-15-5229-2015 (cit. on p. 39).
- Beecken, J., Mellqvist, J., Salo, K., Ekholm, J., and Jalkanen, J. P. (2014). “Airborne Emission Measurements of SO₂, NO_x and Particles from Individual Ships Using a Sniffer Technique”. In: *Atmos. Meas. Tech.* 7(7), 1957–1968. DOI: 10.5194/amt-7-1957-2014 (cit. on pp. 38, 104).
- Beirle, S., Boersma, K. F., Platt, U., Lawrence, M. G., and Wagner, T. (2011). “Megacity Emissions and Lifetimes of Nitrogen Oxides Probed from Space”. In: *Science* 333(6050), 1737–1739. DOI: 10.1126/science.1207824 (cit. on p. 222).
- Beirle, S., Platt, U., von Glasow, R., Wenig, M., and Wagner, T. (2004). “Estimate of Nitrogen Oxide Emissions from Shipping by Satellite Remote Sensing”. In: *Geophys. Res. Lett.* 31(18), 4–7. DOI: 10.1029/2004GL020312 (cit. on p. 40).
- Beirle, S., Platt, U., Wenig, M., and Wagner, T. (2003). “Weekly Cycle of NO₂ by GOME Measurements: A Signature of Anthropogenic Sources”. In: *Atmos. Chem. Phys.* 3(6), 2225–2232. DOI: 10.5194/acp-3-2225-2003 (cit. on p. 101).
- Belbruno, E. and Gott III, J. R. (2005). “Where Did The Moon Come From?” In: *The Astronomical Journal* 129(3), 1724–1745. DOI: 10.1086/427539 (cit. on p. 4).
- Bell, E. A., Boehnke, P., Harrison, T. M., and Mao, W. L. (2015). “Potentially Biogenic Carbon Preserved in a 4.1 Billion-Year-Old Zircon”. In: *Proc. Natl. Acad. Sci. U.S.A.* 112(47), 14518–14521. DOI: 10.1073/pnas.1517557112 (cit. on p. 5).
- Bell, J. and Treshow, M. (2002). *Air Pollution and Plant Life*. Chichester, West Sussex, UK: Wiley (cit. on pp. 16, 17).
- Bell, T. L., Rosenfeld, D., and Kim, K. M. (2009). “Weekly Cycle of Lightning: Evidence of Storm Invigoration by Pollution”. In: *Geophys. Res. Lett.* 36(23), 1–5. DOI: 10.1029/2009GL040915 (cit. on p. 101).
- Berg, N., Mellqvist, J., Jalkanen, J. P., and Balzani, J. (2012). “Ship Emissions of SO₂ and NO₂: DOAS Measurements from Airborne Platforms”. In: *Atmos. Meas. Tech.* 5(5), 1085–1098. DOI: 10.5194/amt-5-1085-2012 (cit. on pp. 39, 136).

- Boersma, K. F., Eskes, H. J., Dirksen, R. J., van der A, R. J., Veefkind, J. P., Stammes, P., Huijnen, V., Kleipool, Q. L., Sneep, M., Claas, J., Leitão, J., Richter, A., Zhou, Y., and Brunner, D. (2011). “An Improved Tropospheric NO₂ Column Retrieval Algorithm for the Ozone Monitoring Instrument”. In: *Atmos. Meas. Tech.* 4(9), 1905–1928. DOI: 10.5194/amt-4-1905-2011 (cit. on pp. 208, 209).
- Bogumil, K., Orphal, J., Homann, T., Voigt, S., Spietz, P., Fleischmann, O. C., Vogel, A., Hartmann, M., Kromminga, H., Bovensmann, H., Frerick, J., and Burrows, J. P. (2003). “Measurements of Molecular Absorption Spectra with the SCIAMACHY Pre-Flight Model: Instrument Characterization and Reference Data for Atmospheric Remote-Sensing in the 230-2380 Nm Region”. In: *J. Photochem. Photobiol. A: Chem.* 157(2-3), 167–184. DOI: 10.1016/S1010-6030(03)00062-5 (cit. on pp. 85, 175).
- Bollmann, M., Bosch, T., Colijn, F., Ebinghaus, R., Körtzinger, A., Latif, M., Matthiessen, B., Melzner, F., Oshlies, A., Petersen, S., Proelß, A., Quaas, M., Requate, T., Reusch, T., Rosenstiel, P., Schrottko, K., Sichelschmidt, H., Siebert, U., Soltwedel, R., Sommer, U., Stattegger, K., Sterr, H., Sturm, R., Treude, T., Vafeidis, A., van Bernem, C., van Beusekom, J., Visbeck, M., Wahl, M., Wallmann, K., and Weinberger, F. (2010). *World Ocean Review: Living with the Oceans*. Hamburg: Maribus GmbH. URL: http://aquaticcommons.org/15582/1/WOR1_english.pdf (cit. on pp. 25, 26, 28, 29).
- Borrell, P., Bultjes, P., Grennfelt, P., and Hov, O. (1997). *Photo-Oxidants, Acidification and Tools: Policy Applications of EUROTRAC Results: The Report of the EUROTRAC Application Project*. Berlin: Springer (cit. on p. 22).
- Bösch, T., Rozanov, V., Richter, A., Peters, E., Rozanov, A., Wittrock, F., Merlaud, A., Lampel, J., Schmitt, S., de Haij, M., Berkhout, S., Henzing, B., Apituley, A., den Hoed, M., Vonk, J., Tiefengraber, M., Müller, M., and Burrows, J. P. (2018). “BOREAS – a New MAX-DOAS Profile Retrieval Algorithm for Aerosols and Trace Gases”. In: *Atmos. Meas. Tech.* 11(12), 6833–6859. DOI: 10.5194/amt-11-6833-2018 (cit. on p. 77).
- Böttcher, J. (2013). *Handbuch Offshore-Windenergie. Rechtliche, technische und wirtschaftliche Aspekte*. München: Oldenbourg (cit. on p. 16).
- Bouvier, A. and Wadhwa, M. (2010). “The Age of the Solar System Redefined by the Oldest Pb–Pb Age of a Meteoritic Inclusion”. In: *Nat. Geosci.* 3(9), 637–641. DOI: 10.1038/ngeo941 (cit. on p. 4).
- Bovensmann, H., Burrows, J. P., Buchwitz, M., Frerick, J., Noël, S., Rozanov, V. V., Chance, K. V., and Goede, A. P. H. (1999). “SCIAMACHY: Mission Objectives and Measurement Modes”. In: *J. Atmos. Sci.* 56, 127–150 (cit. on pp. 63, 74).
- Brasseur, G. and Solomon, S. (2005). *Aeronomy of the Middle Atmosphere. Chemistry and Physics of the Stratosphere and Mesosphere*. 3rd ed. Dordrecht: Springer (cit. on p. 14).
- Brasseur, G. P. (1999). *Atmospheric Chemistry and Global Change*. Oxford: Oxford University Press (cit. on pp. 8, 10, 12–14, 22–24).
- Brimblecombe, P. (2002). “The Great London Smog and Its Immediate Aftermath”. In: *London Smog 50th Anniversary*. Ed. by T. Williamson. Brighton: NSCA, 182–195 (cit. on p. 17).
- Brimblecombe, P. (2006). “The Clean Air Act after 50 Years”. In: *Weather* 61(11), 311–314. DOI: 10.1256/wea.127.06 (cit. on p. 17).

- Brodie, P. (2015). *Commercial Shipping Handbook*. 3rd ed. London: Informa Law from Routledge. URL: <https://doi.org/10.4324/9781315774695> (cit. on p. 34).
- Brunekreef, B. and Holgate, S. T. (2002). "Air Pollution and Health". In: *The Lancet* 360(9341), 1233–1242. DOI: 10.1016/S0140-6736(02)11274-8 (cit. on p. 17).
- Budd, G. E. and Jackson, I. S. C. (2016). "Ecological Innovations in the Cambrian and the Origins of the Crown Group Phyla". In: *Philos. Trans. R. Soc. B: Biol. Sci.* 371(1685), 20150287. DOI: 10.1098/rstb.2015.0287 (cit. on p. 6).
- Burrows, J. P., Hölzle, E., Goede, A. P. H., Visser, H., and Fricke, W. (1995). "SCIAMACHY - Scanning Imaging Absorption Spectrometer for Atmospheric Cartography". In: *Acta Astronaut.* 35, 445–451 (cit. on p. 74).
- Burrows, J. P., Weber, M., Buchwitz, M., Rozanov, V., Ladstätter-Weissenmayer, A., Richter, A., DeBeek, R., Hoogen, R., Bramstedt, K., Eichmann, K. U., and Eisinger, M. (1999). "The Global Ozone Monitoring Experiment (GOME): Mission Concept and First Scientific Results". In: *J. Atmos. Sci.* 56(2), 151–175. DOI: 10.1175/1520-0469(1999)056<0151:TGOMEG>2.0.CO;2 (cit. on pp. 63, 74).
- Burrows, J. P., Platt, U., and Borrell, P. (2011). *The Remote Sensing of Tropospheric Composition from Space*. Berlin: Springer (cit. on pp. 22, 63).
- Čampara, L., Hasanspahić, N., and Vujičić, S. (2018). "Overview of MARPOL ANNEX VI Regulations for Prevention of Air Pollution from Marine Diesel Engines". In: *SHS Web Conf.* 58, 01004. DOI: 10.1051/shsconf/20185801004 (cit. on pp. 34, 36).
- Cariou, P. (2011). "Is Slow Steaming a Sustainable Means of Reducing CO₂ Emissions from Container Shipping?" In: *Transport. Res. D-Tr. E.* 16(3), 260–264. DOI: 10.1016/j.trd.2010.12.005 (cit. on p. 189).
- Cavosie, A., Valley, J., Wilde, S., and E.I.M.F. (2005). "Magmatic $\Delta^{18}\text{O}$ in 4400–3900 Ma Detrital Zircons: A Record of the Alteration and Recycling of Crust in the Early Archean". In: *Earth Planet. Sci. Lett.* 235(3), 663–681. DOI: 10.1016/j.epsl.2005.04.028 (cit. on p. 5).
- Chappuis, J. (1880). "Sur le spectre d'absorption de l'ozone". In: *C. R. Acad. Sci. Paris* 91, 985–986 (cit. on p. 63).
- Chen, G., Huey, L. G., Trainer, M., Nicks, D., Corbett, J., Ryerson, T., Parrish, D., Neuman, J. A., Nowak, J., Tanner, D., Holloway, J., Brock, C., Crawford, J., Olson, J. R., Sullivan, A., Weber, R., Schauffler, S., Donnelly, S., Atlas, E., Roberts, J., Flocke, F., Hübler, G., and Fehsenfeld, F. (2005). "An Investigation of the Chemistry of Ship Emission Plumes during ITCT 2002". In: *J. Geophys. Res.* 110(D10), 1–15. DOI: 10.1029/2004JD005236 (cit. on p. 31).
- Cheng, Y., Wang, S., Zhu, J., Guo, Y., Zhang, R., Liu, Y., Zhang, Y., Yu, Q., Ma, W., and Zhou, B. (2019). "Surveillance of SO₂ and NO₂ from Ship Emissions by MAX-DOAS Measurements and the Implications Regarding Fuel Sulfur Content Compliance". In: *Atmos. Chem. Phys.* 19(21), 13611–13626. DOI: 10.5194/acp-19-13611-2019 (cit. on pp. 40, 109, 110).
- Chu Van, T., Ramirez, J., Rainey, T., Ristovski, Z., and Brown, R. (2019). "Global Impacts of Recent IMO Regulations on Marine Fuel Oil Refining Processes and Ship Emissions". In: *Transport. Res. D-Tr. E.* 70, 123–134. DOI: 10.1016/j.trd.2019.04.001 (cit. on p. 35).

- Clémer, K., Van Roozendaal, M., Fayt, C., Hendrick, F., Hermans, C., Pinardi, G., Spurr, R., Wang, P., and De Mazière, M. (2010). “Multiple Wavelength Retrieval of Tropospheric Aerosol Optical Properties from MAXDOAS Measurements in Beijing”. In: *Atmos. Meas. Tech.* 3(4), 863–878. DOI: 10.5194/amt-3-863-2010 (cit. on p. 77).
- Clemittshaw, K. C. (2015). “Tropospheric Chemistry and Composition | Hydroxyl Radical”. In: *Encyclopedia of Atmospheric Sciences (Second Ed.)* Ed. by G. R. North, J. Pyle, and F. Zhang. Oxford: Academic Press, 232–238. DOI: 10.1016/B978-0-12-382225-3.00429-1 (cit. on p. 19).
- Corbett, J. J., Fischbeck, P. S., and Pandis, S. N. (1999). “Global Nitrogen and Sulfur Inventories for Ongoing Ships”. In: *J. Geophys. Res.* 104(D3), 3457–3470. DOI: 10.1029/1998JD100040 (cit. on p. 33).
- Corbett, J. J. and Koehler, H. W. (2003). “Updated Emissions from Ocean Shipping”. In: *J. Geophys. Res.* 108(D20), 4650. DOI: 10.1029/2003JD003751 (cit. on p. 30).
- Corbett, J. J., Winebrake, J. J., Green, E. H., Kasibhatla, P., Eyring, V., and Lauer, A. (2007). “Mortality from Ship Emissions: A Global Assessment”. In: *Environ. Sci. Technol.* 41(24), 8512–8518. DOI: 10.1021/es071686z (cit. on pp. 33, 34).
- Cornu, A. M. and Spottiswoode, W. (1879). “Sur la limite ultraviolette du spectre solaire”. In: *Proc. R. Soc. Lond.* 29(196-199), 47–55. DOI: 10.1098/rsp1.1879.0011 (cit. on p. 63).
- Cox, C. and Wathes, C. (1995). *Bioaerosols Handbook*. Boca Raton: CRC Press/Lewis Taylor & Francis Group (cit. on p. 14).
- Crutzen, P. J. (2006). “The “Anthropocene””. In: *Earth System Science in the Anthropocene*. Ed. by E. Ehlers and T. Krafft. Berlin: Springer, 13–18. DOI: 10.1007/3-540-26590-2_3 (cit. on p. 6).
- Dalrymple, G. B. (2001). “The Age of the Earth in the Twentieth Century: A Problem (Mostly) Solved”. In: *Geological Society London Special Publications* 190(1), 205–221. DOI: 10.1144/GSL.SP.2001.190.01.14 (cit. on p. 4).
- Demtröder, W. (2007). *Laserspektroskopie. Grundlagen und Techniken*. 5th ed. Berlin: Springer (cit. on p. 41).
- Demtröder, W. (2009). *Experimentalphysik 2. Elektrizität und Optik*. 5th ed. Berlin: Springer (cit. on p. 41).
- Demtröder, W. (2010). *Experimentalphysik 3. Atome, Moleküle und Festkörper*. 4th ed. Berlin: Springer (cit. on pp. 41, 49).
- Demtröder, W. (2013). *Molekülphysik. Theoretische Grundlagen und experimentelle Methoden*. 2nd ed. München: De Gruyter Oldenbourg (cit. on p. 41).
- Diesch, J. M., Drewnick, F., Klimach, T., and Borrmann, S. (2013). “Investigation of Gaseous and Particulate Emissions from Various Marine Vessel Types Measured on the Banks of the Elbe in Northern Germany”. In: *Atmos. Chem. Phys.* 13(7), 3603–3618. DOI: 10.5194/acp-13-3603-2013 (cit. on p. 109).
- Dincer, I. and Zamfirescu, C. (2011). *Sustainable Energy Systems and Applications*. New York: Springer (cit. on p. 7).
- DNV (2008). “Marpol 73/78 Annex VI - Regulations of Air Pollution from Ships - Technical and Operational Implications”. In: *Fuel*, 1–32 (cit. on p. 34).

- Dobson, G. M. B. and Harrison, D. N. (1926). "Measurements of the Amount of Ozone in the Earth's Atmosphere and Its Relation to Other Geophysical Conditions". In: *Proceedings of the Royal Society of London A* 110(756), 660–693. DOI: 10.1098/rspa.1926.0040 (cit. on pp. 63, 77).
- ECSP (2020). *Port of Rotterdam - Chemical Park - The Netherlands*. Chemical Parks in Europe. URL: <https://chemicalparks.eu/parks/port-of-rotterdam> (visited on 04/30/2020) (cit. on p. 213).
- Emeis, S. (2010). *Surface-Based Remote Sensing of the Atmospheric Boundary Layer*. Dordrecht: Springer (cit. on p. 16).
- Endresen, Ø., Sørgard, E., Sundet, J., Dalsøren, S., Isaksen, I., and Berglen, T. (2003). "Emission from International Sea Transportation and Environmental Impact". In: *J. Geophys. Res.* 108(D17), 1–22. DOI: 10.1029/2002JD002898 (cit. on p. 33).
- EU (2005). "Directive 2005/33/EC of the European Parliament and of the Council of 6 July 2005 Amending Directive 1999/32/EC". In: *Off. J. Eur. Union* 48 (L 191), 59–69. URL: <https://eur-lex.europa.eu/legal-content/EN/TXT/PDF/?uri=CELEX:32005L0033&from=EN> (cit. on p. 37).
- EU (2016). "Directive (EU) 2016/802 of the European Parliament and of the Council of 11 May 2016 Relating to a Reduction in the Sulphur Content of Certain Liquid Fuels". In: *Off. J. Eur. Union* 59 (L 132), 58–78. URL: <https://eur-lex.europa.eu/legal-content/EN/TXT/PDF/?uri=CELEX:32016L0802&from=en> (cit. on p. 37).
- Eyring, V., Bovensmann, H., Cionni, I., Dall'Amico, M., Franke, K., Khlystova, I., Klinger, C., Lauer, A., Paxian, A., Righi, M., and Schreier, M. (2010a). *Impact of Ship Emissions on Atmosphere and Climate, SeaKLIM Final Report*. DLR, 23. URL: http://www.pa.op.dlr.de/SeaKLIM/SeaKLIM_Nachwuchsgruppe_Schlussbericht_FINAL.pdf (cit. on pp. 31–33).
- Eyring, V., Isaksen, I. S., Berntsen, T., Collins, W. J., Corbett, J. J., Endresen, O., Grainger, R. G., Moldanova, J., Schlager, H., and Stevenson, D. S. (2010b). "Transport Impacts on Atmosphere and Climate: Shipping". In: *Atmos. Environ.* 44(37), 4735–4771. DOI: 10.1016/j.atmosenv.2009.04.059 (cit. on pp. 30, 33).
- Eyring, V., Köhler, H. W., Lauer, A., and Lemper, B. (2005a). "Emissions from International Shipping: 2. Impact of Future Technologies on Scenarios until 2050". In: *J. Geophys. Res.* 110(D17), D17306. DOI: 10.1029/2004JD005620 (cit. on p. 30).
- Eyring, V., Köhler, H. W., van Aardenne, J., and Lauer, A. (2005b). "Emissions from International Shipping: 1. The Last 50 Years". In: *J. Geophys. Res.* 110(D17), D17305. DOI: 10.1029/2004JD005619 (cit. on pp. 29, 30).
- Fegley Jr, B. and Schaefer, L. (2012). "Chemistry of the Earth's Earliest Atmosphere". In: *Chapter 13.3 in "The Treatise on Geochemistry"* (cit. on pp. 4, 5).
- Finlayson-Pitts, B. and Pitts, J. (1986). *Atmospheric Chemistry. Fundamentals and Experimental Techniques*. New York: Wiley (cit. on p. 16).
- Foken, T. and Nappo, C. (2008). *Micrometeorology*. Berlin: Springer (cit. on p. 14).
- Frieß, U., Monks, P. S., Remedios, J. J., Rozanov, A., Sinreich, R., Wagner, T., and Platt, U. (2006). "MAX-DOAS O₄ Measurements: A New Technique to Derive Information on Atmospheric Aerosols: 2. Modeling Studies". In: *J. Geophys. Res.* 111(D14), D14203. DOI: 10.1029/2005JD006618 (cit. on p. 77).

- FuelsEurope (2015). *Statistical Report 2015*. Brussels: FuelsEurope. URL: <https://www.fuelseurope.eu/wp-content/uploads/2017/05/fuelseurope-statistical-report-2015.pdf> (visited on 06/11/2020) (cit. on p. 32).
- FuelsEurope (2016). *Statistical Report 2016*. Brussels: FuelsEurope. URL: https://www.fuelseurope.eu/wp-content/uploads/2017/05/graphs_fuels_europe-_2016_v14_web-2.pdf (visited on 06/11/2020) (cit. on p. 32).
- Gaffney, J. S. and Marley, N. A. (2003). "Atmospheric Chemistry and Air Pollution". In: *The Scientific World JOURNAL* 3, 199–234. DOI: 10.1100/tsw.2003.18 (cit. on pp. 16, 17).
- Galloway, J. N., Aber, J. D., Erisman, J. W., Seitzinger, S. P., Howarth, R. W., Cowling, E. B., and Cosby, B. J. (2003). "The Nitrogen Cascade". In: *BioScience* 53(4), 341–356. DOI: 10.1641/0006-3568(2003)053[0341:TNC]2.0.CO;2 (cit. on p. 33).
- Gardiner Jr., W. (1999). *Gas-Phase Combustion Chemistry*. New York: Springer (cit. on p. 20).
- Garratt, J. (1994). *The Atmospheric Boundary Layer*. Cambridge, United Kingdom: Cambridge University Press (cit. on p. 16).
- Georgoulias, A. K., Boersma, K. F., van Vliet, J., Zhang, X., van der A, R., Zanis, P., and de Laat, J. (2020). "Detection of NO₂ Pollution Plumes from Individual Ships with the TROPOMI/S5P Satellite Sensor". In: *Environ. Res. Lett. in press*. DOI: 10.1088/1748-9326/abc445 (cit. on pp. 40, 156).
- Ghosh, N., Mukhopadhyay, P., Shah, A., and Panda, M. (2016). *Nature, Economy and Society. Understanding the Linkages*. Springer India. DOI: 10.1007/978-81-322-2404-4 (cit. on p. 28).
- Gifford, F. A. (1961). "Use of Routine Meteorological Observations for Estimating Atmospheric Dispersion". In: *Nuclear Safety* 2(4), 47–51 (cit. on p. 130).
- Goldthau, A., Keating, M., and Kuzemko, C. (2018). *Handbook of the International Political Economy of Energy and Natural Resources*. Cheltenham: Edward Elgar Publishing (cit. on p. 32).
- Gomez, L., Navarro-Comas, M., Puentedura, O., Gonzalez, Y., Cuevas, E., and Gil-Ojeda, M. (2014). "Long-Path Averaged Mixing Ratios of O₃ and NO₂ in the Free Troposphere from Mountain MAX-DOAS". In: *Atmos. Meas. Tech.* 7(10), 3373–3386. DOI: 10.5194/amt-7-3373-2014 (cit. on pp. 89, 91).
- Grainger, J. F. and Ring, J. (1962). "Anomalous Fraunhofer Line Profiles". In: *Nature* 193, 762. DOI: 10.1038/193762a0 (cit. on p. 54).
- Greenblatt, G. D., Orlando, J. J., Burkholder, J. B., and Ravishankara, A. R. (1990). "Absorption Measurements of Oxygen between 330 and 1140 Nm". In: *J. Geophys. Res.* 95(D11), 18577. DOI: 10.1029/JD095iD11p18577 (cit. on p. 89).
- Haken, H. and Wolf, H. C. (2004). *Atom- und Quantenphysik. Einführung in die experimentellen und theoretischen Grundlagen*. 8th ed. Berlin: Springer (cit. on p. 41).
- Haken, H. and Wolf, H. C. (2006). *Molekülphysik und Quantenchemie. Einführung in die experimentellen und theoretischen Grundlagen*. 5th ed. Berlin: Springer (cit. on pp. 41, 50).

- Halpern, B. S., Walbridge, S., Selkoe, K. A., Kappel, C. V., Micheli, F., D'Agrosa, C., Bruno, J. F., Casey, K. S., Ebert, C., Fox, H. E., Fujita, R., Heinemann, D., Lenihan, H. S., Madin, E. M. P., Perry, M. T., Selig, E. R., Spalding, M., Steneck, R., and Watson, R. (2008). "A Global Map of Human Impact on Marine Ecosystems". In: *Science* 319(5865), 948–952. DOI: 10.1126/science.1149345 (cit. on p. 30).
- Harndorf, H. and Reißig, M. (2017). *Emissionsstrategien für Großmotoren in der Schifffahrt - Herausforderung und Lösungsansätze*. Frankfurt: Schiffsbetriebstechnische Gesellschaft Flensburg (STGF) (cit. on p. 36).
- Hartley, W. N. (1880). "On the Probable Absorption of Solar Radiation by Atmospheric Ozone". In: *Chem News* 42, 268 (cit. on p. 63).
- Hartley, W. N. (1881). "On the Absorption Spectrum of Ozone". In: *J Chem Soc Trans* 39, 57–60. DOI: 10.1039/CT8813900057 (cit. on p. 63).
- Hartmann, D. L. (2016). "Atmospheric Radiative Transfer and Climate". In: *Global Physical Climatology (Second Ed.)* Amsterdam: Elsevier, 49–94. DOI: 10.1016/B978-0-12-328531-7.00003-7 (cit. on p. 49).
- Havenbedrijf Rotterdam N.V. (2016). *Facts & Figures on the Rotterdam Energy Port and Petrochemical Cluster*. Rotterdam: Port of Rotterdam Authority, Department of Industry and Bulk Cargo. URL: <https://www.portofrotterdam.com/sites/default/files/facts-figures-energy-port-and-petrochemical-cluster.pdf?token=vHfZySB6> (visited on 04/30/2020) (cit. on p. 213).
- Hecht, E. (2005). *Optik*. 4th ed. München: De Gruyter Oldenbourg (cit. on p. 41).
- Hewitt, C. and Jackson, A. (2009). *Atmospheric Science for Environmental Scientists*. Oxford: Wiley (cit. on p. 22).
- Holton, J. R. (2004). *An Introduction to Dynamic Meteorology*. 4th ed. Amsterdam: Academic Press (cit. on p. 14).
- Hönninger, G. and Platt, U. (2002). "Observations of BrO and Its Vertical Distribution during Surface Ozone Depletion at Alert". In: *Atmos. Environ.* 36(15-16), 2481–2489 (cit. on p. 202).
- Hönninger, G., von Friedeburg, C., and Platt, U. (2004). "Multi Axis Differential Optical Absorption Spectroscopy (MAX-DOAS)". In: *Atmos. Chem. Phys.* 4(1), 231–254. DOI: 10.5194/acp-4-231-2004 (cit. on p. 74).
- Ialongo, I., Herman, J., Krotkov, N., Lamsal, L., Boersma, K. F., Hovila, J., and Tamminen, J. (2016). "Comparison of OMI NO₂ Observations and Their Seasonal and Weekly Cycles with Ground-Based Measurements in Helsinki". In: *Atmos. Meas. Tech.* 9(10), 5203–5212. DOI: 10.5194/amt-9-5203-2016 (cit. on p. 101).
- Ialongo, I., Hakkarainen, J., Hyttinen, N., Jalkanen, J. P., Johansson, L., Boersma, K. F., Krotkov, N., and Tamminen, J. (2014). "Characterization of OMI Tropospheric NO₂ over the Baltic Sea Region". In: *Atmos. Chem. Phys.* 14(15), 7795–7805. DOI: 10.5194/acp-14-7795-2014 (cit. on p. 40).
- IEA (2009). *Transport, Energy and CO₂. Moving towards Sustainability*. Paris: OECD Publishing. URL: <https://doi.org/10.1787/9789264073173-en> (cit. on pp. 28, 29).

- IMO (2003). *Safety of Navigation Circular 227 - Guidelines for the Installation of a Shipborne Automatic Identification System (AIS)*. SN / Circ . 227. London: International Maritime Organization (IMO) (cit. on p. 86).
- IMO (2004). *Automatic Identification Systems*. London: International Maritime Organization (IMO) (cit. on p. 86).
- IMO (2008a). *Resolution MEPC.176(58) - Amendments to the Annex of the Protocol of 1997 to Amend the International Convention for the Prevention of Pollution from Ships, 1973, As Modified By the Protocol of 1978 Relating Thereto (Revised MARPOL Annex VI)*. London: International Maritime Organization (IMO) (cit. on pp. 34, 36).
- IMO (2008b). *Resolution MEPC.177(58) - Amendments to the Technical Code on Control of Emission of Nitrogen Oxides from Marine Diesel Engines (NOx Technical Code 2008)*. London: International Maritime Organization (IMO) (cit. on p. 36).
- IMO (2009). *Revised MARPOL Annex VI. Regulations for the Prevention of Air Pollution from Ships and NOx Technical Code 2008*. 2nd ed. London: International Maritime Organization (IMO) (cit. on p. 34).
- IMO (2013). *MARPOL: Annex VI and NTC 2008 with Guidelines for Implementation*. London: International Maritime Organization (IMO) (cit. on pp. 34, 36).
- IMO (2015). *Resolution A.1106(29) - Revised Guidelines for the Onboard Operational Use of Shipborne Automatic Identification Systems (AIS)*. SN / Circ . 227. London: International Maritime Organization (IMO), 19 (cit. on p. 86).
- IMO (2017). *Resolution MEPC.286(71) - Amendments to MARPOL Annex VI (Designation of the Baltic Sea and the North Sea Emission Control Areas for NOx Tier III Control) (Information to Be Included in the Bunker Delivery Note)*. London: International Maritime Organisation (IMO) (cit. on p. 34).
- IMO (2018). *Resolution MEPC.305(73) - Amendments to MARPOL Annex VI (Prohibition on the Carriage of Non-Compliant Fuel Oil for Combustion Purposes for Propulsion or Operation on Board a Ship)*. London: International Maritime Organization (IMO) (cit. on p. 34).
- IMO (2020). *Emission Control Areas (ECAs) Designated under MARPOL Annex VI*. Emission Control Areas (ECAs) designated under MARPOL Annex VI. URL: [http://www.imo.org/en/OurWork/Environment/PollutionPrevention/AirPollution/Pages/Emission-Control-Areas-\(ECAs\)-designated-under-regulation-13-of-MARPOL-Annex-VI-\(NOx-emission-control\).aspx](http://www.imo.org/en/OurWork/Environment/PollutionPrevention/AirPollution/Pages/Emission-Control-Areas-(ECAs)-designated-under-regulation-13-of-MARPOL-Annex-VI-(NOx-emission-control).aspx) (visited on 06/09/2020) (cit. on p. 38).
- International Air Transport Association (IATA) (2015). "IATA Annual Review 2015". In: URL: <http://www.iata.org/about/Documents/iata-annual-review-2015.pdf> (cit. on p. 29).
- IPCC (2013). *Climate Change 2013: The Physical Science Basis. Contribution of Working Group I to the Fifth Assessment Report of the Intergovernmental Panel on Climate Change*. Cambridge, United Kingdom: Cambridge University Press, 1535. DOI: 10.1017/CB09781107415324 (cit. on p. 8).
- Jacob, D. (1999). *Introduction to Atmospheric Chemistry*. Princeton, NJ: Princeton University Press (cit. on pp. 18–22).
- Jacobson, M. (2012). *Air Pollution and Global Warming. History, Science, and Solutions*. Cambridge, United Kingdom: Cambridge University Press (cit. on p. 15).

- Jakosky, B. M. and Haberle, R. M. (1992). “The Seasonal Behavior of Water on Mars”. In: *Mars*. Ed. by H. H. Kieffer. Tucson, AZ: University of Arizona Press, 969–1016. DOI: 10.2307/j.ctt207g59v.32 (cit. on p. 5).
- Johansson, L., Jalkanen, J.-P., and Kukkonen, J. (2017). “Global Assessment of Shipping Emissions in 2015 on a High Spatial and Temporal Resolution”. In: *Atmos. Environ.* 167, 403–415. DOI: 10.1016/j.atmosenv.2017.08.042 (cit. on p. 32).
- Jonson, J. E., Tarrason, L., and Bartnicki, J. (2000). *Effects of International Shipping on European Pollution Levels*. Oslo, Norway: The Norwegian Meteorological Institute (cit. on p. 33).
- Jorgensen, S. (2012). *Encyclopedia of Environmental Management, Four Volume Set*. Boca Raton: CRC Press (cit. on p. 16).
- Kabashkin, I., Yatskiv, I., and Prentkovskis, O. (2018). *Reliability and Statistics in Transportation and Communication. Selected Papers from the 17th International Conference on Reliability and Statistics in Transportation and Communication, RelStat'17, 18-21 October, 2017, Riga, Latvia*. Cham, Switzerland: Springer International Publishing (cit. on pp. 35, 36).
- Kakkar, R. (2015). *Atomic and Molecular Spectroscopy. Basic Concepts and Applications*. New Delhi: Cambridge University Press (cit. on p. 50).
- Kampa, M. and Castanas, E. (2008). “Human Health Effects of Air Pollution”. In: *Environ. Pollut.* 151(2), 362–367. DOI: 10.1016/j.envpol.2007.06.012 (cit. on p. 18).
- Kasting, J. F. (1993). “Earth’s Early Atmosphere”. In: *Science* 259(5097), 920–926. DOI: 10.1126/science.11536547 (cit. on pp. 5, 6).
- Kasting, J. F. (2002). “Life and the Evolution of Earth’s Atmosphere”. In: *Science* 296(5570), 1066–1068. DOI: 10.1126/science.1071184 (cit. on p. 5).
- Kasting, J. F. (2013). “What Caused the Rise of Atmospheric O₂?” In: *Chem. Geol.* 362, 13–25. DOI: 10.1016/j.chemgeo.2013.05.039 (cit. on p. 5).
- Kattner, L. (2019). “Measurements of Shipping Emissions with In-Situ Instruments”. PhD Thesis. Bremen: University of Bremen. URL: <https://nbn-resolving.org/urn:nbn:de:gbv:46-00108613-19> (cit. on pp. 85, 185, 223).
- Kattner, L., Mathieu-Üffing, B., Burrows, J. P., Richter, A., Schmolke, S., Seyler, A., and Wittrock, F. (2015). “Monitoring Compliance with Sulfur Content Regulations of Shipping Fuel by In Situ Measurements of Ship Emissions”. In: *Atmos. Chem. Phys.* 15(17), 10087–10092. DOI: 10.5194/acp-15-10087-2015 (cit. on pp. 39, 109, 110, 117).
- Kaynak, B., Hu, Y., Martin, R. V., Sioris, C. E., and Russell, a. G. (2009). “Comparison of Weekly Cycle of NO₂ Satellite Retrievals and NO_x Emission Inventories for the Continental United States”. In: *J. Geophys. Res.* 114(D5), 1–10. DOI: 10.1029/2008JD010714 (cit. on p. 101).
- Kim, Y., Platt, U., Gu, M., and Iwahashi, H. (2009). *Atmospheric and Biological Environmental Monitoring*. Dordrecht: Springer (cit. on p. 17).
- Kongsberg Maritime (2020). *Seapath 330+ Datasheet*. Specification sheet. Kongsberg, Norway: Kongsberg Gruppen ASA, 2. URL: <http://www.shipserv.com/ShipServ/pages/attachments/54162/Seapath%20330+%20Datasheet.pdf> (visited on 07/06/2020) (cit. on p. 178).

- Kurucz, R. L. (1984). "Solar Flux Atlas from 296 to 1300 Nm". In: *National Solar Observatory Atlas*. Sunspot, New Mexico: Harvard University (cit. on p. 73).
- Lack, D. A., Cappa, C. D., Langridge, J., Bahreini, R., Buffaloe, G., Brock, C., Cerully, K., Coffman, D., Hayden, K., Holloway, J., Lerner, B., Massoli, P., Li, S. M., McLaren, R., Middlebrook, A. M., Moore, R., Nenes, A., Nuaaman, I., Onasch, T. B., Peischl, J., Perring, A., Quinn, P. K., Ryerson, T., Schwartz, J. P., Spackman, R., Wofsy, S. C., Worsnop, D., Xiang, B., and Williams, E. (2011). "Impact of Fuel Quality Regulation and Speed Reductions on Shipping Emissions: Implications for Climate and Air Quality". In: *Environ. Sci. Technol.* 45(20), 9052–9060. DOI: 10.1021/es2013424 (cit. on p. 39).
- Lampel, J., Pöhler, D., Tschritter, J., Frieß, U., and Platt, U. (2015). "On the Relative Absorption Strengths of Water Vapour in the Blue Wavelength Range". In: *Atmos. Meas. Tech.* 8(10), 4329–4346. DOI: 10.5194/amt-8-4329-2015 (cit. on pp. 68, 85).
- Lange, B., Markus, T., and Helfst, L. P. (2014). *Auswirkungen von Abgasnachbehandlungsanlagen (Scrubbern) auf die Umweltsituation in Häfen und Küstengewässern*. 83/2014. Dessau-Roßlau: Umweltbundesamt (UBA) (cit. on p. 36).
- Lauer, A., Eyring, V., Hendricks, J., Jöckel, P., and Lohmann, U. (2007). "Global Model Simulations of the Impact of Ocean-Going Ships on Aerosols, Clouds, and the Radiation Budget". In: *Atmos. Chem. Phys.* 7(19), 5061–5079. DOI: 10.5194/acp-7-5061-2007 (cit. on p. 33).
- Lawrence, M. G. and Crutzen, P. J. (1999). "Influence of NO_x Emissions from Ships on Tropospheric Photochemistry and Climate". In: *Nature* 402(6758), 167–170. DOI: 10.1038/46013 (cit. on p. 33).
- Leighton, P. A. (1961). *Photochemistry of Air Pollution*. New York: Academic Press (cit. on pp. 17, 21).
- Lelieveld, J., Evans, J. S., Fnais, M., Giannadaki, D., and Pozzer, A. (2015). "The Contribution of Outdoor Air Pollution Sources to Premature Mortality on a Global Scale". In: *Nature* 525(7569), 367–371. DOI: 10.1038/nature15371 (cit. on p. 9).
- Lelieveld, J., Peters, W., Dentener, F. J., and Krol, M. C. (2002). "Stability of Tropospheric Hydroxyl Chemistry". In: *J. Geophys. Res.* 107(D23), ACH 17-1-ACH 17–11. DOI: 10.1029/2002JD002272 (cit. on p. 18).
- Levine, J. S. (2003). "Biomass Burning: The Cycling of Gases and Particulates from the Biosphere to the Atmosphere". In: *Treatise on Geochemistry*. Ed. by H. D. Holland and K. K. Turekian. Amsterdam: Elsevier Science, 143–158. DOI: 10.1016/B0-08-043751-6/04143-8 (cit. on p. 19).
- Liu, F., Beirle, S., Zhang, Q., Dörner, S., He, K., and Wagner, T. (2016). "NO_x Lifetimes and Emissions of Cities and Power Plants in Polluted Background Estimated by Satellite Observations". In: *Atmos. Chem. Phys.* 16(8), 5283–5298. DOI: 10.5194/acp-16-5283-2016 (cit. on p. 222).
- Maloni, M., Paul, J. A., and Gligor, D. M. (2013). "Slow Steaming Impacts on Ocean Carriers and Shippers". In: *Maritime Economics & Logistics* 15(2), 151–171. DOI: 10.1057/me1.2013.2 (cit. on p. 189).
- Maloof, A. C., Porter, S. M., Moore, J. L., Dudás, F. Ö., Bowring, S. A., Higgins, J. A., Fike, D. A., and Eddy, M. P. (2010). "The Earliest Cambrian Record of Animals and Ocean Geochemical Change". In: *GSA Bulletin* 122(11-12), 1731–1774. DOI: 10.1130/B30346.1 (cit. on p. 6).

- Marine Institute (2015). *National Research Vessel Celtic Explorer – Technical Specifications*. Rinnville, Oranmore, Co. Galway: Marine institute, 2. URL: <https://www.marine.ie/Home/sites/default/files/MIFiles/Docs/ResearchVessels/MI-210sq-Tech%20Spec%20CE-Update%202015%20FINAL.pdf> (visited on 02/21/2020) (cit. on p. 170).
- Marinò, A. and Bucci, V. (2018). *Technology and Science for the Ships of the Future: Proceedings of NAV 2018: 19th International Conference on Ship & Maritime Research*. Amsterdam: IOS Press (cit. on p. 35).
- Martin, D. O. (1976). “Comment On”The Change of Concentration Standard Deviations with Distance”. In: *Journal of the Air Pollution Control Association* 26(2), 145–147. DOI: 10.1080/00022470.1976.10470238 (cit. on pp. 131, 132, 138).
- Masieri, S., Premuda, M., Bortoli, D., Kostadinov, I., Petritoli, A., Ravegnani, F., and Giovanelli, G. (2009). “Cruise Ships Flow Rate Emission Evaluated by Means of a Passive DOAS Instrument”. In: *Proc. SPIE. Remote Sensing for Environmental Monitoring, GIS Applications, and Geology IX* 7478, 471–480. DOI: 10.1117/12.830309 (cit. on p. 39).
- Mason, J., Burt, J. E., Muller, P. O., and Blij, H. de (2016). *Physical Geography. The Global Environment*. 5th ed. New York: Oxford University Press (cit. on p. 15).
- Mathur, K. (2018). *Fundamentals of Fiber Optics Communications*. Gurgaon, India: ZORBA Books (cit. on p. 58).
- Matthias, V., Aulinger, A., Backes, A., Bieser, J., Geyer, B., Quante, M., and Zeretzke, M. (2016). “The Impact of Shipping Emissions on Air Pollution in the Greater North Sea Region-Part 2: Scenarios for 2030”. In: *Atmos. Chem. Phys.* 16(2), 759–776. DOI: 10.5194/acp-16-759-2016 (cit. on pp. 33, 37, 79).
- McCormac, B. (2012). *Introduction to the Scientific Study of Atmospheric Pollution*. Dordrecht: Springer (cit. on p. 15).
- McLaren, R., Wojtal, P., Halla, J. D., Mihele, C., and Brook, J. R. (2012). “A Survey of NO₂:SO₂ Emission Ratios Measured in Marine Vessel Plumes in the Strait of Georgia”. In: *Atmos. Environ.* 46(2), 655–658. DOI: 10.1016/j.atmosenv.2011.10.044 (cit. on pp. 39, 109).
- McLauchlan, K. (2004). *Molecular Physical Chemistry. A Concise Introduction*. In collab. with Royal Society of Chemistry (Great Britain). London: Royal Society of Chemistry (cit. on p. 50).
- Meier, A. C. (2018). “Measurements of Horizontal Trace Gas Distributions Using Airborne Imaging Differential Optical Absorption Spectroscopy”. PhD Thesis. Bremen: University of Bremen (cit. on pp. 40, 138, 140, 156, 157).
- Meier, A. C., Schönhardt, A., Bösch, T., Richter, A., Seyler, A., Ruhtz, T., Constantin, D. E., Shaiganfar, R., Wagner, T., Merlaud, A., Van Roozendaal, M., Belegante, L., Nicolae, D., Georgescu, L., and Burrows, J. P. (2017). “High-Resolution Airborne Imaging DOAS Measurements of NO₂ above Bucharest during AROMAT”. In: *Atmos. Meas. Tech.* 10(5), 1831–1857. DOI: 10.5194/amt-10-1831-2017 (cit. on pp. 63, 74, 156, 157, 163).
- Meller, R. and Moortgat, G. K. (2000). “Temperature Dependence of the Absorption Cross Sections of Formaldehyde between 223 and 323 K in the Wavelength Range 225-375 Nm”. In: *J. Geophys. Res.* 105(D6), 7089–7101. DOI: 10.1029/1999JD901074 (cit. on pp. 85, 174).
- Miller, S. L. and Urey, H. C. (1959). “Organic Compound Synthesis on the Primitive Earth”. In: *Science* 130(3370), 245–251. DOI: 10.1126/science.130.3370.245 (cit. on p. 4).

- Mohanakumar, K. (2008). *Stratosphere Troposphere Interactions. An Introduction*. Dordrecht: Springer (cit. on p. 44).
- Mojzsis, S. J., Harrison, T. M., and Pidgeon, R. T. (2001). “Oxygen-Isotope Evidence from Ancient Zircons for Liquid Water at the Earth’s Surface 4,300 Myr Ago”. In: *Nature* 409(6817), 178–181. DOI: 10.1038/35051557 (cit. on p. 5).
- Moldanova, J., Fridell, E., Popovicheva, O., Demirdjian, B., Tishkova, V., Faccinnetto, A., and Focsa, C. (2009). “Characterisation of Particulate Matter and Gaseous Emissions from a Large Ship Diesel Engine”. In: *Atmos. Environ.* 43, 2632–2641. DOI: 10.1016/j.atmosenv.2009.02.008 (cit. on p. 32).
- Narula, K. (2018). *The Maritime Dimension of Sustainable Energy Security*. Lecture Notes in Energy. Singapore: Springer (cit. on pp. 31, 35).
- NASA (2017). *Layers of the Sun*. Ed. by H. Zell. URL: http://www.nasa.gov/mission_pages/iris/multimedia/layerzoo.html (visited on 06/20/2020) (cit. on p. 47).
- National Research Council (1997). *Boundary Layer Dynamics*. In collab. with Commission on Physical Sciences, Mathematics, and Applications, Naval Studies Board, and Panel on Boundary Layer Dynamics. Compass Series. Washington, DC: The National Academies Press. URL: <https://doi.org/10.17226/5710> (cit. on p. 15).
- North P&I (2019). *LNG as a Marine Fuel*. Newcastle upon Tyne: North of England P&I Association. URL: <https://www.nepia.com/publications/lng-as-a-marine-fuel/> (cit. on p. 35).
- Noxon, J. F. (1975). “Nitrogen-Dioxide in Stratosphere and Troposphere Measured by Ground-Based Absorption Spectroscopy”. In: *Science* 189(4202), 547–549 (cit. on pp. 63, 74).
- Ortega, I., Koenig, T., Sinreich, R., Thomson, D., and Volkamer, R. (2015). “The CU 2-D-MAX-DOAS Instrument – Part 1: Retrieval of 3-D Distributions of NO₂ and Azimuth-Dependent OVOC Ratios”. In: *Atmos. Meas. Tech.* 8(6), 2371–2395. DOI: 10.5194/amt-8-2371-2015 (cit. on pp. 124, 125).
- OSPAR Commission (2010). *Quality Status Report 2010*. London: OSPAR Commission (cit. on p. 29).
- Palmer, P. I. (2017). *The Atmosphere. A Very Short Introduction*. Oxford: Oxford University Press (cit. on p. 7).
- Pandya, R. J., Solomon, G., Kinner, A., and Balmes, J. R. (2002). “Diesel Exhaust and Asthma: Hypotheses and Molecular Mechanisms of Action”. In: *Environ. Health Perspect.* 110 (SUPPL. 1), 103–112. DOI: 10.1289/ehp.02110s1103 (cit. on p. 34).
- Pasquill, F. (1961). “The Estimation of the Dispersion of Windborne Material.” In: *Meteorol. Mag.* 90, 33–49 (cit. on pp. 130–132).
- Perner, D., Ehhalt, D. H., Pätz, H. W., Platt, U., Röth, E. P., and Volz, A. (1976). “OH - Radicals in the Lower Troposphere”. In: *Geophys. Res. Lett.* 3(8), 466–468. DOI: 10.1029/GL003i008p00466 (cit. on pp. 63, 74).
- Peters, E. (2013). “Improved MAX-DOAS Measurements and Retrievals Focused on the Marine Boundary Layer”. Ph.D. thesis. Bremen: University of Bremen (cit. on pp. 63, 67, 183).

- Peters, E., Wittrock, F., Großmann, K., Frieß, U., Richter, A., and Burrows, J. P. (2012). “Formaldehyde and Nitrogen Dioxide over the Remote Western Pacific Ocean: SCIAMACHY and GOME-2 Validation Using Ship-Based MAX-DOAS Observations”. In: *Atmos. Chem. Phys.* 12(22), 11179–11197. DOI: 10.5194/acp-12-11179-2012 (cit. on p. 185).
- Planck, M. (1949). *Scientific Autobiography, and Other Papers*. Trans. by F. Gaynor. New York: Philosophical Library (cit. on p. 41).
- Planck, M. and Masius, M. (1914). *The theory of heat radiation*. Philadelphia: P. Blakiston’s Son & Co. (cit. on p. 45).
- Platt, U. and Perner, D. (1980). “Direct Measurements of Atmospheric CH₂O, HNO₂, O₃, NO₂, and SO₂ by Differential Optical Absorption in the near UV”. In: *J. Geophys. Res.* 85(C12), 7453–7458. DOI: 10.1029/JC085iC12p07453 (cit. on pp. 63, 66).
- Platt, U. and Stutz, J. (2008). *Differential Optical Absorption Spectroscopy*. Berlin: Springer (cit. on pp. 63, 66).
- Prata, A. J. (2014). “Measuring SO₂ Ship Emissions with an Ultraviolet Imaging Camera”. In: *Atmos. Meas. Tech.* 7(5), 1213–1229. DOI: 10.5194/amt-7-1213-2014 (cit. on p. 39).
- Premuda, M., Masieri, S., Bortoli, D., Kostadinov, I., Petritoli, A., and Giovanelli, G. (2011). “Evaluation of Vessel Emissions in a Lagoon Area with Ground Based Multi Axis DOAS Measurements”. In: *Atmos. Environ.* 45(29), 5212–5219. DOI: 10.1016/j.atmosenv.2011.05.067 (cit. on p. 39).
- Richter, A. (1997). “Absorptionsspektroskopische Messungen stratosphärischer Spurengase über Bremen, 53° N”. PhD Thesis. Bremen: University of Bremen (cit. on pp. 63, 67, 73).
- Richter, A., Begoin, M., Hilboll, A., and Burrows, J. P. (2011). “An Improved NO₂ Retrieval for the GOME-2 Satellite Instrument”. In: *Atmos. Meas. Tech.* 4(6), 1147–1159. DOI: 10.5194/amt-4-1147-2011 (cit. on p. 40).
- Richter, A., Eyring, V., Burrows, J. P., Bovensmann, H., Lauer, A., Sierk, B., and Crutzen, P. J. (2004). “Satellite Measurements of NO₂ from International Shipping Emissions”. In: *Geophys. Res. Lett.* 31, L23110. DOI: 10.1029/2004GL020822 (cit. on p. 40).
- Ritz, D., Hausmann, M., and Platt, U. (1992). “An Improved Open Path Multi-Reflection Cell for the Measurement of NO₂ and NO₃”. In: *Proc. SPIE* 1715, 200–211. DOI: 10.1117/12.140211 (cit. on p. 74).
- Roedel, W. and Wagner, T. (2011). *Physik unserer Umwelt. Die Atmosphäre*. 4th ed. Berlin: Springer (cit. on pp. 11, 12, 14).
- Rozanov, V. V., Rozanov, A. V., Kokhanovsky, A. A., and Burrows, J. P. (2014). “Radiative Transfer through Terrestrial Atmosphere and Ocean: Software Package SCIATRAN”. In: *J. Quant. Spectrosc. Radiat. Transf.* 133, 13–71. DOI: 10.1016/j.jqsrt.2013.07.004 (cit. on pp. 85, 174, 175).
- Sabljić, A. (2009). *Environmental and Ecological Chemistry - Volume 1*. Oxford: EOLSS Publishers Company Limited (cit. on p. 17).
- Schaefer, L. and Fegley, B. (2010). “Chemistry of Atmospheres Formed during Accretion of the Earth and Other Terrestrial Planets”. In: *Icarus* 208(1), 438–448. DOI: 10.1016/j.icarus.2010.01.026 (cit. on pp. 4, 5).

- Schmidt, G. A., Ruedy, R. A., Miller, R. L., and Lacis, A. A. (2010). "Attribution of the Present-Day Total Greenhouse Effect". In: *J. Geophys. Res.* 115(D20), D20106. DOI: 10.1029/2010JD014287 (cit. on p. 8).
- Schönhardt, A., Altube, P., Gerilowski, K., Krautwurst, S., Hartmann, J., Meier, A. C., Richter, A., and Burrows, J. P. (2015). "A Wide Field-of-View Imaging DOAS Instrument for Two-Dimensional Trace Gas Mapping from Aircraft". In: *Atmos. Meas. Tech.* 8(12), 5113–5131. DOI: 10.5194/amt-8-5113-2015 (cit. on pp. 63, 74, 156).
- Schönhardt, A., Richter, A., Wittrock, F., Kirk, H., Oetjen, H., Roscoe, H. K., and Burrows, J. P. (2008). "Observations of Iodine Monoxide Columns from Satellite". In: *Atmos. Chem. Phys.* 8(3), 637–653. DOI: 10.5194/acp-8-637-2008 (cit. on p. 74).
- Schreier, S. F., Peters, E., Richter, A., Lampel, J., Wittrock, F., and Burrows, J. P. (2015). "Ship-Based MAX-DOAS Measurements of Tropospheric NO₂ and SO₂ in the South China and Sulu Sea". In: *Atmos. Environ.* 102, 331–343. DOI: 10.1016/j.atmosenv.2014.12.015 (cit. on p. 185).
- Schreier, S. F., Richter, A., Wittrock, F., and Burrows, J. P. (2016). "Estimates of Free-Tropospheric NO₂ and HCHO Mixing Ratios Derived from High-Altitude Mountain MAX-DOAS Observations in the Mid-Latitudes and Tropics". In: *Atmos. Chem. Phys.* 16(5), 2803–2817. DOI: 10.5194/acp-16-2803-2016 (cit. on pp. 89, 91).
- Scottish and Southern Energy (SSE) (2020). *Peterhead*. Peterhead. URL: <https://sse.com/whatwedo/ourprojectsandassets/thermal/Peterhead/> (visited on 05/01/2020) (cit. on p. 220).
- Seinfeld, J. H. and Pandis, S. N. (2006). *Atmospheric Chemistry and Physics. From Air Pollution to Climate Change*. 2nd ed. Hoboken, NJ: Wiley (cit. on pp. 6–9, 11, 12, 14, 15, 17, 19, 21–24).
- Serdychenko, A., Gorshelev, V., Weber, M., Chehade, W., and Burrows, J. P. (2014). "High Spectral Resolution Ozone Absorption Cross-Sections – Part 2: Temperature Dependence". In: *Atmos. Meas. Tech.* 7(2), 625–636. DOI: 10.5194/amt-7-625-2014 (cit. on pp. 85, 174, 175).
- Seyler, A. (2011). "Implementierung und Charakterisierung eines Inklinometers in einem MAX-DOAS". Bachelor Thesis. Bremen: University of Bremen (cit. on p. 183).
- Seyler, A. (2014). "Retrieval of Shipping Emissions from MAX-DOAS Measurements – Ableitung von Schiffsemissionen aus MAX-DOAS-Messungen". Master Thesis. Bremen: University of Bremen (cit. on pp. 81, 82).
- Seyler, A., Meier, A. C., Wittrock, F., Kattner, L., Mathieu-Üffing, B., Peters, E., Richter, A., Ruhtz, T., Schönhardt, A., Schmolke, S., and Burrows, J. P. (2019). "Studies of the Horizontal Inhomogeneities in NO₂ Concentrations above a Shipping Lane Using Ground-Based Multi-Axis Differential Optical Absorption Spectroscopy (MAX-DOAS) Measurements and Validation with Airborne Imaging DOAS Measurements". In: *Atmos. Meas. Tech.* 12(11), 5959–5977. DOI: 10.5194/amt-12-5959-2019 (cit. on pp. 123, 125, 126, 128, 145, 147, 149, 151, 155, 159–161, 164).
- Seyler, A., Wittrock, F., Kattner, L., Mathieu-Üffing, B., Peters, E., Richter, A., Schmolke, S., and Burrows, J. P. (2017). "Monitoring Shipping Emissions in the German Bight Using MAX-DOAS Measurements". In: *Atmos. Chem. Phys.* 17(18), 10997–11023. DOI: 10.5194/acp-17-10997-2017 (cit. on pp. 79, 80, 84, 87, 88, 90, 93, 101, 102, 106–108, 112, 115, 192).

- Sherwood, S. C., Dixit, V., and Salomez, C. (2018). “The Global Warming Potential of Near-Surface Emitted Water Vapour”. In: *Environ. Res. Lett.* 13(10), 104006. DOI: 10.1088/1748-9326/aae018 (cit. on p. 8).
- Singh, H. B. (1987). “Reactive Nitrogen in the Troposphere”. In: *Environ. Sci. Technol.* 21(4), 320–327. DOI: 10.1021/es00158a001 (cit. on p. 21).
- Sinreich, R., Merten, A., Molina, L., and Volkamer, R. (2013). “Parameterizing Radiative Transfer to Convert MAX-DOAS dSCDs into near-Surface Box-Averaged Mixing Ratios”. In: *Atmos. Meas. Tech.* 6(6), 1521–1532. DOI: 10.5194/amt-6-1521-2013 (cit. on pp. 89–91).
- Sleep, N. H., Bird, D. K., and Pope, E. (2012). “Paleontology of Earth’s Mantle”. In: *Annu. Rev. Earth Planet. Sci.* 40(1), 277–300. DOI: 10.1146/annurev-earth-092611-090602 (cit. on p. 5).
- Smith, T. W. P., Jalkanen, J. P., Anderson, B. A., Corbett, J. J., Faber, J., Hanayama, S., O’Keeffe, E., Parker, S., Johansson, L., Aldous, L., Raucci, C., Traut, M., Ettinger, S., Nelissen, D., Lee, D. S., Ng, S., Agrawal, A., Winebrake, J. J., Hoen, M., Chesworth, S., and Pandey, A. (2015). *Third IMO Greenhouse Gas Study 2014. Executive Summary and Final Report*. London: International Maritime Organization (IMO) (cit. on p. 32).
- Sokhi, R. S. (2008). *World Atlas of Atmospheric Pollution*. London: Anthem Press (cit. on pp. 17, 18).
- Solomon, S., Sanders, R. W., Schmeltekopf, A. L., and Sanders, R. W. (1987). “On the Interpretation of Zenith Sky Absorption Measurements”. In: *J. Geophys. Res.* 92(D7), 8311–8319. DOI: 10.1029/JD092iD07p08311 (cit. on pp. 54, 63, 65, 74, 78).
- Sommer, S. G., Christensen, M. L., Schmidt, T., and Jensen, L. S. (2013). *Animal Manure Recycling. Treatment and Management*. Chichester, West Sussex, UK: Wiley (cit. on p. 7).
- Sperling, E. A., Frieder, C. A., Raman, A. V., Girguis, P. R., Levin, L. A., and Knoll, A. H. (2013). “Oxygen, Ecology, and the Cambrian Radiation of Animals”. In: *Proc. Natl. Acad. Sci. U.S.A.* 110(33), 13446–13451. DOI: 10.1073/pnas.1312778110 (cit. on p. 6).
- Statistische Ämter des Bundes und der Länder (Statistikamt Nord) (2019). *Anzahl der Ankünfte von Kreuzfahrtschiffen im Hamburger Hafen in den Jahren 2005 bis 2018*. URL: <https://de.statista.com/statistik/daten/studie/29729/umfrage/ankuenfte-von-kreuzfahrtschiffen-in-hamburg/> (cit. on p. 80).
- Stenersen, D. and Thonstad, O. (2017). *GHG and NOx Emissions from Gas Fuelled Engines*. OC2017 F-108. Trondheim: SINTEF Ocean AS, 52 (cit. on p. 35).
- Strahan, S. E. and Douglass, A. R. (2018). “Decline in Antarctic Ozone Depletion and Lower Stratospheric Chlorine Determined From Aura Microwave Limb Sounder Observations”. In: *Geophys. Res. Lett.* 45(1), 382–390. DOI: 10.1002/2017GL074830 (cit. on p. 9).
- Stull, R. B. (1988). *An Introduction to Boundary Layer Meteorology*. Dordrecht: Springer (cit. on p. 15).
- Stutz, J. and Platt, U. (1997a). “A New Generation of DOAS Instruments”. In: *Instrument Development for Atmospheric Research and Monitoring. Lidar Profiling, DOAS and Tunable Diode Laser Spectroscopy*. Ed. by J. Bösenberg, D. Brassington, and P. C. Simon. Springer Science & Business Media, 370–378 (cit. on p. 74).

- Stutz, J. and Platt, U. (1997b). "Improving Long-Path Differential Optical Absorption Spectroscopy with a Quartz-Fiber Mode Mixer". In: *Appl. Opt.* 36(6), 1105–1115. DOI: 10.1364/AO.36.001105 (cit. on p. 74).
- Sutton, O. G. (1932). "A Theory of Eddy Diffusion in the Atmosphere". In: *Proceedings of the Royal Society of London A* 135(826), 143–165. DOI: 10.1098/rspa.1932.0025 (cit. on p. 130).
- Sutton, O. G. (1953). *Micrometeorology. A Study of Physical Processes in the Lowest Layers of the Earth's Atmosphere*. Ney York: McGraw-Hill (cit. on pp. 130, 131).
- Takashima, H., Irie, H., Kanaya, Y., and Syamsudin, F. (2012). "NO₂ Observations over the Western Pacific and Indian Ocean by MAX-DOAS on *Kaiyo* , a Japanese Research Vessel". In: *Atmos. Meas. Tech.* 5(10), 2351–2360. DOI: 10.5194/amt-5-2351-2012 (cit. on p. 185).
- Tan, W., Liu, C., Wang, S., Xing, C., Su, W., Zhang, C., Xia, C., Liu, H., Cai, Z., and Liu, J. (2018). "Tropospheric NO₂ , SO₂ , and HCHO over the East China Sea, Using Ship-Based MAX-DOAS Observations and Comparison with OMI and OMPS Satellite Data". In: *Atmos. Chem. Phys.* 18(20), 15387–15402. DOI: 10.5194/acp-18-15387-2018 (cit. on p. 185).
- TEMIS (2020). *Tropospheric NO₂ from Satellites*. Tropospheric NO₂ from satellites. URL: <http://www.temis.nl/airpollution/no2.html> (visited on 08/03/2020) (cit. on p. 209).
- Thalman, R. and Volkamer, R. (2013). "Temperature Dependent Absorption Cross-Sections of O₂-O₂ Collision Pairs between 340 and 630 Nm and at Atmospherically Relevant Pressure." In: *Phys. Chem. Chem. Phys.* 15, 15371–81. DOI: 10.1039/c3cp50968k (cit. on pp. 85, 174).
- Turekian, K. K. and Holland, H. D. (2013). *Treatise on Geochemistry*. Amsterdam: Elsevier Science (cit. on p. 9).
- Turner, D. B. (1970). *Workbook of Atmospheric Dispersion Estimates*. Revised 1970. Cincinnati, Ohio: U.S. Dept. of Health, Education, and Welfare, Public Health Service, Environmental Health Service (cit. on p. 132).
- Umweltbundesamt (2017). *Aktuelle Luftdaten*. URL: <https://www.umweltbundesamt.de/daten/luftbelastung/aktuelle-luftdaten> (visited on 05/16/2017) (cit. on p. 113).
- UNCTAD (2012). *Review of Maritime Transport 2012*. New York: United Nations. URL: https://unctad.org/en/PublicationsLibrary/rmt2012_en.pdf (visited on 06/11/2020) (cit. on p. 80).
- UNCTAD (2013). *Review of Maritime Transport 2013*. New York: United Nations. URL: https://unctad.org/en/PublicationsLibrary/rmt2013_en.pdf (visited on 06/11/2020) (cit. on pp. 25, 26).
- UNCTAD (2014). *Review of Maritime Transport 2014*. New York: United Nations. URL: https://unctad.org/en/PublicationsLibrary/rmt2014_en.pdf (visited on 06/11/2020) (cit. on p. 25).
- UNCTAD (2015). *Review of Maritime Transport 2015*. New York: United Nations. URL: https://unctad.org/en/PublicationsLibrary/rmt2015_en.pdf (visited on 06/11/2020) (cit. on pp. 25, 29, 80).
- UNCTAD (2016). *Review of Maritime Transport 2016*. New York: United Nations. URL: https://unctad.org/en/PublicationsLibrary/rmt2016_en.pdf (visited on 06/11/2020) (cit. on p. 28).

- UNCTAD (2018a). *50 Years of Review of Maritime Transport, 1968–2018*. New York: United Nations. URL: https://unctad.org/en/PublicationsLibrary/dt12018d1_en.pdf (visited on 06/11/2020) (cit. on pp. 26, 27).
- UNCTAD (2018b). *Review of Maritime Transport 2018*. Review of Maritime Transport. New York: United Nations. URL: https://unctad.org/en/PublicationsLibrary/rmt2018_en.pdf (visited on 06/11/2020) (cit. on pp. 26–29, 80).
- UNCTAD (2019). *Review of Maritime Transport 2019*. Review of Maritime Transport. New York: United Nations. URL: https://unctad.org/en/PublicationsLibrary/rmt2019_en.pdf (visited on 06/11/2020) (cit. on pp. 26–29, 80, 213).
- Vallero, D. A. (2008). *Fundamentals of Air Pollution*. 4th ed. Amsterdam: Elsevier (cit. on pp. 17, 18).
- Van Roy, W. and Scheldeman, K. (2016). *Best Practices Airborne MARPOL Annex VI Monitoring*. Compliance monitoring pilot for MARPOL Annex VI (CompMon). URL: <https://ec.europa.eu/transparency/regexpert/index.cfm?do=groupDetail.groupDetailDoc&id=29311&no=7> (visited on 11/02/2020) (cit. on p. 104).
- Vandaele, A. C., Hermans, C., Simon, P. C., Roozendaal, M. V., Guilmot, J. M., Carleer, M., and Colin, R. (1996). “Fourier Transform Measurement of NO₂ Absorption Cross-Section in the Visible Range at Room Temperature”. In: *J. Atmos. Chem.* 25, 289–305 (cit. on pp. 68, 85, 174, 175).
- Veefkind, J. P., Aben, I., McMullan, K., Förster, H., de Vries, J., Otter, G., Claas, J., Eskes, H. J., de Haan, J. F., Kleipool, Q., van Weele, M., Hasekamp, O., Hoogeveen, R., Landgraf, J., Snel, R., Tol, P., Ingmann, P., Voors, R., Kruizinga, B., Vink, R., Visser, H., and Levelt, P. F. (2012). “TROPOMI on the ESA Sentinel-5 Precursor: A GMES Mission for Global Observations of the Atmospheric Composition for Climate, Air Quality and Ozone Layer Applications”. In: *Remote Sens. Environ.* 120, 70–83. DOI: 10.1016/j.rse.2011.09.027 (cit. on pp. 40, 156).
- Vinken, G. C. M., Boersma, K. F., van Donkelaar, A., and Zhang, L. (2014). “Constraints on Ship NO_x Emissions in Europe Using GEOS-Chem and OMI Satellite NO₂ Observations”. In: *Atmos. Chem. Phys.* 14(3), 1353–1369. DOI: 10.5194/acp-14-1353-2014 (cit. on p. 40).
- Vojnovic, B. and Volpi, D. (2012). *Notes on Optical Fibres and Fibre Bundles*. Oxford: Gray Institute, Department of Oncology, University of Oxford. URL: <http://users.ox.ac.uk/~atdgroup/referencematerial/Notes%20on%20optical%20fibres%20and%20fibre%20bundles.pdf> (visited on 06/30/2020) (cit. on p. 41).
- Wagner, T., Apituley, A., Beirle, S., Dörner, S., Friess, U., Remmers, J., and Shaiganfar, R. (2014). “Cloud Detection and Classification Based on MAX-DOAS Observations”. In: *Atmos. Meas. Tech.* 7(5), 1289–1320. DOI: 10.5194/amt-7-1289-2014 (cit. on pp. 91, 94, 129).
- Wagner, T., Dix, B., Friedeburg, C. V., Frieß, U., Sanghavi, S., Sinreich, R., and Platt, U. (2004). “MAX-DOAS O₄ Measurements: A New Technique to Derive Information on Atmospheric Aerosols - Principles and Information Content”. In: *J. Geophys. Res.* 109(D22), 1–19. DOI: 10.1029/2004JD004904 (cit. on pp. 77, 89).
- Wallace, J. M. and Hobbs, P. V. (2006). *Atmospheric Science. An Introductory Survey*. 2nd ed. Amsterdam: Academic Press (cit. on pp. 7–10, 12, 13, 19, 20, 22–24).

- Wan, Z., Zhou, X., Zhang, Q., and Chen, J. (2019). “Do Ship Emission Control Areas in China Reduce Sulfur Dioxide Concentrations in Local Air? A Study on Causal Effect Using the Difference-in-Difference Model”. In: *Marine Pollution Bulletin* 149, 110506. DOI: 10.1016/j.marpolbul.2019.110506 (cit. on p. 37).
- Wan, Z., Zhu, M., Chen, S., and Sperling, D. (2016). “Pollution: Three Steps to a Green Shipping Industry”. In: *Nature* 530, 275–277. DOI: 10.1038/530275a (cit. on pp. 31, 32).
- Wang, P., Richter, A., Bruns, M., Rozanov, V. V., and Burrows, J. P. (2005). “Measurements of Tropospheric NO₂ with an Airborne Multi-Axis DOAS Instrument”. In: *Atmos. Chem. Phys.* 5(2), 337–343. DOI: 10.5194/acp-5-337-2005 (cit. on p. 63).
- Wang, Y., Li, A., Xie, P. H., Wagner, T., Chen, H., Liu, W. Q., and Liu, J. G. (2014). “A Rapid Method to Derive Horizontal Distributions of Trace Gases and Aerosols near the Surface Using Multi-Axis Differential Optical Absorption Spectroscopy”. In: *Atmos. Meas. Tech.* 7(6), 1663–1680. DOI: 10.5194/amt-7-1663-2014 (cit. on pp. 89–91).
- Warhaft, Z. (1997). *An Introduction to Thermal-Fluid Engineering. The Engine and the Atmosphere*. Cambridge, United Kingdom: Cambridge University Press (cit. on p. 133).
- Wayne, R. P., Barnes, I., Biggs, P., Burrows, J. P., Canosa-Mas, C. E., Hjorth, J., Le Bras, G., Moortgat, G. K., Perner, D., Poulet, G., Restelli, G., and Sidebottom, H. (1991). “The Nitrate Radical: Physics, Chemistry, and the Atmosphere”. In: *Atmos. Environ.* 25A(1), 1–203. DOI: 10.1016/0960-1686(91)90192-A (cit. on p. 22).
- Wayne, R. P. (1992). “Atmospheric Chemistry: The Evolution of Our Atmosphere”. In: *J. Photochem. Photobiol. A* 62(3), 379–396. DOI: 10.1016/1010-6030(92)85066-4 (cit. on pp. 4–6).
- Wayne, R. P. (2000). *Chemistry of Atmospheres. An Introduction to the Chemistry of the Atmospheres of Earth, the Planets, and Their Satellites*. 3rd ed. Oxford: Oxford University Press (cit. on pp. 4, 5, 8, 10–12, 22, 23).
- WHO (2006). *Air Quality Guidelines. Global Update 2005. Particulate Matter, Ozone, Nitrogen Dioxide, and Sulfur Dioxide*. Copenhagen: World Health Organization (cit. on p. 34).
- WHO (2020). *Air Pollution*. Air pollution. URL: <https://www.who.int/westernpacific/health-topics/air-pollution> (visited on 07/30/2020) (cit. on p. 1).
- Winebrake, J. J., Corbett, J. J., Green, E. H., Lauer, A., and Eyring, V. (2009). “Mitigating the Health Impacts of Pollution from Oceangoing Shipping: An Assessment of Low-Sulfur Fuel Mandates”. In: *Environ. Sci. Technol.* 43(13), 4776–4782. DOI: 10.1021/es803224q (cit. on p. 34).
- Winnes, H. and Fridell, E. (2009). “Particle Emissions from Ships: Dependence on Fuel Type”. In: *J. Air Waste Manage. Assoc.* 59(12), 1391–1398. DOI: 10.3155/1047-3289.59.12.1391 (cit. on p. 32).
- Winnes, H. and Fridell, E. (2010). “Emissions of NOX and Particles from Manoeuvring Ships”. In: *Transport. Res. D-Tr. E.* 15(4), 204–211. DOI: 10.1016/j.trd.2010.02.003 (cit. on p. 32).
- Witrock, F. (2006). “The Retrieval of Oxygenated Volatile Organic Compounds by Remote Sensing Techniques”. PhD Thesis. Bremen: University of Bremen (cit. on p. 77).

- Wittrock, F., Oetjen, H., Richter, A., Fietkau, S., Medeke, T., Rozanov, A., and Burrows, J. P. (2004). “MAX-DOAS Measurements of Atmospheric Trace Gases in Ny-Ålesund - Radiative Transfer Studies and Their Application”. In: *Atmos. Chem. Phys.* 4(4), 955–966. DOI: 10.5194/acp-4-955-2004 (cit. on p. 74).
- Yang, M., Bell, T. G., Hopkins, F. E., and Smyth, T. J. (2016). “Attribution of Atmospheric Sulfur Dioxide over the English Channel to Dimethyl Sulfide and Changing Ship Emissions”. In: *Atmos. Chem. Phys.* 16(8), 4771–4783. DOI: 10.5194/acp-16-4771-2016 (cit. on pp. 32, 39, 110).
- Zahnle, K., Schaefer, L., and Fegley, B. (2010). “Earth’s Earliest Atmospheres”. In: *Cold Spring Harb. Perspect. Biol.* 2(10), a004895. DOI: 10.1101/cshperspect.a004895 (cit. on pp. 4–6).
- Zeldovich, Y. B. (1946). “The Oxidation of Nitrogen in Combustion and Explosions”. In: *Acta Physicochimica USSR* 21, 577–628 (cit. on p. 20).
- Zhang, F., Chen, Y., Tian, C., Lou, D., Li, J., Zhang, G., and Matthias, V. (2016). “Emission Factors for Gaseous and Particulate Pollutants from Offshore Diesel Engine Vessels in China”. In: *Atmos. Chem. Phys.* 16(10), 6319–6334. DOI: 10.5194/acp-16-6319-2016 (cit. on p. 31).

Acknowledgements/Danksagung

Prof. John P. Burrows danke ich ganz besonders dafür, dass er mir die Möglichkeit gegeben hat, im Institut für Umweltphysik an solch einem brandaktuellen und auch gesellschaftlich hochrelevanten Thema zu forschen und meine Doktorarbeit zu schreiben. Ich danke ihm für seine Ideen, Vorschläge und stetige Unterstützung und auch für seinen unermüdlichen Einsatz für meine Vertragsverlängerungen!

Prof. Markus Quante vom HZG danke ich für die freundliche Übernahme des Zweitgutachtens trotz der momentan schwierigen Coronavirus-Lage und sein Interesse an meiner Arbeit.

Mein größter Dank gilt Folkard Wittrock, Enno Peters und Andreas Richter. Folkard danke ich für die tolle Betreuung, dein beeindruckendes praktisches und theoretisches Fachwissen und die immer gute und stets lustige Büro-Atmosphäre. Mit dir auf Messkampagne zu fahren oder Messgeräte auf- oder abzubauen macht einfach richtig Spaß, auch im tiefsten Winter auf Neuwerk. Enno danke ich ebenfalls für die gute Betreuung, die tolle Arbeitsatmosphäre im Büro, die vielen gemeinsamen Messkampagnen und auch für die unzähligen gemeinsamen Stunden beim Schrauben und Werkeln im Labor, die zwar manchmal anstrengend, manchmal auch frustrierend, aber immer überaus unterhaltsam waren.

Bei Andreas weiß ich gar nicht wo ich anfangen und enden soll. Dir auch vielen Dank für die gute Betreuung. Vielen Dank für die vielen hilfreichen Vorschläge und Kommentare, auch zu dieser Arbeit. Vielen Dank für viele interessante Diskussionen auf dem Weg zur Mensa, für dein enormes Fachwissen und für viele gute Ideen. Tausend Dank für deinen meist sofortigen Software-Support für deine Programme, seien es zu behebbende Fehler oder gewünschte Erweiterungen der Funktionen. Vielen Dank auch für deinen unermüdlichen Einsatz in unzähligen Verwaltungsangelegenheiten. Auch mit dir machen Messkampagnen und Gerätewartungen und -reparaturen wirklich viel Spaß und mit dir hatte ich in de Bilt wahrscheinlich die lustigste Autofahrt meines Lebens. Jeder der die Bremer DOAS-Gruppe kennt, weiß was er an dir hat.

Neben Folkard, Andreas und Enno danke ich auch den weiteren beiden Mitglieder unseres ehemaligen MESMART-Teams, Lisa Kattner und Barbara Matthieu-Üffing, für euren unermüdlichen Einsatz beim Aufbau und bei der Wartung der Messgeräte auf Neuwerk und auf der Celtic Explorer, ohne den die hier präsentierten Messungen und diese Arbeit nicht möglich gewesen wären. Vielen Dank für die Bereitstellung und Aufarbeitung der in-situ Vergleichsdaten. Von euch habe ich eine Menge über in-situ-Spurengasmessungen gelernt.

Die Zusammenarbeit und der Austausch mit euch hat uns allen glaube ich unglaublich weitergeholfen. Die vielen tollen "Ausflüge" nach Neuwerk, per Fähre, Schiff, Wattwagen, Trecker oder zu Fuß durchs Watt werden mir immer in Erinnerung bleiben, genau wie die gemeinsamen Schiffsreisen auf der Celtic Explorer.

Vielen Dank auch an das BSH und die Projektverantwortlichen Norbert Theobald und Stefan Schmolke, sowie den später hinzugestoßenen Andreas Weigelt. Ohne euren Einsatz für das MESMART-Kooperationsprojekt wären die hier gezeigten Messungen auch nicht möglich gewesen. Stefan danke ich auch für seine überaus hilfreichen Kommentare und Vorschläge zu meinen Forschungsergebnissen bei all unseren MESMART-Meetings. Andreas danke ich vielmals für seinen unermüdlichen Einsatz für die Messgeräte auf mehreren Celtic-Explorer-Fahrten und seine intensive Auseinandersetzung mit meinen Veröffentlichungen und seine hilfreichen Kommentare dazu. Vielen Dank auch für unseren tollen persönlichen Austausch, sei es vor Ort in Sülldorf oder Wedel, oder am Telefon, das ist mir immer wieder eine besondere Freude.

Mein besonderer Dank geht an Anja Schönhardt und Andreas Meier, ohne deren AirMAP-Gerät und deren Einsatz für die NOSE-Kampagne ich keine so tollen Vergleichsmessungen zur Validation gehabt hätte. Vielen Dank in dem Zuge auch an Thomas Ruthz von der FU Berlin, der all die tollen Messflüge mit der Cessna möglich macht.

Many thanks to all people from the DOAS-Group, present and past, for the friendly and pleasant working atmosphere, for all your helpful advice and support, many fruitful discussions, hundreds of tasteful cakes in the DOAS meeting, and many nice shared experiences and group activities.

Ein weiterer besonderer Dank geht an Lisa Behrens und Tim Bösch, die mir immer mit Rat und Tat zur Seite standen. Tim danke ich für unsere gemeinsamen Semester der Lehre im physikalischen Praktikum, wobei mir sowohl die Zusammenarbeit mit dir als auch die Arbeit mit den Studentinnen und Studenten immer viel Spaß gemacht hat. Lisa danke ich besonders für die vielen Gespräche und Diskussionen auf unseren unzähligen Fahrradfahrten zur Uni, die für meine Forschung als auch für diese Arbeit oft sehr hilfreich waren. Euch beiden danke ich nochmal ausdrücklich für unser tolles freundschaftliches Verhältnis und den niemals langweiligen und oft sehr hilfreichen Austausch über alle erdenklichen Themen.

Auch Andreas Meier, Bram Sanders und Andreas Hilboll gebührt noch ein besonderer Dank für ihre stetige Hilfe mit und den regen Austausch über alle möglichen Software-Fragen und -Probleme. Bram danke ich für die stets überaus unterhaltsamen kleinen Python- und Linux/Unix-Lektionen und die vielen kurzen, interessanten Einblicke in die holländische Kultur. A je to!

Andreas Hilboll, der leider im Rahmen der Corona-Pandemie verstorben ist, gebührt ein besonderer Dank für alles, was ich von dir über Python und Linux gelernt habe, was auch für die Auswertung der hier präsentierten Messdaten stets unglaublich hilfreich war. Ich danke dir für deine stets überaus hilfreichen Kommentare, Anmerkungen und deine wohldurchdachten Fragen bei Präsentationen und in persönlichen Gesprächen, und unsere Diskussionen über alle möglichen Themen. Du warst mir ein wirklich guter Freund geworden und dein Tod hinterlässt eine große Lücke in unser aller Leben. Ich werde dich nie vergessen.

Ich hätte vorher nie gedacht, dass man auf der Arbeit so viele tolle Freunde finden kann und ich freue mich auf die weitere Zusammenarbeit mit euch, und den weiteren persönlichen Kontakt zu allen, die das IUP zwischenzeitlich verlassen haben.

Vielen Dank auch an das Wasserstraßen- und Schifffahrtsamt (WSA) Cuxhaven und die Hamburg Port Authority (HPA) für die Unterstützung auf Neuwerk und beim Gerätetransport dorthin. Vielen Dank auch an das HPA für das zur Verfügung stellen der Winddaten von Neuwerk und Scharhörn.

We acknowledge the free use of tropospheric NO₂ column data from the OMI sensor from www.temis.nl.

Many thanks also to the Irish Marine Institute in Galway with their research vessel *Celtic Explorer* and its amazing crew, that made our several research cruises possible. Vielen Dank auch an das BSH für die Möglichkeit, unsere Luft-Messgeräte auf ihren regulären Monitoring-Fahrten einsetzen zu dürfen und vielen Dank auch an die vielen, hier nicht einzeln aufgezählten BSH-Kollegen, die ich auf den Schiffsreisen kennengelernt habe und die mir immer mit Rat und Tat zur Seite standen.

Ein besonderer Dank geht auch an meine Familie und besonders meine Eltern, die immer für mich da waren und mich immer unterstützt haben, ebenso wie Leonies Familie.

Ein ganz besonderer Dank geht auch an Leonie und Merle, die mir immer eine Quelle der Kraft und Freude waren.